THE UNIVERSITY OF ASTON IN BIRMINGHAM

"THE STUDY OF GAMMA-RAYS ASSOCIATED WITH FAST NEUTRON INTERACTIONS IN EXTENDED ASSEMBLIES"

Thesis submitted for the degree of

Doctor of Philosophy, in the Department of Physics

THESIS
539.122164 POU
189804 14 APR 1976

by

Mashallah Pourmansoori, B.Sc., M.Sc., M.Inst.P.

September, 1975.

ABSTRACT

The thesis is written in two parts. The first part describes the experimental measurements on the γ-rays emitted following the inelastic scattering of 14 MeV neutrons in both small and extended samples of the possible fusion reactor materials Iron and LiF. The source neutrons were produced by the $^{3}H(d,n)^{4}He$ reaction at an incident deuteron energy of 120 Kev using a S.A.M.E.S. type J accelerator. The γ-rays were detected using a shielded NaI(Tl) scintillation counter and the spurious background was reduced by suitably gating the γ-ray signals by a time of flight system based on the detection of the ^{4}He-particle associated with the instant of neutron production. Differential γ-ray production cross-sections were measured for the small samples, the results of which were analysed using a least squares fit and were used as a control with which to compare the differential cross-section measurements for the extended samples. In each case the results are compared with the predictions of a Monte Carlo type of calculation which took into account multiple neutron scattering and Compton degradation of the γ-ray energy at various angles to the neutron beam direction.

The second part of the thesis is concerned with a detailed feasibility study of the possible implementation of a similar experiment on the 3 MeV Dynamitron using neutrons from the $D(d,n)^{3}He$ reaction. The detection of the ^{3}He-particles in the presence of large numbers of scattered deuterons is considered and a design for a suitable magnetic discriminator system is presented. The suitability of various deuterium targets is considered and an experimental investigation into the behaviour of a heavy ice target is shown to be promising. A complete design for a suitable experimental arrangement is given.

ACKNOWLEDGMENTS

I would like to thank and express my gratitude to my supervisor, Dr. A. J. Cox, for supervising and directing this project and for his continuous interest and guidance throughout the whole of the project. In addition, I thank Professor S. E. Hunt, the head of the Physics Department, for his interest in the project and I am very indebted to Dr. P. N. Cooper of the Nuclear Physics Group for his advice during the work. Thanks are also due to Messrs. J. Phull and H. Biggs, the laboratory technical staff for their assistance.

I wish to express my appreciation for the three years University fee and expenses awarded by the Technical Department of the British Council in London. I am also very grateful to the Ministry of Science and Higher Education of Iranian Government for the award of three years' research scholarship, and to the Jundi Shapoor University, Ahwaz, Iran for granting me leave of absence and financial support for the period of this project.

Finally, I wish to thank my wife Ashraf and my son Ramin for their patience and understanding throughout the period.

Mashallah Pourmansoori

University of Aston in Birmingham

September 1975.

CONTENTS

Chapter 4 — Page No.

Chapter 1

1. General Introduction

1.1 Introduction

In fast neutron interactions with light and medium mass nuclei, the inelastic scattering events are mostly following by γ-ray production from the (n,n' γ) reaction.

The (n,γ) reaction is energetically possible, but the cross-section of this type of reaction at neutron energies in the MeV range is negligible compared to the (n,n' γ) reaction.

The investigation of fast neutron interactions in extended assemblies is of interest from the shielding design point of view in fission and fusion power reactors and, on the other hand, it provides a test of the theoretical description of the reaction mechanism and nuclear structure.

The present study is mostly concerned with extended samples of reactor materials and with the effect of multiple scattering on the emergent γ-ray spectrum.

At high neutron energies in addition to the (n,n' γ) reaction, charged particle reactions such as (n,p), (n,α), and (n,2n) reactions become possible. The threshold energy for the first two reactions for medium mass nuclei ($A \lesssim 80$) is about 5.0 MeV, while for the last one it is greater than 10MeV.

At incident neutron energies of less than about7MeV, the nuclear interactions with nuclei have been described by the compound nucleus theory[1] which gives a good fit to the experimental data.[2,3]

The direct interaction theory accounts for neutron interactions with nuclei at energies > 10 MeV. This theory shows acceptable fits to the experimental measurements.[4,5,6]

In the range of 10 to 20 MeV incident neutron the reaction mechanism could be expressed as a mixture of compound and direct reactions.[7]

The gamma-ray angular distribution measurements for the investigation of nuclear reaction mechanisms, and nuclear energy levels have been reported by many authors.[8-12].

The present work is concerned with neutron energies of 14 MeV and 2-5 MeV.

In work of this type it is necessary to reduce the spurious gamma-ray background in order to observe the gamma-rays associated with the inelastic neutron scattering. This is usually done by using a gating system based on taking the detection of the particle associated with neutron production as a zero time signal.

The first part of the thesis is devoted to the experimental results using the $T(d,n)^4He$ reaction with 120 KeV deuterons from the S.A.M.E.S. accelerator and the theoretical interpretation of these results.

The second part of the thesis describes a feasibility study concerned with the possibility of using gating system for 2-5 MeV neutrons produced by the $D(d,n)^3He$ reaction with using the Dynamitron facility at the Radiation Centre, University of Birmingham.

The gamma-ray spectra following the inelastic scattering of 14 MeV neutrons at different angles in the range of zero to 90^o in both extended and small samples of iron and lithium fluoride were measured, and the experimental results from the extended samples were compared with the theoretical prediction of multiple scattering calculations.

The angular distribution results obtained from small samples were compared with the previous measurements where available.

1.2 Survey of the theory of inelastic scattering

The investigation of inelastic scattering of particles by nuclei is a special case of the reaction B(x,y)C, where the incident and outgoing particles, x, and y are of the same type, but have different energies. C represents an excited state of the target nucleus B; the excitation energy is found from the difference in the energies of the x and y particles. In most cases of neutron inelastic scattering a nucleus that is raised to an excited state will decay to its ground state with the emission of γ-radiation. In the following sections the different types of reaction mechanism are described.

1.2.1 Compound Nucleus (C.N.) formation

The idea of the Compound Nucleus is that the incident particle, x, entering the nucleus B combines with B to form a compound nucleus C, in which the excitation energy is shared among many nucleons. The lifetime of C is approximately 10^{-15} sec., and it is long compared to the transit time of the particle x, through the nucleus which is about 10^{-22} sec. The expression for the cross-section of a nuclear reaction in compound nucleus theory is in the form of:

$$\sigma(x,y) = \sigma_c(x) P_c(y) \quad \ldots\ldots\ldots\ldots\ldots\ldots \quad (1.1)$$

where $\sigma_c(x)$ is the cross-section for the formation of compound system from the incident particle x, and the target nucleus B, and $P_c(y)$ is the probability that the compound system, once formed will decay by emission of particle y. In the compound nucleus reaction the model describing these properties consists in replacing the nucleus by a one-body potential which acts upon the incident nucleon.

This potential $V = V_o + iV_i$ is complex, and the real part

represents the average potential in the nucleus, and the imaginary part causes an absorption which describes the formation of the compound nucleus. It can be understood that the nuclear matter is partly transparent for the incoming particles, and by its analogy to the description of light in matter this is called "optical model".

1.2.2 Statistical Theory

In the relation $\sigma(x,y) = \sigma_c(x)P_c(y)$, the $\sigma_c(x)$ is most readily calculated from the "optical model" by:

$$\sigma_c(x) = \pi \lambda^2 \sum_i (2\ell + 1)\, Ti \quad \ldots\ldots\ldots\ldots\ldots \quad (1.2)$$

where λ is the reduced de Broglie wavelength of the incident particles, and Ti the transmission coefficient for particles entering the nucleus, and ℓ is the orbital angular momentum quantum number of the particles.

The value of Ti can be found by matching the wave functions and their first derivatives which describe the particles inside and outside the nucleus at the edge of the nucleus.

The second part, i.e. $P_c(y)$ is less straightforward. Derivation of the $P_c(y)$ is based on the principle of Fermi-Dirac statistics.[13]

1.2.3 Direct interaction

The Compound nucleus theory considers that the bombarding particle interacts with the nucleus as a whole, but in direct interaction the bombarding particles interact with a single nucleon or small complex of nucleons. In the Compound nucleus theory the nucleus excites uniformly and evaporation of low-energy nucleons follows.

As the kinetic energy of the bombarding particle increases,

the Compound nucleus model fails to explain some of the observed phenomena, and one such observation is the occurrence of high energy neutrons and protons in the emitted particles. In direct interactions the incident particles interact during a time of the order of the time it takes the particle to traverse a nuclear diameter.

The cross-sections for the direct reaction and compound nucleus process are different. The angular distribution of the emitted particles, and angular correlation between these particles, and subsequent γ-radiation can differ markedly for the two reaction mechanisms. In direct interaction the angular distribution is more forward peaked than the Compound nucleus reaction.

1.3 Multiple scattering

A fraction of the incident neutrons are scattered only once. Because of the decrease of the neutron flux in the scattering material, the spatial distribution of the singly scattered neutrons can be given by an exponential form, but the rest of the neutrons are scattered for a second or more times. The spatial distributions of these multiple scattered neutrons cannot be described by a simple exponential expression.

The effect of the multiple scattering in γ-ray production cross-section measurements is to cause an increase in the γ-ray yield, due to effective increase in the neutron flux, and consequently the cross-section is artificially high.

The probability of the multiple scattering effect depends on the dimension of the sample and on the scattering cross-section. A simple Monte Carlo type computer programme to account for the effect of multiple scattering of fast neutrons in extended samples in order to take care of the finite size of the neutron beam incident on to the extended sample, has been developed in this work.

1.4 Survey of experimental methods

The possible experimental methods for the measurement of the angular distribution in fast neutron interactions with scattering material are surveyed and discussed below.

1.4.1 "Open" geometry (Minimum shielding)

The open geometry as in the case of ring geometry described below must be carried out in a large experimental room so that by keeping the apparatus as far as possible from the neutron source the scattered background in the gamma-ray detector is reduced. The open geometry has been used by many experimenters.[15,16] In the case of ring geometry, a ring shaped scatterer is used. The axis of this ring passes through the neutron source and γ-ray detector. Because of the symmetry around the ring axis, the γ-rays from different sectors of the ring entering the detector make the same angles with the incident neutrons. For angular distribution measurements the scattering angle can be varied by changing the relative position of the detector compared to the scatterer. In this case the energy and the intensity of the neutrons striking the scatterer remain constant. The ring geometry has been applied by Hosoe and Suzuki.[14] They achieved background reduction by surrounding the neutron source by a block of paraffin wax with boric oxide. A plan view of a ring geometry arrangement is shown in Figure 1.1.

1.4.2 "Closed" geometry (Massive shielding)

This geometry is intended to reduce the background as much as possible by shielding the γ-ray detector from the neutron source, scattered neutrons and unwanted γ-radiation. If a limited space only is available for the experimental arrangement, then a closed geometry has to be used. The most common geometry used

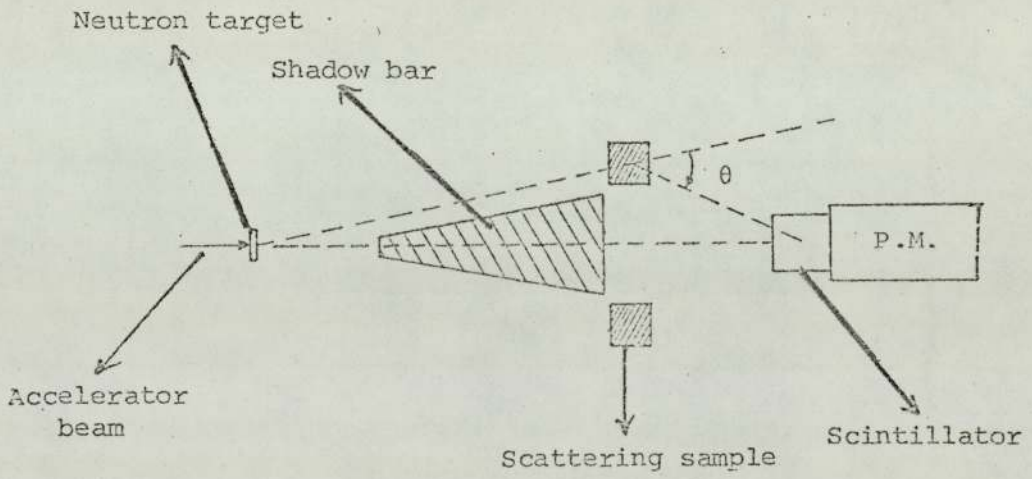

Figure 1.1 A typical ring geometry arrangement.

by several authors [17,18] is a closed geometry with massive shield around the gamma-ray detector.

A plan view of such a closed geometry can be seen in Figure 1.2.

1.5 Time-of-flight technique

The background reduction in neutron scattering experiments using either 'Open' geometry or 'Closed' geometry can be achieved by using a time-of-flight technique. In this method the moment of production of a neutron at the target is fixed by a start signal. There are two methods for obtaining the start signal for the time-of-flight technique. These are, the 'pulsed source method' and the 'Associated particle method'.

A survey of recent literature indicates that nanosecond beam pulsing and associated particle methods have been used on several Van de Graaff accelerators, cyclotrons, and linear accelerators. In all of these experiments it is necessary to use a system with good energy resolution $\left(\frac{E_n}{\Delta E_n}\right)$ which depends on the time resolution $\left(\frac{t_n}{\Delta t_n}\right)$. The energy resolution can be increased either by increasing t_n, i.e. increasing the flight path, or by decreasing Δt_n, but since the neutron flux varies inversely with the square of the flight path, it becomes clear that it is advantageous to decrease Δt_n, rather than to increase flight path.

1.5.1 Pulsed source method

In this technique short duration pulses of neutrons can be obtained by using Klystron bunching [19]; although this usually gives poor energy resolution, because the bunching process produces an appreciably larger energy spread in the incident ion beam, but the Mobley magnet compression method has proved to be a reliable method for achieving sharp ion pulses with Van de Graaff accelerators. The actual performance of a Mobley system has been described

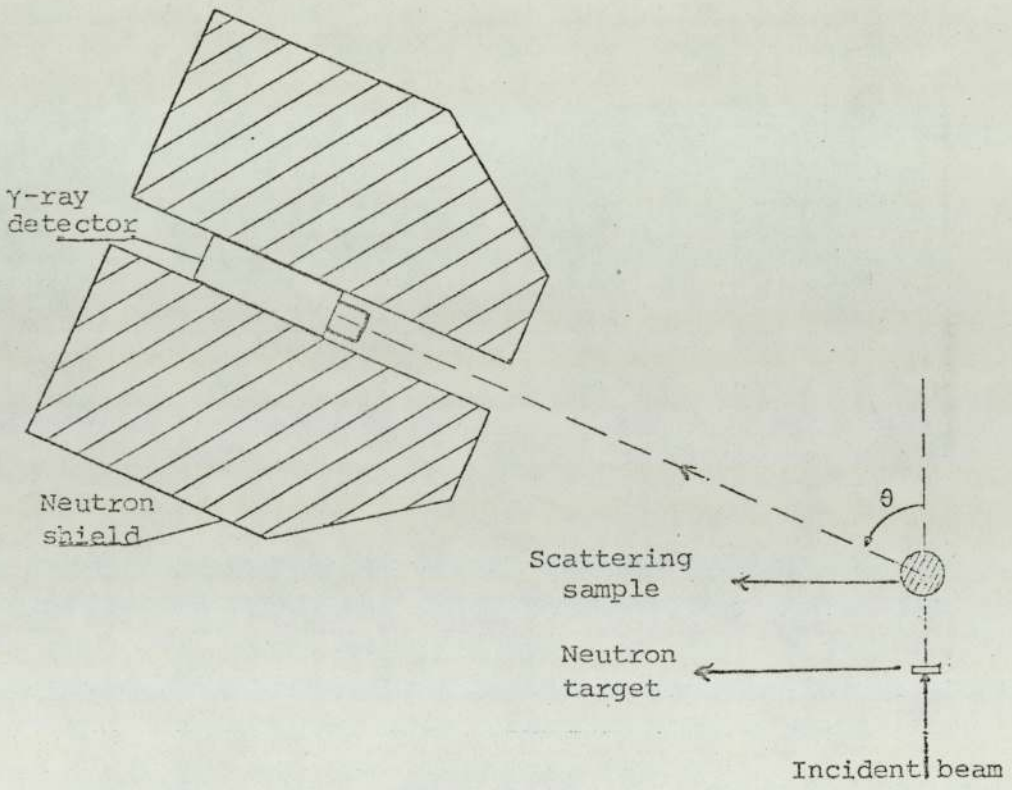

Figure 1.2 A typical closed geometry arrangement.

by Cranberg et al.[20]

An rf ion source and a beam chopper, located in the high voltage terminal, produce pulses of about 10ns. width, and 1.0 μsec. spacing, and after acceleration the Mobley magnet system compresses the pulses to about 1.0ns. width. The peak current is about several mA, and the accelerator delivers the beam to the target in bunches of about 1.0ns duration, and 1.0μ sec. apart. The time resolution of such a device is of the order of 2.0ns, this means that because of the duration of the beam pulse and the time uncertainties in the electronic system, the flight time for a neutron of a given energy is uncertain to about 2.0n sec.

1.5.2 Accociated particle method

This method, which is described in detail in Chapter 8 for establishing the starting time of the neutron production, requires the detection of an associated charged-particle with the emission of each neutron. The technique is used for both the 2-5 MeV and 14 MeV work.

The difficulty in developing an associated particle method for $D(d,n)^3He$ reaction is the detection of ^3He-particles from the reaction well resolved from the deuteron elastically scattered, and also from protons and tritons which are produced by the competing $D(d,p)^3H$ reaction.

In order to discriminate between ^3He-particles and elastically scattered deuterons at low bombarding deuteron energies of a few hundred KeV in some experiments [21,22] thin metal foils have been used. At higher deuteron energies Shapiro et al.[23] have used a magnetic analyser to separate the ^3He-particles and elastically scattered deuteron from the target. The electrostatic deflection method has been used by Put et al.[85]

Experiments based on the associated particle method at

incident deuteron energies in the MeV region can be done for the D-d reaction without using a magnetic analyser, or electrostatic deflector. Schuster [24] has developed an associated particle system, and the high count rate of elastically scattered deuterons in the ^{3}He-detector have been successfully minimized by using a thin low-mass deuterated polyethylene target.

Chapter 2

2. Introduction to Part I

The study of 14 MeV neutron interactions and the consequent gamma-rays are of interest from several points of view. It is relevant to the energy deposited in the neutron absorption in the blanket and the surrounding materials of a fusion reactor, and to the breeding of new tritium fuel in a deuterium-tritium fusion reactor.

Fusion Reactors

A fusion reactor is an assembly in which a nuclear fusion reaction is maintained and controlled for the production of energy. Nuclear fusion is a nuclear reaction between light atomic nuclei as a result of which a heavier nucleus is formed and a quantity of nuclear energy is released. In a fission reaction practically all the energy remains with the fission products, and the neutrons sustain the reaction. In contrast in the fusion reaction it is the neutrons that carry the energy away and the reaction is supported by the remainder of the reaction products. High energy neutron absorption is therefore an inherent necessity of the D-T fusion reactor blanket in order to extract the energy. The 14 MeV neutrons of the fusion reaction are usually above the threshold for (n,n'), (n,2n), (n,α) and (n,p) reactions, in contrast to the situation of the about 2.0 MeV fission neutrons. It is therefore necessary to consider the cross-section data for these reactions when considering both breeding and shielding materials. Fig.2.1 shows a diagram of a possible fusion reactor.

In a D-T fusion reaction, 17.6 MeV of energy is released in the form of 14.1 MeV neutrons and 3.5 MeV α-particles. The neutrons escape from the plasma zone with little interaction and they are captured in a zone surrounding the plasma, called the

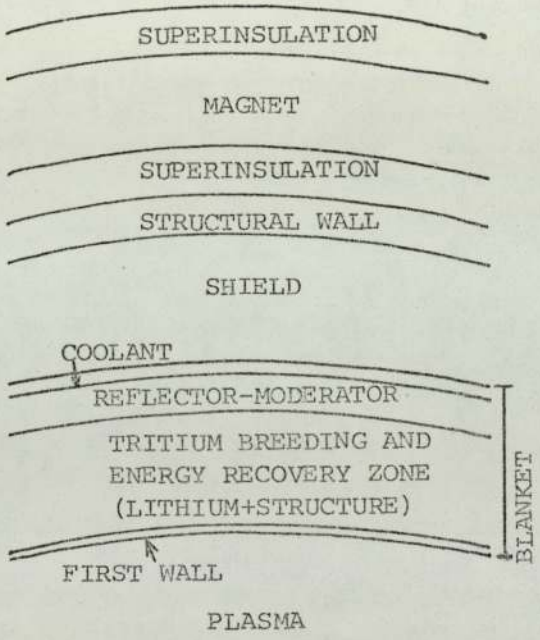

Figure 2.1. The schematic of blanket and shield regions of a fusion reactor design.

blanket, where the kinetic energy is converted to heat The blanket is expected to incorporate lithium in one form or another to breed new tritium. The plasma is confined by superconducting magnets cryogenically cooled to about $4^{\circ}K$. Thus, an additional region, called the magnet shield is required to further protect the magnet from radiation damage. Therefore the performance of blankets and shields is important for future fusion reactor design.

Among the important neutronic and photonic properties of these systems are the total energy deposition per fusion event, the spatial distribution of the nuclear heating, and the tritium breeding ratio. Determination of the total energy production per fusion reaction is very important in the economic prediction of these systems. The spatial distribution of the heating rate is needed for the heat transfer design. Most recent fusion reactor designs operate on the deuterium-tritium cycle, and in this case the new fuel can be bred by surrounding the fusion reactor with a neutron moderator (blanket). Because tritium is not available in sufficient abundance, this type of fusion reactor would have to rely on the breeding of tritium through capture of neutrons by lithium, which is

$$^{7}Li + n \longrightarrow T + {}^{4}He + n$$

$$\text{and} \quad {}^{6}Li + n \longrightarrow T + {}^{4}He$$

As it is shown in the above relations the material used for the blanket can be natural lithium, i.e. 7.56% ^{6}Li and 92.44% ^{7}Li. The lithium can be used in the form of solid lithium alloy or compound lithium.

If the reactor is to operate on the deuterium-tritium cycle, then tritium production in the blanket must be at a rate larger than the consumption of tritium in the plasma, i.e. the breeding

ratio which is defined as the number of the tritium atoms produced in the blanket per fusion reaction must be greater than unity.

The gamma-rays produced by neutron interactions in the reactor surrounding deposit energy in various parts of the reactor; therefore the study of γ-ray production in the investigation of fusion reactors is important.

The study requires a measurement of changes in γ-ray energy spectra and gamma-ray angular distributions as the scattering samples change from small samples to large samples.

The energy spectra and angular distribution measurements of the gamma-rays from the interaction of 14 MeV neutrons with small and large samples of iron and lithium fluoride are discussed in Chapter 6.

Chapter 3

3. Gamma-ray Attenuation

3.1 Interaction of gamma-rays with matter

The subject of gamma-ray interaction processes has been treated extensively by many authors. A broadly descriptive reference is the discussion by Bethe and Ashkin.[52] In view of the many references in existence, only enough of an outline will be given here to provide the orientation needed for the γ-ray attenuation problem, especially in the case of calculating the γ-ray absorption coefficient of the medium.

The three main processes by which γ-rays are attenuated in a medium are:

(i) the photoelectric effect, (ii) pair production,

(iii) Compton scattering.

Photoelectric effect In the photoelectric effect an incident photon transfers all its energy to one of the atomic electrons, ejecting it from the atom. The kinetic energy of the emitted electron is equal to the incident photon energy less the ionization energy of the electron. Hence the photoelectric process can occur with a given atomic electron only if the energy of the photon is greater than the electron binding energy. In principle, some of the excess photon energy goes into the kinetic energy of the recoiling atom, but this is always a negligible fraction. On the other hand, the excess momentum carried by the recoil atom plays an important role. The momentum cannot be conserved in the photoelectric effect on a free electron, therefore the binding of the electron to the atom is very important for photoelectric effect. For photon energies very large compared with the ionization energy, the electron appears to be only lightly bound and the photoelectric effect becomes relatively improbable. Hence as the photon energy

increases, the cross-section for the photoelectric emission decreases.

Pair production In pair production all the energy of the incident photon is transformed into creating an electron pair, i.e. an electron and a positron. The kinetic energy of the pair is equal to the incident photon energy less twice the rest mass of the electron, therefore pair production has a threshold at 1.02 Mev below which it cannot take place. As in the case of photoelectric effect, the pair production cannot take place in free space; to conserve momentum it can occur only in the electric field of the particle which can carry away some of the momentum in the recoil. The cross-section is rapidly rising as a function of energy above the threshold, in the region below 10 MeV.

3.2 Compton Scattering

In addition to the two purely absorptive processes in the interaction of γ-rays mentioned there are several other ways in which γ-rays can be scattered. The most important of these is Compton scattering. If a gamma-ray photon, which according to the quantum theory has energy $h\nu$ and momentum $h\nu/c$ where h is the Planck's constant, ν is its frequency (here c is the velocity of light) collides with an electron assumed to be free, then some of the momentum will be transferred from the photon to the electron. Since the momentum and energy conservation laws apply to the collision, the photon must have lost energy, that is $(h\nu)_f$ is less than $(h\nu)_i$ where the subscripts f and i refer to final and initial respectively. The frequency of the radiation has been lowered by the collision. Compton scattering provides a method of lowering the energy of photons by successive collisions, until they have been sufficiently degraded to be absorbed photoelectrically.

The equation describing the change of photon energy during a Compton collision can be easily shown from conservation of energy and momentum that

$$E = E_o \left[1 + E_o/0.51 (1 - \text{Cos } \theta)\right]^{-1} \quad \ldots\ldots\ldots\ldots \quad (3.1)$$

where E_o is the initial photon energy, E is the photon energy after being scattered, and θ is the deflection angle of photon. Glancing collisions, i.e. $\theta \simeq 0$ will transfer very little energy. Equation (3.1) gives the energy of the scattered photon in terms of the initial energy and the scattering angle. The recoiling electron has a kinetic energy given by:

$$E_e = E_o - E = E_o \times \frac{(1 - \text{Cos } \theta) \frac{E_o}{0.51}}{1 + \frac{E_o}{0.51}(1 - \text{Cos } \theta)} \quad \ldots\ldots\ldots\ldots \quad (3.2)$$

The kinetic energy of the electron has its maximum value when Cos $\theta = -1$ or $\theta = 180^{o}$, and the photon is scattered directly backward. The electron energy, in this case, is

$$E_{e_{max}} = \frac{E_o}{1 + \frac{0.51}{2\,E_o}} \qquad \text{..... (3.3)}$$

The electron receives the minimum energy in the case that the photon continues with its initial frequency in the forward direction, and the electron is ejected with very nearly zero velocity in a direction perpendicular to that of the photon path.

A photon must be deflected through a large angle for its energy to be appreciably degraded in a single collision. The high energy photons scattered through a right angle will have energies of about 0.51 MeV, and those back-scattered through 180^{o} will have energies of about 0.25 MeV. A short and simple computer programme in Algol is written from which the values of scattered photon energies and electron recoil energies can be obtained for various incident photon energies and angles of deflection.. The layout of this computer programme and its output data for several incident photon energies is shown in Appendix B.

The probability that an unpolarized photon of initial energy $h\nu_o/0.51$ should be scattered through an angle θ into a solid angle $d\Omega$, which called the Compton differential cross-section per electron, $\frac{d\sigma(\theta)}{d\Omega}$ is given by the Klein-Nishina[49] formula:

$$\frac{d\sigma(\theta)}{d\Omega} = r_o^2\, d\Omega\, \frac{1+\text{Cos}^2\theta}{2} \times \frac{1}{\left[1+\frac{h\nu_o}{0.51}\,(1-\text{Cos}\,\theta)\right]^2} \times \left\{ 1 + \frac{\left(\frac{h\nu_o}{0.51}\right)^2 (1-\text{Cos}\,\theta)^2}{(1+\text{Cos}^2\theta)\left[1+\frac{h\nu_o}{0.51}\,(1-\text{Cos}\,\theta)\right]} \right\} \qquad \text{.....(3.4)}$$

The differential cross-section per electron predicted by this formula

as a function of θ is shown in Fig. (3.1). The total Compton scattering cross-section per electron σ_t which is obtained by integrating the equation 3.4 over all angles gives the relation:

$$\sigma_t = 2\pi r_o^2 \left\{ \frac{1+\frac{h\nu_o}{0.51}}{\left(\frac{h\nu_o}{0.51}\right)^3} \left[\frac{2\,\frac{h\nu_o}{0.51}\left(1+\frac{h\nu_o}{0.51}\right)}{1+2\left(\frac{h\nu_o}{0.51}\right)} - \ell n\left(1+2\,\frac{h\nu_o}{0.51}\right)\right] + \right.$$

$$\left. \frac{1}{2\,\frac{h\nu_o}{0.51}}\ \ell n\left(1+\frac{h\nu_o}{0.51}\right) - \frac{1+3\,\frac{h\nu_o}{0.51}}{\left(1+2\,\frac{h\nu_o}{0.51}\right)^2} \right\} \qquad (3.5)$$

where r_o is the classical radius of the electron, 2.82×10^{-13} cm. Fig. 3.2 shows the total scattering and absorption cross-sections per electron as a function of photon energy for light and heavy elements given by White.[25] From this figure it is realised that over a considerable range of gamma-ray energies, which includes much of the radiation emitted by a nuclear reactor, the Compton cross-section predominates over the photoelectric and pair-production cross-sections, and since equal masses of all materials except hydrogen contain roughly the same number of electrons; approximately 3×10^{23} electrons per gram, it follows that in this energy region equal masses of all materials will be about equally effective as gamma-ray attenuators.

3.3 The attenuation of γ-rays in matter

The rate at which gamma-rays are attenuated is determined primarily by the atomic number and density of the shielding material, and to a lesser extent by the geometrical configuration. The illumination of a large area of an extended thick shield by an uncollimated beam of photons is very difficult to treat theoretically, but it is simpler to take a collimated narrow beam.

In the case of a perfect geometry the attenuation is found to be exponential and is given by:

$$\phi(x) = \phi_o \exp(-\mu x) \qquad (3.6)$$

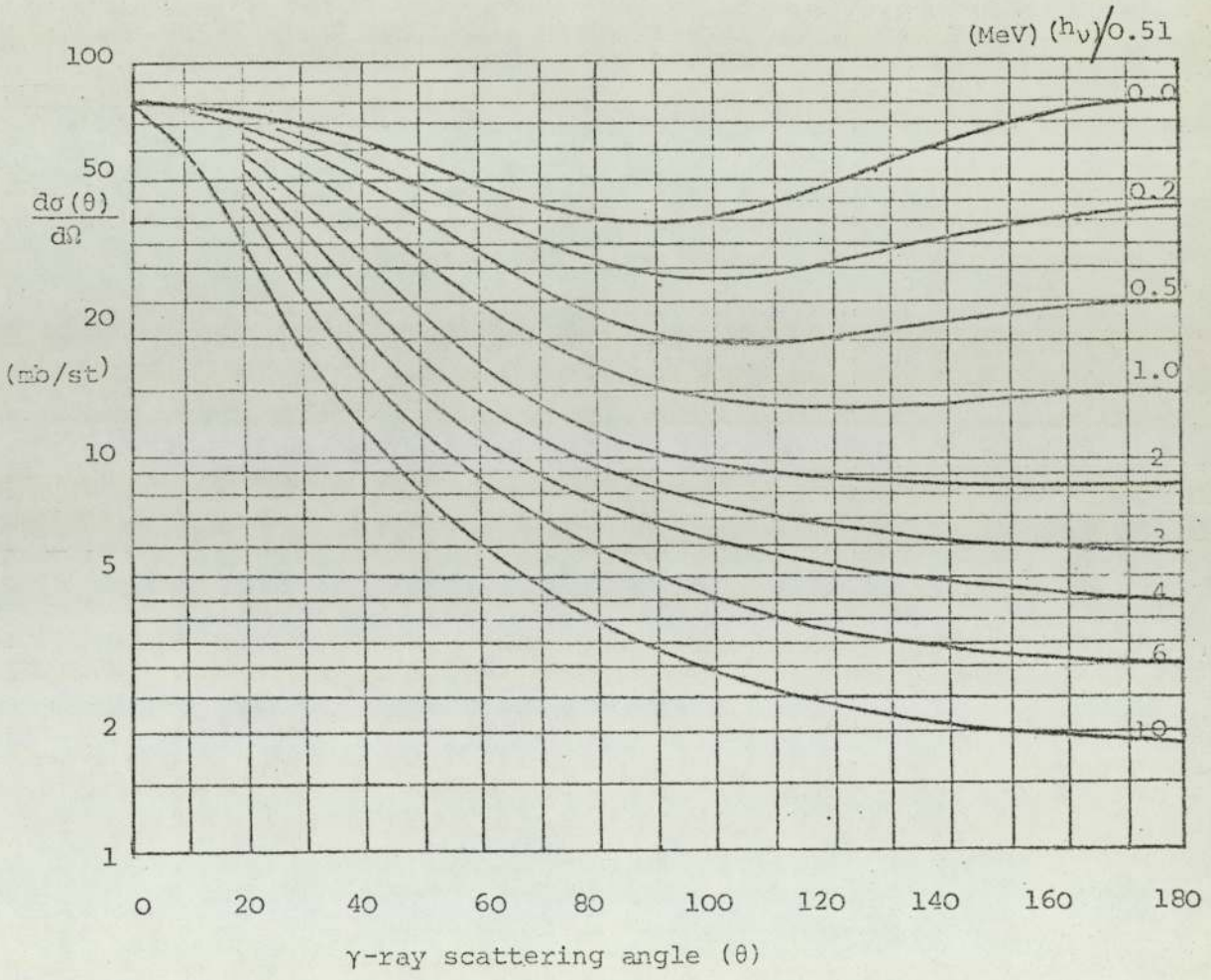

Figure 3.1 Compton differential cross-section per electron as a function of energy and scattering angle.

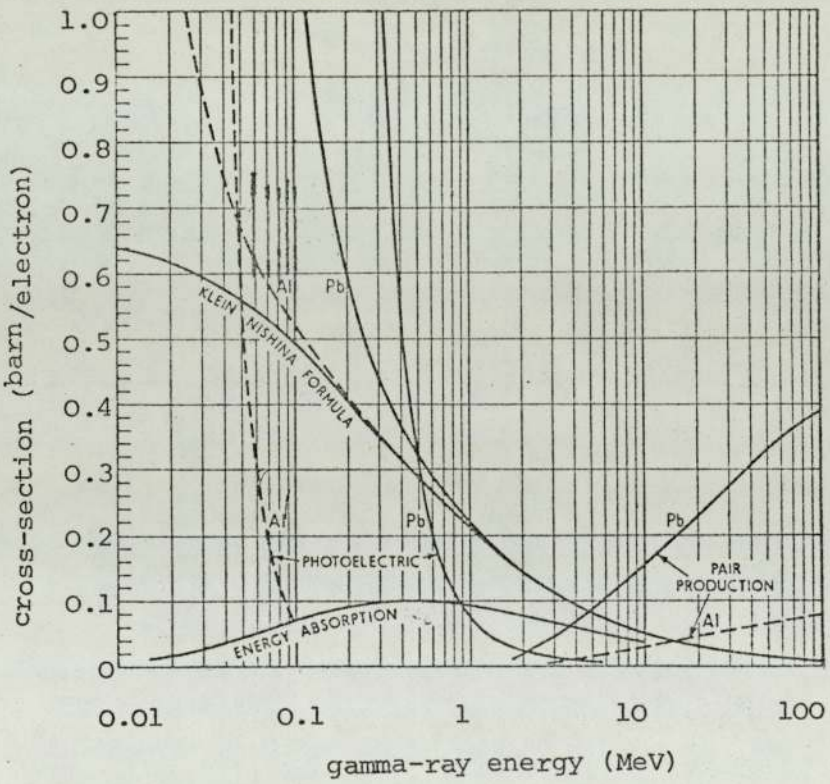

Figure 3.2 Scattering and absorption cross-sections per electron for light and heavy elements as a function of γ-ray energy.

where ϕ_o is the incident intensity, $\phi(x)$ is the intensity observed through an absorber of thickness x, and μ is the linear absorption coefficient.

The total absorption coefficient, which appears in equation (3.6) is the sum of the absorption coefficients for the three different processes. In addition, the absorption coefficient depends on the nature of the incident γ-rays as well as the nature of the absorbing material. Consequently , the absorption coefficient of γ-rays cannot be described by a single formula. Each partial cross-section or absorption coefficient must be evaluated as a function of energy for a given material. Values of mass absorption coefficient $\frac{\mu}{\rho}$ where ρ is the density of absorber, are plotted in figures (3.3) and (3.4) from tabulated data by White.[25]

In the γ-ray energy ranges from 0.01 to 100 MeV. as it can be seen from the Figures 3.3 and 3.4 at low energies, the removal of photons from the beam is mainly due to the photoelectric effect, which becomes more important as the atomic number Z of the absorber is increased, and as the photon energy decreased.

At high photon energies, and for high Z, the pair production predominates.

In between there is a region in which the Compton scattering process is the most important, and in which equal masses of all materials are therefore about equally effective. This region (0.5 to 10 MeV), happens to be the one which is most important in reactor technology.

Over most of the energy range covered in figures 3.3 and 3.4 the variation of the mass absorption coefficients with atomic number is smooth, and values for elements not shown in the figures can be obtained by interpolation, but this is not the case for high atomic number and low γ-ray energy.

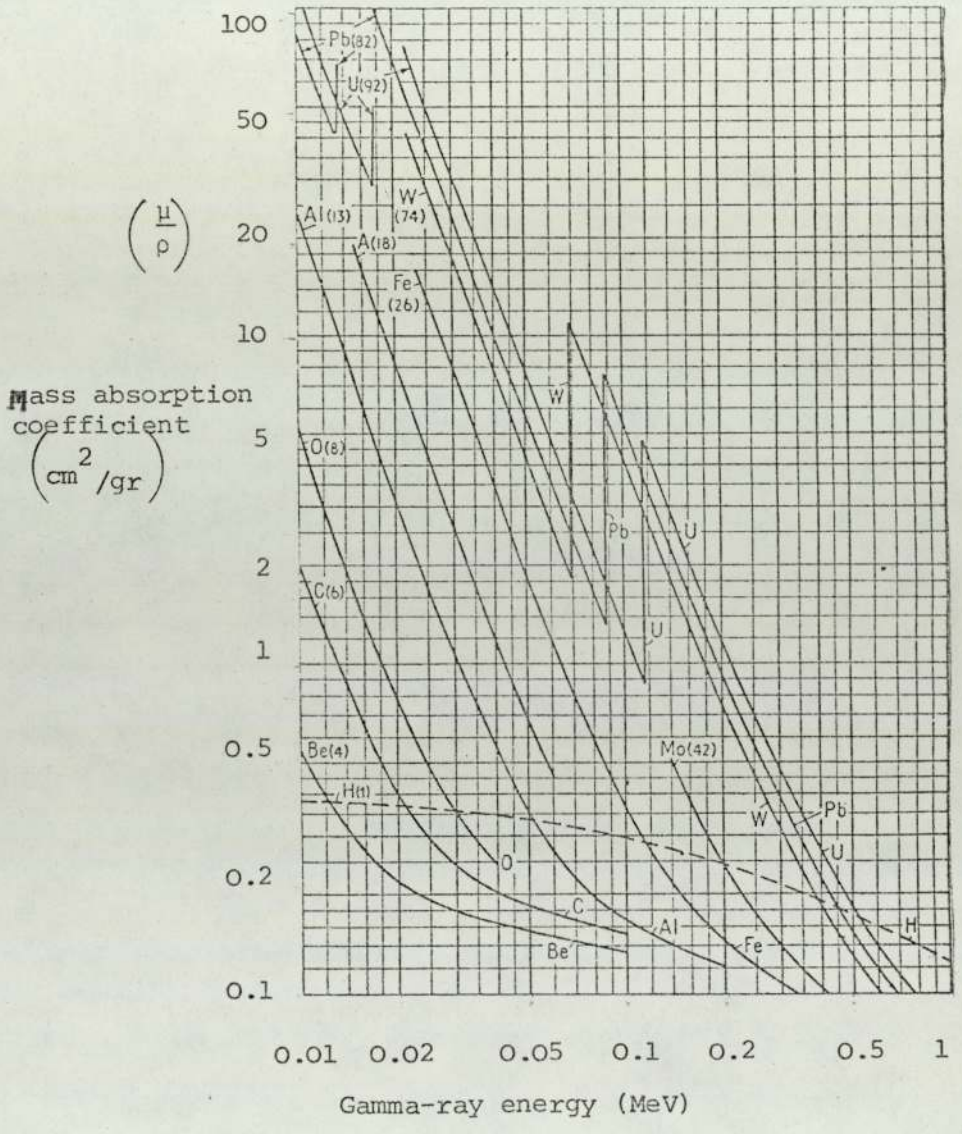

Figure 3.3 Mass absorption coefficients as a function of atomic number and γ-ray energy (E_γ = 0.01 - 1.0 MeV)

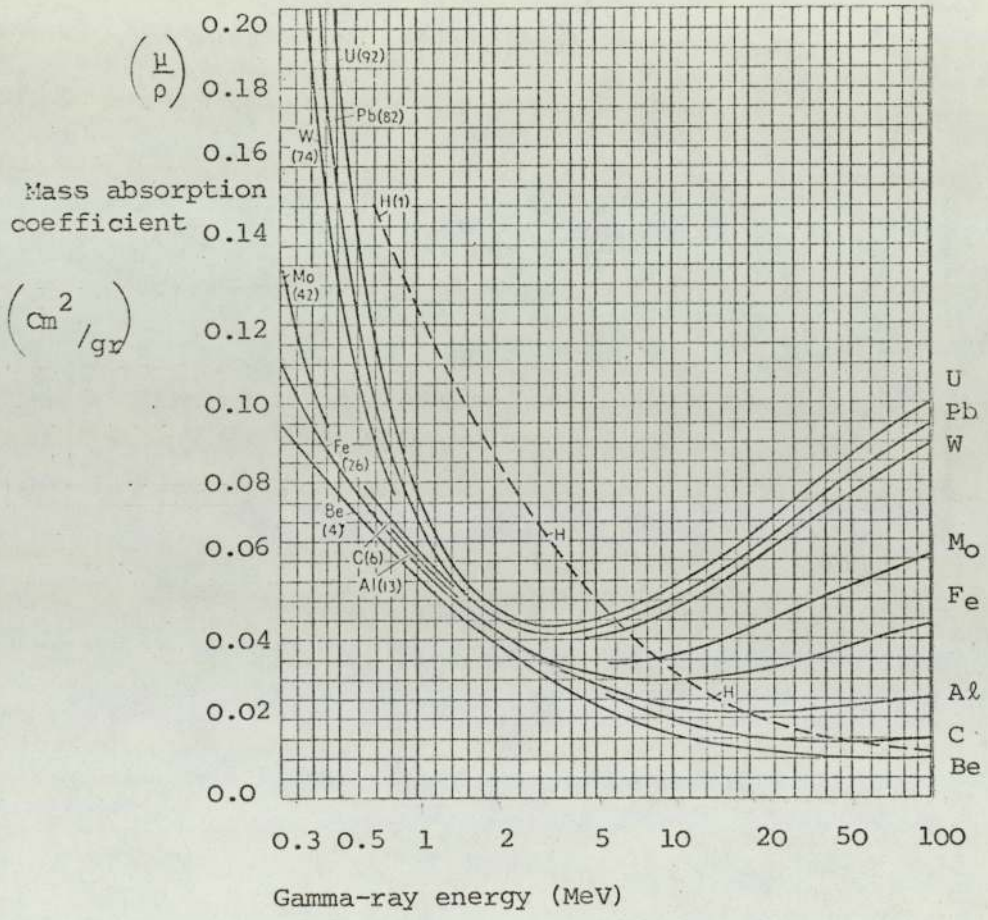

Figure 3.4 Mass absorption coefficients as a function of atomic number and γ-ray energy (E_γ = 0.3 - 100 MeV)

An extensive tabulation for the mass absorption coefficients for different materials is given by Latysheve[26] and Victoreen.[27] The mass absorption coefficients $\frac{\mu}{\rho}$ is proportional to the total photon interaction cross-section per atom σ_t, i.e. to the sum of the cross-sections for all the elementary scattering and absorption processes, and it is given by:

$$\frac{\mu}{\rho} = \sigma_t \times \frac{N_o}{M} \quad \ldots\ldots\ldots\ldots\ldots\ldots\ldots\ldots \quad (3.7)$$

where N_o is Avogadro's number, and M is the atomic weight of the absorber material.

When the absorber is a chemical compound or a mixture, its mass absorption coefficient $\frac{\mu}{\rho}$ can be approximately evaluated from the coefficients $\frac{\mu i}{\rho i}$ for the constituent elements according to the weighted average by the formula shown below:

$$\frac{\mu}{\rho} = \Sigma_i \, w_i \, \frac{\mu_i}{\rho_i} \quad \ldots\ldots\ldots\ldots\ldots\ldots\ldots\ldots \quad (3.8)$$

where w_i is the proportion by weight of the ith constituent.

As an example, for lithium fluoride compound (LiF), $m_{7Li} = 7.0$ and $m_{19F} = 19.0$; therefore,

$$\frac{\mu}{\rho}(LiF) = \frac{7}{26} \, \frac{\mu}{\rho}(Li) + \frac{19}{26} \, \frac{\mu}{\rho}(F)$$

where $\frac{\mu}{\rho}$ (Li) and $\frac{\mu}{\rho}$ (F) are the mass absorption coefficients for lithium and fluorine respectively.

Since the absorption coefficient is a function of gamma-ray energy and depends on the Z number of the sample material, therefore in the correction for self-absorption of γ-rays by the scattering sample in differential cross-section measurements, and also in the calculation of the γ-ray yield following the multiple scattering of neutrons in extended samples the values of μ were found from the above discussion.

Chapter 4

4. Experimental arrangement for d-T reaction

The gamma-rays associated with the scattering of 14.0 MeV neutrons produced by a S.A.M.E.S. type J accelerator were studied using the associated time-of-flight system to gate the γ-ray signals in order to reduce the background.

The emergent gamma-ray spectra from both the extended and small samples of possible fusion reactor materials were studied, and in the case of extended samples the results were compared to the prediction of the theoretical model. Fig. (4.1) shows a schematic diagram of the geometry and the following sections discuss the arrangement in detail.

4.1 Neutron Source

The 14.0 MeV neutrons were produced using the $T(d,n)^4He$ reaction with a deuteron beam of energy up to 120 KeV from the accelerator incident on to a titanium-tritide target.

4.2 The S.A.M.E.S. accelerator

The S.A.M.E.S. Type J accelerator shown in Fig. 4.2 . The accelerating voltage, produced by an electrostatic generator hermetically sealed in a hydrogen atmosphere can be varied from zero to 160kV. Deuterium gas, from a reservoir, is admitted to the ion source through a thermally activated palladium leak. The ion source is excited by a 100 MHz oscillator and can produce currents on target of 200μA. under favourable conditions of steady running. Extraction into the acceleration system is effected by applying a zero to 6kV repelling voltage to the electrode. The ions are concentrated at the entrance of the extraction canal by the magnetic field located at the base of the ion source bottle. An oil immersed Cockcroft-Walton multiplier circuit supplies the zero to 45kV required for beam focussing. These units, which are situated inside the high voltage terminal, are

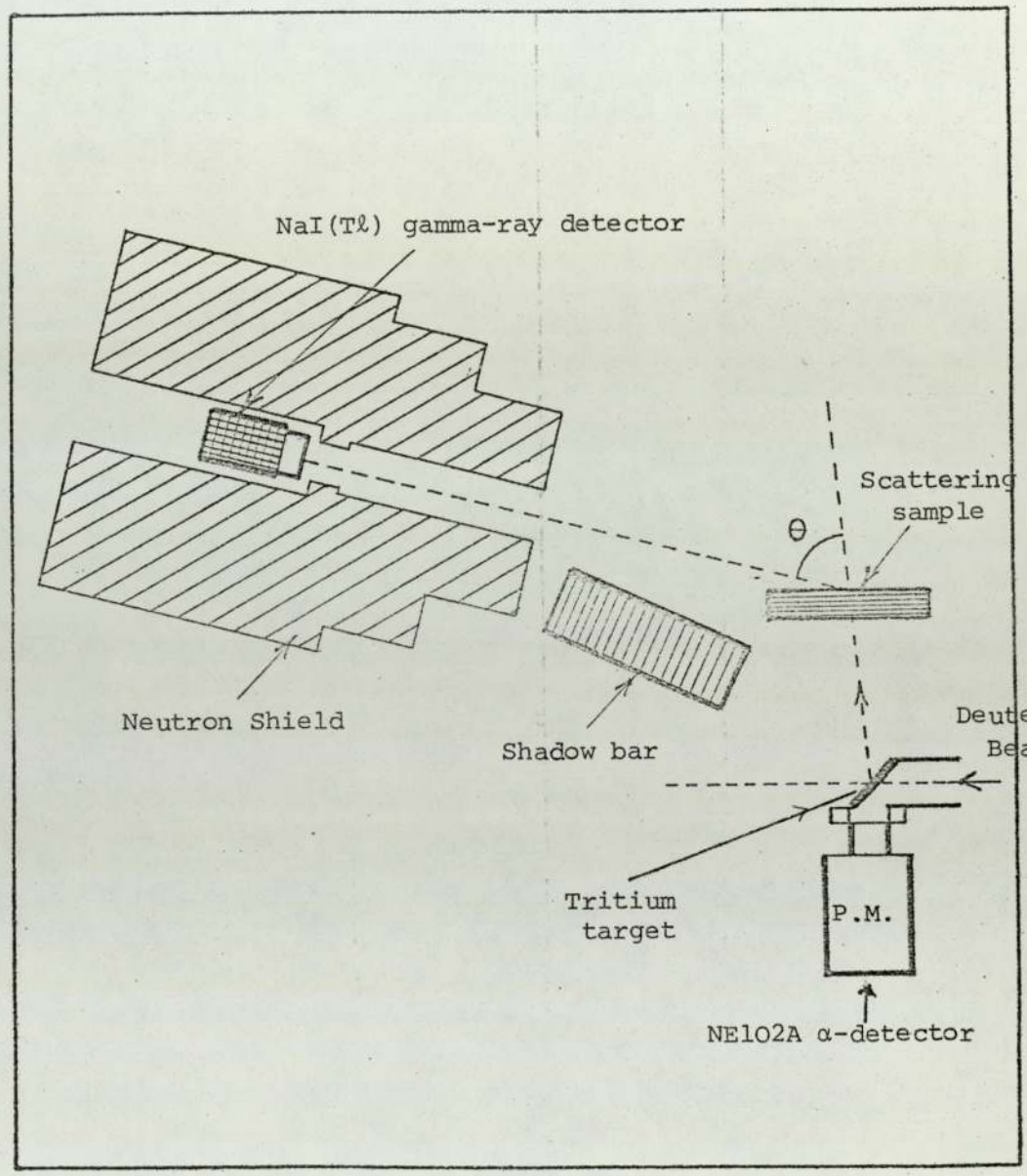

Figure 4.1 A schematic diagram of the experimental arrangement.

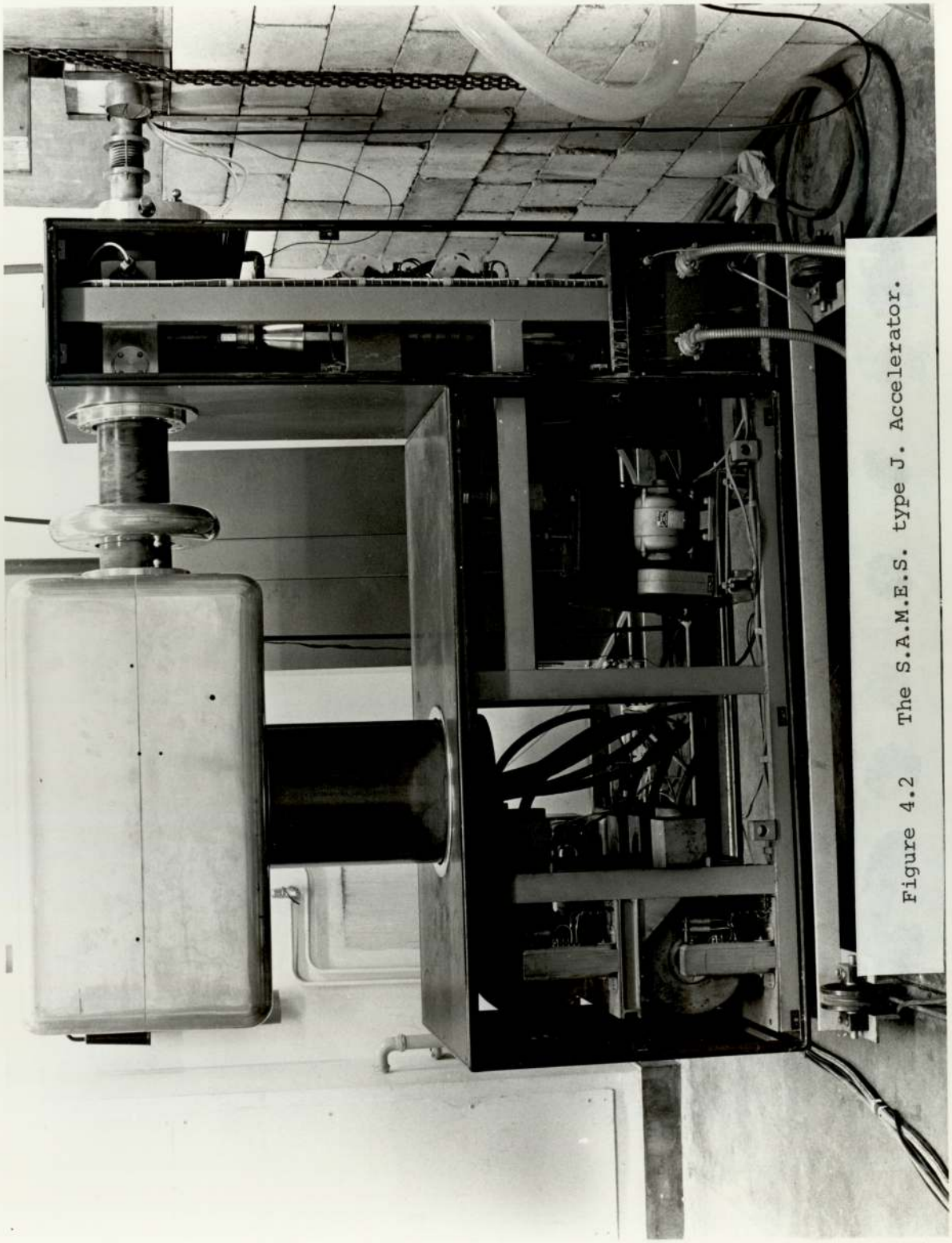

Figure 4.2 The S.A.M.E.S. type J. Accelerator.

controlled through a system of isolation transformers that are fed from variable transformers.

4.3 The beam tube

A long beam tube was used to bypass other experimental equipment in the experimental room. The beam tube was evacuated to a pressure of about 2×10^{-6} torr. The main pumping stage was part of the S.A.M.E.S. accelerator, but because of the length of the drift tube, an auxiliary pumping stage was provided at the other end of the beam tube. A liquid nitrogen cold finger was positioned above the auxiliary pumping stage for providing a good vacuum in the target assembly, and to prevent oil, carbon, etc. depositing on the target. Because of the length of the beam tube a pair of electrostatic quadrupole lenses described by Baynham[53] was used to focus the deuteron beam onto the target.

4.4 The tritium target assembly

The tritium titanium target consisted of a disc of titanium loaded with tritium, and is contained in a circular stainless steel case with a water cooling system supplied by Multivolt Ltd. The target could be rotated by a small electric motor, and the area of the target used was restricted by an aperture plate in the shape of a vertical slit 10mm x 1mm placed in the end of the beam tube. The target assembly is shown in Fig. 4.3.

4.5 The alpha-particle detector

It was possible to detect the α-particles either by a scintillation or a semiconductor detector. The organic plastic scintillator NE102A has a fast response time for nanosecond time-of-flight measurements, and has a low γ-ray detection efficiency, and low neutron detection efficiency if thin enough. The silicon surface barrier semiconductor detector has been widely used for α-particle

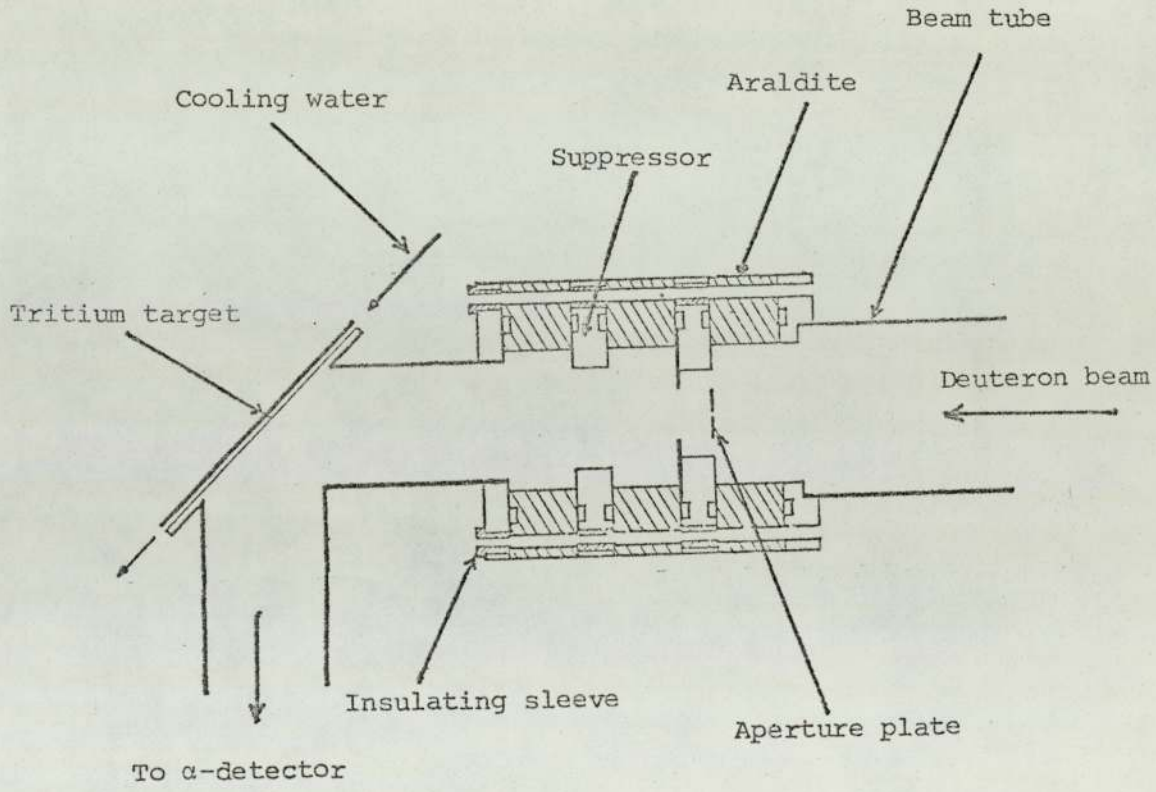

Figure 4.3. A schematic view of the tritium target assembly.

detection, because it has a relatively low response to the neutrons and γ-rays and in addition has a fast response time. It is, however, very susceptible to neutron radiation damage. Hence in the present experiment NE102A scintillator was used. In order to mount the photomultiplier tube inside the evacuated target assembly, a similar system to that reported by O'Neill[28] was used. The scintillator sheet was attached to a perspex light pipe which formed the vacuum sealing flange. The photomultiplier could be viewed through the side of the perspex flange outside the vacuum system. Alpha-particles emitted at 90° to the deuteron beam have an energy of 3.5 MeV, and the range of these in NE102A plastic scintillator according to the manufacturer's data sheet is 0.025mm. Figure 4.4 shows the range of α-particles in NE102A plastic scintillator. The scintillator used was a 0.5mm thick, so that the α-particle detection would be 100% efficient. The scintillator was shielded against β-particles emitted by the tritium target and also deuterons scattered by the target. The β-particles are produced in the decay of tritium with a half-life of 12.3 years, and with a maximum energy of 18.6 KeV, have a maximum range of 0.0022mm in aluminium.[29] The maximum deuteron energy scattered from the target at 90° is 120 KeV, and has a range of 0.001mm in aluminium.[30] Therefore, an aluminium foil of 0.0044mm thick was used to shield the scintillator from both sources of radiations. Since the range of 3.5 MeV alpha-particles in aluminium is 0.017mm,[30] this foil has a negligible effect on the α-particles.

An aluminium plate having an aperture of 10.9mm x 18.9mm was placed in front of the 3 x 3cm sheet of scintillator which limited the angle of acceptance of the α-particles to a cone with half angle 6° in the horizontal plane, and 3.5° in the vertical plane.

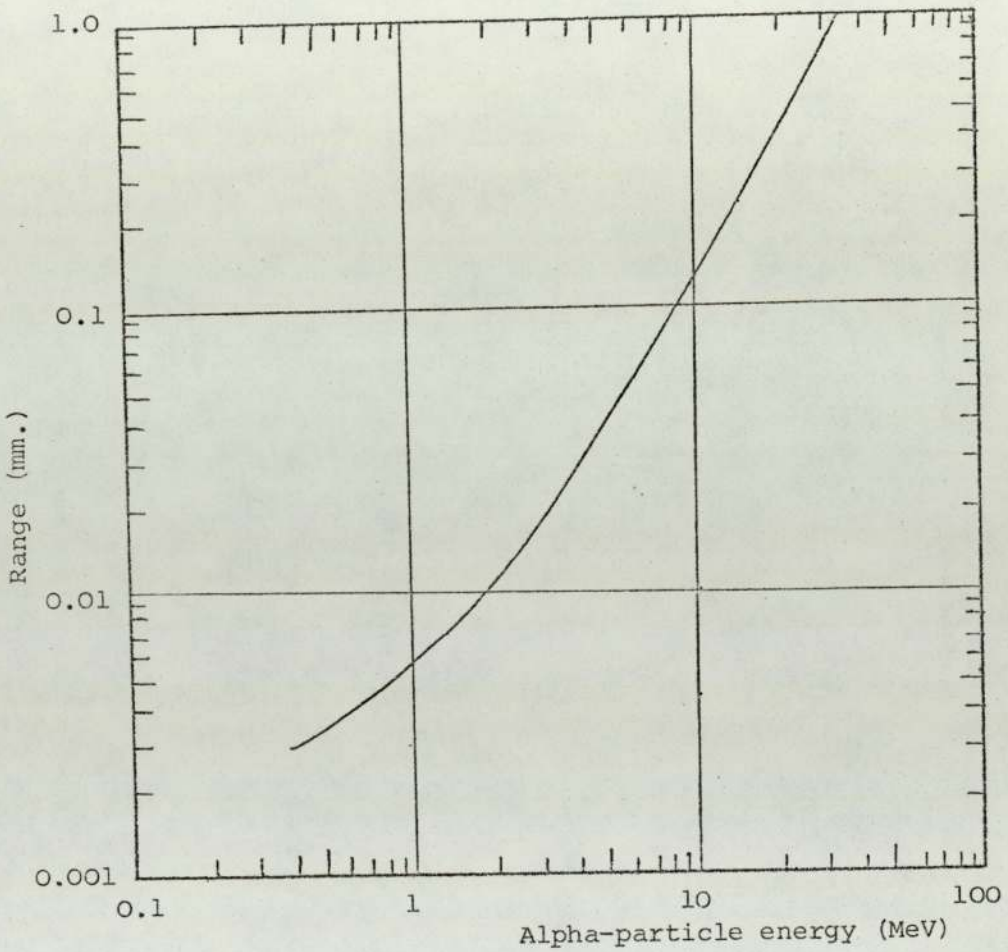

Figure 4.4. The range of α-particles in NE102A plastic scintillator.

The alpha-detector scintillator light pipe, aperture plate, and photomultiplier are shown in figure 4.5. The dynode chain of the Philips 56 AVP Photomultiplier tube used for the α-detector is illustrated in figure 4.6. the base flange of the α-detector was insulated from the main body of the detector and target assembly by using insulating spacers and nylon bolts. The α-particle detector system as a whole can be seen in figure 4.7.

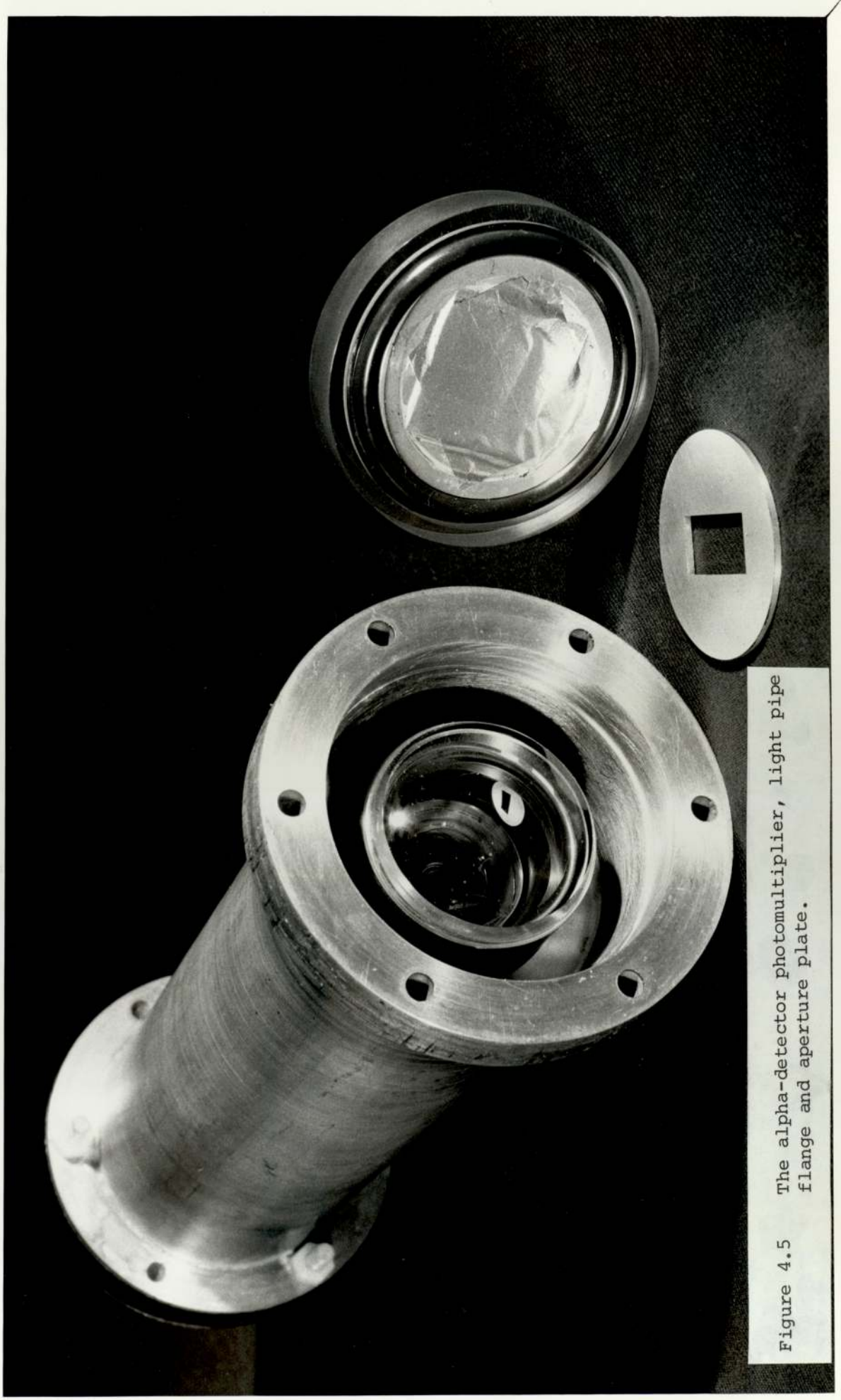

Figure 4.5 The alpha-detector photomultiplier, light pipe flange and aperture plate.

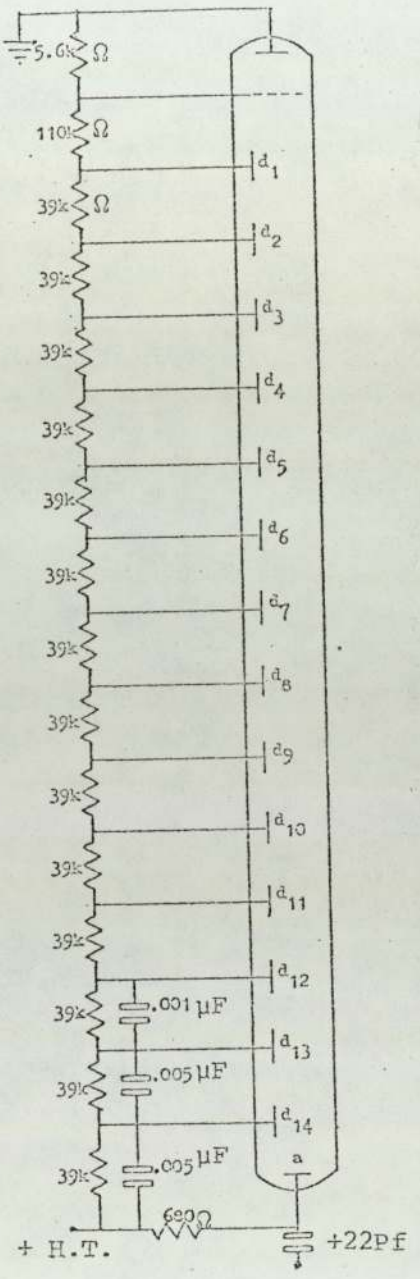

Figure 4.6. The dynode chain circuit of the 56 A.V.P. photomultiplier tube for alpha-detector.

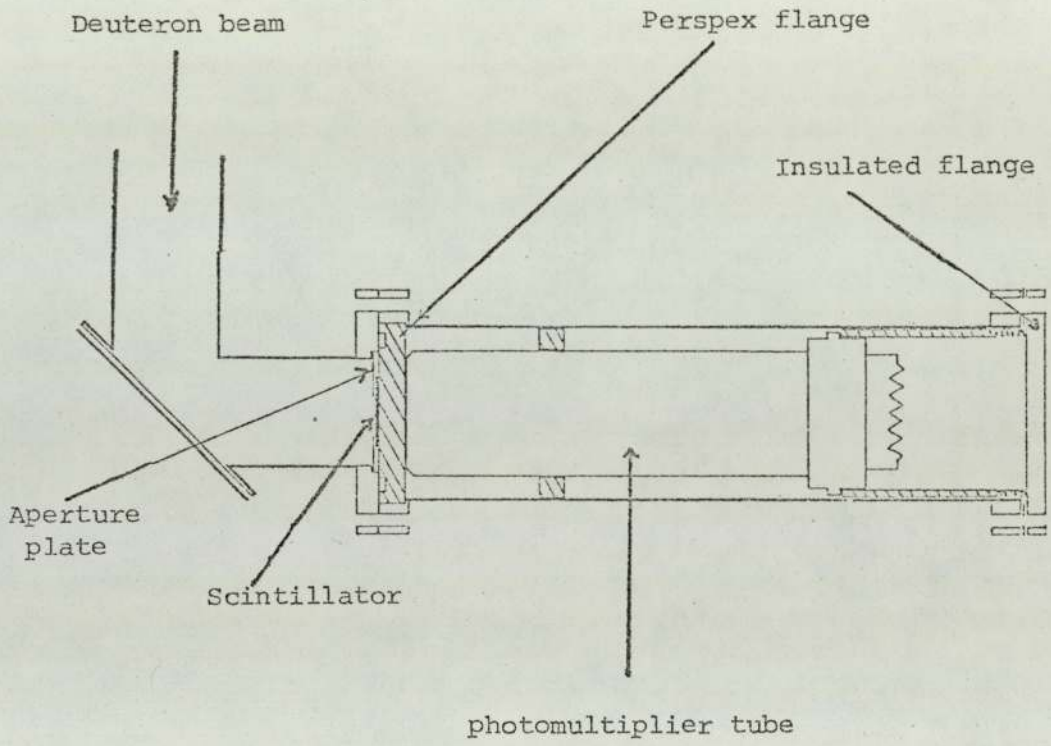

Figure 4.7 The alpha-particle detector arrangement.

4.6 Electronic System

The electronic system used for the present work is similar to that described by Allenby.[31] Improvements, however, have been made to the sensitivity and timing resolution. The fast timing pulses from the gamma-detector were taken from the anode of the 58 A.V.P. photomultiplier tube and fed to the input of a Constant Fraction Discriminator, (C.F.D.) (ORTEC Unit 463). The timing system is shown in Fig.4.8. The C.F.D. triggers at a constant fraction of the input pulse height,[32,33] which can be set at various values in order to eliminate the "time walk" effect. This is the shift in the time of crossing the triggering level of pulses with different pulse heights starting at the same time. The "time walk" effect is shown in Fig.4.9. The output from the C.F.D. used as a 'start' pulse for the Time-to-pulse-Height Convertor (T.P.H.C.) (ORTEC Unit 447). The anode pulses from the 56 A.V.P. photomultiplier tube of the α-particle detector were taken through an emitter follower to a 100 MHz discriminator (ORTEC Unit 436), and after passing through a delay unit, were used as a "stop" pulse for the T.P.H.C. A time spectrum obtained from this system for a small sample of iron at a scattering angle of 20° is shown in Fig.4.10. From this figure it can be seen that the time resolution measured as the full width at half maximum (F.W.H.M.) is about 2.5n.sec.

The output from the T.P.H.C. passes through the Single Channel Analyser (S.C.A.), (ORTEC Unit 420A) whose window width was set from the information obtained from the time spectrum at each experiment.

The full width at 1/10 maximum (F.W.T.M.) in Fig.4.10 about 8.0n.sec. and this determines the width of the 'window' set over

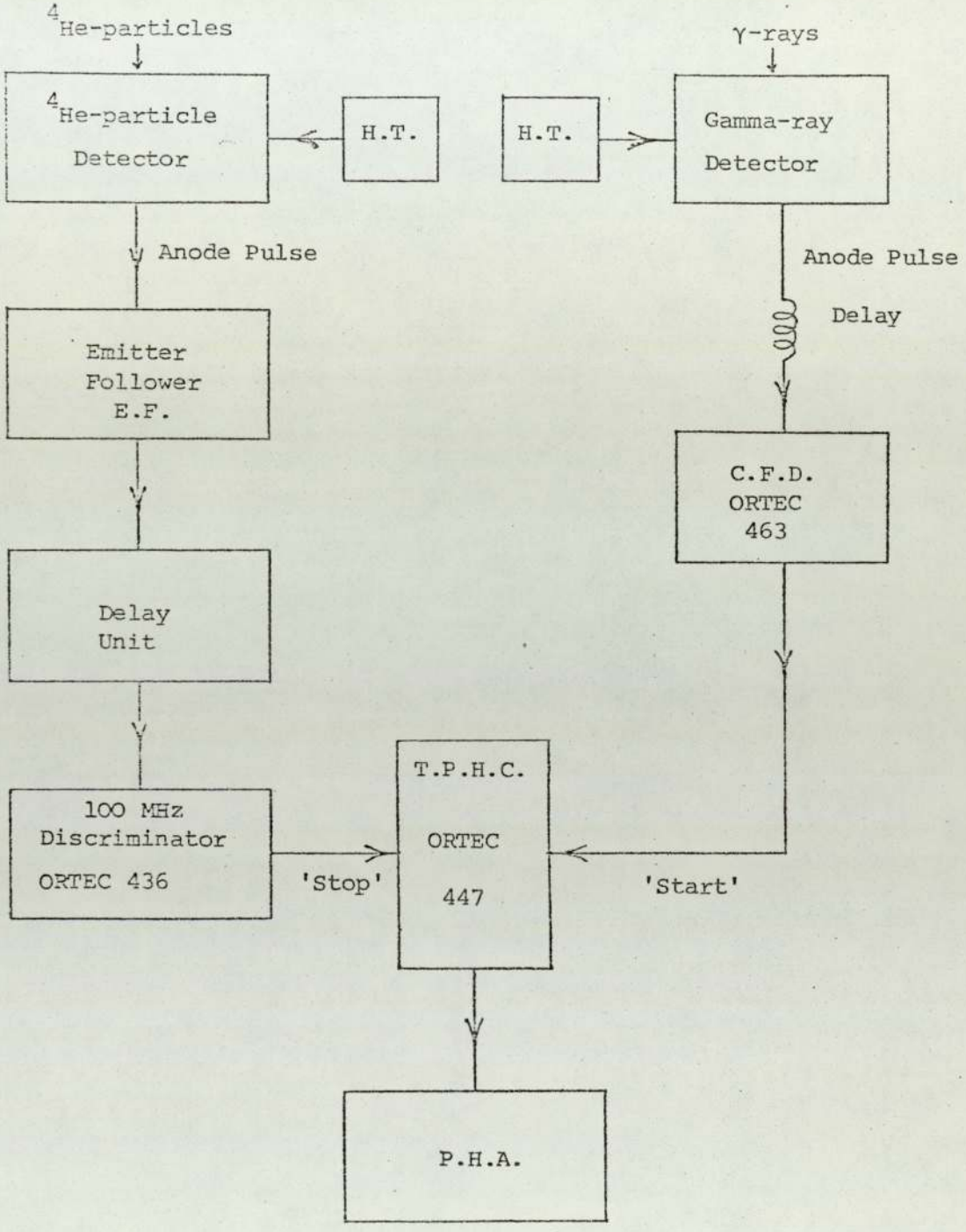

Figure 4.8 Block diagram for the time of flight system.

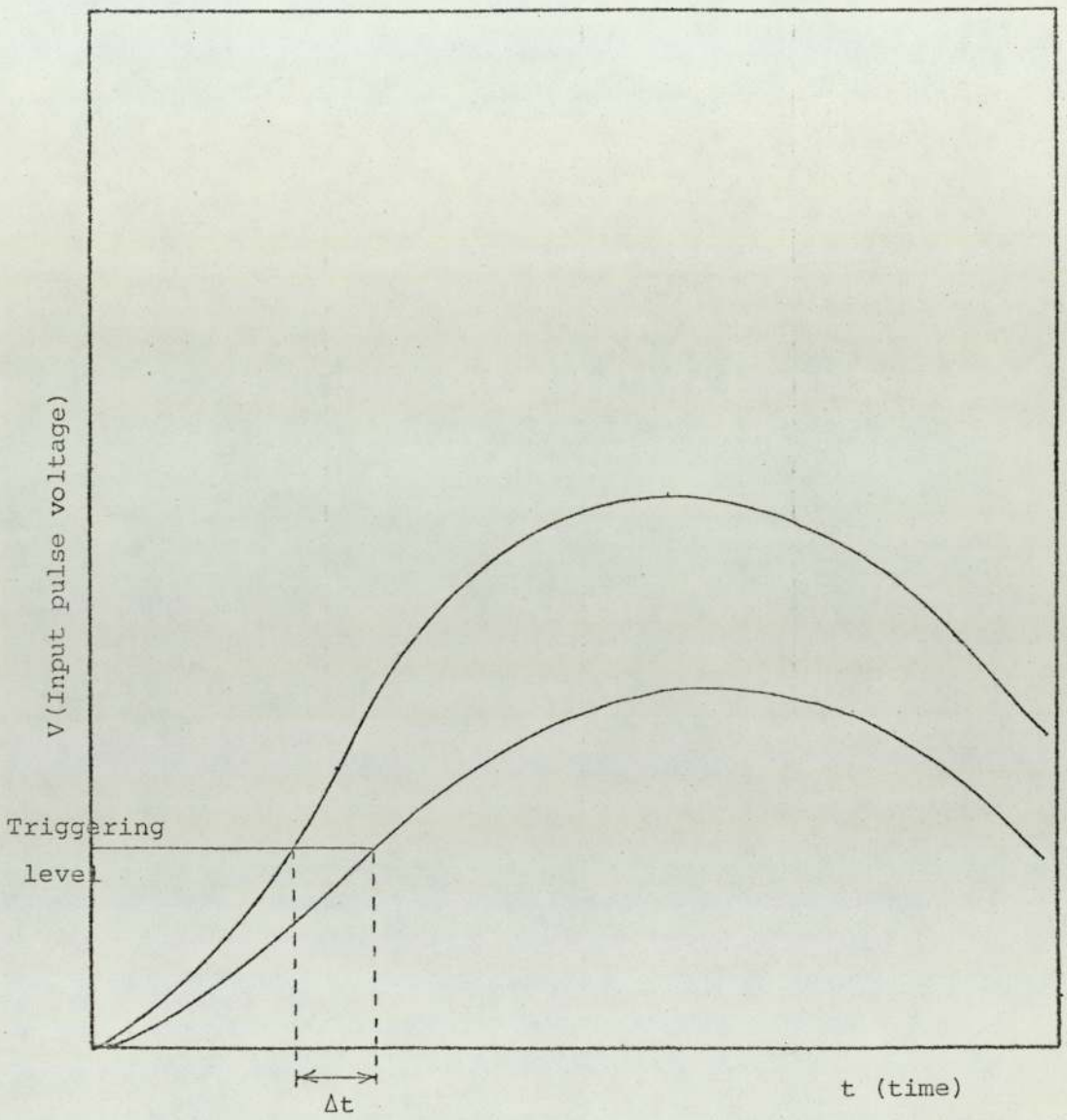

Figure 4.9. A sketch illustrating 'walk' effect.

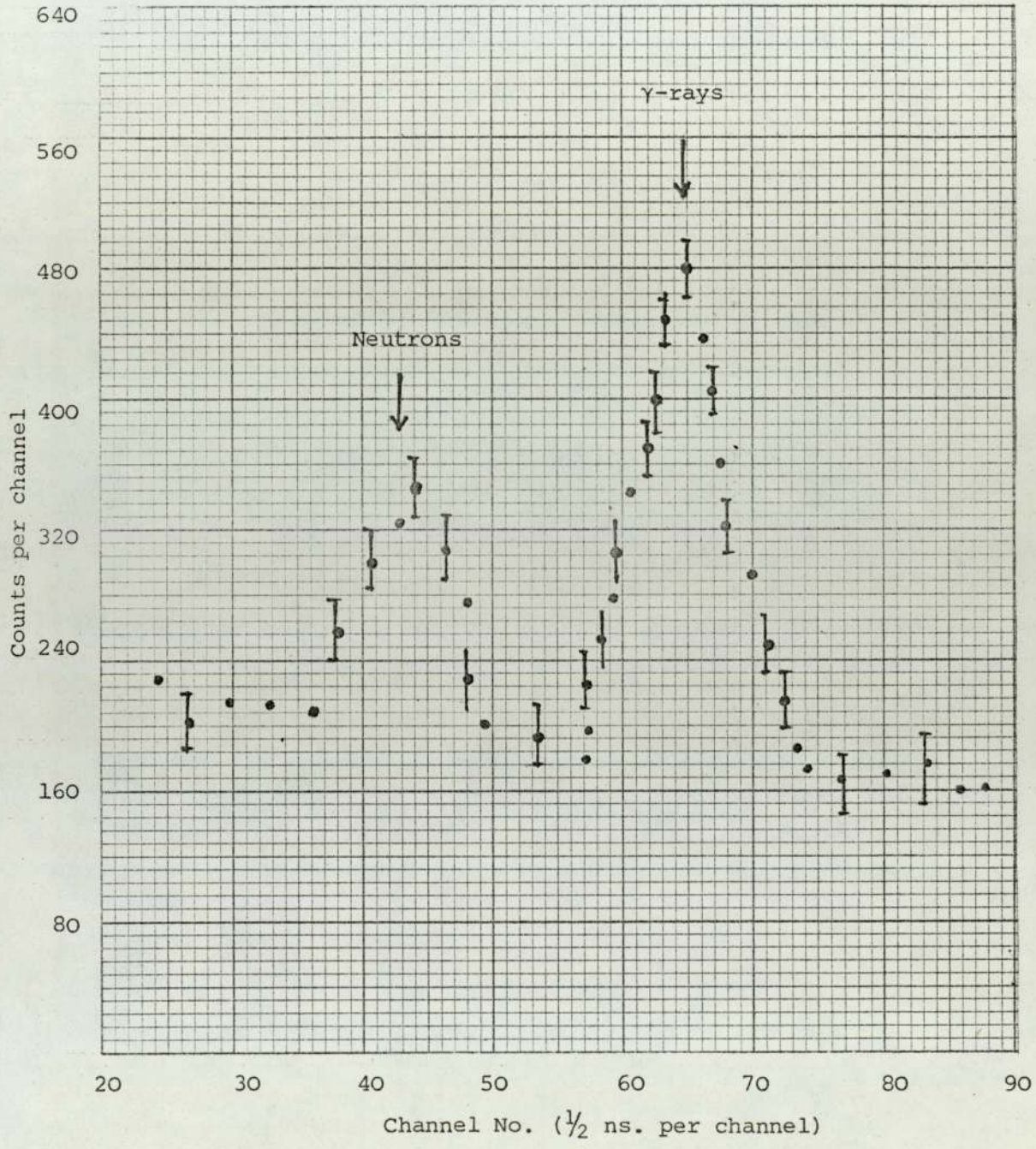

Figure 4.10. The time spectrum from iron sample at a scattering angle of 20°.

the gamma-ray peak on the time spectrum. This is the portion of the time spectrum which is passed by the S.C.A. Pulses from the S.C.A. are used to open the linear gate to allow the γ-ray energy pulses to reach the pulse-Height-Analyser.

If the width of the 'window' in the S.C.A. is reduced, the background radiation in the energy spectrum will be reduced, but the reduction of the S.C.A. 'window' must not exceed a certain value, because then a portion of the γ-ray peak could be lost in the energy spectrum.

The energy line pulses were obtained from the 13th dynode of the 58 A.V.P. photomultiplier tube of the γ-ray detector, and after passing through the preamplifier (ORTEC Unit 113), linear amplifier (ORTEC Unit 485), and linear delay (ORTEC Unit 425) finally reach the linear gate (ORTEC Unit 426) which the output from this unit allows the γ-ray energy pulses to be stored as the energy spectrum in the 100 channel Pulse-Height-Analyser (P.H.A.). A schematic diagram of the electronic gating system is shown in figure 4.11.

The data accumulated by the 100-channel Pulse-Height-Analyser was printed out on paper tape. The rack mounted time-of-flight and energy analysis electronic system is shown in figure 4.12.

4.7 The angular range of neutrons in d-T reaction

The angular ranges of the neutrons corresponding to the α-particles emitted at $90^{\circ} \pm 6^{\circ}$ to the incident deuteron beam from the $T(d,n)^4He$ reaction can be calculated from the reaction kinetics. Benveniste and Zenger[34] have investigated the kinetics of this reaction and they have found the following relation, which relate the neutron and α-particle angles of emission in the Lab. System:

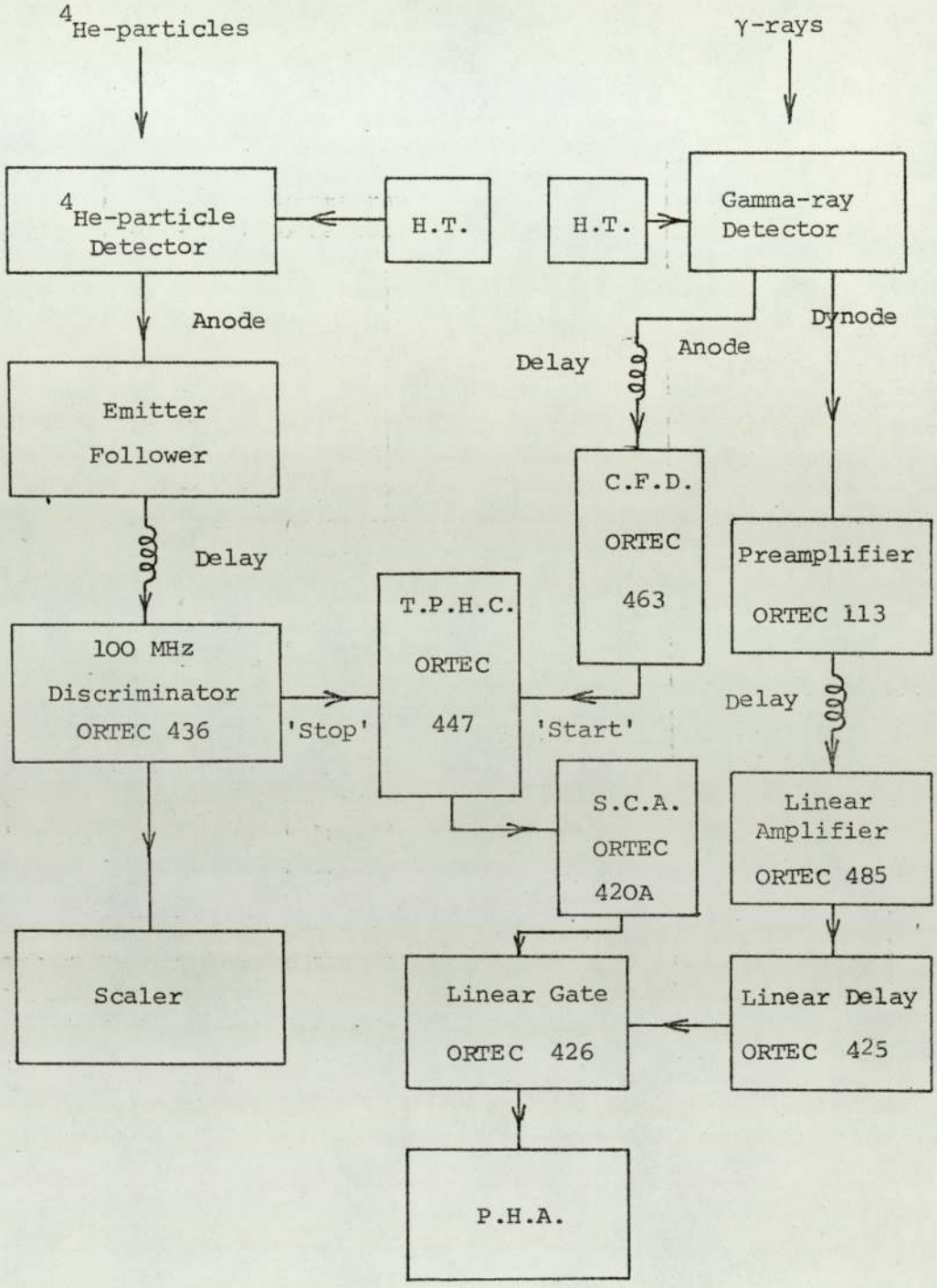

Figure 4.11 Electronic arrangement for the Associated Particle method and γ-ray energy accumulation.

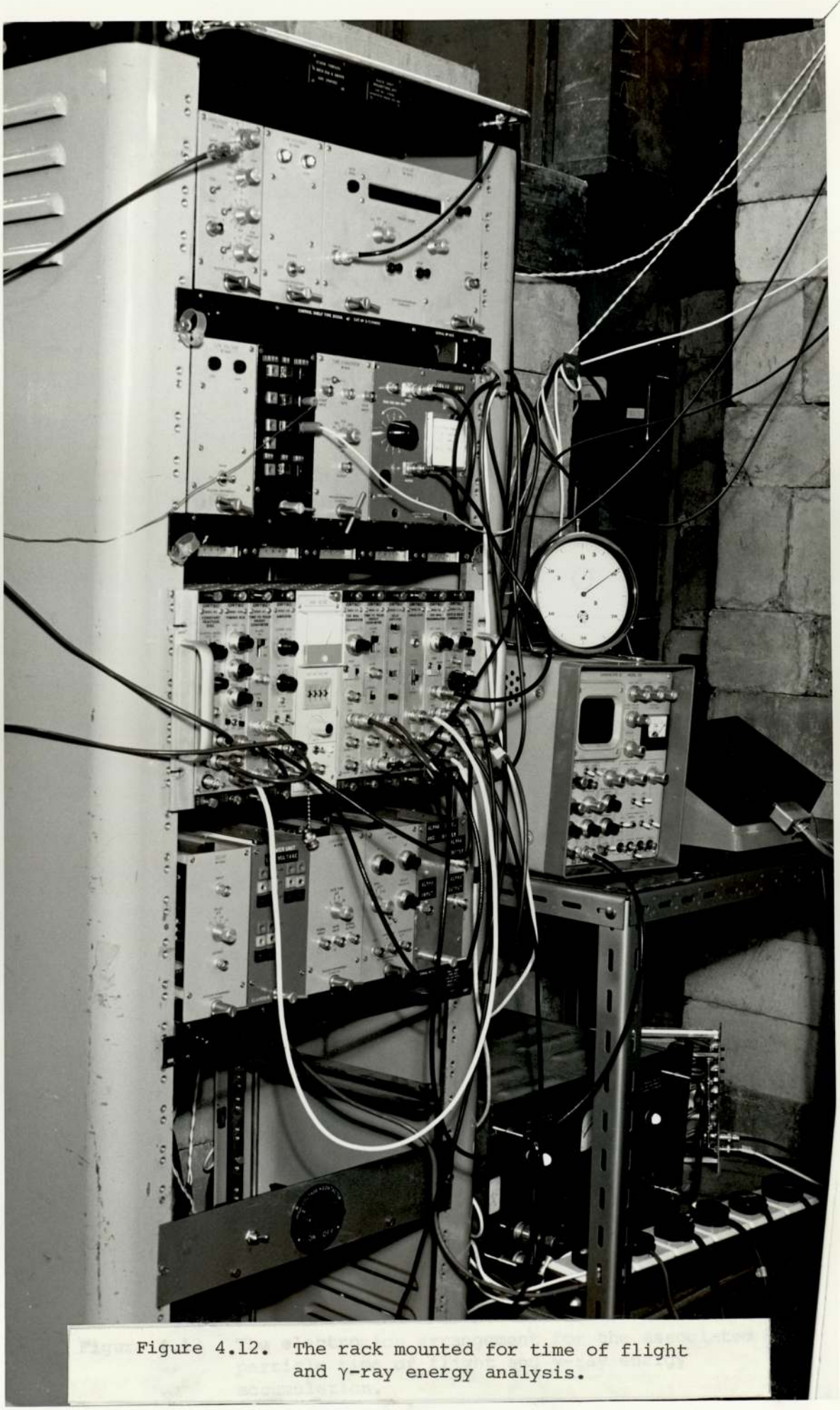

Figure 4.12. The rack mounted for time of flight and γ-ray energy analysis.

$$\tan \phi_\alpha = \frac{\frac{1}{2} \sin^2\phi_n + \sin \phi_n \left(\frac{1}{\gamma^2} - \sin^2\phi_n\right)^{\frac{1}{2}}}{-\sin^2\phi_n + \cos \phi_n \left(\frac{1}{\gamma^2} - \sin^2\phi_n - \frac{m_\alpha}{m_m}\right)^{\frac{1}{2}}} \quad \ldots\ldots\ldots\ldots \quad (4.1)$$

$$\text{and} \quad \frac{1}{\gamma^2} = \frac{m_\alpha}{m_n} \cdot \frac{m_d + m_T}{m_d} \quad \frac{m_T}{m_d + m_T} + \frac{Q}{E_d} \quad \ldots\ldots\ldots\ldots\ldots \quad (4.2)$$

where m_α and m_n are the α-particle and neutron masses respectively, m_d and m_T are the deuteron and triton masses. E_d is the incident deuteron energy in the Lab. System, and Q is the energy released in the reaction (Q = 17.6 MeV).

From the equations (4.1) and (4.2) it can be seen that the relation between ϕ_n and ϕ_α depends on the incident deuteron energy. The tritium target used was a 'thick' target, i.e. its thickness is greater than the range of deuteron incident on it, and as a result deuterons of all energies from the bombarding energy to zero yield neutrons. Figure 4.13 shows the variation of ϕ_α and corresponded ϕ_n for various deuteron energies were calculated from equations 4.1 and 4.2.

Figure 4.13 shows that the α-particles detected in the range of 84° to 96° define a neutron beam in the angular range from 76.5° to 96°.

Angular straggling of the deuteron and α-particle in the target have been neglected in the calculations. This effect gives an uncertainty of 0.5° in the results of calculations, and since the angular resolution of the system is about $\pm 6^\circ$, it is therefore negligible.

4.8 The dependence of neutron yield on deuteron energy

The neutron yield, $y(\phi)$, per incident deuteron energy and per unit solid angle at a neutron emission angle ϕ_n is given by:

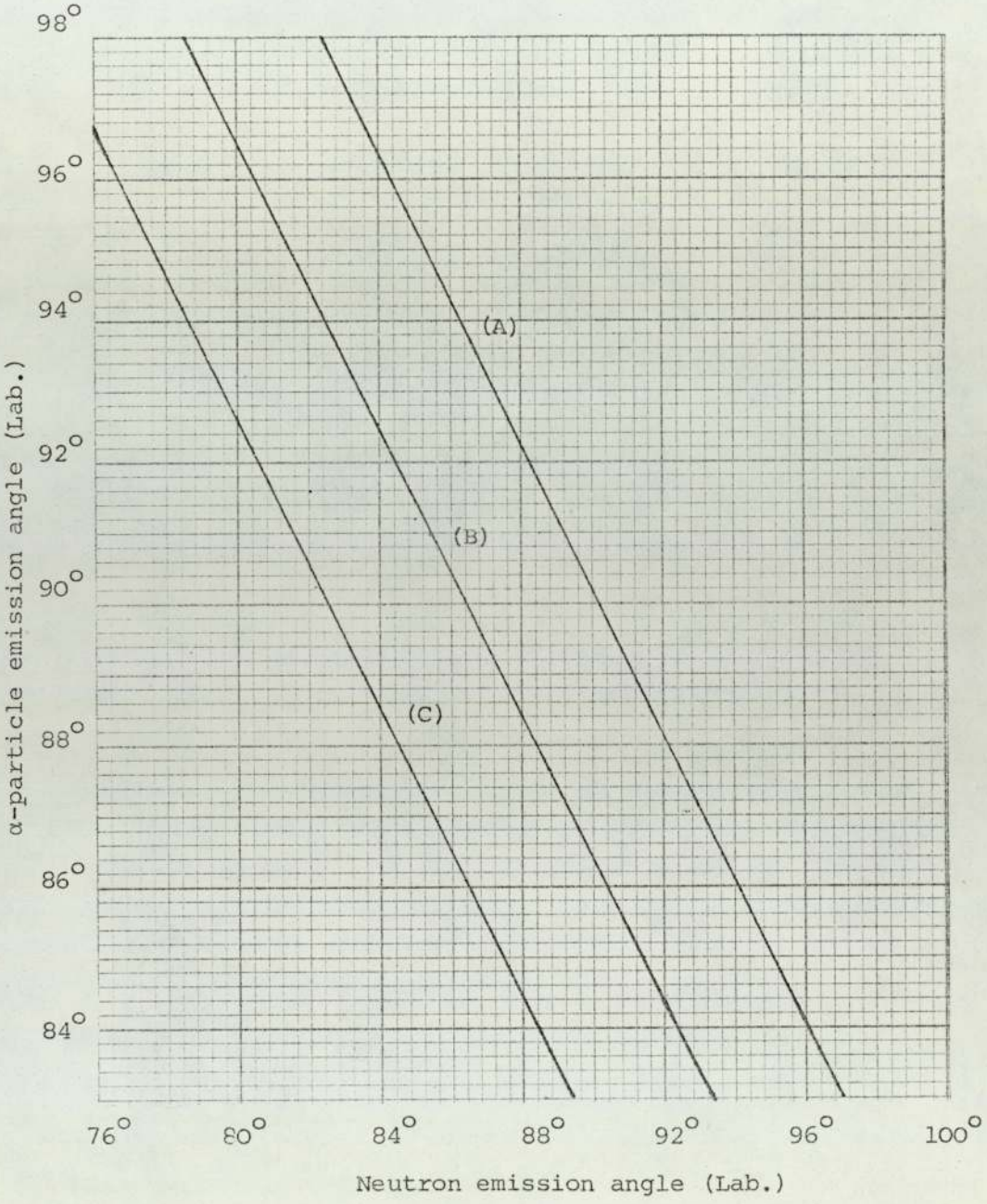

Figure 4.13 Relation between α-particle and neutron angles emission in the Lab. for various incident deuteron energies.

(A) - E_d = 0

(B) - E_d = 30 KeV

(C) - E_d =120 KeV

$$y(\phi) = \int_{o}^{E_{d_{max}}} \frac{\frac{d\sigma}{d\Omega} N}{\frac{dE_d}{dx}} \, dE_d \quad \ldots\ldots\ldots\ldots\ldots\ldots \quad (4.3)$$

where $\frac{d\sigma}{d\Omega}$ is the differential cross-section of neutron production from the d-T reaction per unit solid angle at a deuteron energy E_d, and neutron emission angle ϕ_n. N is the number of tritium atoms per unit volume, and $\frac{dE_d}{dx}$ is the energy loss rate of deuteron in the tritium-titanium target.

In the above relation the deuteron energy is treated as a variable in the range of E_{dmax} which is about 150 KeV to zero, as the deuteron energy slows down in the target.

The differential neutron production cross-section of the d-T reaction has been found to be isotropic in the centre of mass system for deuteron energy up to about 200 KeV by Bame and Perry,[35] and up to 570 KeV by Argo et al.[36] Several measurements of the variation of the differential cross-section with respect to the incident deuteron energy for the energy ranges up to 500 KeV are given by Benveniste & Zenger.[34] The differential cross-section for the $T(d,n)^4He$ reaction is shown in Figure 4.14.

4.8.1 Energy loss of deuteron in tritium titanium target

The factor $\frac{dE_d}{dx}$ in equation 4.3 is the rate of the energy loss of deuteron in tritium-titanium target, and it can be calculated as the sum of the energy losses in the constituents, i.e. titanium and tritium, and the relation is given by:

$$\frac{dE_d}{dx} = \frac{48}{48+3} \left(\frac{dE_d}{dx}\right)_{Ti} + \frac{3}{48+3} \left(\frac{dE_d}{dx}\right)_{T} \quad \ldots\ldots\ldots \quad (4.4)$$

where the factors $\left(\frac{dE_d}{dx}\right)_{Ti}$ and $\left(\frac{dE_d}{dx}\right)_{T}$ are the rate of energy losses in normal titanium and tritium respectively.

48 is the mass number of titanium, and 3 is the mass number of tritium.

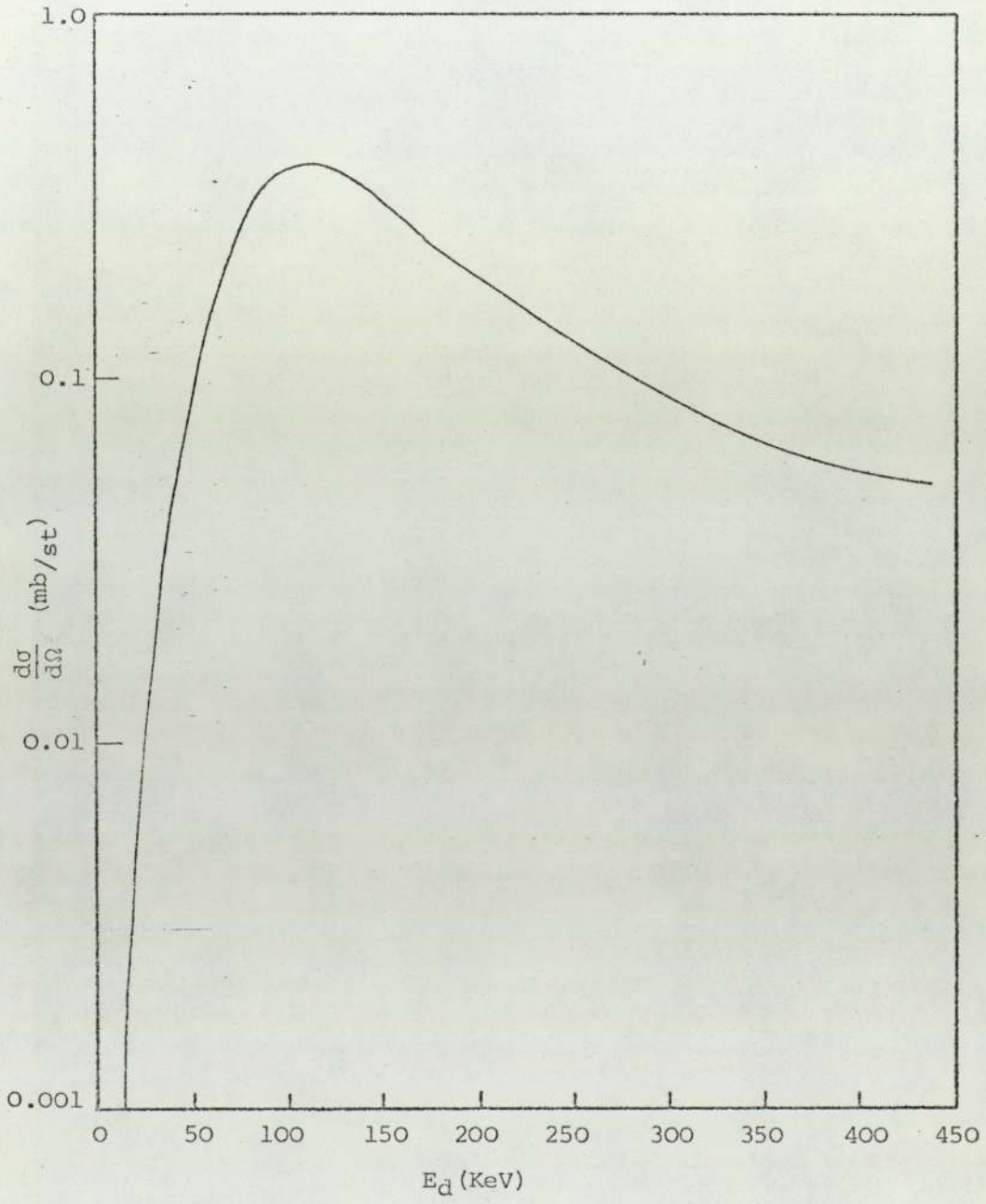

Figure 4.14 The differential cross-section as a function of deuteron energy for the d-T reaction.

The energy loss of deuteron in tritium-titanium target has been calculated using equation 4.4. Figure 4.15 shows the result of this calculation.

4.8.2 The Anisotropy factor

The anisotropy factor, $\frac{d\Omega'}{d\Omega}$, is needed to convert the centre of mass differential cross-section to the Laboratory frame of reference, as follows:

$$\frac{d\sigma(\theta)}{d\Omega} = \frac{d\sigma(\theta)}{d\Omega'} \times \frac{d\Omega'}{d\Omega} \quad \ldots\ldots\ldots\ldots\ldots\ldots\ldots\ldots \quad (4.5)$$

where Ω indicates the solid angle in the Laboratory system, and Ω' is the solid angle in centre of mass system.

The anisotropy factor, $\frac{d\Omega'}{d\Omega}$ is given by:

$$\frac{d\Omega'}{d\Omega} = \frac{\mathrm{Sin}\theta_n \, d\theta_n}{\mathrm{Sin}\phi_n \, d\phi_n} \quad \ldots\ldots\ldots\ldots\ldots\ldots\ldots\ldots \quad (4.6)$$

where the relation between the centre of mass angle θ_n and the Laboratory angle ϕ_n for neutron emission is given by the following relation:

$$\mathrm{Cos}\ \theta_n = \gamma \sin^2\phi_n \pm \cos\phi_n \left(1 - \gamma^2 \sin^2\phi_n\right)^{\frac{1}{2}} \quad \ldots\ldots \quad (4.7)$$

where $\gamma = \frac{V_{c.m.}}{V_n''}$

Figure 4.16 shows the Laboratory and centre of mass reference frames for an inelastic scattering event. The neutron anisotropy factor against the neutron emission angle, ϕ_n, is shown in Figure 4.17 for deuteron energies of zero to 200 KeV in steps of 100 KeV.

Over the range of interest for the ϕ_n, the anisotropy factor, $\frac{d\Omega'}{d\Omega}$, is approximately constant and close to unity within an error of 1.0 to 1.5 per cent.

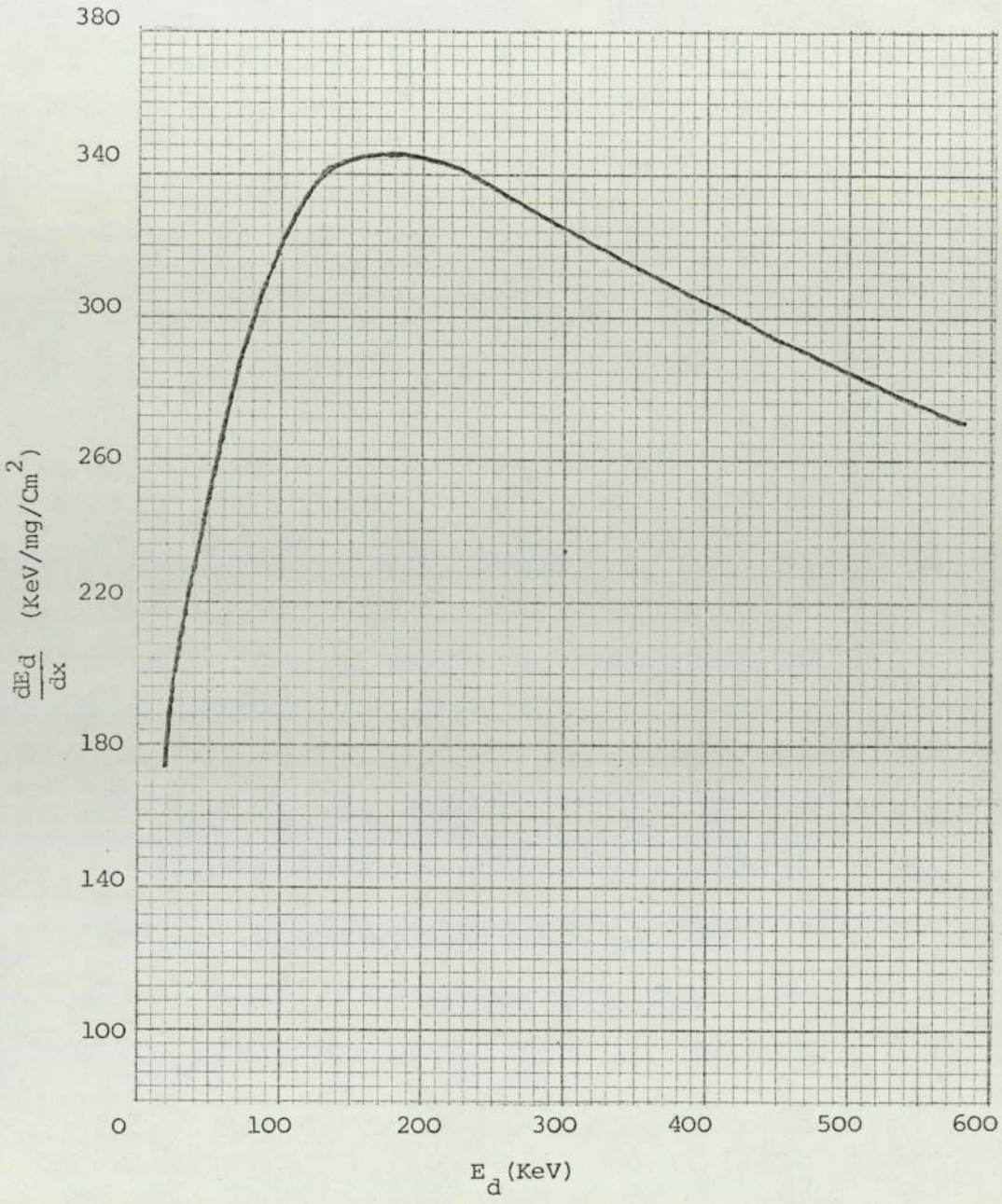

Figure 4.15. The energy loss rate of deuteron in titanium-tritium target.

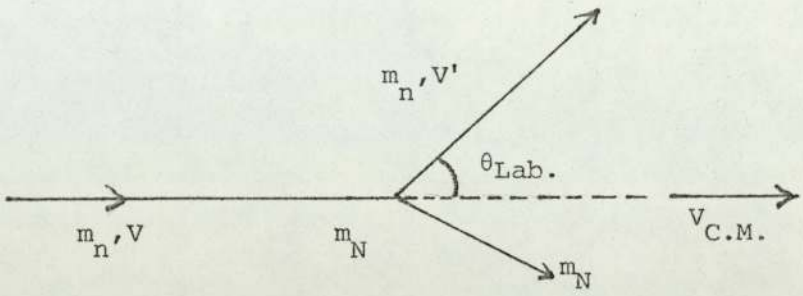

(A)

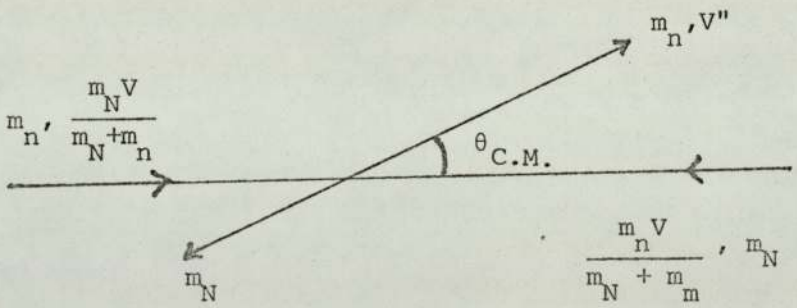

(B)

Figure 4.16 The illustration of an inelastic event in Lab. and C.M. frame of references.

(A) - Laboratory system (Lab.)

(B) - Centre of mass system (C.M.)

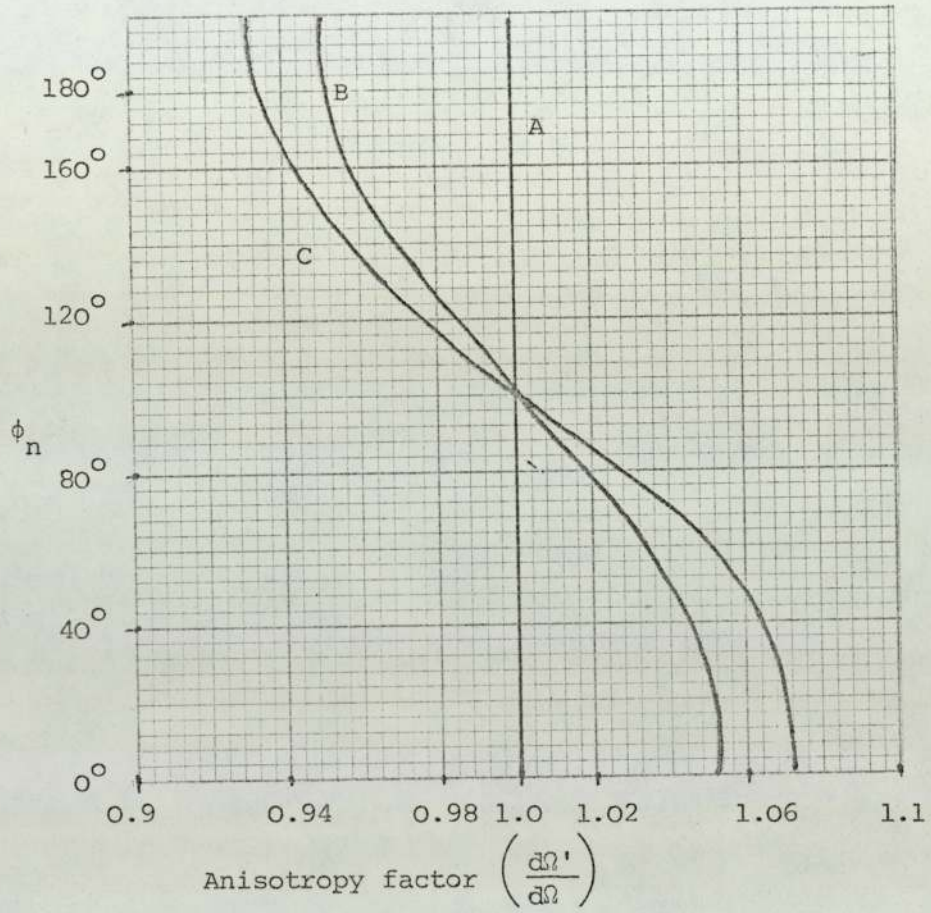

(A) - E_d = 0

(B) - E_d = 100 KeV

(C) - E_d = 200 KeV

Figure 4.17. The neutron anisotropy factor versus neutron angles for incident deuteron energies of 0.0, 100 and 200 KeV.

4.8.3 The Neutron yield

With the above information the neutron yield as a fuction of deuteron energy can be calculated. The neutron yield, y, from deuterons in the energy interval E_d to $E_d + dE_d$ can be obtained using equation 4.3 and it gives the following relation:

$$Y(\phi, E_d) \propto \frac{\left(\frac{d\sigma}{d\Omega'}\right)\left(\frac{d\Omega'}{d\Omega}\right)}{\frac{dE_d}{dx}} \, dE_d \quad \ldots\ldots\ldots\ldots\ldots\ldots (4.8)$$

To obtain the relative neutron yield versus deuteron energy, the relation 4.8 was evaluated numerically in 10KeV steps, taking at each step mean values of $\frac{d\sigma(\theta)}{d\Omega}$ and $\frac{dE_d}{dx}$ from figures 4.14 and 4.15 respectively. The result of this evaluation can be seen in figure 4.18.

4.9 The Neutron Beam Profile

The neutron beam profile is the relative neutron yield at each neutron emission angle. As it can be seen from figure 4.14 the values of the differential cross-sections depend on the incident deuteron energy, E_d. From the kinematics of the d-T reaction it is known that the value of ϕ_n depends on the incident deuteron energy for a certain value of ϕ_α where ϕ_n and ϕ_α are the neutron and α-particle angles of emission respectively in the Laboratory system; therefore, the neutron yield varies with ϕ_n.

The neutron beam profile is found using the information given in figures 4.13 and 4.18.

For each value of ϕ_n from 76° to 96° inclusive, figure 4.19 shows the range of E_d contributes to the neutron yield. Figure 4.18 shows that the intensity of the neutron yield is a function of deuteron energy and this figure is then used to obtain the relative yield that this range of values of E_d can produce. This is found from the area under the curve in the relevant range of E_d. The

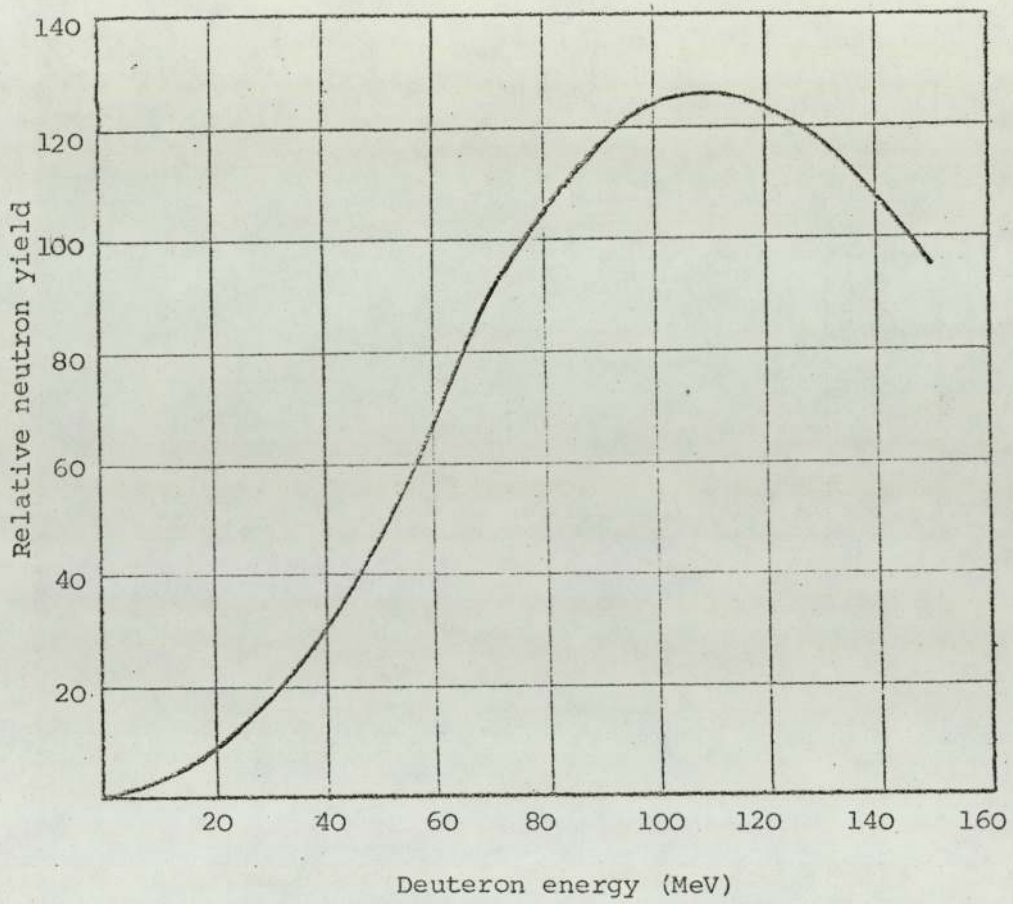

Figure 4.18 The relative neutron yield as a function of incident deuteron energy.

resultant neutron beam profile is shown in Figure 4.19. It can be seen that the full width at half maximum of the beam profile is 12^{o}.

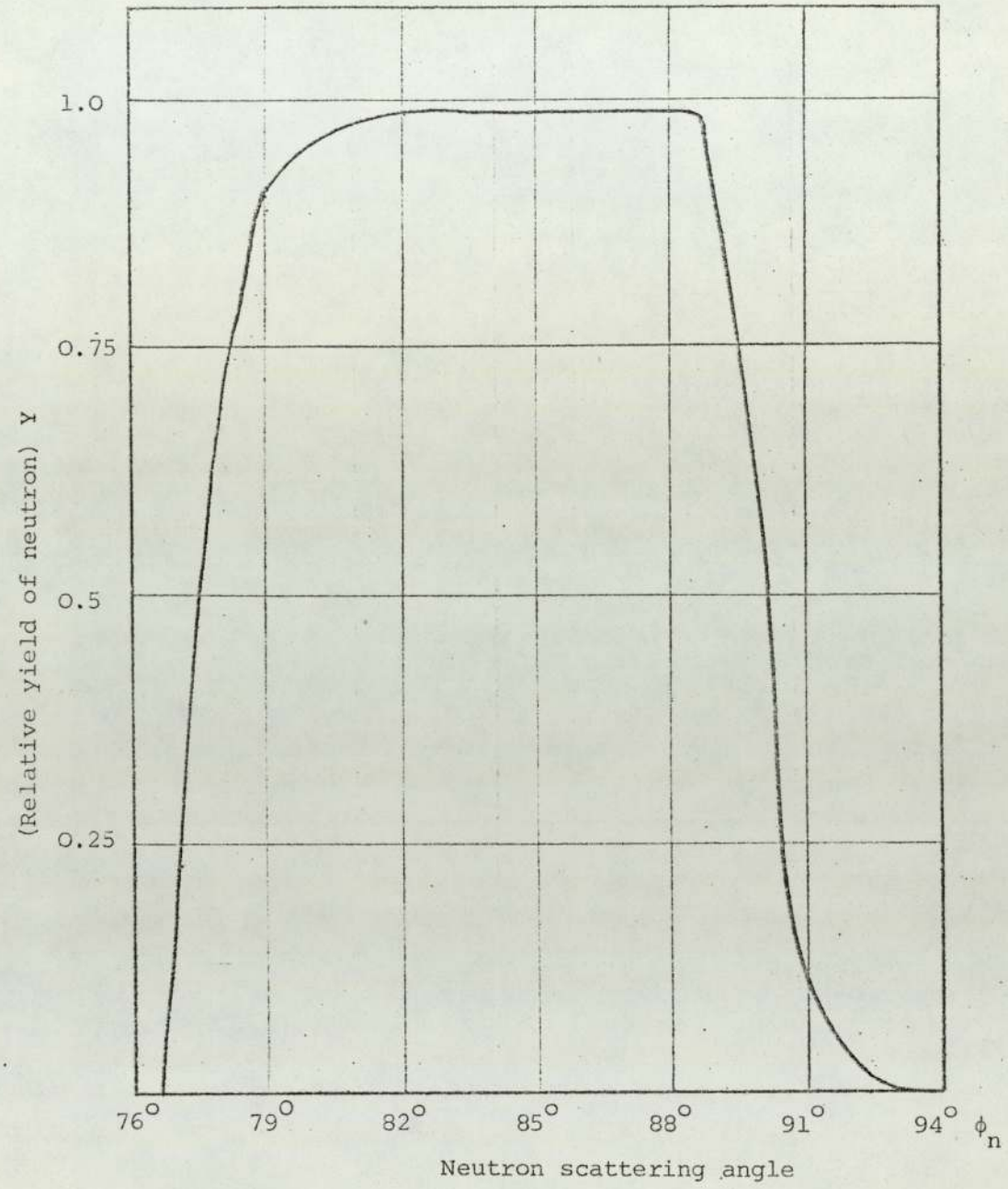

Figure 4.19 The resultant neutron beam profile

4.10 Gamma-ray detectors

The two major properties considered in the choice of the gamma-ray detector were the detector efficiency, the neutron response and sensitivity of the detector. Potentially the two most useful detectors for gamma-ray detection are the Ge(Li) semiconductor detector and the NaI(Tℓ) scintillator detector. The properties of each one reviewed below.

4.10.1 The Ge(Li) semiconductor detector

As mentioned in Chapter 3, the interaction processes producing secondary ionizing electrons are the photoelectric effect, Compton scattering and pair production ($E_\gamma \geq 1.02$ MeV) which allow the γ-ray to be detected. The probability of these processes increases with the atomic number of the detector material. Germanium has an atomic number of 32 and consequently the detector has a poor efficiency for gamma-ray detection relative to NaI(Tℓ). The great advantage of the Ge(Li) detector is its excellent energy resolution, however the detector is very sensitive and susceptible to damage caused by continued exposure to fast neutrons. Fast neutrons produce crystal defects such as the displacement of atoms from their equilibrium sites leaving vacancies and interstitial atoms in the lattice. Radiation damage mainly affects energy resolution of the detector and its timing accuracy. Mann and Yntema[38] give a figure of 10^{11} neutrons/cm^2 as a typical allowable integrated fast neutrons exposure for the Ge(Li) detector. ORTEC, manufacturers of Ge(Li) detectors state that a rapid deterioration is produced by a fast neutron exposure of more than 10^8 neutrons/cm^2.

The calculated time for the detector to receive an integrated exposure of 10^8 n/cm^2 is about 200h.

4.10.2 The NaI(Tℓ) Scintillator detector

Iodine has an atomic number of 127. This makes the NaI(Tℓ) a very good γ-ray absorbing material relative to the Ge(Li). For this reason, and as NaI is a very dense material, 3.67 gm/cm^3, it has a very good intrinsic γ-ray detection efficiency. On the other hand, the NaI(Tℓ) detector is sensitive to neutrons. Because of the variation of neutron reaction cross-section with energy, the neutron response is very energy dependent. For slow neutrons the major response is from capture in the iodine. This reaction has a cross-section of 7.0 barn[39] for neutrons of 2200m/sec. The resulting γ-ray energy spectrum corresponding to ^{128}I is almost continuous with a maximum at 6.71 MeV which is the binding energy of neutrons in ^{128}I.

The predominant neutron detection mechanism in the fast neutron energy range (0.5 MeV to 14.5 MeV) is by inelastic scattering.[39] In the lower energy range the induced activity is mainly due to the radiative capture with the iodine, and at the high energy end of the range, the induced activity results mainly from the (n,2n) and (n,p) reactions with the iodine. These reactions, which lead to an increase in the background, have a cross-section of 1.3 barn and 0.23 barn for neutrons of 14.5 MeV[39] respectively. Shafroth et al.[41] have shown that in NaI (Tℓ) fast neutron capture is significant for neutron energies up to about 1.0 MeV.

Van Loef and Lind[42] have studied the (n,n'γ) process in NaI(Tℓ) crystal for neutron energies in the range 0.52 to 3.15 MeV.

4.10.3 Choice of detector

The Ge(Li) and NaI(Tℓ) detectors are sensitive to neutrons. The two most significant points favouring the use of the Ge(Li) detector are its excellent energy resolution and fast

rising output pulses. The high efficiency of the NaI(Tℓ) crystal is its most favourable property and in addition it has low sensitivity to neutron damage. As a result of comparison between the detection efficiency and energy resolution, NaI(Tℓ) scintillator detector was used.

4.11 Gamma-ray detection system

The gamma-ray detector used in present study was a 3"x 3" NaI(Tℓ) scintillator which is supplied by Nuclear Enterprises. It was optically coupled by a plano-concave perspex plate to a Phillips 58 A.V.P. photomultiplier tube which has 14-dynodes and is shown in figure 4.20. The dynode resistance chain used to supply voltage to the 14 stages of photomultiplier can be seen in figure 4.21. The construction of the scintillation detector as a whole is shown in figure 4.22. The gain obtainable from a photomultiplier tube depends on the voltage applied between the dynodes according to the following relation:[55]

$$A = (K.V_d)^n \quad \ldots\ldots\ldots\ldots\ldots\ldots\ldots\ldots \quad (4.9)$$

where A is the amplification, K is a constant, depends on the material of dynodes, V_d is the potential difference between successive dynodes, and finally n is the number of dynodes. Therefore a variation in the voltage, V_d, between dynodes will change the amplification, and stabilization of the voltage supply to the photomultiplier tube is important especially for the spectrometry measurements.

4.12 Energy resolution

The energy resolution of a scintillator detector can be measured by observing the ratio of the peak-to-valley of the two gamma-ray energy lines of ^{60}Co gamma-ray source.

The Philips 58 A.V.P. photomultiplier tube has a photo -

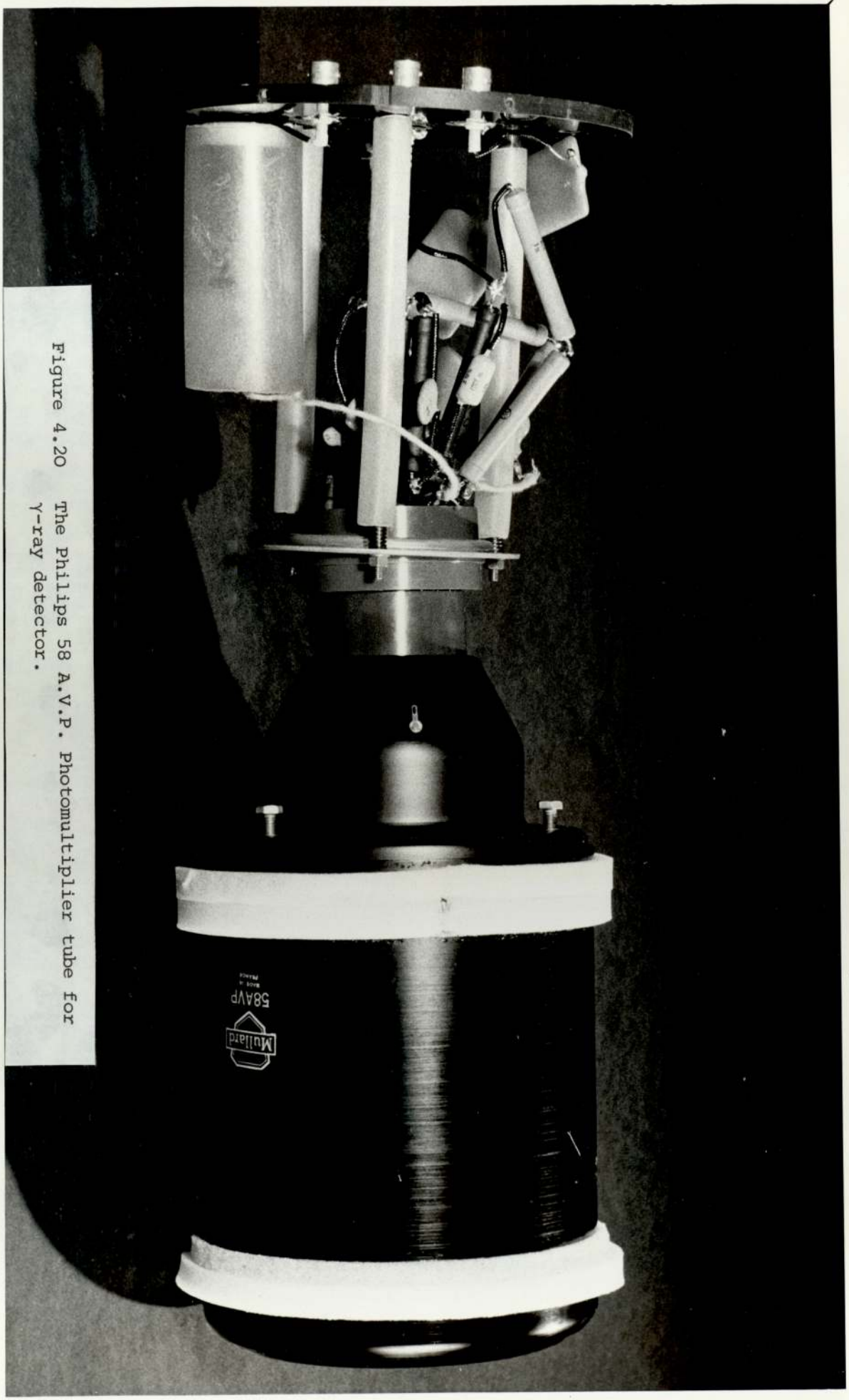

Figure 4.20 The Philips 58 A.V.P. Photomultiplier tube for γ-ray detector.

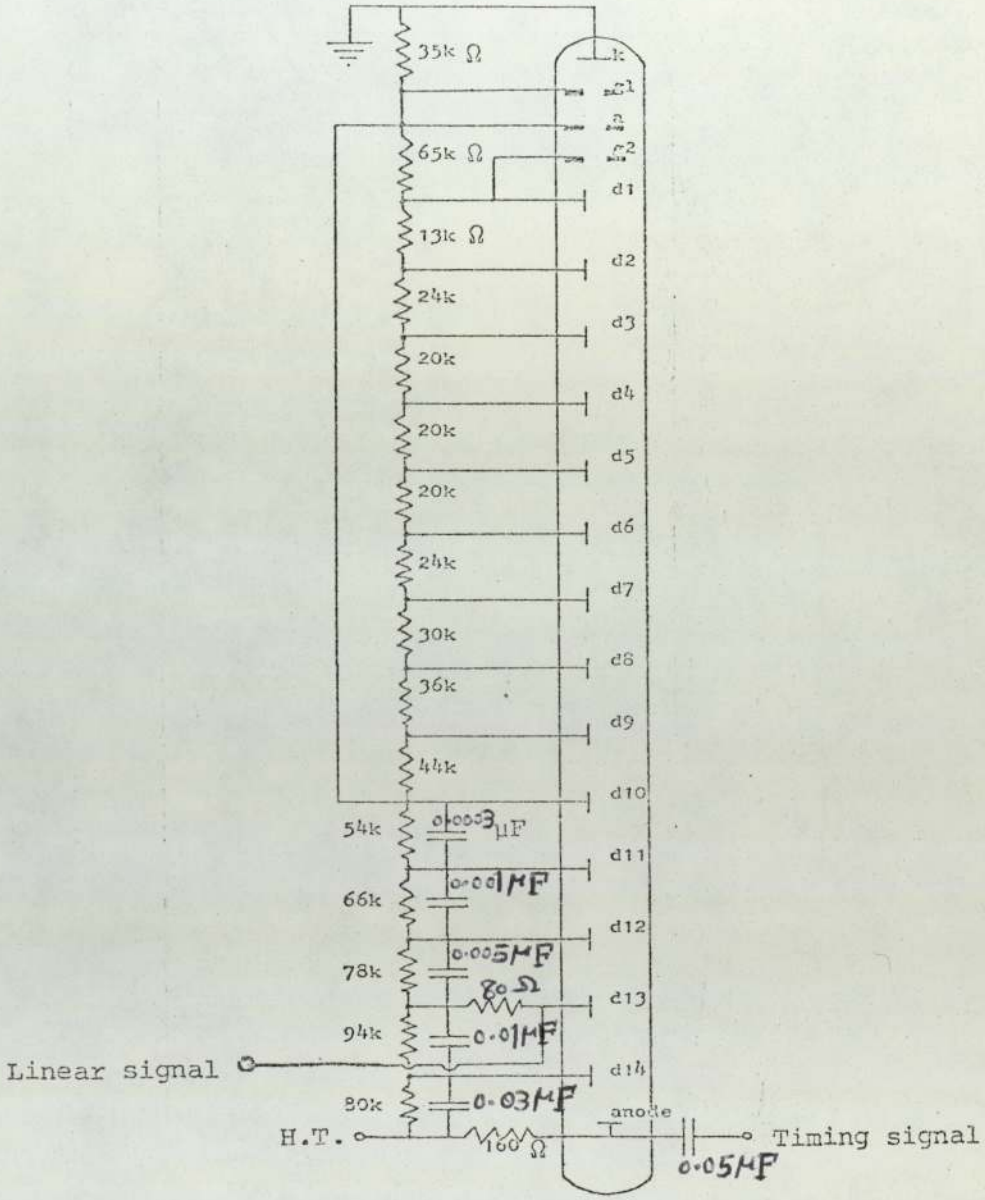

Figure 4.21. The dynode chain circuit of the 58 A.V.P. photomultiplier tube for gamma-ray detector.

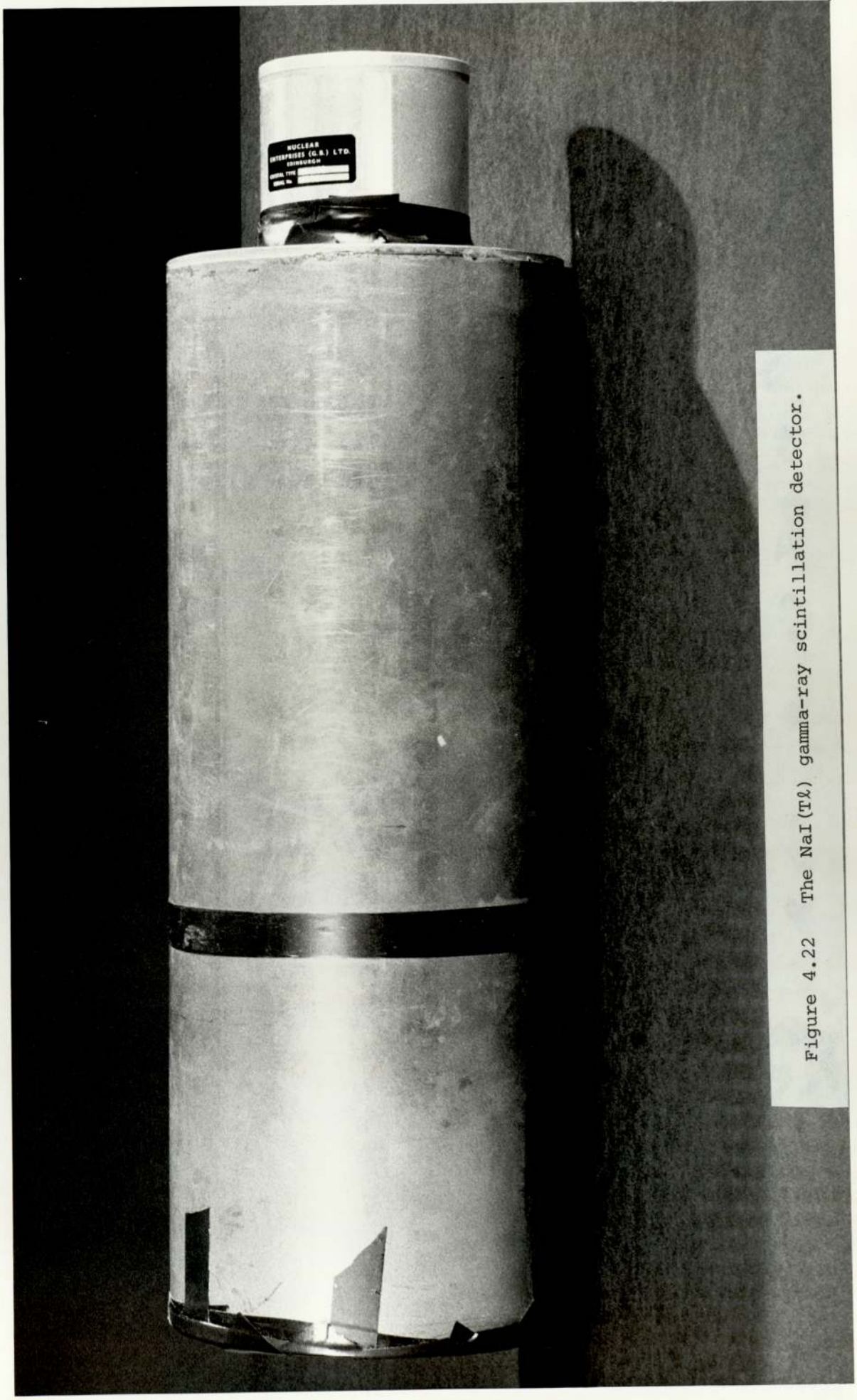

Figure 4.22 The NaI(Tℓ) gamma-ray scintillation detector.

cathode diameter of 110mm, and this photomultiplier has a much better energy resolution than the Philips 56 A.V.P. tubes which are used in many other experiments.

A poor energy resolution with a 56 A.V.P. photomultiplier tube is reported by Gupta and Nath.[43] Figure 4.23 shows the spectrum of ^{60}Co with the 58 A.V.P. photomultiplier tube. As can be seen the peak to valley ratio as defined in the figure is 3 to 1.

4.13 Detector Shielding

Adequate detector shielding is needed, because the NaI (Tℓ) scintillator as was mentioned already is sensitive to neutrons.

A steel shadow bar is placed between the neutron source and detector so that it prevents neutrons coming directly from the neutron source entering the detector and causing a high background. In addition, the NaI (Tℓ) detector is shielded from the scattered neutrons by using lead, boric oxide, and paraffin wax in the shape of cylinders, and this construction also shields against spurious γ-rays. The cross-section of the detector shield, and the effect of the shielding materials are shown in figures 4.24 and 4.25 respectively. The mobile gamma-ray detector shielding construction can be seen in figure 4.26.

4.14 Gamma-ray detector efficiency

The number of counts in the peak which consists of the normal total absorption peak and counts due to some γ-rays produced originally by the photoelectric effect being degraded in energy due to Compton scattering which emerging from the sample must be corrected for the detector efficiency.

The full energy peak efficiency $\varepsilon(E_\gamma)$ is defined as the ratio of the number of γ-ray counts of energy E_γ in the full absorption peak to the number of counts of γ-rays with energy E_γ

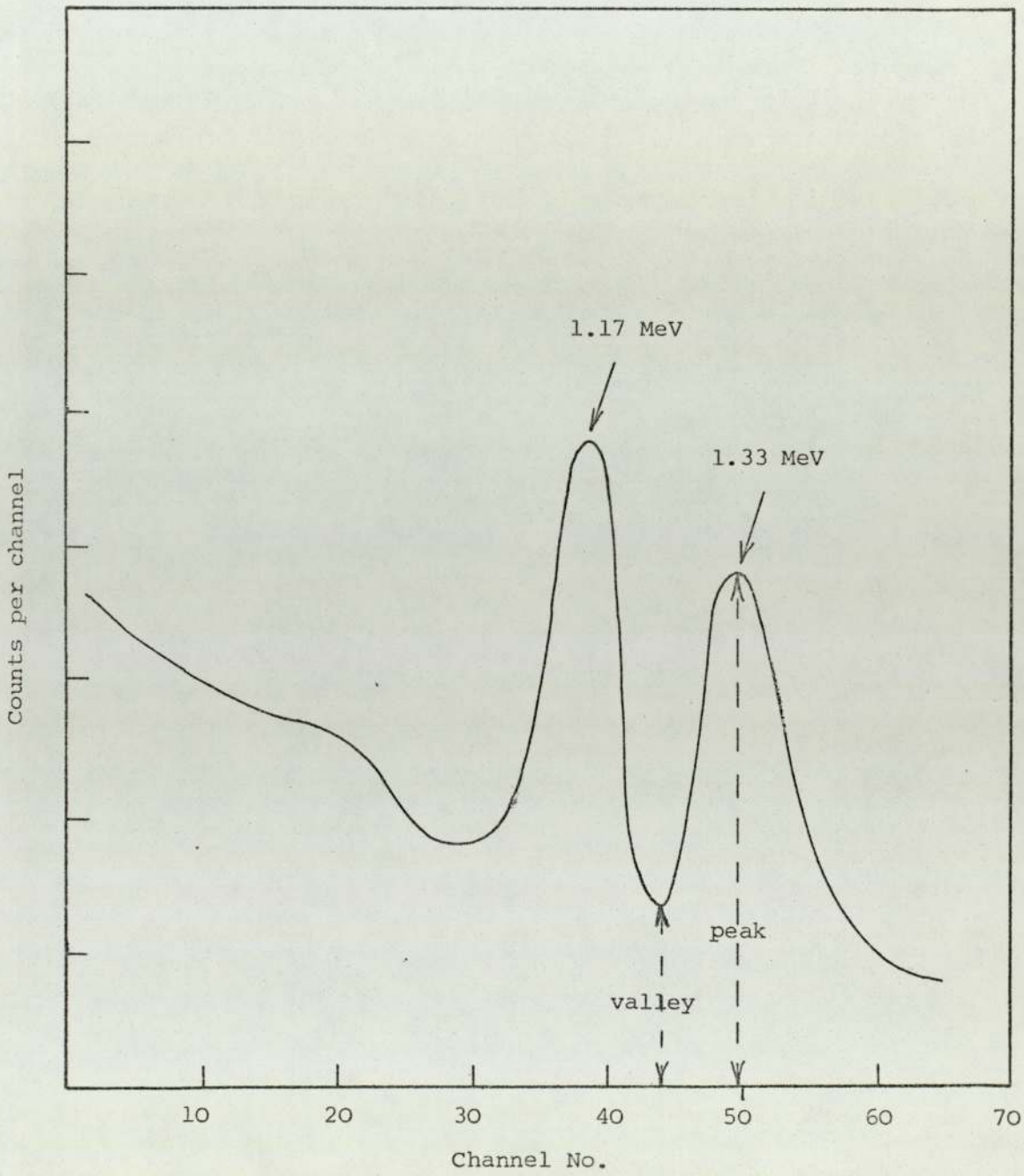

Figure 4.23. Sketch of ^{60}Co γ-ray spectrum illustrating the peak to valley ratio.

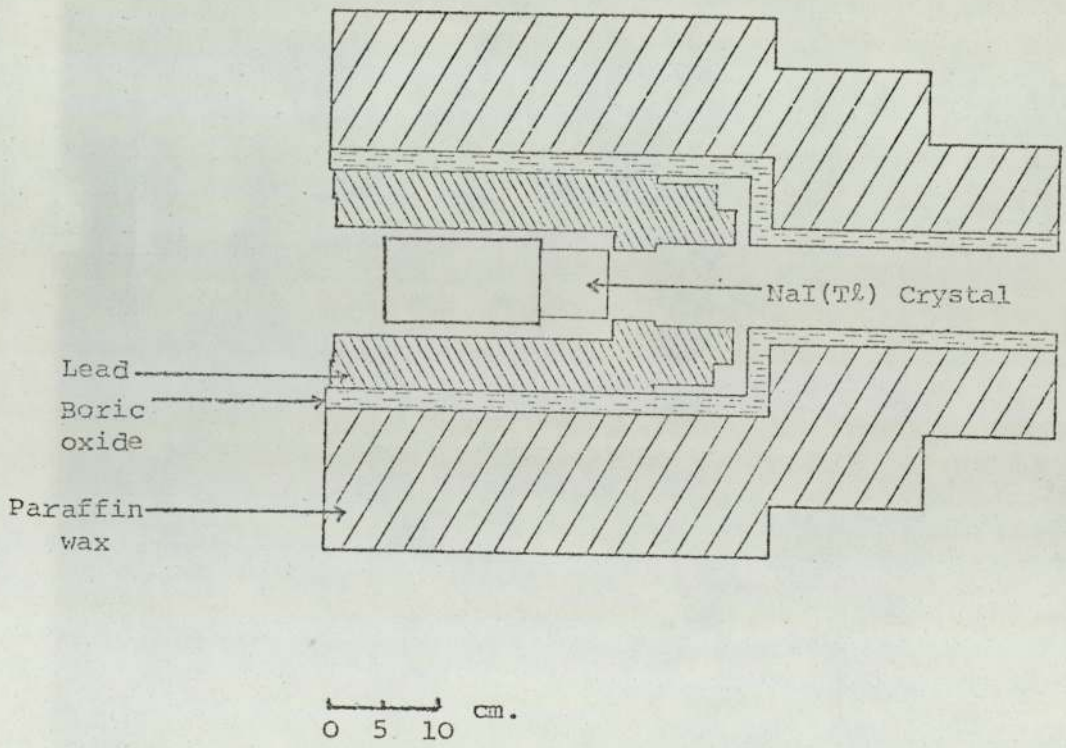

Figure 4.24. Cross-section of the gamma-ray detector shielding.

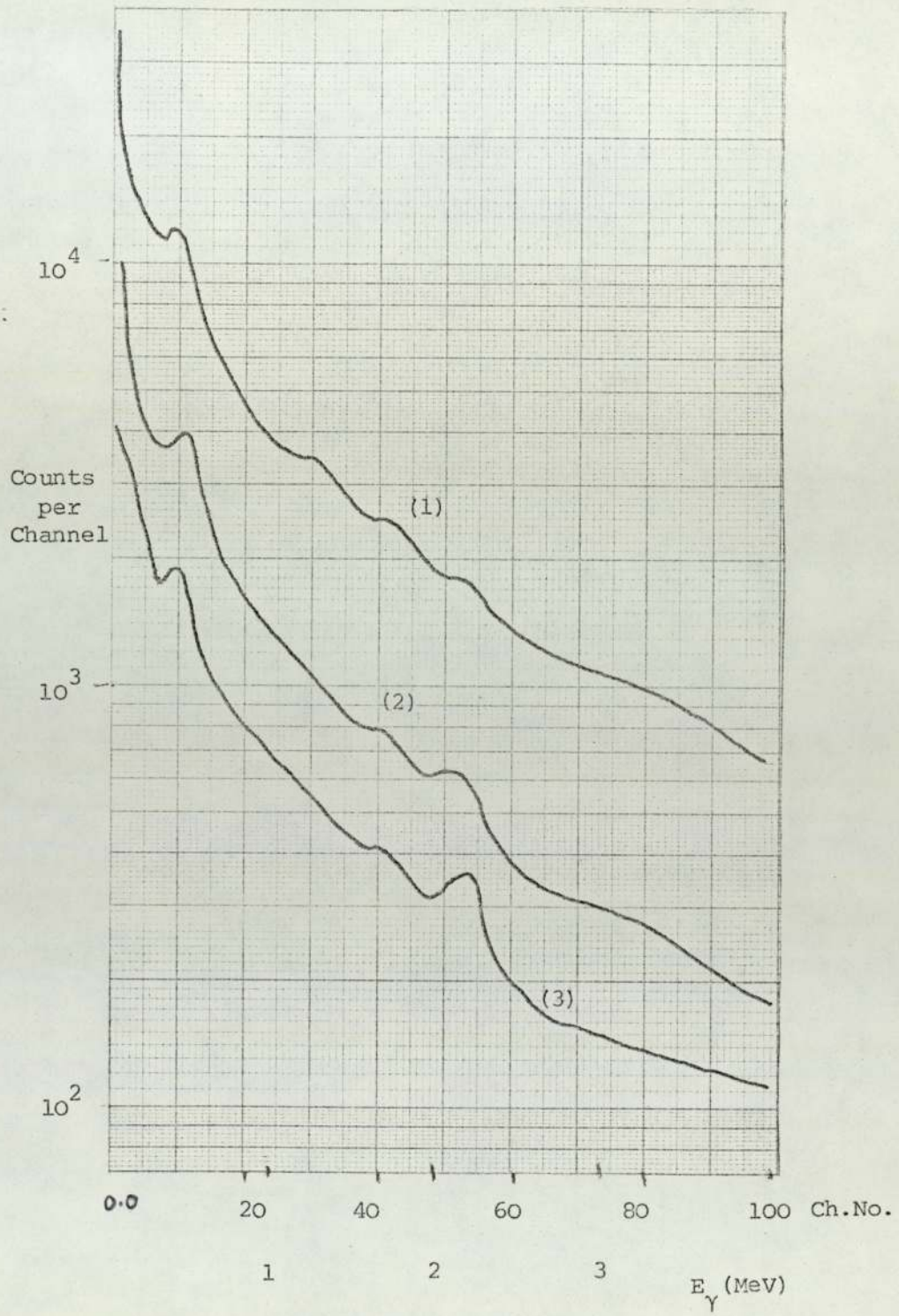

Figure 4.25. The effect of various degrees of shielding in γ-ray detector.

(1) Spectrum with no shield.

(2) Spectrum with shielded detector.

(3) Spectrum with shielded detector and shadow bar.

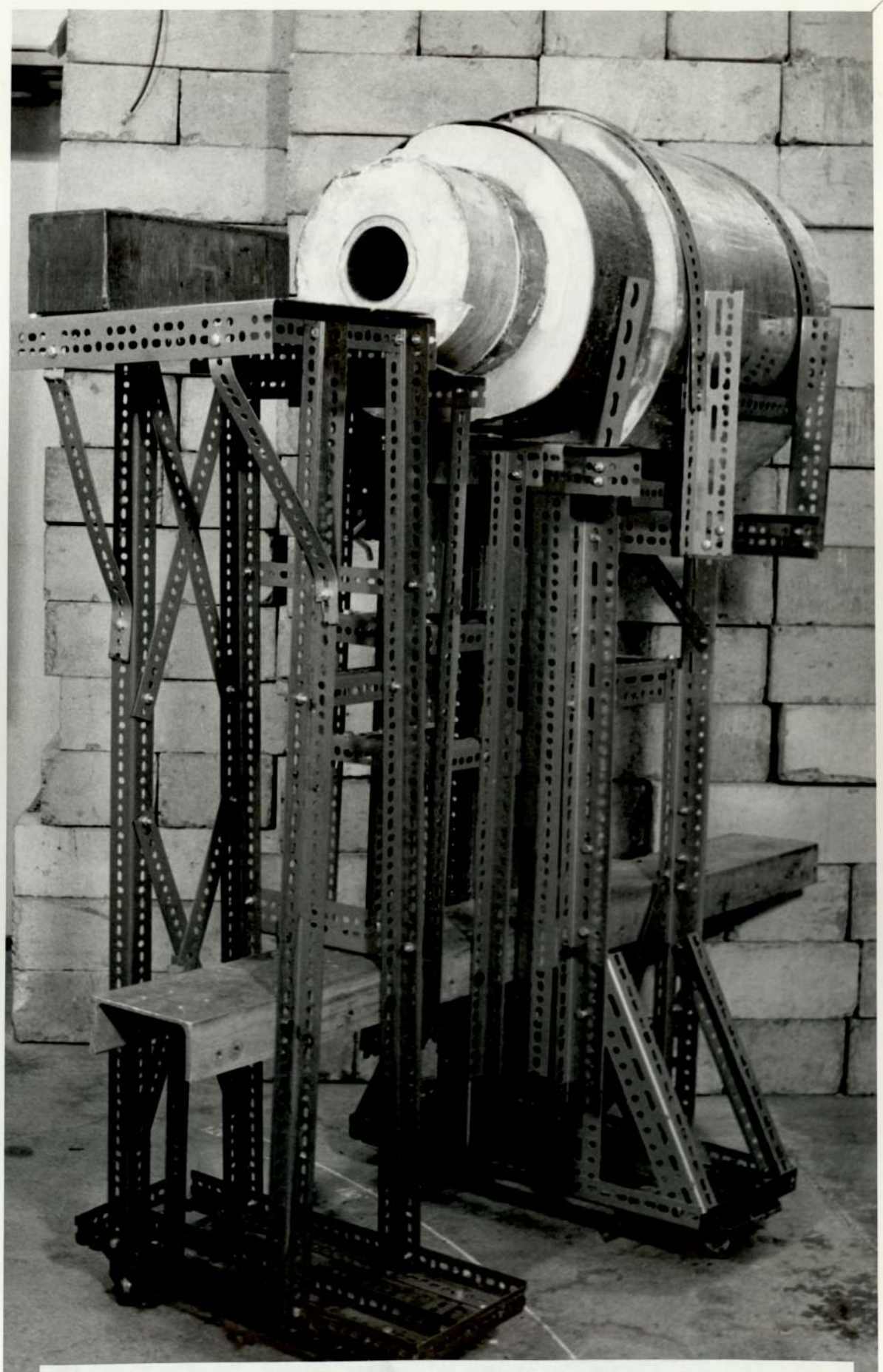

Figure 4.26 The mobile γ-ray detector shielding construction and shadow bar.

incident on the scintillator.

The peak efficiency is measured experimentally rather than computed by a Monte Carlo technique. In this work the experimental measurements are applied to obtain the γ-ray detector efficiency by the following formula:

$$\varepsilon\ (E_\gamma) = \frac{P(E_\gamma)}{t} \cdot \frac{4\pi}{S.F(E_\gamma)} \quad \ldots\ldots\ldots\ldots\ldots\ (4.10)$$

where $P(E_\gamma)$ is the total count in the photopeak, t is the accumulation time for the γ-ray spectrum from a standard γ-ray source, S is the number of disintegrations of the source per second, and $F(E_\gamma)$ is the fraction of disintegrations producing the gamma-rays of interest. The value of $F(E_\gamma)$ is unity for all the standard γ-ray sources used except for ^{137}CS where it is 0.935.

This is because in the decay of $^{137}_{55}Cs \xrightarrow{\bar{\beta}} {}^{137}_{56}Ba$

6.5% of the transitions go straight to the ground state of ^{137}Ba when no γ-ray is emitted. The standard isotopic γ-ray sources used were ^{137}Cs, ^{54}Mn, ^{22}Na & ^{60}Co with γ-ray energies of 0.662 MeV, 0.835 MeV, (0.511, 1.28) MeV, and (1.17, 1.33) MeV respectively.

Energy spectra from the γ-ray sources were measured with the discriminator level set at its lowest level. The number of γ-ray counts in the full energy peak was found by the method suggested by Heath.[44] Here the low energy side of the peak was completed to be symmetrical with the high energy side. The accumulation time, t, was measured by a calibrated stopwatch. Figure 4.27 represents the result of the experimental measurement which is the peak efficiency of the γ-ray detector versus incident γ-ray energy.

4.15 Gamma-ray energy calibration

The long lived isotopic gamma-ray sources can be used

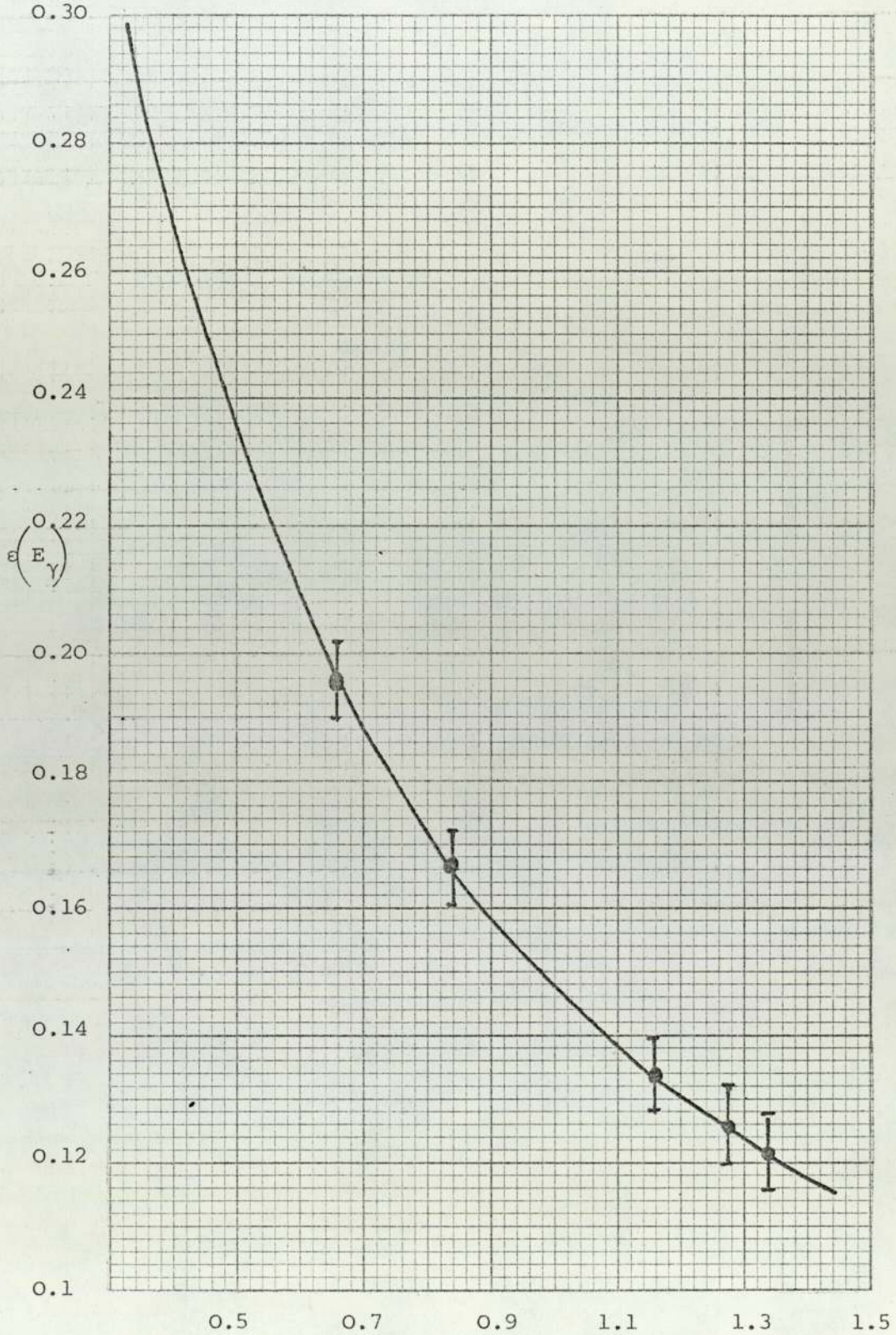

Figure 4.27 Gamma-ray detector efficiency versus gamma-ray energy.

to calibrate the γ-ray energy scale up to about 1.3 MeV. Standard sources of 1.0μCi activities were used. The four standard γ-ray sources used are listed in table 4.1.

Isotope	E_γ (MeV)	Half Life
^{137}Cs	0.662	30 years
^{54}Mn	0.835	303 days
^{22}Na	0.511	2.6 years
	1.28	
^{60}Co	1.173	5.26 years
	1.332	

Table 4.1 Standard γ-ray sources.

The pulses are displayed on a pulse-height analyser and were found to be linear with energy to within ± 1% for the γ-ray sources used, provided that the count rate in the detector was kept constant for each measurement. For the energy calibration, the discriminator level, on the Constant fraction discriminator was set to zero. The linear line for the γ-ray energy is taken from the dynode 13 of the 58 A.V.P. photomultiplier tube, and after passing through the preamplifier and main amplifier, the pulses were gated, and analysed by the pulse height analyser.

The linear delay, and the linear gate were included in the γ-ray energy calibration, because a slight decrease of pulse amplitude bypassing through these units was noticed. Figure 4.29 shows the energy line part of the electronic circuitry which was used for energy calibration.

4.16 Time resolution

In coincidence measurements the minimum resolving time which can be obtained without loss of the coincidences events is determined by the spread in the apparent time of arrival of the pulses at the coincidence circuit. The function of the coincidence circuit is to build up a spectrum of γ-ray detector events which arrive in the correct time interval after the production of a source neutron from the reaction. The electronics circuitry needed to provide this were the timing line and the linear line. The timing line, deals with time analysis of the detector events, and the linear line, deals with energy analysis of the events, and in fact the timing line was used to gate the linear line. The time resolution available from a scintillator detector depends mainly on the characteristics of the output signal from the photomultiplier. The spread in delay between the emission of the light pulse by the scintillator, and the beginning of the pulse from the photomultiplier is mainly determined by the spread in the delay in emission of the first photoelectron by the photo-cathode. It has been reported by Post and Schiff[46] that the mean time delay for the emission of the first photoelectron can be shown as:

$$\bar{t} = \left(1 + \frac{1}{R}\right) \frac{\tau}{R} \quad \ldots\ldots\ldots\ldots\ldots\ldots \quad (4.11)$$

where τ is the decay time of the scintillator and R is the total number of photoelectrons produced by the photocathode. Thus to obtain the best time resolution from a scintillator detector, the scintillator should have a short decay time and high light output, and the photomultiplier transit time should be low and in addition a high proportion of the light incident on the photocathode should result in the emission of electrons.

The flight path is chosen so that γ-ray and elastically scattered neutron events are completely resolved in time. Careful consideration of the design of the photocathode[47] and the first dynode geometry and with the addition of focussing grids, proper voltage in the photomultiplier tube will reduce the timing error. The Philips 58 A.V.P. photomultiplier tube used in this experiment has transit time spread of 1.0 nsec, and a photocathode diameter of 110mm.

Clearly, the time resolution in the coincidence experiment is very important as the better the time resolution the closer the detector can be placed to the sample with a consequent improvement in the signal to background ratio.

4.17 Discriminator setting for the α-particle and γ-ray detector pulses

The spectra of both the alpha-particle and gamma-ray detectors were displayed on the pulse height analyser by suitably shaping the pulses with the linear amplifier. To check the discriminator setting for both the α and γ-detectors the two electronic arrangements shown in figures 4.28 and 4.29 respectively were used.

The α-particle pulses were discriminated by a level fixed on the 100MHz Discriminator (ORTEC 436), to eliminate low energy noise, but to pass the pulses due to 3.5 MeV alpha-particles from the $T(d,n)^4He$ reaction. As it can be seen in figure 4.28, the α-detector output is amplified by a linear amplifier (ORTEC 485), and the resulting pulses gated by the output of the 100MHz discriminator. As the discriminator level was increased, pulses below this level were not passed and therefore were not available to open the gate. Thus the lower energy region of the spectrum was removed. Figure 4.30 shows a pulse height spectrum of α-particles produced in the deuteron bombardment of the tritium target. The discrimina-

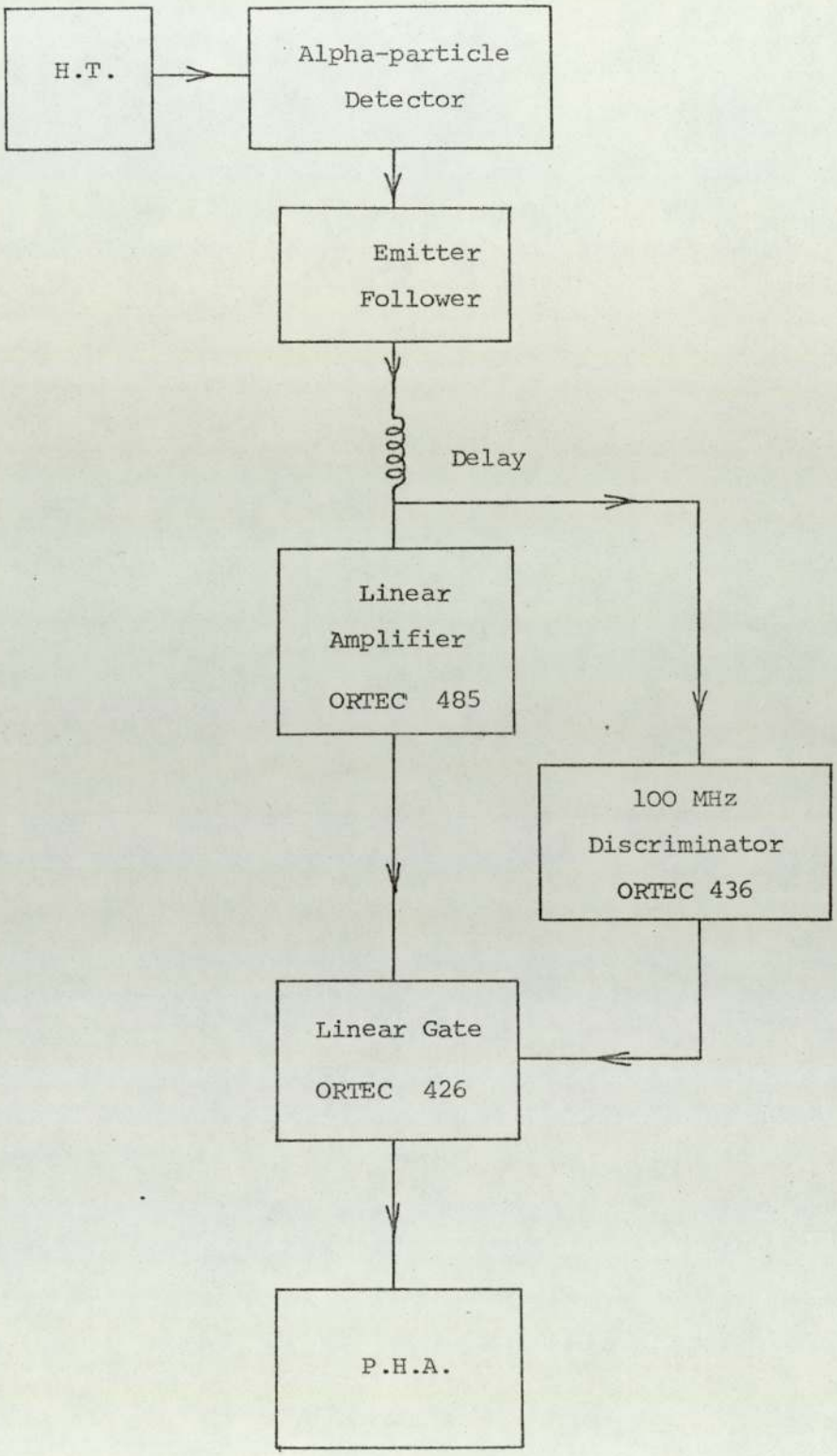

Figure 4.28. Electronic arrangement for setting the α-particle detector discriminator level.

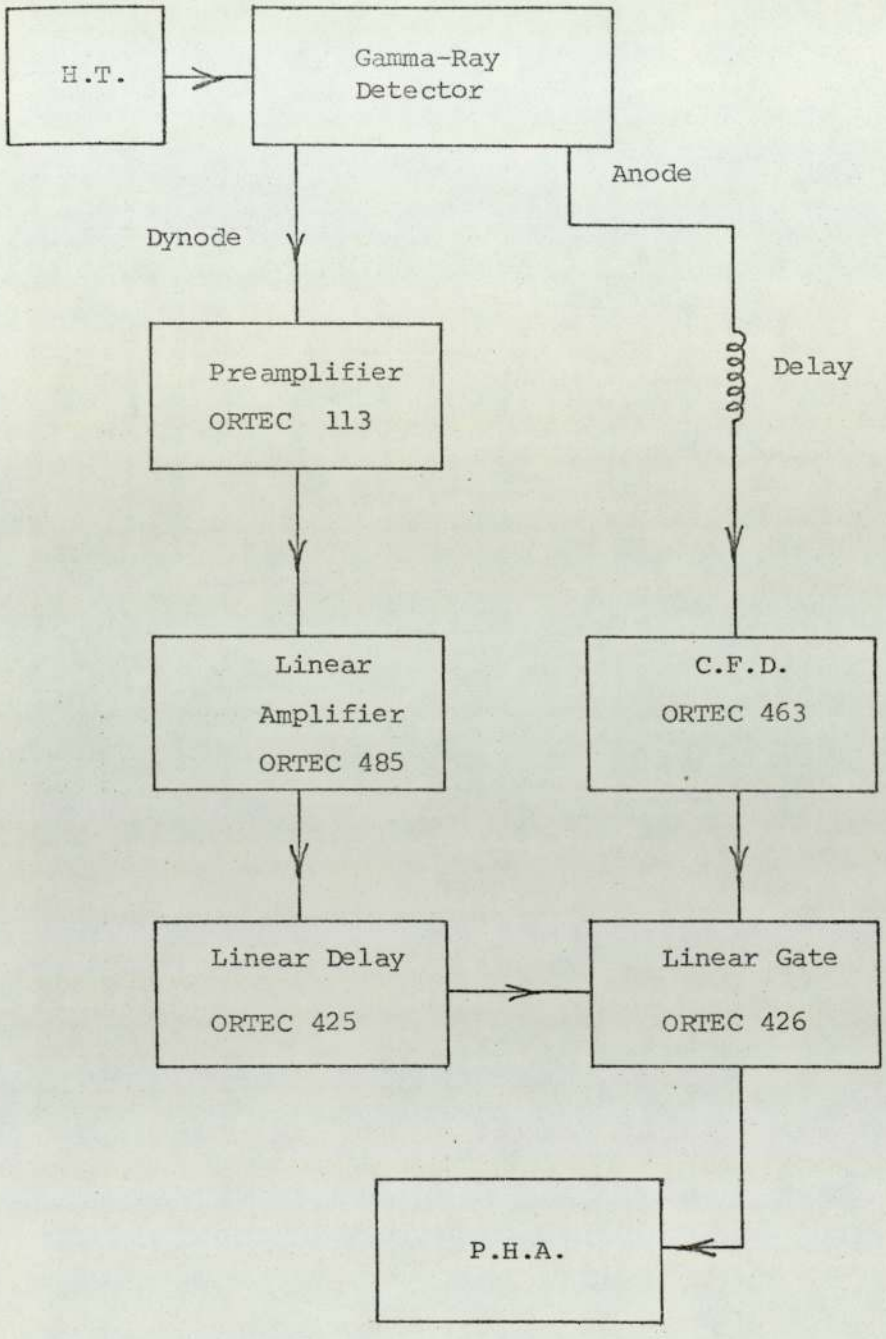

Figure 4.29. Electronic arrangement for setting the gamma-ray detector discriminator level.

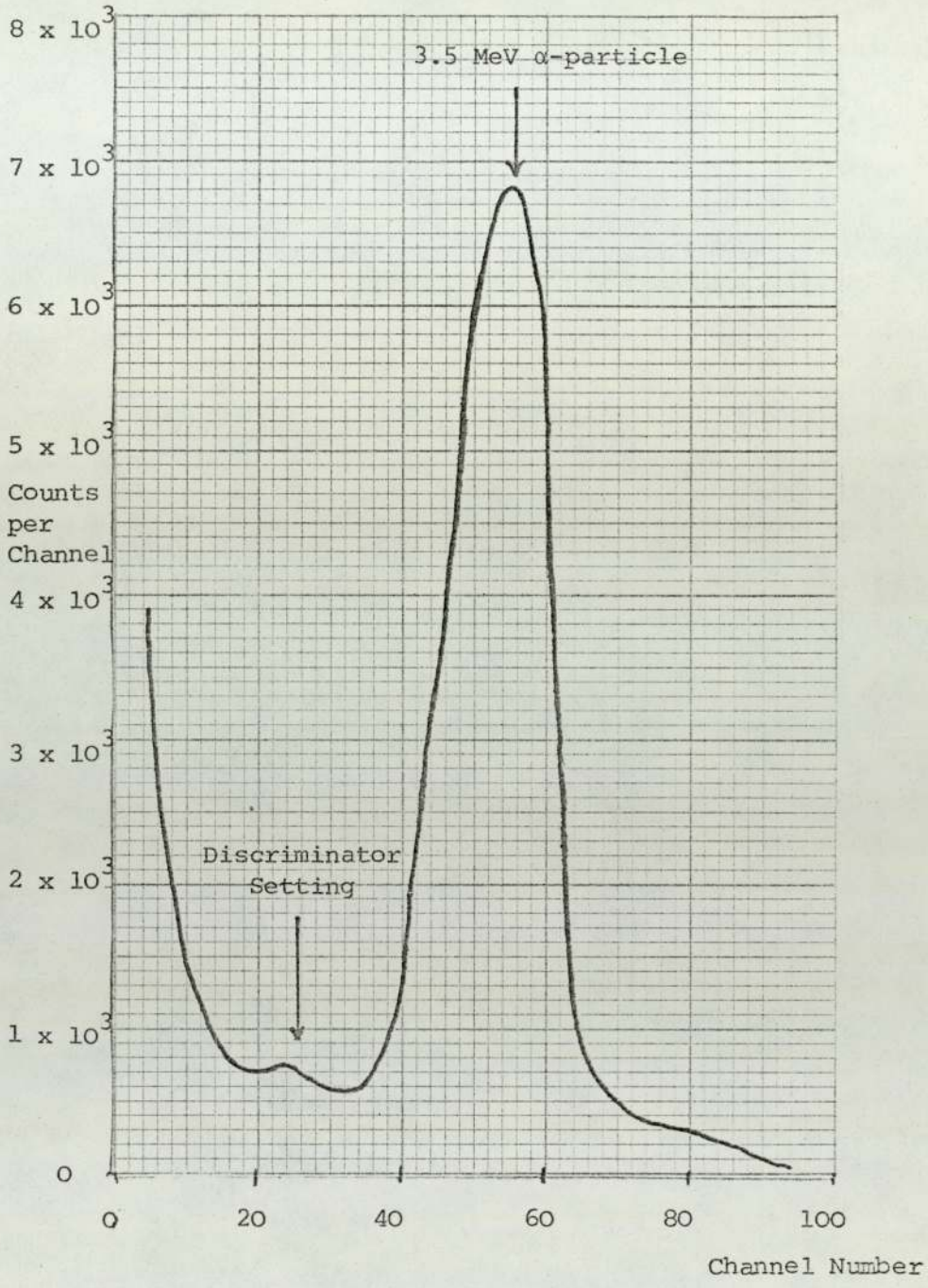

Figure 4.30 The pulse height spectrum for the α-particle with discriminator setting.

tor level as determined by the above method is shown in the figure.

The gamma-ray discriminator level was set by the same technique used for the α-particle discriminator level. The detailed electronic system can be seen in figure 4.29. This level was set at those values appropriate to the gamma-ray energies being investigated in each experiment for removing the low amplitude pulses due to scattered neutron background coming to the γ-ray detector.

4.18 Gamma-ray energy spectrum

In figure 4.31 an example of the γ-ray energy spectrum from a small sample of iron at a scattering angle of 45^{o} is shown. The intense γ-ray peak is that of 0.847 MeV which can be seen clearly. Other γ-ray energies are also detected, a peak being resolved at 1.24 MeV. The 0.847 MeV photopeak is situated on the Compton distributions due to the partial detection of these higher gamma-rays. In order to measure P(θ), i.e. the total counts in the photopeak, the method by Covell[45] is used. Covell's method for estimating the intensity of a single γ-ray in a complicated spectrum is to measure a calibrated fraction of the area of the total absorption peak. In this method a known fraction of the full energy peak was used. A line was drawn across the base of the photopeak, as shown in figure 4.32. In order to find the total number of the Counts in the peak it is necessary to measure a reference spectrum, which should show the γ-ray photopeak of approximately the same energy with the background subtraction. Then the fraction of the total count above the line drawn in figure 4.32 can be determined.

For example, the reference source for the energy spectrum of iron sample used was ^{54}Mn with a photopeak energy of 0.835 MeV.

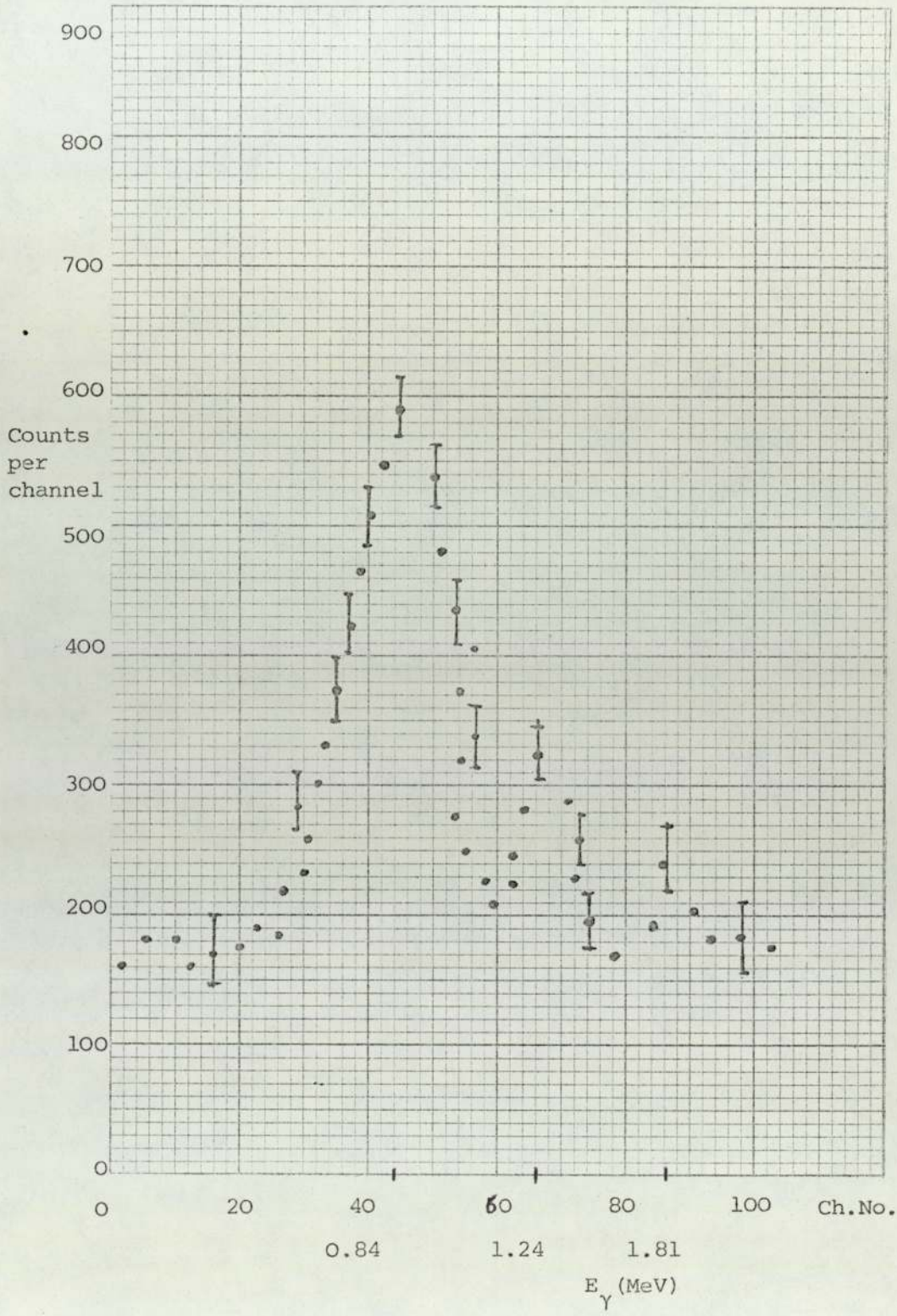

Figure 4.31. A typical spectrum of gamma-ray energies from small iron sample (scattering angle 45^{o}).

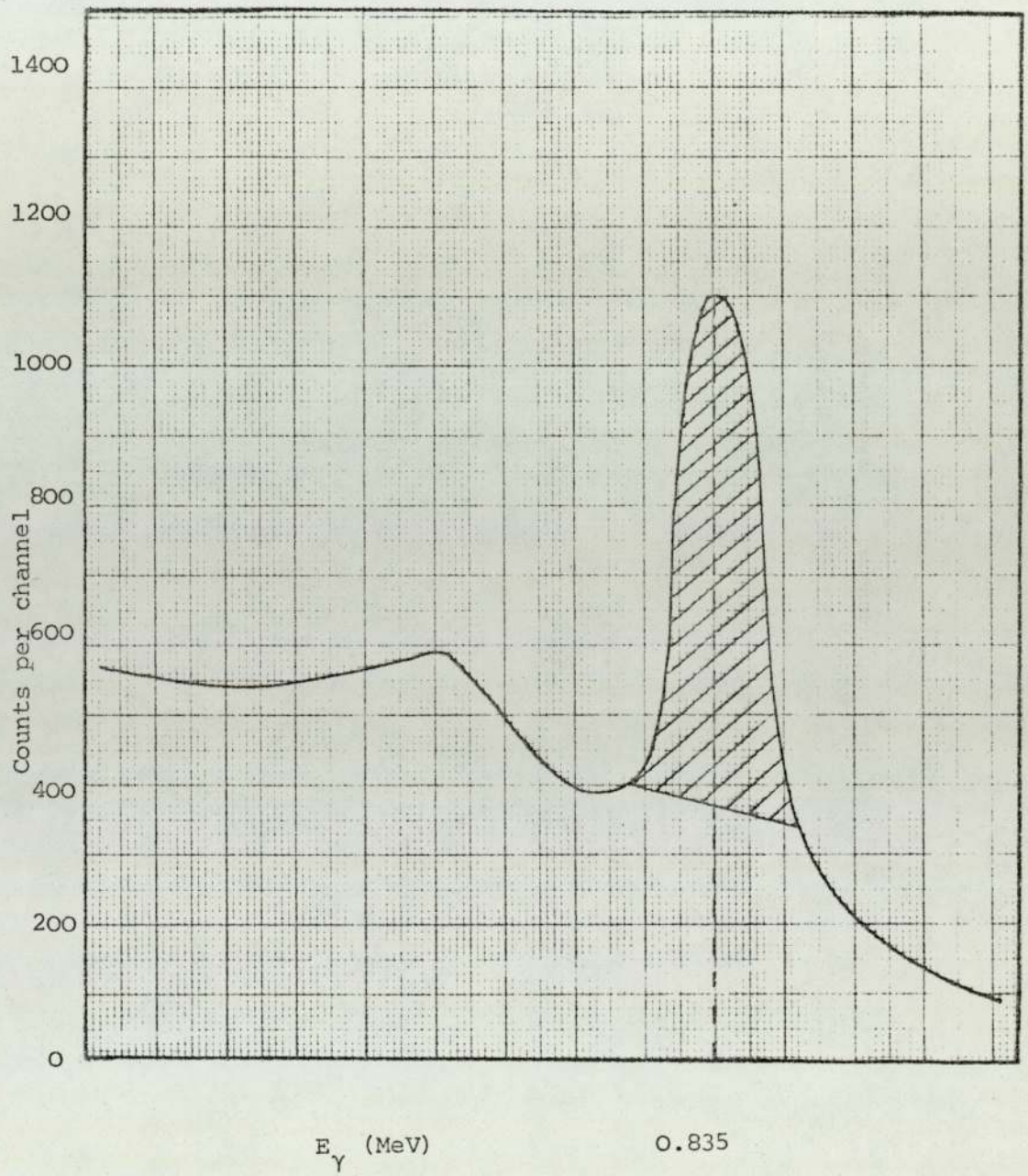

Figure 4.32. A sketch of gamma-ray energy spectrum of ^{54}Mn illustrating Covell's method.

Chapter 5

5. Experimental Results

5.1 Introduction

In order to explain the results it is necessary to account for the changes in the γ-ray spectrum that take place both between the small and large samples and between different angular positions of the detector. The first part of the present chapter presents the experimental results in this area. The second part of the chapter deals with the variation of effective gamma-ray production cross-section with scattering angles.

5.2 Experimental method

The energy spectra measurements are taken at several angles in the range of 0^{o} to 90^{o} in order to obtain the required data. The Pulse-Height Analyser is put in the 'Add' mode for the period of a run with a fixed number of α-particles coincident with the neutron emission from the d-T reaction. During this time period which is measured by a calibrated stopwatch, the scattering sample must be in place in the neutron beam. Therefore, the pulse height spectrum which is obtained represents the gamma-radiation from the scatterer, together with the background radiation which is defined here as the total radiation coming from the experimental equipment and other sources except from the scattering sample.

In order to remove the background radiation from the spectrum, the scattering sample is removed from the neutron beam, and the pulse-height analyser is set in the 'subtract' mode for the same number of α-particles counts in the α-monitor as for the 'Add' mode. In this mode the pulse height analyser subtracts only detected radiation not coming from the scatterer from the previous spectrum; therefore, at the end of run, only radiation due to the

presence of the scattering sample is recorded.

This procedure is repeated until sufficient data for statistical accuracy is accumulated. Data was taken for both the small and large samples in this experiment.

5.3 Iron samples

The iron sample is an alloy containing approximately 90% iron and the other materials are nickel and those amounts of impurities such as carbon and oxygen. The nickel, oxygen, and carbon caused no interference with the experiment due to the small amounts present and the different γ-ray energies they produce. The small iron sample is a square flat plate of 14.0cm dimensions, and 2.0cm thick, while the large sample is rectangular in shape of dimensions 32cm x 31cm x 4cm thick. The iron sample has its natural isotopic abundances, and there is negligible interference from the other isotopes except ^{56}Fe.

Table 5.1 shows the natural compositions of iron.

Isotope	Abundance
^{54}Fe	5.82%
^{56}Fe	91.66%
^{57}Fe	2.19%
^{58}Fe	0.33%

Table 5.1. Isotopic abundances of ^{N}Fe.

5.3.1 Experimental procedure for the iron samples

Both the small and large scattering samples of iron were placed on a vertical stand at a distance of 25.0cm from the neutron target, so as to subtend completely the neutron beam.

The sample face was placed perpendicular to the central axis of the neutron beam. Figure 5.1 shows the position of the large scattering iron sample in the experimental arrangement.

In the procedure of data accumulation mentioned in section 5.2 to subtract the background radiation from the spectrum the iron sample was removed from its position.

5.3.2 Experimental results for the γ-ray spectra from the iron samples.

The gamma-ray energy spectra for the small iron sample were accumulated for five scattering angles : 30°, 45°, 60°, 75° and 90° respectively. Figure 5.2 shows the 60° gamma-ray spectrum. This is typical of the γ-ray energy spectra from small iron sample except that at the lower scattering angle the intensity of the peak was noticed to be larger, and this is illustrated in figure 5.3 which shows the 30° gamma-ray energy spectrum.

In the case of the large iron sample, again the measurements were recorded for all the previous angles from 30° to 90°. A typical gamma-ray spectrum for the large scattering sample at the scattering angle of 30° is shown in figure 5.4, and as can be seen from this figure, the photo-peak of the large sample is now spread out and extends to lower energies due to the emitted gamma-rays being Compton scattered before escaping from the sample. Figures 5.5 and 5.6 show the gamma-ray spectra for the large scattering iron sample at the scattering angles of 45° and 60° respectively.

The spectra obtained from the small sample contain a pronounced peak due to gamma-rays from the transition of the 0.847 MeV

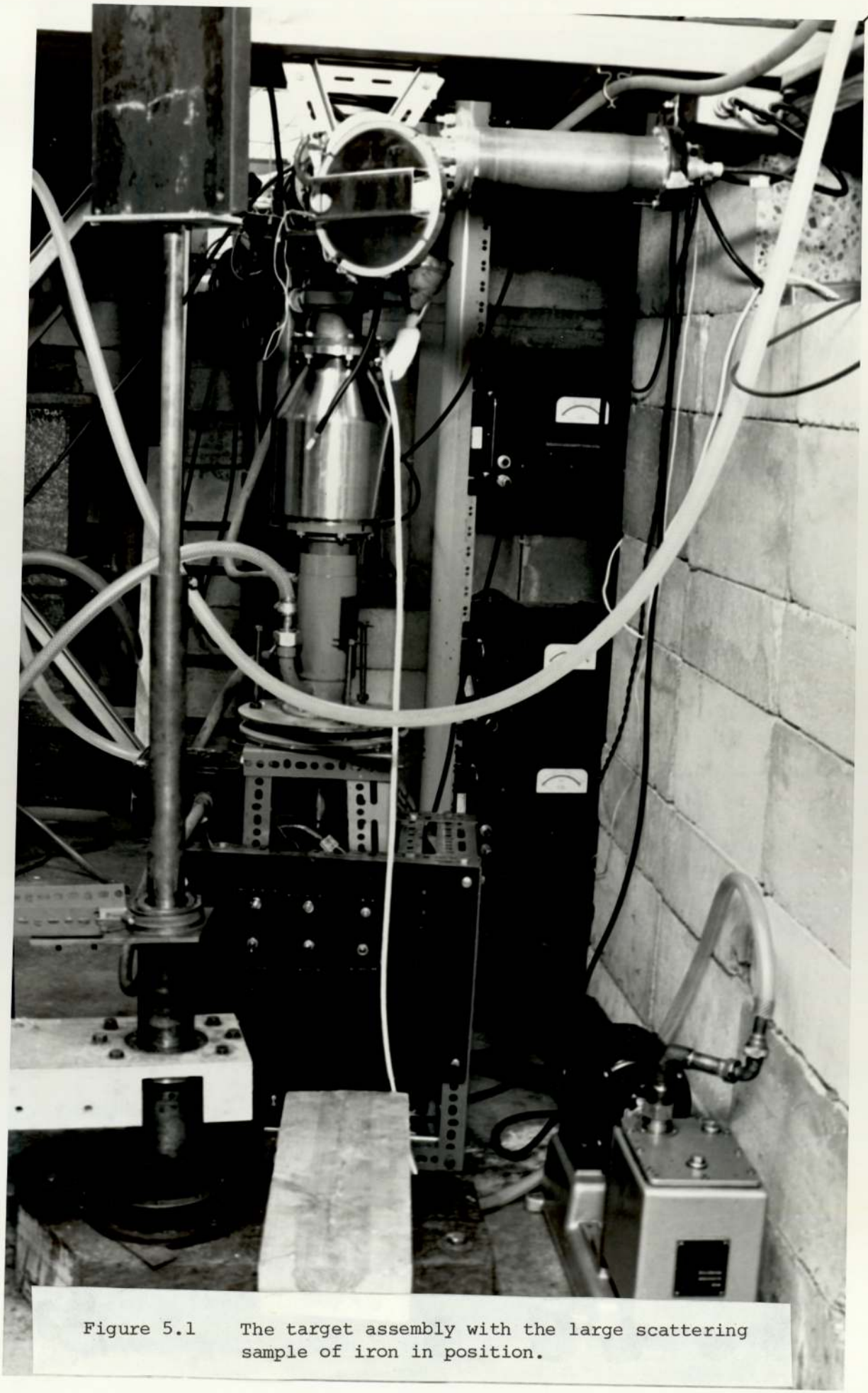

Figure 5.1 The target assembly with the large scattering sample of iron in position.

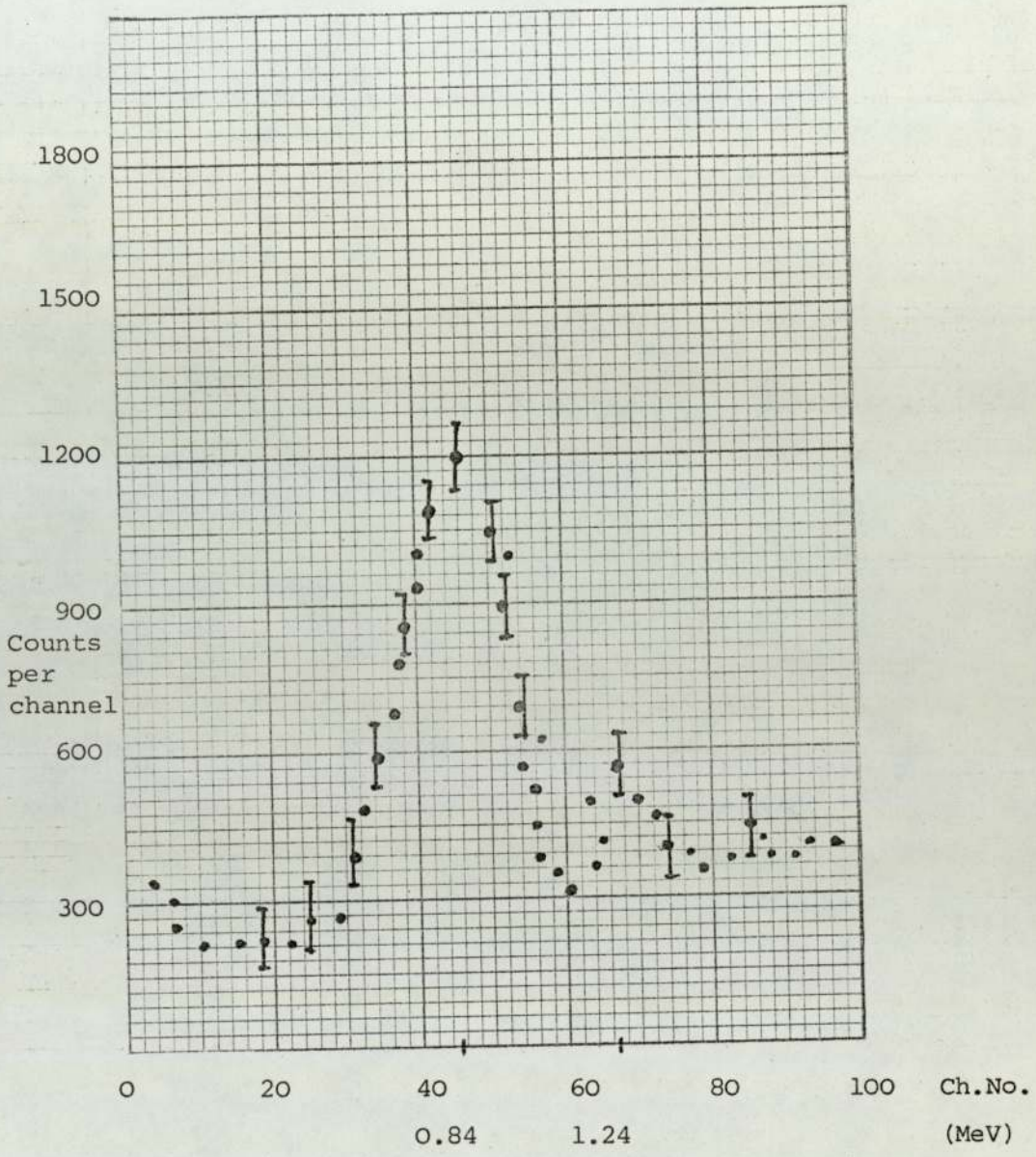

Figure 5.2. The gamma-ray energy spectrum from small iron sample, (scattering angle 60^{o}).

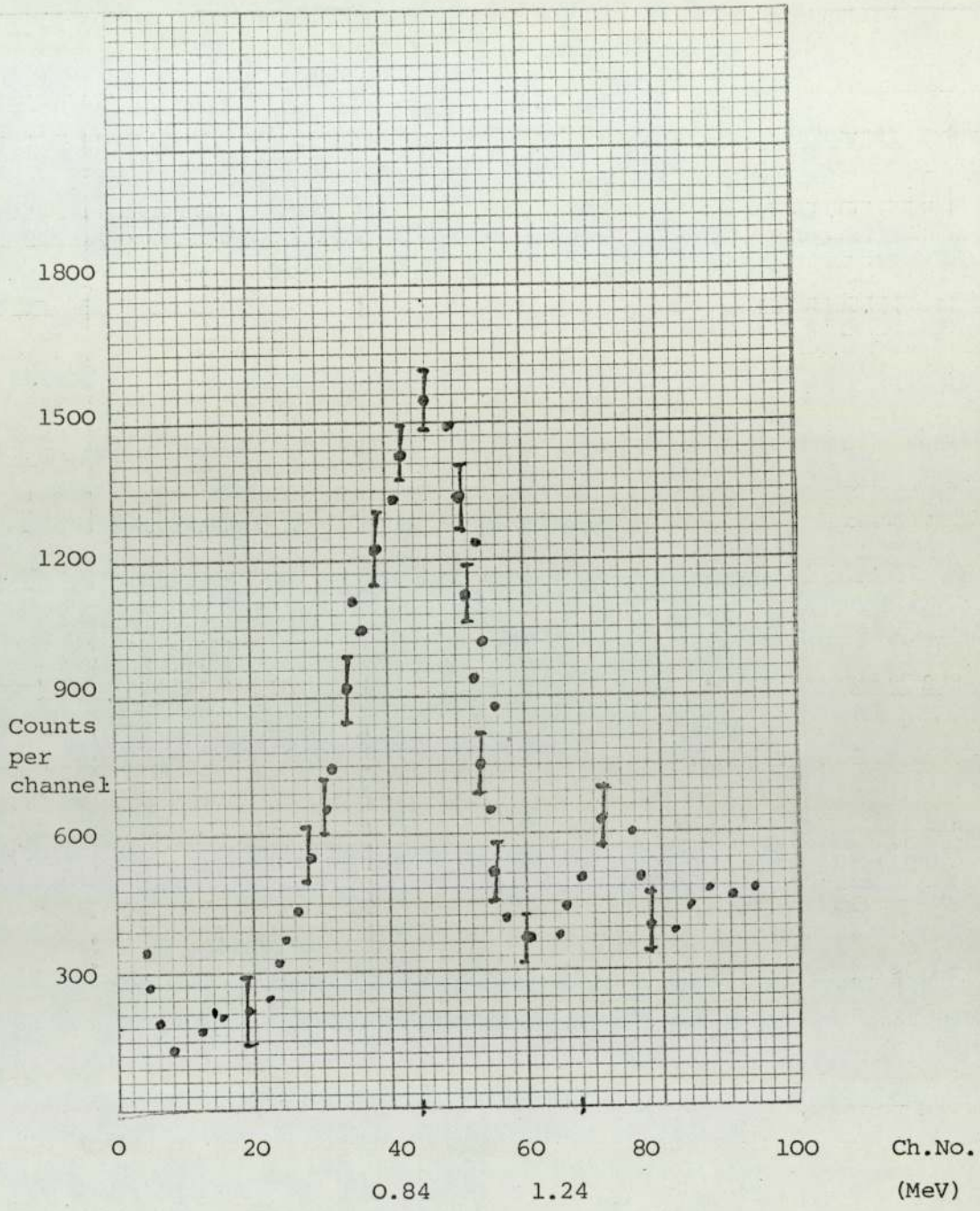

Figure 5.3. The gamma-ray energy spectrum from small iron sample (scattering angle 30^{o}).

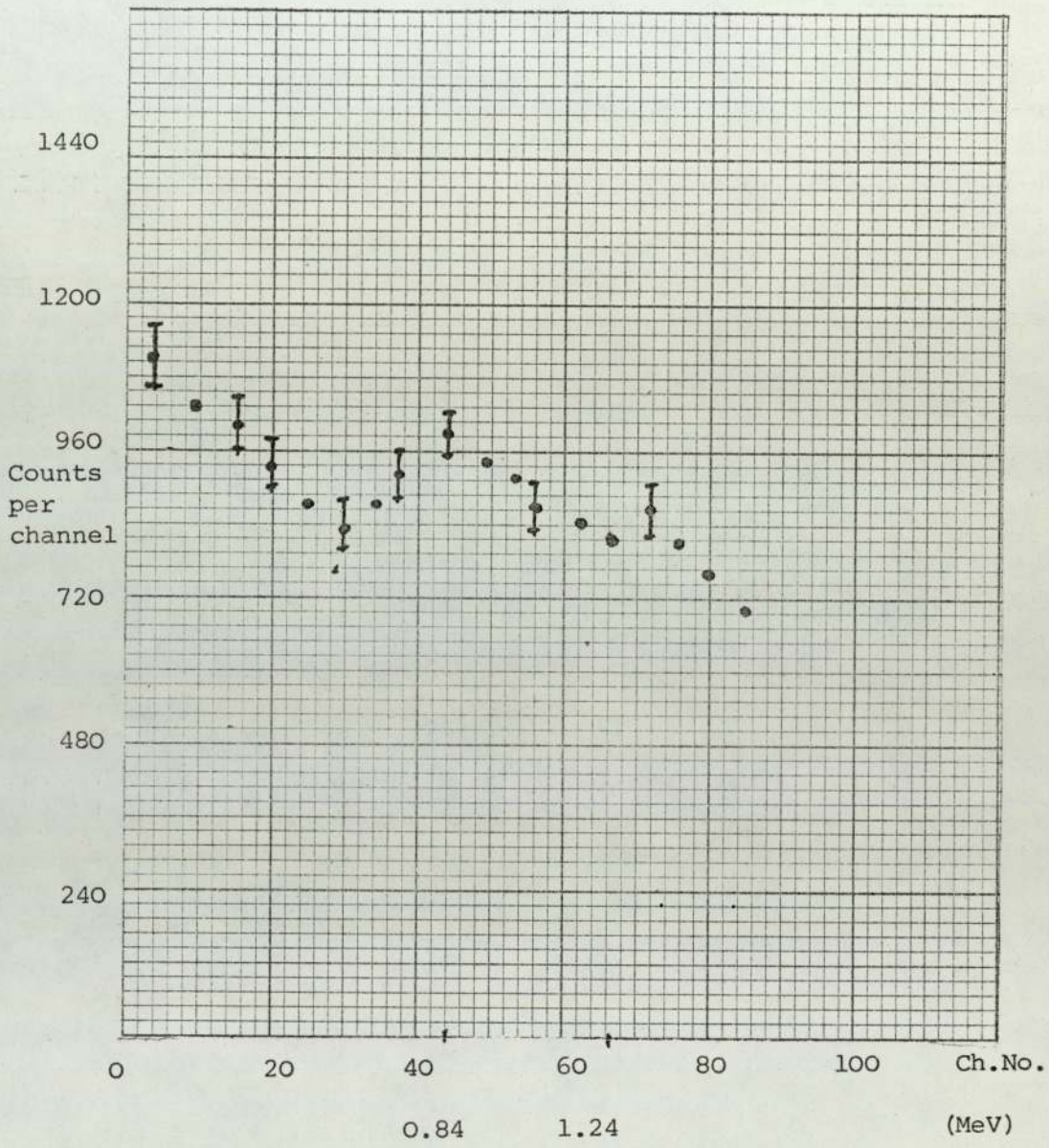

Figure 5.4 The gamma-ray energy spectrum from large iron sample, (scattering angle 30^{o}).

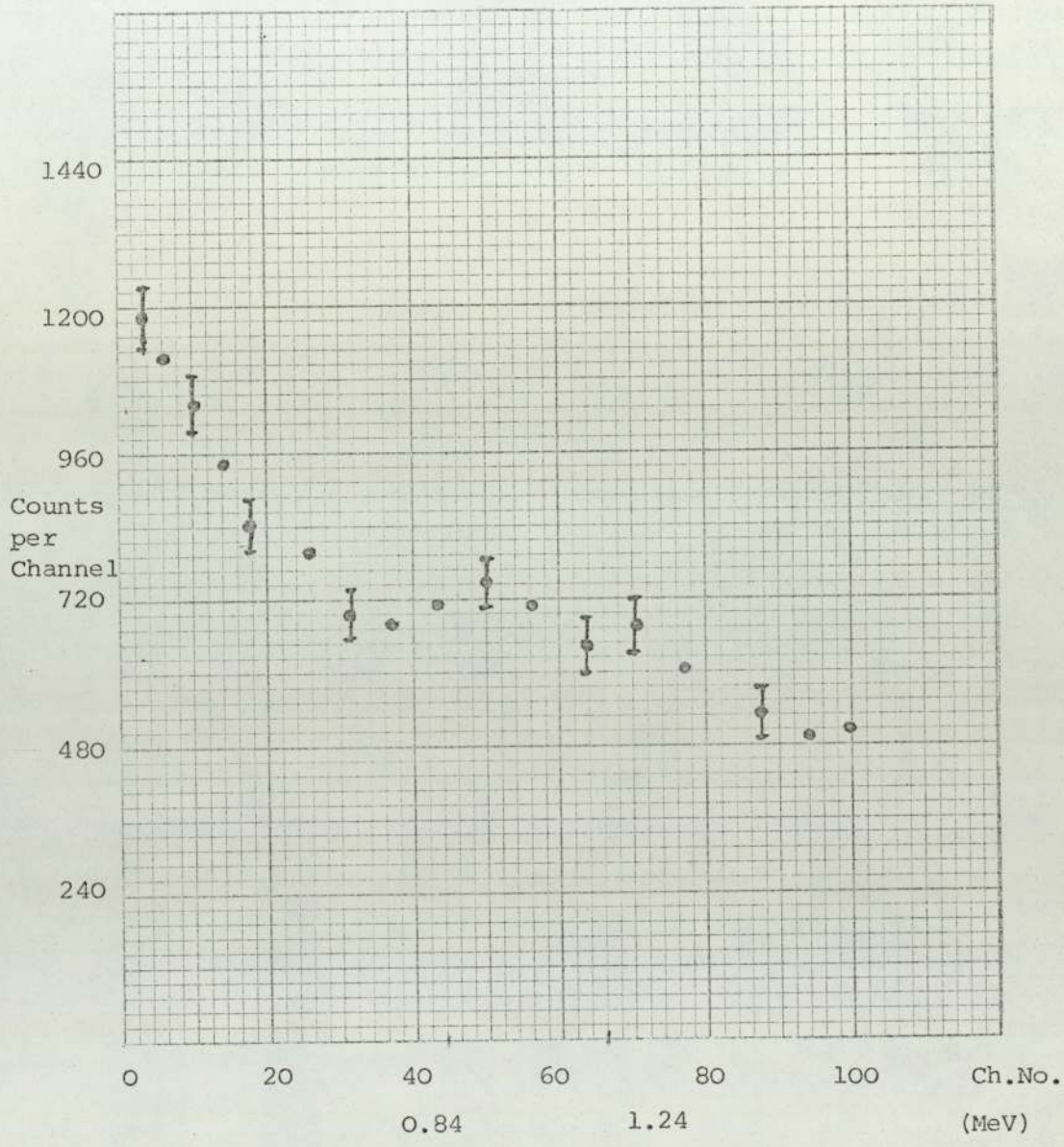

Figure 5.5 The gamma-ray energy spectrum from large iron sample (scattering angle 45^{o}).

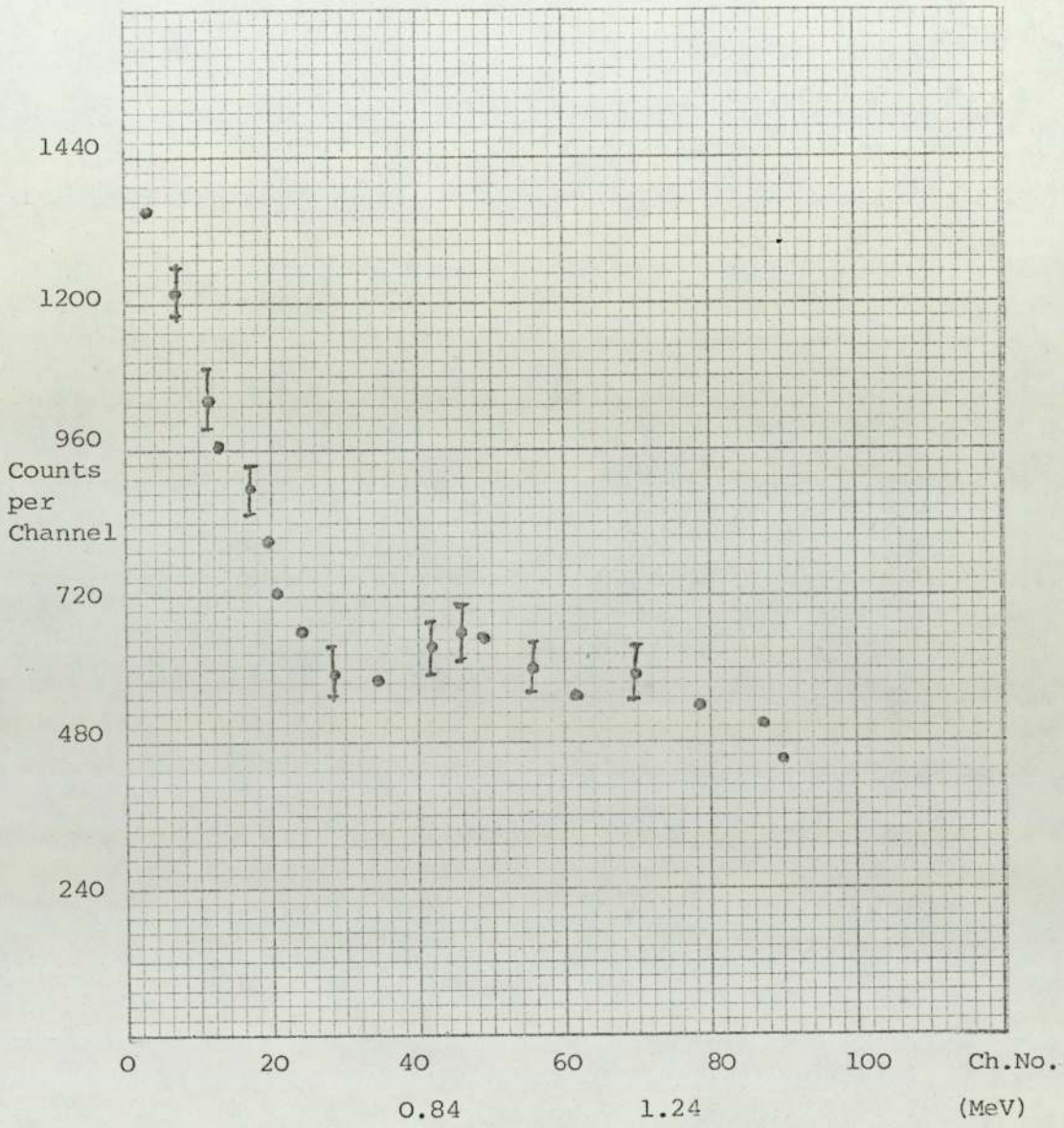

Figure 5.6 The gamma-ray energy spectrum from large iron sample (scattering angle 60^{o})

level to the ground state of ^{56}Fe.

At higher γ-ray energies the statistics are not good enough to be able to see the other peaks. However, in all the spectra measured at the different scattering angles an indication of the presence of peaks at the expected γ-ray energies 1.24 MeV and 1.41 MeV and 1.8 MeV are found. The level structure of ^{56}Fe is shown in figure 5.7 taken from Rao[65]

5.3.3 Possible competing reactions for the interactions of neutrons and iron.

The total non-elastic cross-section for neutrons of 14.1 MeV with ^{56}Fe is given by Stehn et al. [66] as 1.36 ± 0.03 barns.

The (n,2n) reaction may result in the emission of γ-rays of energy 0.805, 0.930, 1.21, and 1.316 MeV which has been reported by Lederer et al. [67] The cross-section for this reaction is 440 ± 90mb.[66]

The cross-sections for the (n,p), (n,n p) and (n,α) reactions are 112 ± 6,[66] 78 ± 40[69] and 60[62] mb respectively which comparing withthe cross-section for (n,n') with the value of 620 ± 160 mb[68] are negligible.

The reaction ^{56}Fe (n,d) ^{55}Mn may yield γ-rays of 0.983 and 0.857 MeV.

The gamma-ray energies from (n,2n) and (n,d) reactions cannot be resolved from the 0.847 MeV by the system used.

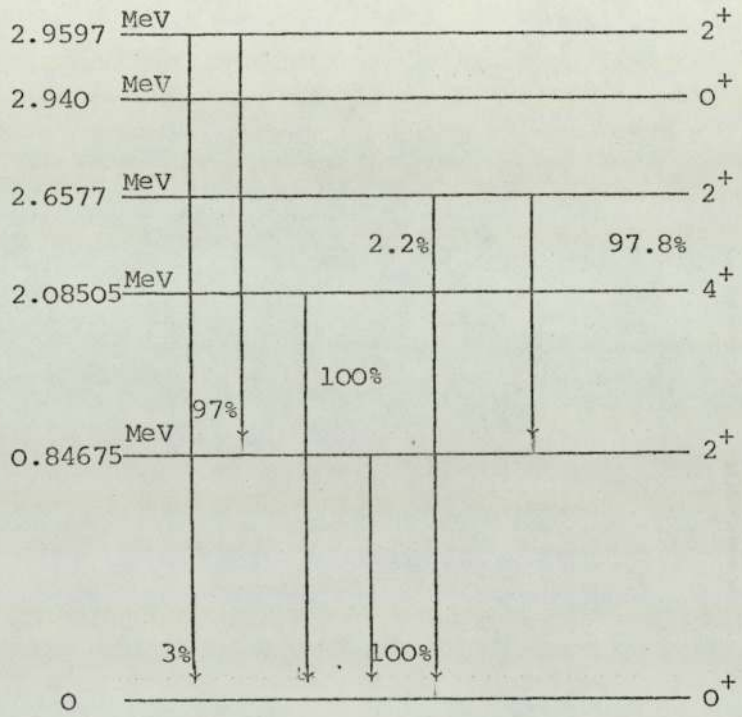

Fig. 5.7 Level structure of ^{56}Fe (65)
and transition probabilities.

5.4 LiF Samples

The LiF compound powder sample was compressed into a stainless steel can of the dimensions 12 cm x 10 cm x 2 cm with wall thickness of 0.2 mm for the small sample, and into a stainless steel can of dimensions 38 cm x 25 cm x 6.25 cm for the large size sample.

The LiF powder is 99% pure. Thus impurities in the samples are negligible.

The reason for not choosing natural elemental Li is because of its high chemical activity especially with water and the potential danger of using it in reasonably large amounts. The LiF sample has its natural isotopic abundances, however there is negligible interference from all the isotopes except ^{7}Li, and ^{19}F. Table 5.2 shows the natural compositions of lithium and fluorine.

5.4.1 Experimental procedure for the LiF samples

Both the small and large scattering samples of LiF were placed on a vertical stand as in the case of iron samples at a distance of 25 cm from the neutron target; the sample face is positioned perpendicular to the direction of the incident neutron beam.

Figure 5.8 shows the position of the small size LiF sample on the vertical stand in the Laboratory.

In the data accumulation which is described in section 5.2 for subtracting the background radiation from the energy spectrum the LiF sample is replaced by a dummy sample consisting of the sample container only.

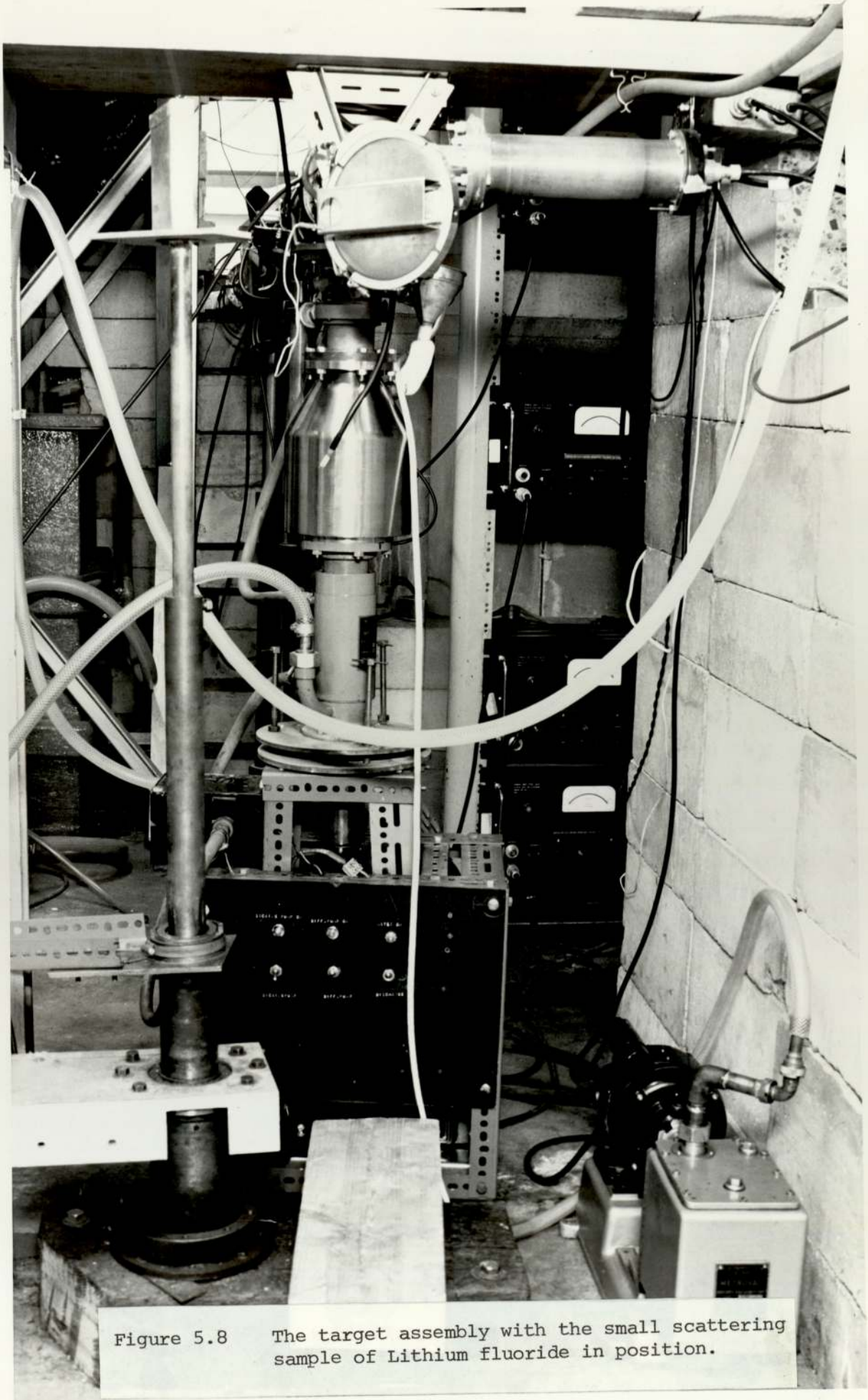

Figure 5.8 The target assembly with the small scattering sample of Lithium fluoride in position.

^{N}Li isotope	Abundance	^{19}F isotope	Abundance
^{6}Li	7.56%	^{19}F	100%
^{7}Li	92.44%		

Table 5.2 Isotopic abundances of ^{N}Li and ^{19}F.

5.4.2 Experimental results for the γ-ray spectra from the LiF samples

Figure 5.9 shows the γ-ray spectrum from the small LiF sample accumulated at the 30° scattering angle. The 0.48 MeV peak is attributed to the γ-ray transition between the first excited level and ground state of ^{7}Li, and the peak about 1.3 MeV corresponds to the γ-ray cascade from the inelastic scattering of neutrons with ^{19}F.

The level structure of both the ^{7}Li(54) and ^{19}F(70) are shown in figures 5.10 and 5.11 respectively. For the large scattering sample of LiF as in the case of small sample the energy spectra measurements were recorded for the same scattering angles as for large iron sample. Figure 5.12 shows a typical γ-ray energy spectra at a scattering angle of 60°, and as can be seen from figure 5.12 similar to the results obtained from large iron sample the photo-peak of the large sample is now spread out and extends to lower energies due to the emitted γ-rays being Compton scattered before escaping from the sample. Figures 5.13 and 5.14 show the γ-ray spectra for the large scattering LiF sample at the scattering angles of 45° and 30° respectively.

For the LiF sample data was accumulated for a longer time in comparison to the iron sample, and this is because of the difference in the inelastic cross-section of the reactions.

5.4.3 Possible competing reactions for the interactions of neutrons and LiF.

It is possible that the (n,α) and (n,2n) reactions in ^{7}Li may result in the emission of γ-rays which either cannot be resolved from the 0.48 MeV γ-ray, or they do not interfere with this peak. The cross-section for (n,α) reaction drops rapidly with incident neutron energy just beyond threshold for inelastic scattering of neutrons with ^{7}Li for the excitation of 0.48 MeV

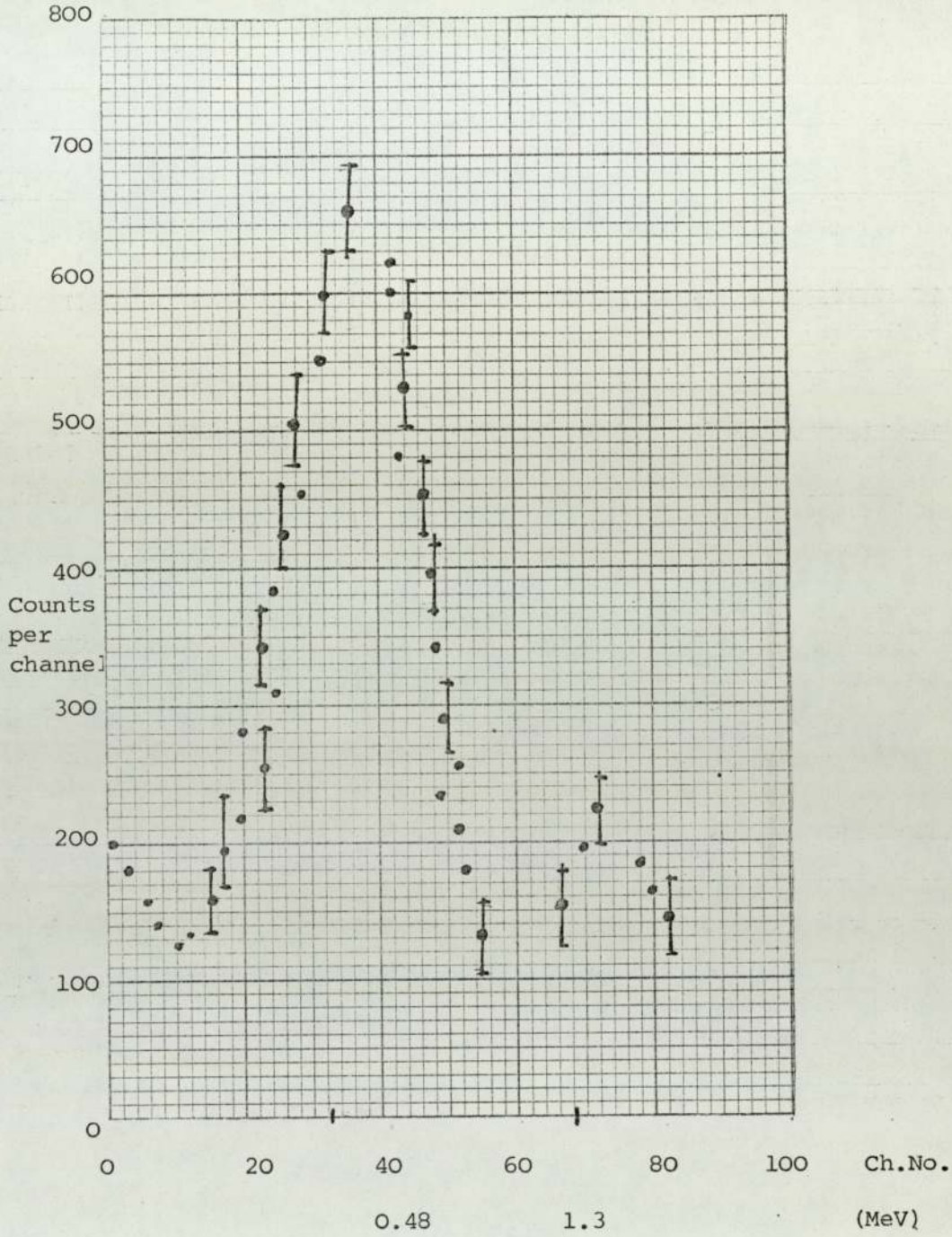

Figure 5.9. The gamma-ray energy spectrum from small LiF sample (scattering angle 30^{o}).

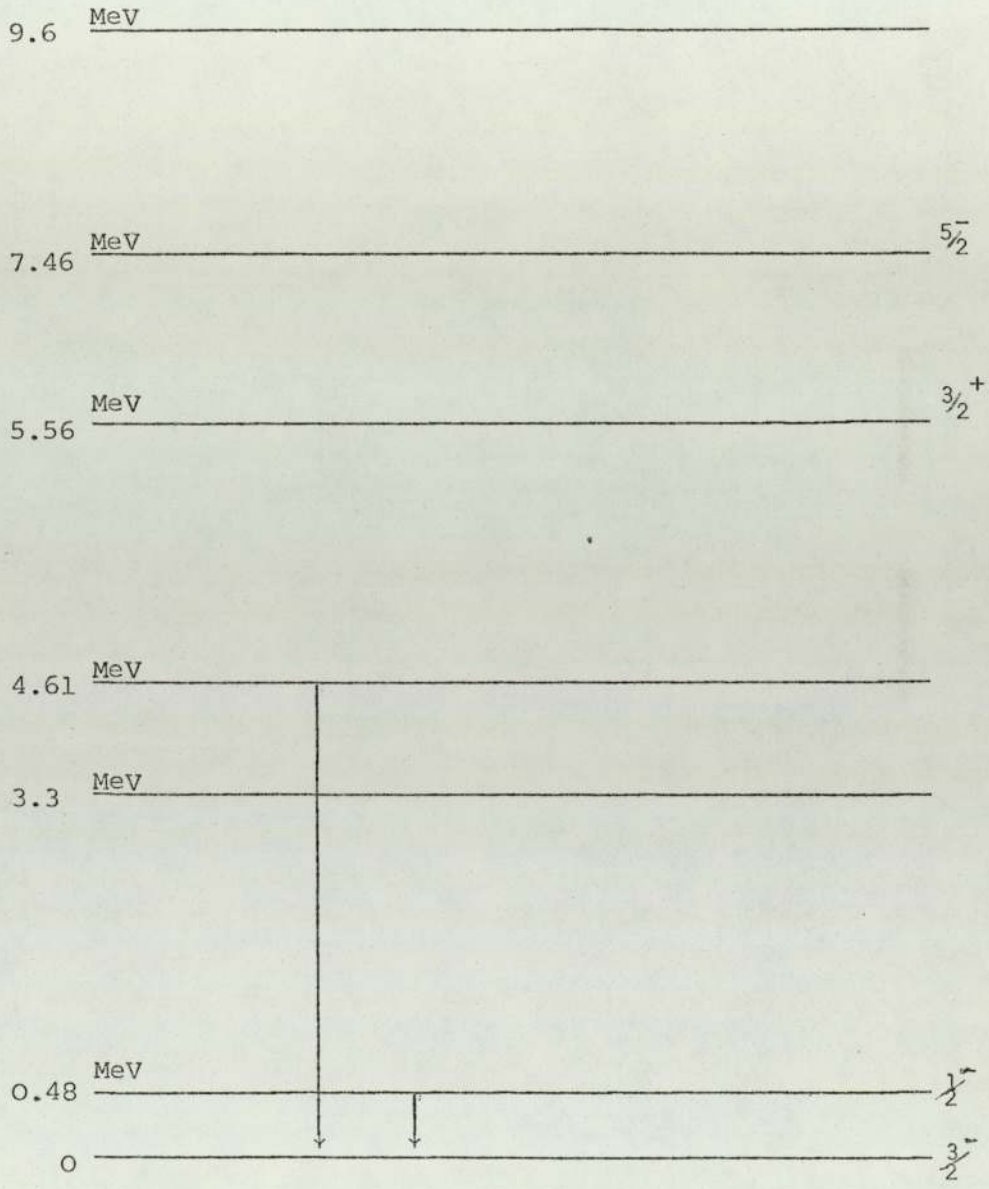

(54)

Fig. 5.10 Level structure of ^{7}Li

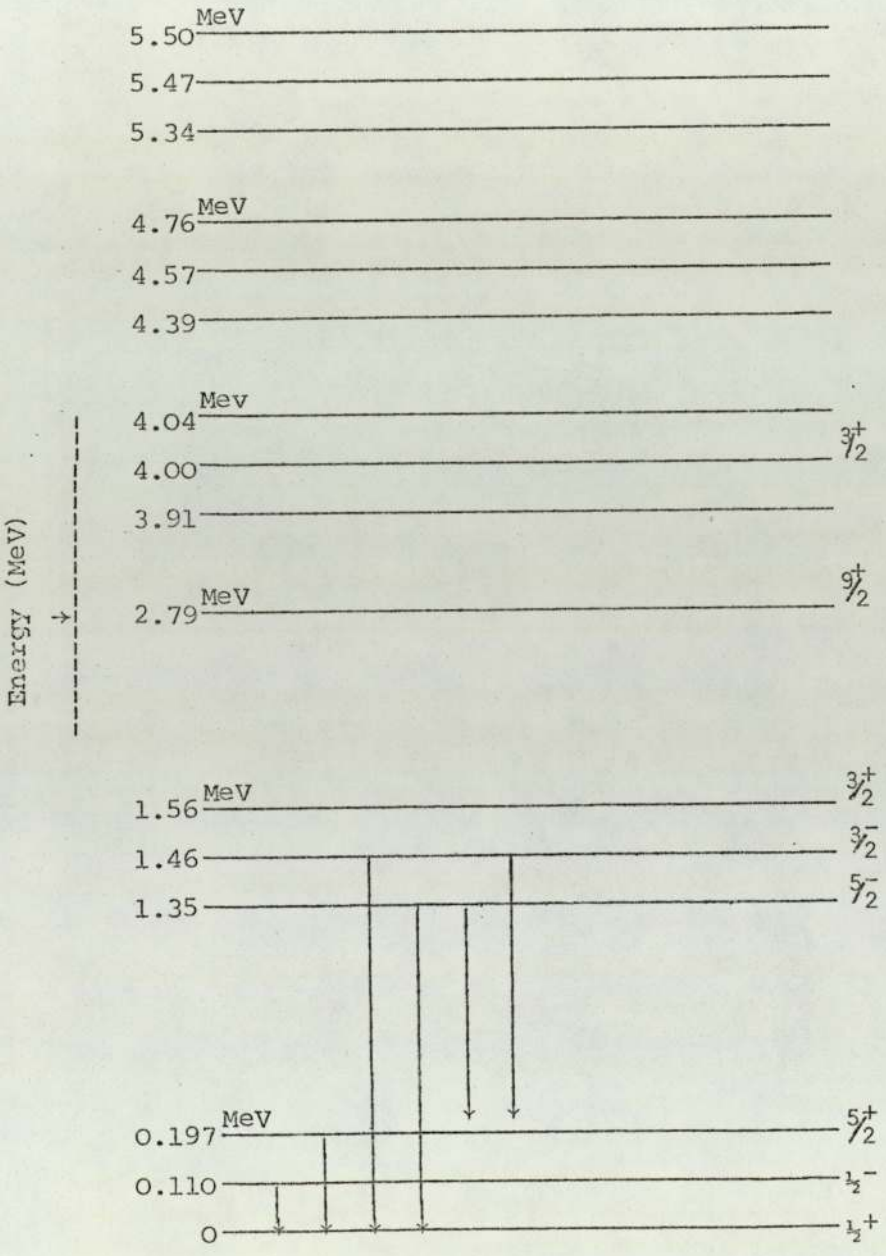

Fig. 5.11 Level structure of $^{19}_{F}$ (70)

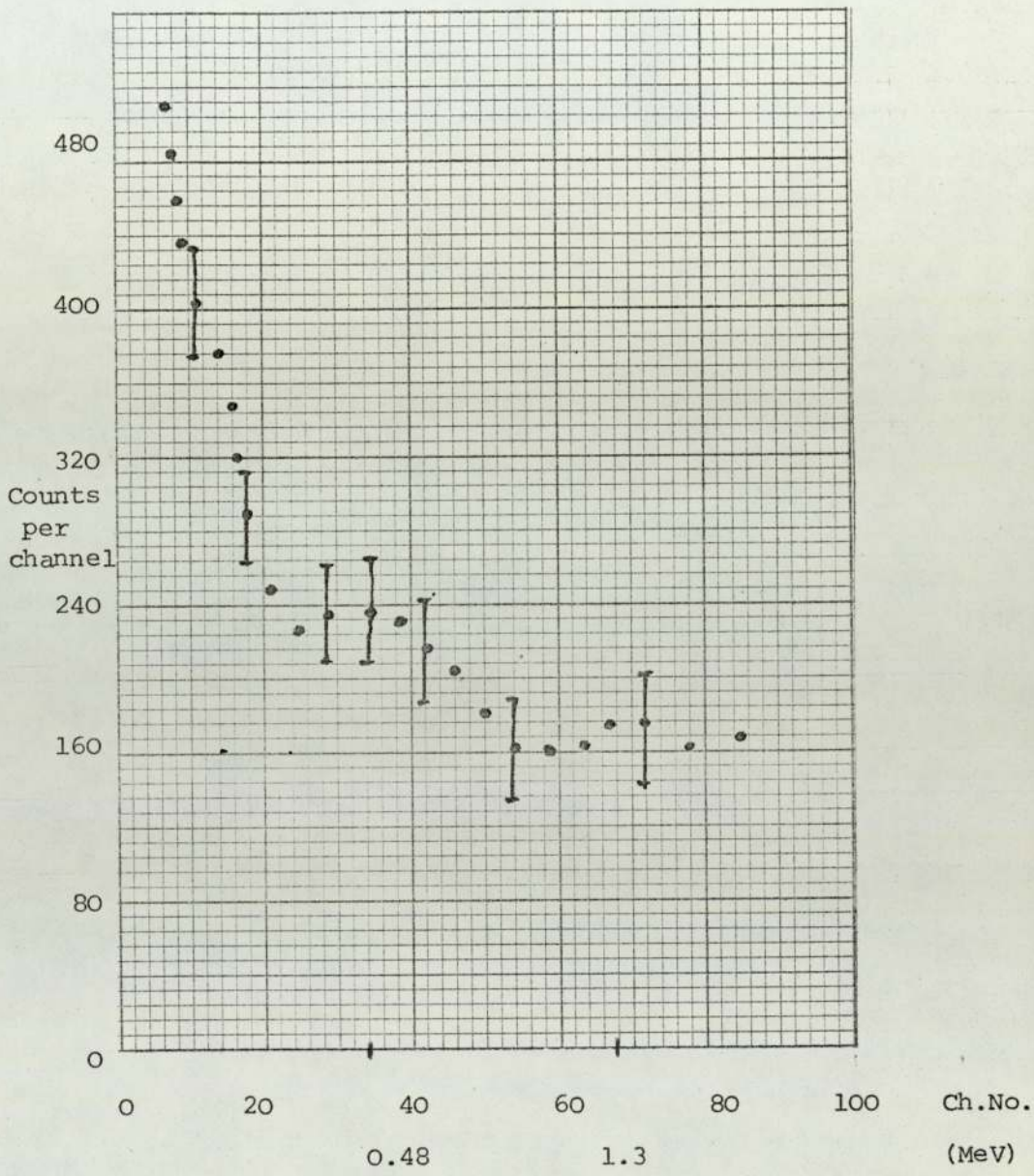

Figure 5.12 The gamma-ray energy spectrum from large LiF sample (scattering angle 60^{o})

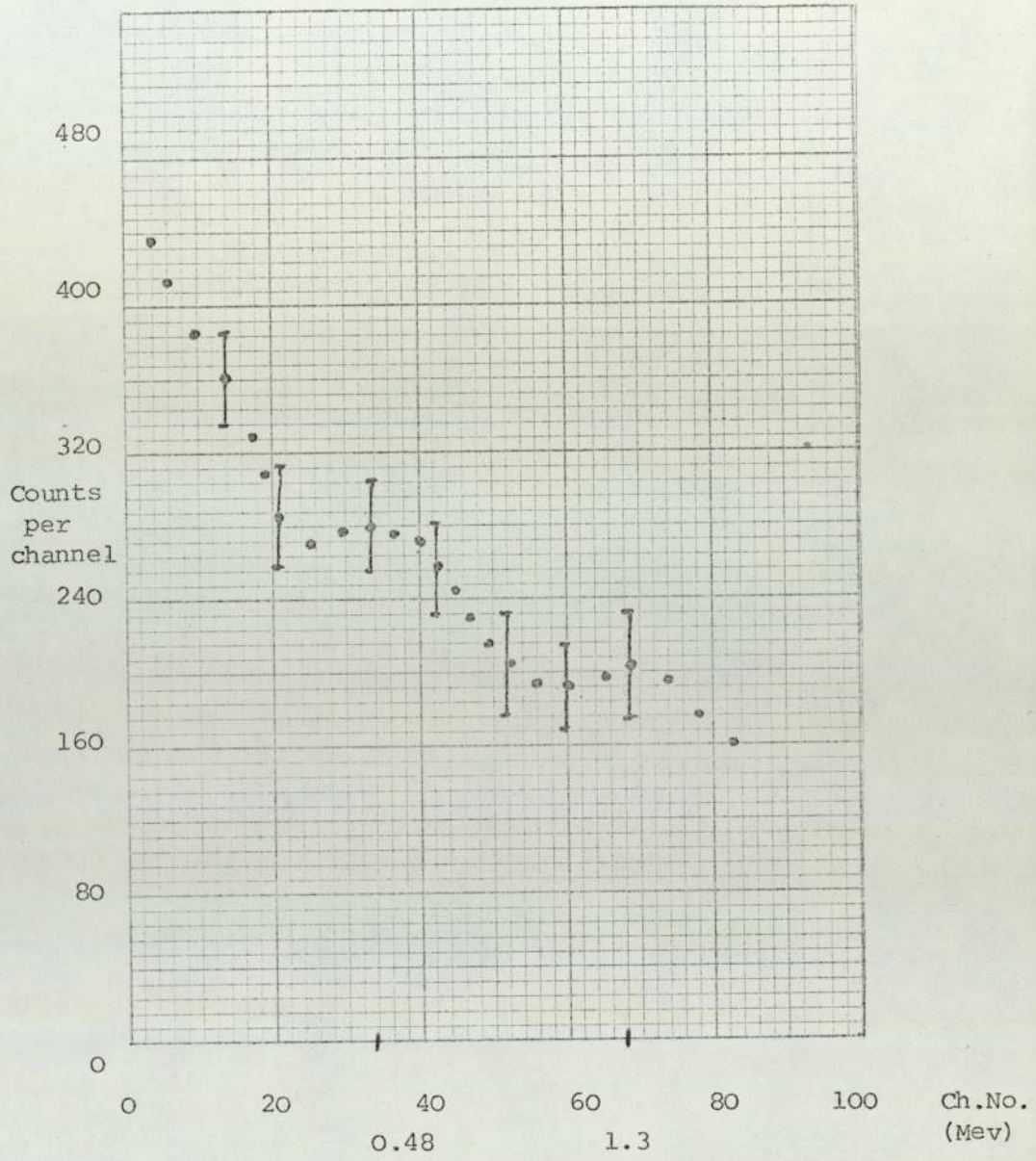

Figure 5.13 The gamma-ray energy spectrum from large LiF sample (scattering angle 45^{o})

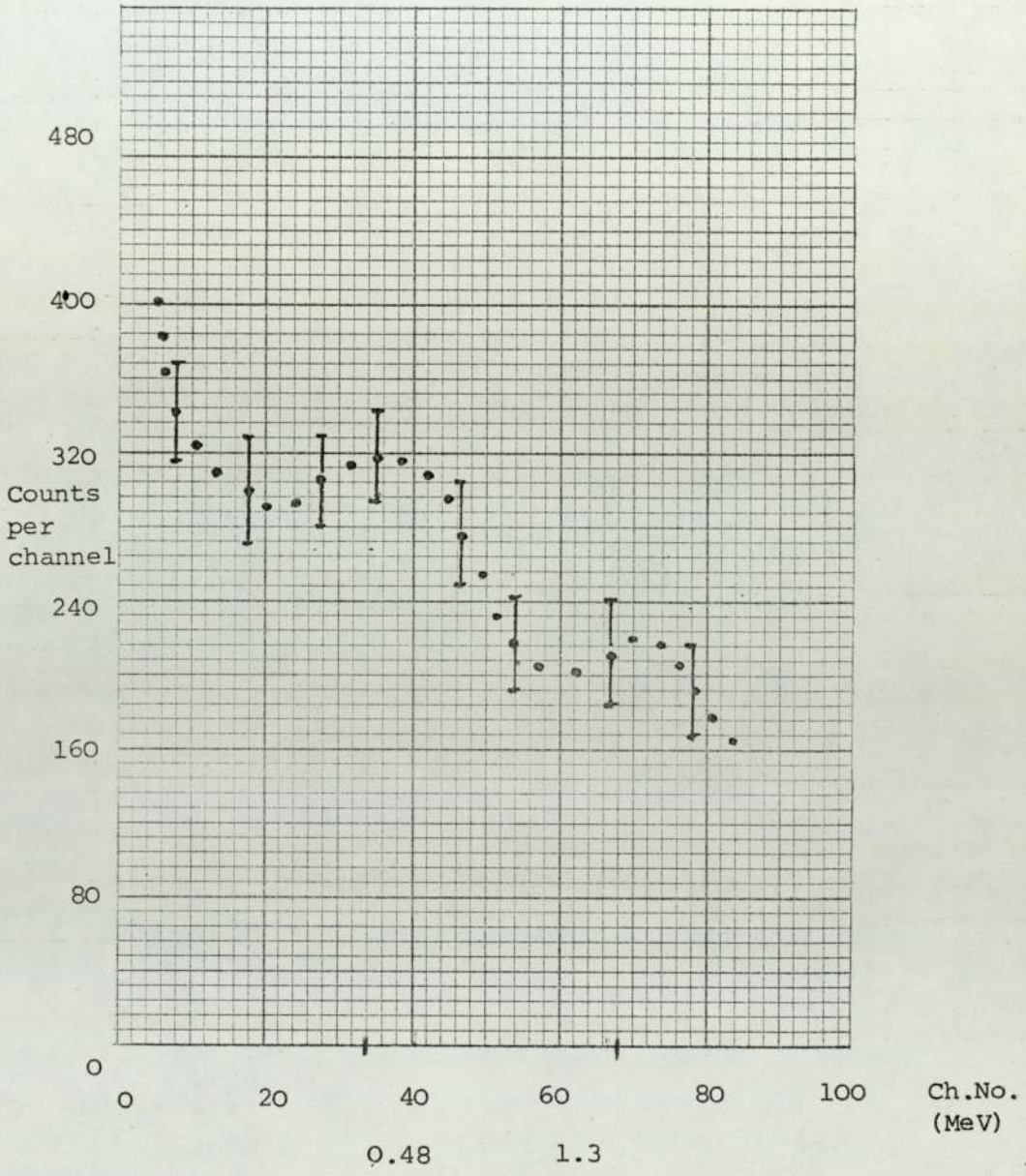

Figure 5.14 The gamma-ray energy spectrum from large LiF sample (scattering angle 30^{o})

level. This case has been reported[71] elsewhere. The cross-section of (n,2n) reaction for ^{7}Li at 14.0 MeV has been measured by Catron et al.[72] The cross-sections for (n,d) and (n,p) reactions at 14.0 MeV neutrons are reported by Battat and Ribe[73] as 9.8 ± 1.1 mb and 5.0 mb respectively, and these are small in comparison with the cross-section for the ^{7}Li (n,n'γ) reaction at 14.0 MeV neutrons of the order of 80 ± 9 mb reported by Benveniste et al.[74]

5.5 Calculation of the differential cross-section.

5.5.1 Introduction.

In order to find the differential γ-ray production cross-section per unit solid angle from the experimental data, the raw experimental data which could be obtained are the gamma-ray energy spectra, and the time integrated asspciated α-particles in a period of measurement at a fixed scattering angle. For small samples the differential cross-section was measured for a certain γ-ray energy, but for the large samples the differential cross-section was measured for γ-rays in various energy ranges, because of the large Compton distribution in the energy spectra resulting from the effect of multiple scattering in large samples.

5.5.2 The Gamma-ray differential cross-section.

Considering a flux of ϕ neutrons per second incident onto the sample, and $G(\theta)$ the number of counts in the full γ-ray energy peak in a unit solid angle at a fixed scattering angle θ produced, per unit time, in a scattering sample containing N nuclei, the differential cross-section is defined by the following relation:

$$\frac{d\sigma(\theta)}{d\Omega} = \frac{G(\theta)}{\left(\phi/A\right)N} \quad \ldots\ldots\ldots\ldots\ldots\ldots\ldots\ldots \quad (5.1)$$

where A is the area of the sample face on which the neutron flux is incident and $\frac{d\sigma(\theta)}{d\Omega}$ is the differential cross-section.

By considering the γ-ray energy spectra the number of gamma-rays in a given energy range or in the photopeak detected during the period of a measurement can be obtained. In the absolute measurement of a differential cross-section for the small samples of iron and LiF the photopeak total count, i.e. $P(\theta)$ has to be corrected for the detector efficiency, and for the absorption of the γ-rays by the scattering sample to obtain the absolute γ-ray yield. In the case of small iron sample the γ-ray of interest is that of 0.847 MeV, which is clearly resolved. The 0.847 MeV photopeak is situated on the Compton distributions due to the partial detection of higher γ-ray energies. To obtain the total counts in the 0.847 MeV peak, the counts under the peak due to these Compton distributions must be subtracted. A method for the subtraction of Compton distribution γ-rays or backscattered, etc. from the peak counts is referred to "stripping" method. In this method the full energy peak count of the higher γ-ray energy present can be determined, and then a point by point subtraction of the spectral shape corresponding to the intensity of the γ-ray is made from the composite spectrum. For this method monoenergetic γ-ray response functions for each of the γ-ray present must be known.

This process cannot be applied in this work, because there may be other γ-rays which their photopeaks are unknown, and the Compton distribution accompanying them cannot be estimated.

To find the full energy count for the small samples a method by Covell[45] was used. (described in Section 4.18)

In addition to the corrections for total counts, several other sources of error must be taken into account which have been

discussed in detail by Allenby,[31] and here these factors will be mentioned briefly only to explain the formula used in calculating the differential cross-sections.

The differential cross-section per nucleus for the production of a γ-ray of energy E_γ after applying all the correction factors can be written as:

$$\frac{d\sigma(\theta)}{d\Omega} = \frac{P(\theta)}{\varepsilon(E_\gamma) \cdot S(\theta,E_\gamma) \cdot \phi(\theta) \cdot F_1 \cdot F_2 \cdot N' \cdot \bar{x}} \quad \ldots(5.2)$$

where in the above formula $\varepsilon(E_\gamma)$ is the detector efficiency and $S(\theta,E_\gamma)$ is the correction factor for the γ-ray absorption in the sample, and in fact it is the fraction of the γ-rays escaping the sample.

The neutron flux $\phi(\theta)$ is given by the α-monitor count. However, the α-monitor count has to be corrected for two effects. The corrections are for background radiation in the detector and for neutron absorption in the target assembly.

The F_1, correction factor is related to background correction. The background correction can be divided into two parts. The first part is due to the detection of source neutron and radiation promptly emitted in fast neutron interaction with the material of target assembly and the second part of the correction is for the detection of γ-rays and β-particles resulting from the activation of the target assembly. Immediately after switching off the deuteron beam, after each run, the background count rate in the α-monitor was noted. This background was entirely due to the γ-rays and β-particles emitted by the active target assembly material. It was found that a fraction 0.055 of the α-particle count was due to this background, therefore to correct for this effect, the neutron flux must be multiplied by $F_1 = 0.945 \pm 0.005$

(this fraction is constant in the range of target currents used to within ± 0.005).

The correction factor, F_2, is for absorption of neutrons in target. The fraction of neutrons escaping the target assembly, before reaching the scattering sample is given by:

$$\exp - \left(x_{Fe} \Sigma_{Fe} + x_w (\Sigma_H + \Sigma_O) \right) \quad \ldots\ldots\ldots\ldots\ldots \quad (5.3)$$

because neutrons from the d-T reaction must pass through the target assembly which consists of 2.50 mm. of steel and 1.30 mm. of water used for cooling the target. x_{Fe} and x_w are the thicknesses of steel and water respectively, and Σ's are the macroscopic cross-sections for non-elastic scattering. In the present case $F_2 = 0.939 \pm 0.048$ where the error ± 0.048 is mainly due to uncertainties in the cross-sections.

$S(\theta, E_\gamma)$ is the fraction of the total γ-ray yield produced in the sample, which escapes from the sample at a scattering angle θ.

The calculation of the correction factor $S(\theta, E_\gamma)$ for the self absorption when the scattering sample plate is placed at 45° to the neutron beam direction has been described by Connell.[63]

When the scattering sample is positioned perpendicular to the neutron beam direction, which is the case of the present experiments, the γ-rays escaping at small scattering angles would traverse a comparatively short distance in the sample, while γ-rays escaping at 90° to the incident neutron beam will traverse the length of the sample.

The self absorption factor $S(\theta, E_\gamma)$ at the scattering angle $\theta = 90^\circ$ gives the relation:

$$S(\theta, E_\gamma) = \frac{1 - e^{-\mu x}}{\mu x} \quad \ldots\ldots\ldots\ldots\ldots\ldots \quad (5.4)$$

where x is the length of the sample, and μ is the absorption coefficient for a given gamma-ray energy in a given sample material.

N' is the number of nuclei of the isotope of natural element in unit volume of the sample material, and it is given by:

$$N' = \frac{N_o \rho I}{Aw} \quad \ldots\ldots\ldots\ldots\ldots\ldots \quad (5.5)$$

where N_o is Avogadro's number, ρ is the density of the sample material, Aw is the atomic weight of the relevant isotope, and I is the fractional abundance of the isotope.

For calculating the values of N' for each isotope the density (ρ), fractional abundance (I) and atomic weight (Aw) were obtained from the Handbook of Chemistry and Physics.[64]

$\bar{x}$ is the weighted sample thickness, which is defined by the following relation:

$$\bar{x} = \frac{\Sigma_i fi\ x_i}{\Sigma_i\ fi} \quad \ldots\ldots\ldots\ldots\ldots\ldots \quad (5.6)$$

where i indicates the labels of the different values of the neutron scattering angles.

The weighting fraction, f_i is proportional to the area under the neutron beam profile curve (fig.4.19).

x_i is the sample thickness at different scattering angles of neutrons. The result of the above sum calculation gives the relation:

$$\bar{x} = (1.610 \pm 0.087)b \quad \ldots\ldots \quad (5.7)$$

where b is the sample thickness.

The reason for calculating $\bar{x}$ is that the neutron beam incident on the scattering sample is divergent, and the thickness of sample traversed by the neutron beam differs for different neutron scattering angles.

5.5.2.1 The gamma-ray differential cross-section for small and large iron samples.

The equation 5.2 used to evaluate the absolute gamma-ray differential cross-section for both the small and large scattering samples of iron. The measured values of the gamma-ray differential cross-section of the 0.847 MeV gamma-ray following the inelastic scattering of 14.0 MeV neutrons from the small iron sample are given in table 5.3. The gamma-ray differential cross-sections for various gamma-ray energy intervals in the case of large iron sample are given in table 5.4. The experimental errors in the results are given for completeness before they are discussed in section 5.5.3.

θ	Cos θ	$\frac{d\sigma(\theta)}{d\Omega}$ $mb/_{st}$
30	0.866	67.5 ± 5.1
45	0.707	74.4 ± 5.6
60	0.500	70.5 ± 5.3
75	0.259	64.2 ± 4.8
90	0.0	60.0 ± 4.6

Table 5.3. Values of the differential cross-section for production of 0.847 MeV γ-ray from ^{56}Fe.

θ	Cos θ	$\frac{d\sigma(\theta)}{d\Omega}$ mb/st				
		E_γ = 1.2 - 1.0 (MeV)	E_γ = 1.0 - 0.8 (Mev)	E_γ = 0.8 - 0.6 (MeV)	E_γ = 0.6 - 0.4 (MeV)	E_γ = 0.4 - 0.2 (MeV)
30	0.866	86 ± 6.5	89 ± 6.7	99 ± 7.5	111 ± 8.4	126.5 ± 9.6
45	0.707	91.5 ± 7	96.3 ± 7.3	104.5 ± 8	105.5 ± 8	130.2 ± 9.9
60	0.500	98.2 ± 7.5	101 ± 7.6	109.1 ± 8.3	118.2 ± 9.2	135 ± 10
75	0.259	95 ± 7.2	98.4 ± 7.4	105 ± 8	113 ± 8.6	129.5 ± 9.8
90	0.0	91.1 ± 7	93 ± 7.1	97 ± 7.4	102.3 ± 7.8	121 ± 9.2

Table 5.4. Values of the differential cross-section for various gamma-ray energy intervals from large iron sample.

5.5.2.2 The gamma-ray differential cross-section for small and large Lithium fluoride samples.

The differential cross-section results for the production of 0.48 MeV gamma-rays in the interaction of 14.0 MeV neutrons with ^{7}Li for the small sample are given in table 5.5 and in the case of large sample the gamma-ray differential cross-section for various gamma-ray energy intervals are shown in table 5.6.

θ	Cos θ	$\frac{d\sigma(\theta)}{d\Omega}$ $mb/_{st}$
30	0.866	11.5 ± 0.9
45	0.707	14.2 ± 1.1
60	0.500	15.5 ± 1.2
75	0.259	15.0 ± 1.2
90	0.0	14.1 ± 1.1

Table 5.5. Values of the differential cross section for the production of 0.48 MeV gamma-rays from ^{7}Li using the small lithium sample.

θ	Cos θ	$\frac{d\sigma(\theta)}{d\Omega}$ mb/st		
		E_γ = 0.48 - 0.36 (MeV)	E_γ = 0.36 - 0.24 (MeV)	E_γ = 0.24 - 0.16 (MeV)
30	0.866	22.5 ± 1.8	25.2 ± 2.1	37.2 ± 3.1
45	0.707	27.2 ± 2.2	30.1 ± 2.4	42.5 ± 3.4
60	0.500	32.4 ± 2.6	36.0 ± 2.8	46.2 ± 3.7
75	0.259	29.5 ± 2.3	33.5 ± 2.6	43.4 ± 3.5
90	0.0	25.0 ± 2.1	31.3 ± 2.5	38.0 ± 3.0

Table 5.6 Values of the differential cross-section for various gamma-ray energy intervals from lithium, using the large lithium fluoride sample.

5.5.3 Experimental errors

The experimental errors in the factors of the equation 5.2 used to calculate the differential cross-sections, and also the total errors are listed in table 5.7 for iron sample, and in table 5.8 for LiF sample respectively.

In order to obtain the total error in the differential cross-sections, the individual errors are added quadratically.

The results of these errors are shown by the error bars in angular distribution curves obtained from the measurements.

5.6 Angular distribution

5.6.1 Angular distribution for iron samples

From the analysis of the gamma-ray spectra for both the small and large scattering samples of ^{56}Fe described in Section 5.3.2 the differential cross-sections for the production of the relevant gamma-rays were obtained.

In the case of small iron sample the differential cross-section for the production of 0.847 MeV gamma-ray was calculated. The result of the calculation is shown in figure 5.15. Also the result of the present calculation has been compared with the results of other workers. (75,76)

The differential cross-section values resulting from the present experiment and from these other workers are shown in figure 5.16 and are seen to be in good agreement.

The solid curve represents a least squares fit to the experimental data points of the legendre polynomial expansion of the form:

$$\frac{d\sigma(\theta)}{d\Omega} = A_o + A_2 P_2 (\cos\theta) + A_4 P_4 (\cos\theta) \quad \ldots\ldots\ldots \quad (5.8)$$

where $P_2 (\cos\theta)$ and $P_4 (\cos\theta)$ are the second and fourth order

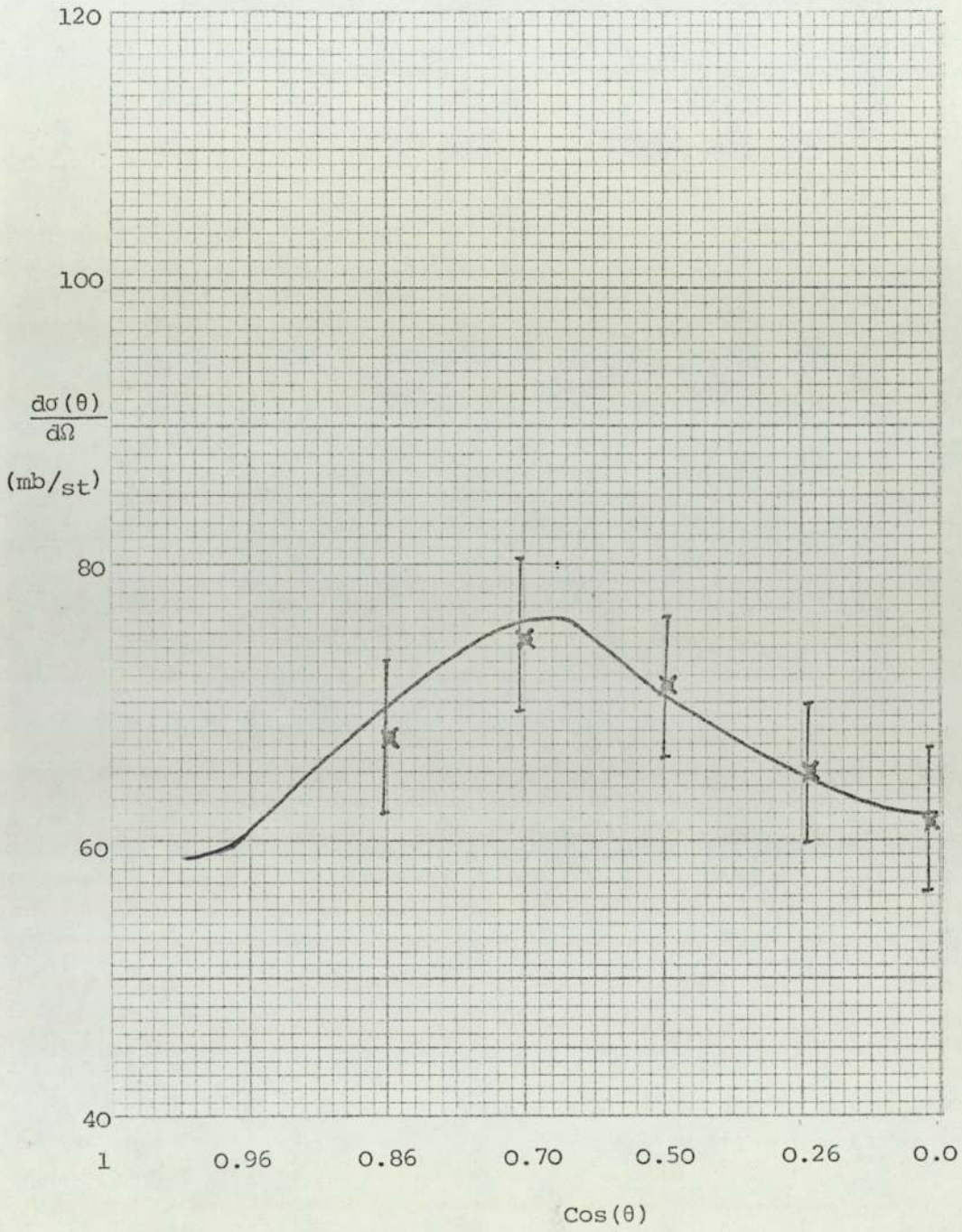

Figure 5.15 The angular distribution for production of 0.847 MeV γ-ray from small iron sample in the present work.

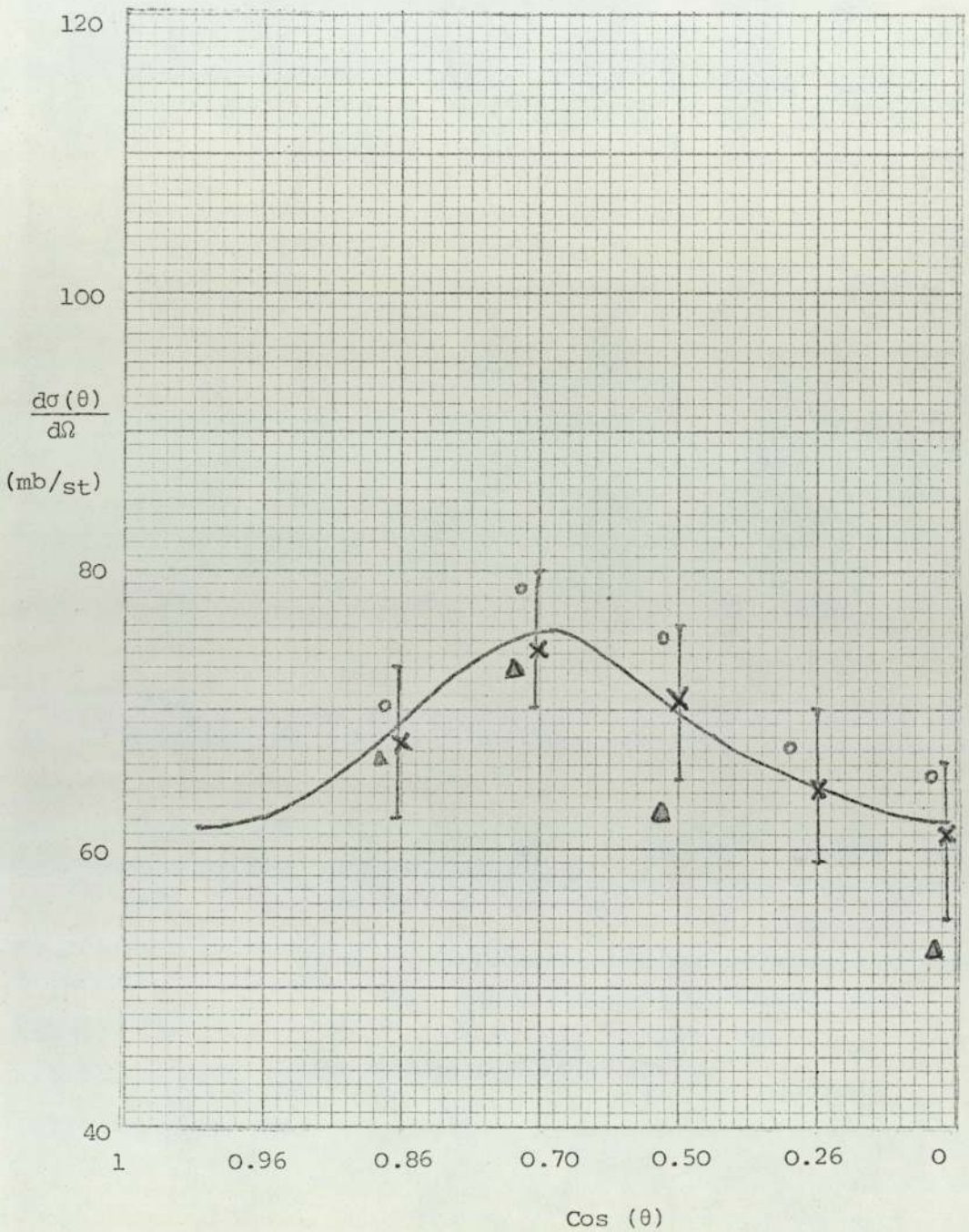

Figure 5.16 The angular distribution for production of 0.847 MeV γ-ray from small iron sample.

X - Present work

O - Ref.75

Δ - Ref.76

Factor	Error
$P(\theta)$	4.0%
$\varepsilon(E_\gamma)$	5.0%
$S(\theta)$	2.0%
$\phi(\theta)$	0.1%
F_1	0.5%
F_2	0.5%
N'	2.1%
$\bar{x}$	3.0%
Total error	7.64%

Table 5.7 The experimental errors for iron sample.

Factor	Error
$P(\theta)$	3.0%
$\varepsilon(E_\gamma)$	5.0%
$S(\theta)$	3.5%
$\phi(\theta)$	0.1%
F_1	0.5%
F_2	0.5%
N'	1.5%
$\bar{x}$	4.0%
Total error	8.06%

Table 5.8 The experimental errors for lithium fluoride sample.

legendre polynomials, and A_o, A_2 and A_4 are constants.

Equation 5.8 was fitted to the differential production cross-section measurements for the ^{56}Fe $(n,n'\gamma)$ ^{56}Fe, 0.847 MeV γ-ray as described in appendix D.

The error bars shown in the angular distribution measurements represent the experimental uncertainties calculated as described in section 5.5.3 and shown in table 5.7. For the large scattering sample of iron the differential cross-section for the various energy regions of the γ-ray energies have been calculated, and the results of these calculations are shown in figure 5.17. No references to similar measurements could be found in the literature. Several points are mostly of note, firstly, the cross-section values for the large sample of iron are larger than the values obtained for small sample. Secondly, in the lower regions of the γ-ray energies in the large scattering sample the γ-ray differential production cross-sections have larger values, and the reasons for these notices are because of the effect of neutron multiple scattering in large sample, which causes more gamma yield and, as a result, larger differential cross-sections values.

5.6.2 Angular distribution for LiF samples

From the analysis of the gamma-ray spectra for both the small and large samples of LiF described in Section 5.4.2 the differential cross-sections for the production of the γ-ray from the samples were obtained.

For small LiF sample the differential cross-section for the production of 0.48 MeV gamma-ray from ^{7}Li was calculated. The result of the calculation is shown in figure 5.18, and the result of the present calculation has been compared with the measurements of other workers.[60,61] and can be seen in figure 5.19.

The differential cross-section measurements from the other

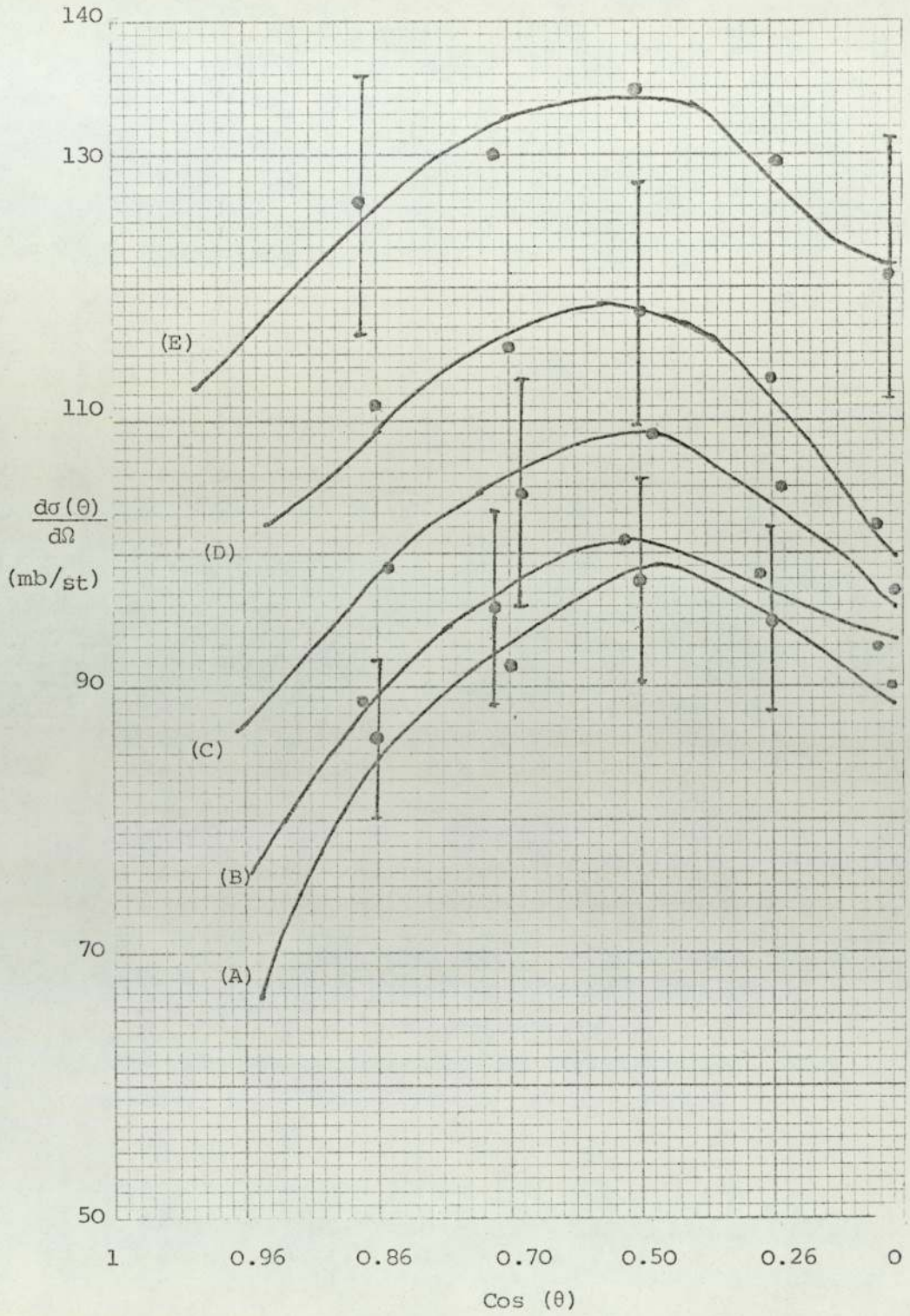

Figure 5.17 The angular distribution for various γ-ray energy intervals from the large iron sample.

(A) : 1.2 - 1.0 MeV, (B) : 1.0 - 0.8 MeV, (C) : 0.8 - 0.6 MeV,

(D) : 0.6 - 0.4 MeV, (E) : 0.4 - 0.2 MeV.

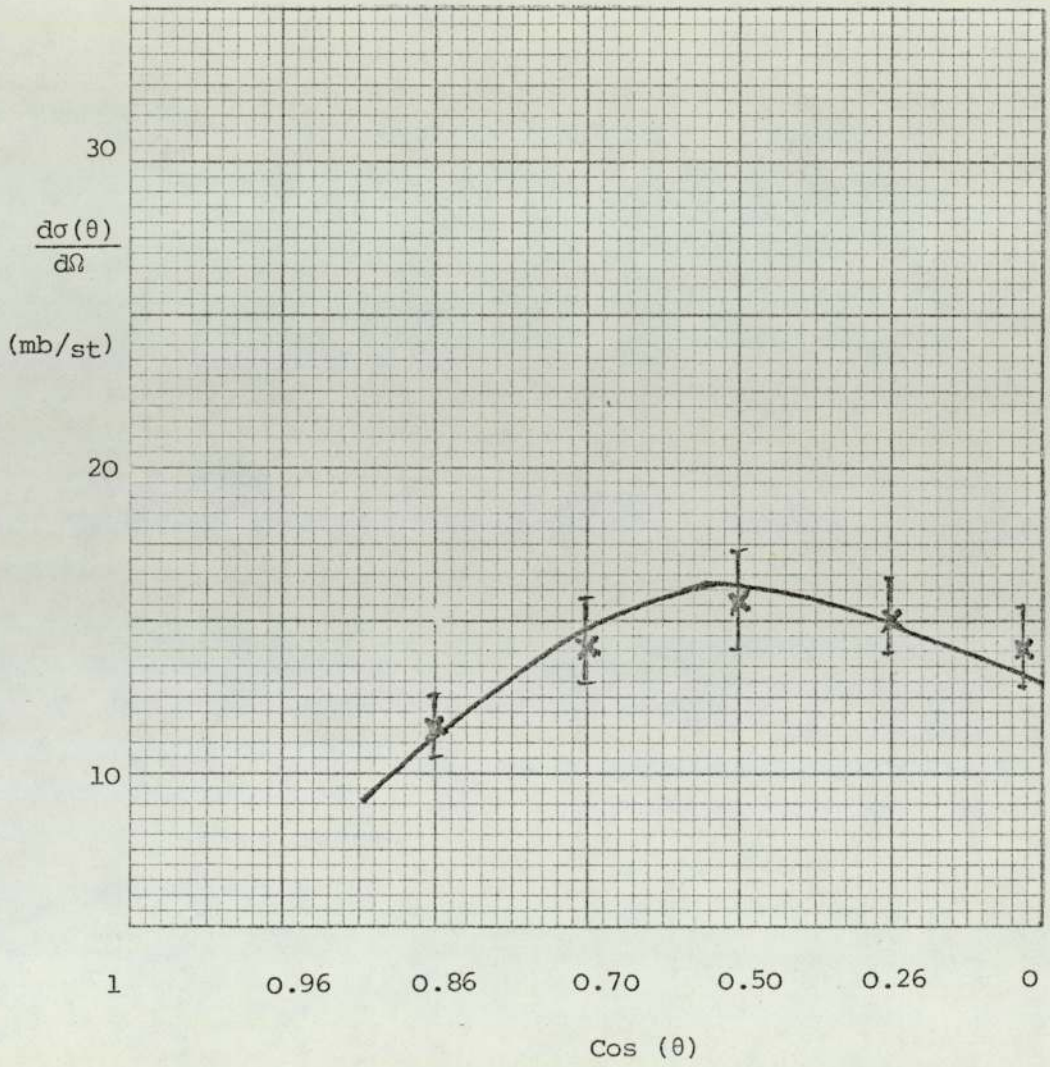

Figure 5.18 The angular distribution for production of 0.48 MeV γ-ray from ^{7}Li using the small lithium fluoride sample in the present work.

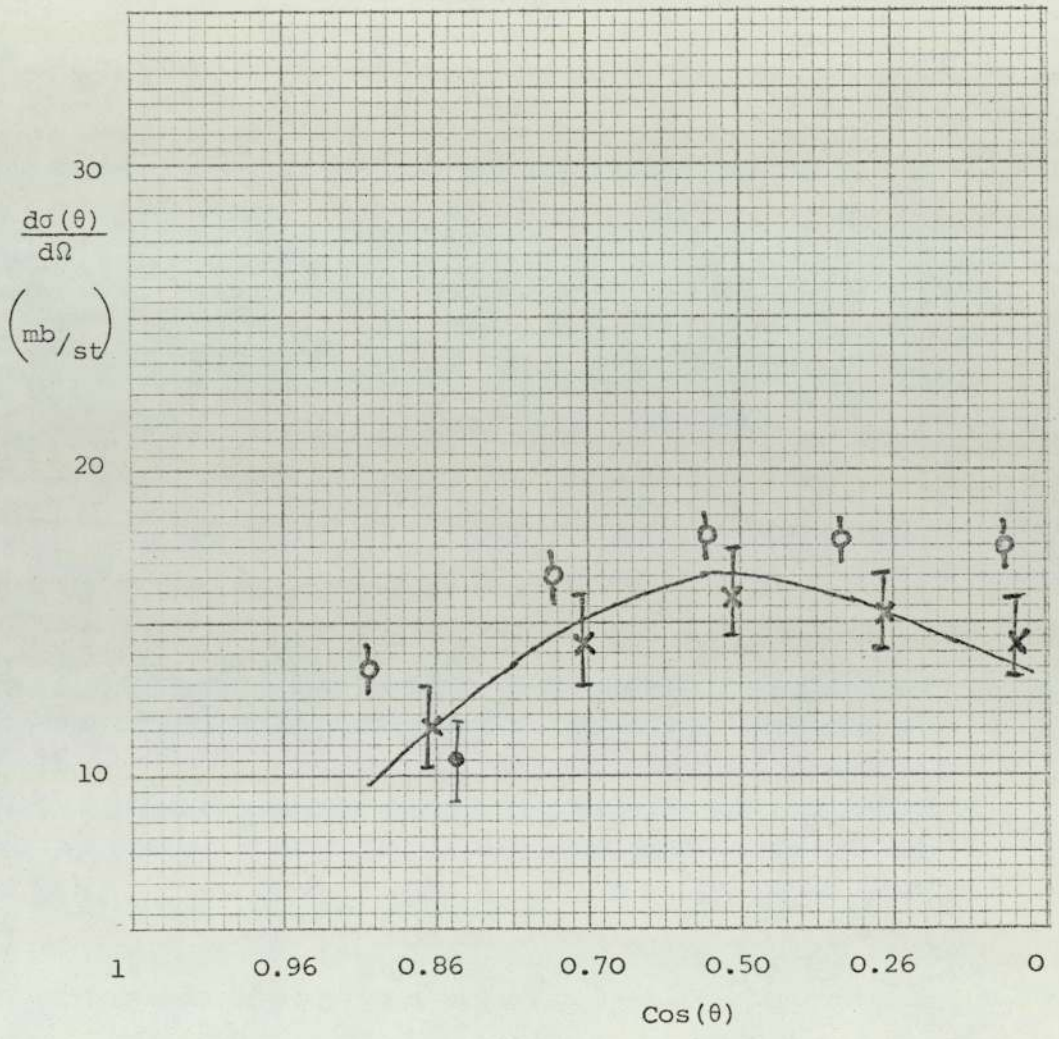

Figure 5.19. The angular distribution for production of 0.48 MeV γ-ray from ^{7}Li using the small lithium fluoride sample.

X - present work

O - Ref.60

● - Ref.61

workers and the present experiment are seen to be in good agreement. Again, as in the case of iron sample, the solid curve represents a least squares fit to the experimental data points of the legendre polynomial expansion, and the error bars in the measurements show the experimental uncertainties described in section 5.5.3 and shown in table 5.8.

In the case of large sample of LiF, the differential cross-sections for the various energy regions of the γ-ray energies were calculated. The results of the calculations for the large sample can be seen in figure 5.20.

As mentioned for the large iron sample no experimental measurements similar to the present experiment for large LiF sample could be found in the literature for comparison. The same two points of significances mentioned for the large samle of iron were noticed in the case of large LiF sample as well, and it can be seen through figure 5.20.

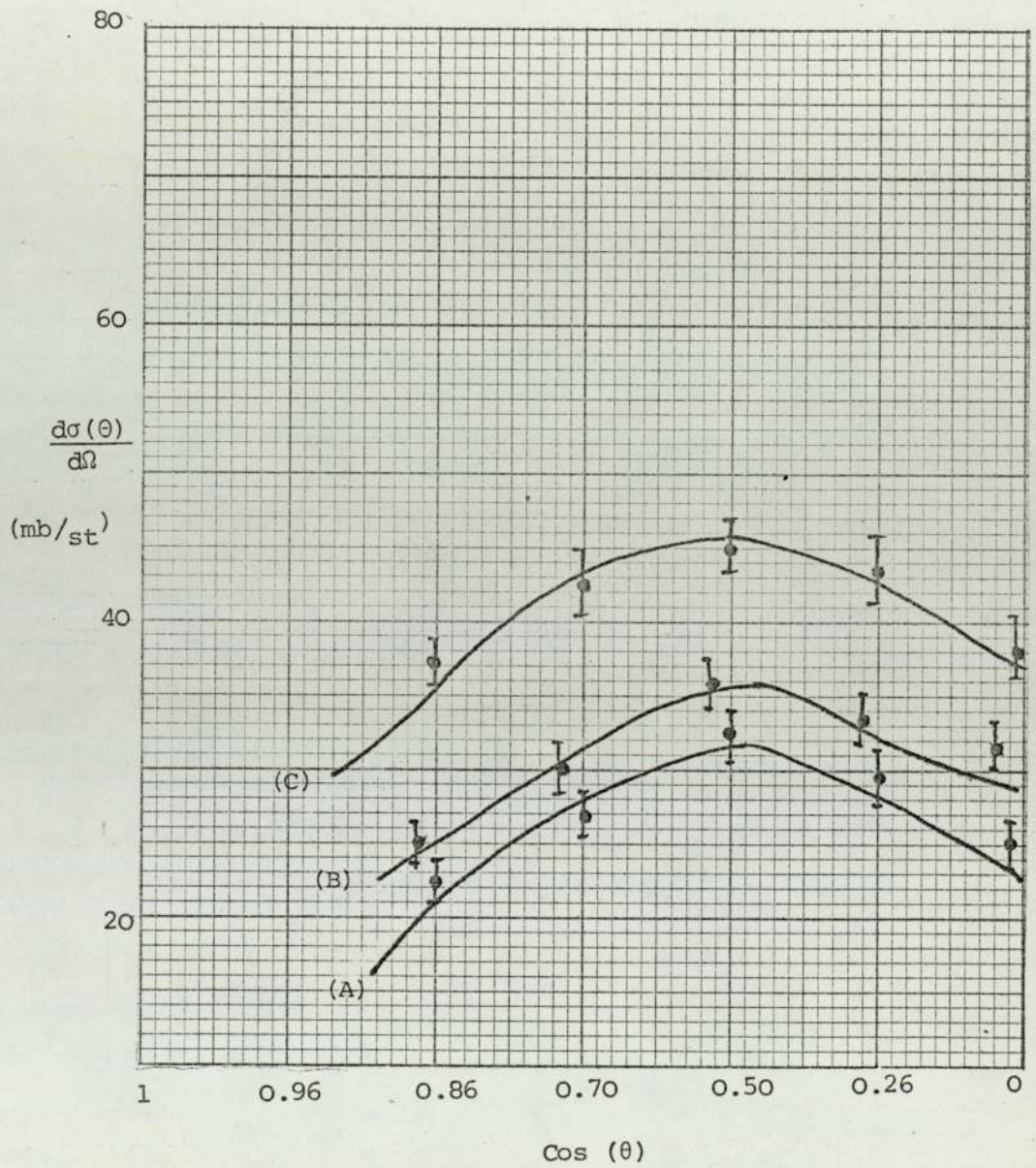

Figure 5.20 The angular distribution for various gamma-ray energy intervals from the large lithium fluoride sample.

(A) : 0.48 - 0.36 MeV, (B) : 0.36 - 0.24 MeV,
(C) : 0.24 - 0.16 MeV.

Chapter 6

6. Comparison of theory and experimental results

6.1 Multiple scattering of neutrons in an extended sample

The effect of multiple neutron inelastic scattering on the γ-ray production cross-section is to cause an increase in the γ-ray yield, due to the effective increase in the neutron flux. The probability of multiple scattering depends on the size of the sample and on the scattering cross-section of neutrons with the sample materials.

The dependence of neutron multiple scattering on the sample size has been reported by Day,[77] who has measured the 0.847 MeV gamma-ray production cross-section in the inelastic scattering of 2.6 MeV neutrons with iron samples of different sizes. In his investigation only the effect of the second neutrons scattered has been taken into account.

Figure 6.1 shows the effect of second scattered neutrons in the total γ-ray production cross-section and neglecting the effect of multiple scattering. In both cases the total cross-sections have been plotted against the sample thickness. From the result of this work it was found that the multiple scattering is appreciable for thin scattering sample in the range of about 0.1 m.f.p., and this is in contrast to Walt[78] who states that multiple scattering is not appreciable for scattering samples less than about 0.2 m.f.p. thickness.

In the present study the thickness and the dimensions of the scattering samples are such that the effect of multiple scattering is significant. The usual theoretical technique for predicting the effect of multiple scattering is the Monte Carlo technique. This is discussed in the following section.

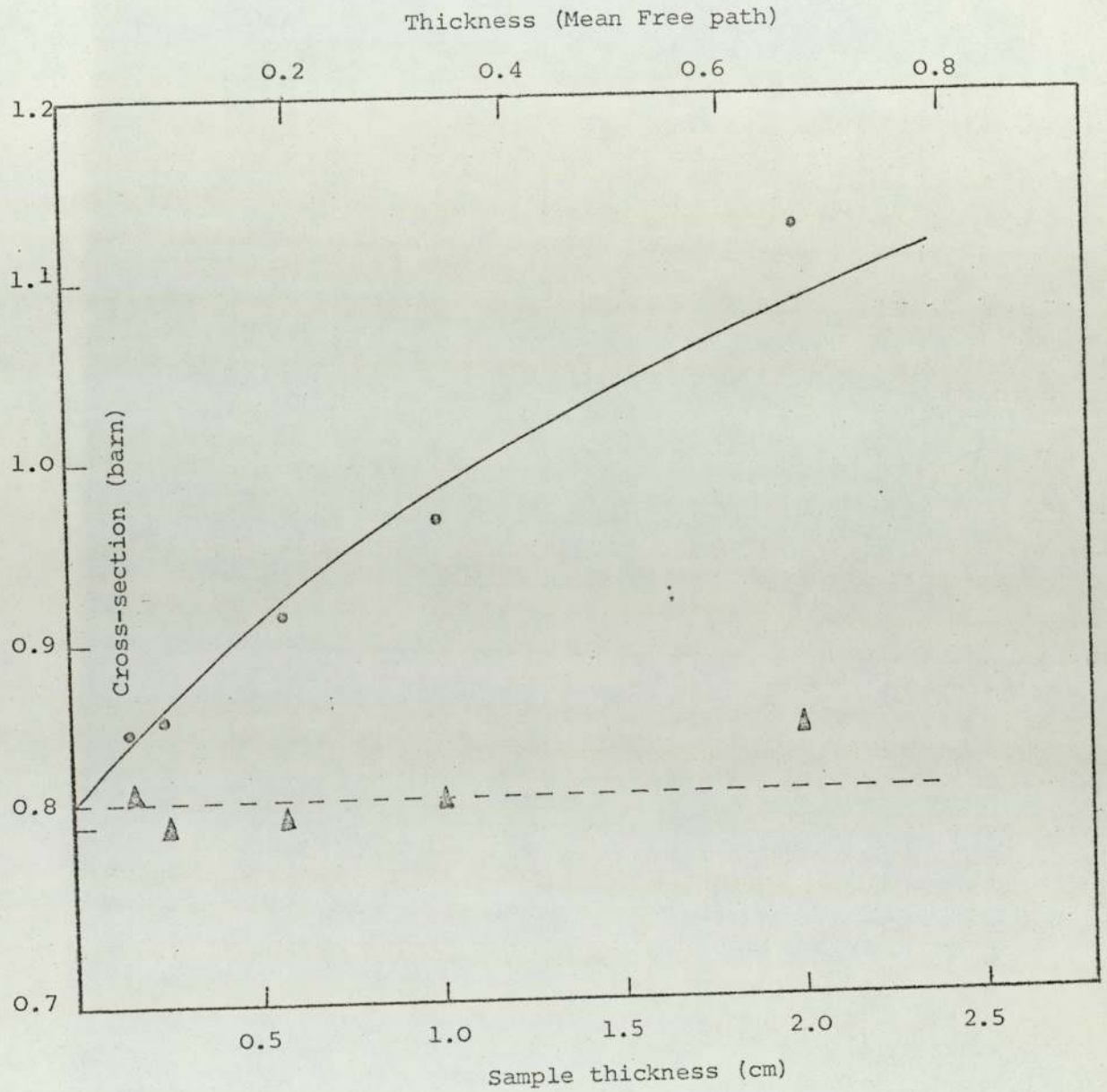

Figure 6.1. The effect of neutron multiple scattering on the γ-ray production cross-section with different sized samples for $^{56}Fe(n,n'\gamma)$ ^{56}Fe 0.847 MeV level.[77]

_____ Theoretical measurement

⊙ Experimental measurement

Δ Corrected for multiple scattering.

6.2 Summary of the MOnte Carlo method in general

The Monte Carlo method consists, in essence, of performing a theoretical experiment with a large number of incident neutrons on a scatterer, and to decide when a neutron suffers a collision, in which direction it is scattered, what its subsequent history might be, the result then represents a possible series of neutron life histories, and only needs to be extended to sufficient cases to give a satisfactory statistical sample. The usefulness of the technique has been greatly extended by the advent of high speed computers.

This method enables not only calculation of the results of a single collision, but also actually follows out step by step the development of what may be called a nuclear cascade.

The Monte Carlo method is a statistical technique used in analysis of some types of physical and mathematical process.

The transport of neutrons and γ-rays in a reactor and shield is an example of a physical process, which can be conveniently handled by this method. Average properties of neutrons and γ-rays such as absorption cross-sections, flux, leakage, and life history are determined in this approach by tracing individual histories chosen from the appropriate probability distributions. Thus, it is necessary to determine regions containing particles, distances to collisions, types of collisions, changes in particle directions, and energy after a collision, and conditions for termination of each particle history.

By tracing neutron histories by a Monte Carlo approach, the effect of the multiple scattering and flux attenuation may be taken into account. Monte Carlo multiple scattering programmes have served their purpose as a useful tool for calculating the theoretical basis to experimental data, but their utility has been greatly

restricted by the large computing effort required. Several Monte Carlo multiple scattering programmes[79,80,81] are in use, but none of them are suited to the present use. In first place they are very large computer programs, and secondly a considerable number of revisions would have had to be made in the programs to adapt them to the present particular problem. Hence a simpler Monte Carlo approach working from first principles was adapted.

6.3 Calculation procedure for multiple scattering by a Monte Carlo approach.

In the present case the sample thickness was divided up into a grid of one centimeter squares. The fraction of neutrons interacting at each grid point was considered. (See Fig.6.2)

In order to simplify the calculation, neutrons were considered to move only along the grid lines after each interaction.

In this case $f_{re} = e^{-\Sigma(1)}_{in}$ is the fraction of neutrons remaining in any one centimeter step, and $f_{int} = (1 - e^{-\Sigma(1)}_{in})$ is the fraction of neutrons interacting.

The f_{re} fraction continues in the forward direction.

In order to reduce the calculation to manageable proportions it was assumed that once the neutron flux at a given point had fallen to $^{1}/_{100}$ of its initial value, it could be neglected. Assuming n reactions, and four possible directions along grid lines, to find the value of n for the case of iron sample, it can be calculated from the relation $\left(\frac{e^{-\Sigma_t}}{4}\right)^n = \frac{1}{100}$ which in this relation Σ_t is the total macroscopic cross-section, and is given by:

$$\Sigma_t = \frac{N_o \rho \sigma_t}{A} \qquad \ldots\ldots\ldots\ldots\ldots\ldots\ldots\ldots \quad (6.1)$$

where N_o is the Avogadro's number, ρ is density, and A is the atomic weight of the element. σ_t is the total microscopic cross-section of neutron interactions with the element. The result of the

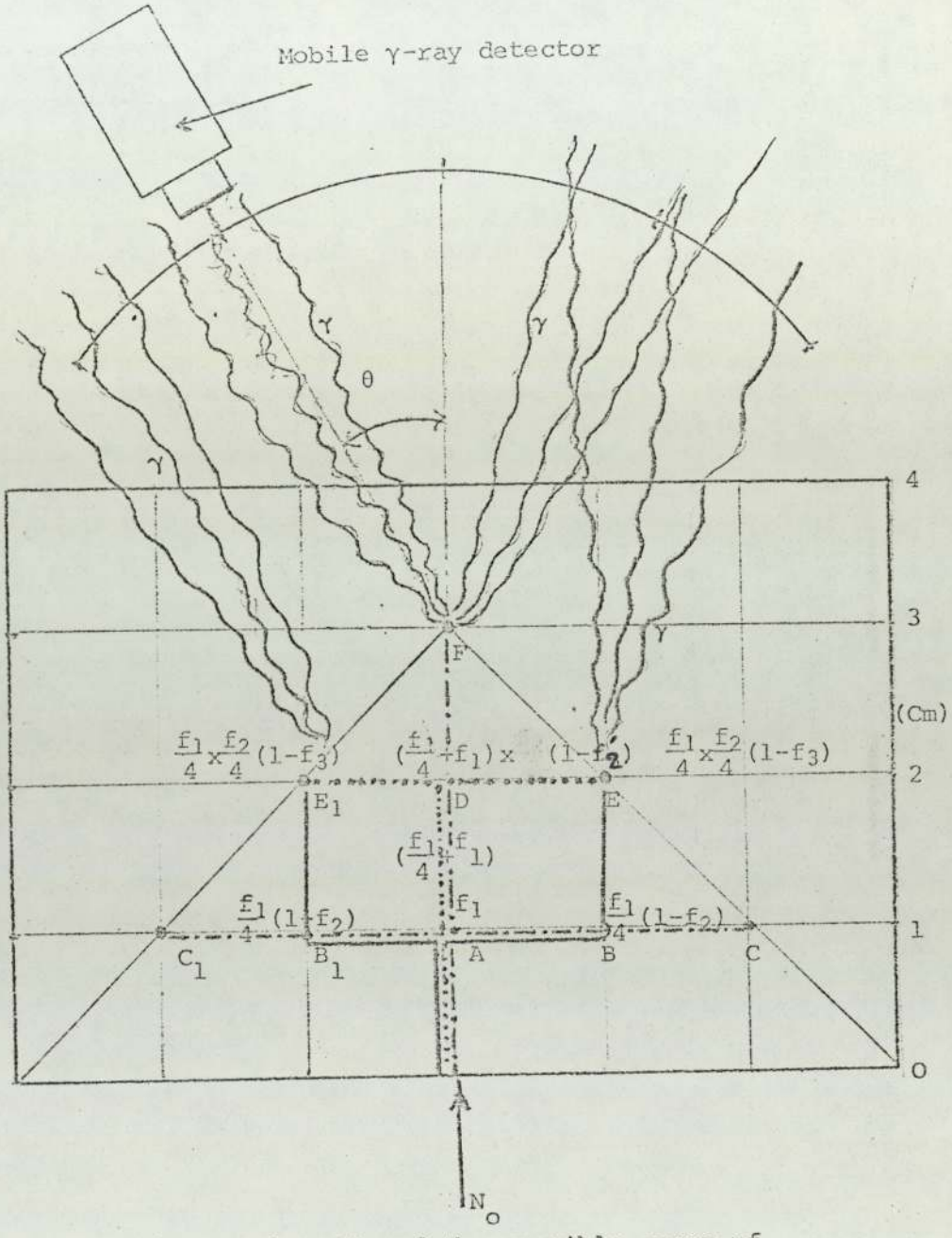

Figure 6.2. A schematic of the possible cases of neutron interactions in one centimeter step along the grid lines.

calculation for the value of n, in the iron sample is three. Hence only three interactions per neutron are considered and the possible neutron interactions in one centimeter steps and along the grid lines for a 4.0 cm. thick iron sheet are shown in figure 6.2, for one incident neutron point.

The solid line traces those neutrons which interact at points A, B, E and also on the left side at the points A, B_1, E_1. The dotted line traces interactions which occur at the points A, D, E and A, D , E_1.

The line shown (-.-.-) traces the interactions which occur at points A, D, F and A, B, C and A, B_1, C_1 . f_1 is the fraction of neutrons remaining after the first interaction at point A, and can be found by $f_1 = e^{-\Sigma(1)}_{in}$, and at this point $(1 - f_1)$ is the fraction of neutrons interacting, and since there is the possibility of four grid line directions from point A, then at points B and B_1. the fraction of remaining neutrons will be $\frac{f_1}{4}$ and the fractions of neutrons interacting at these two points will be $\frac{f_1}{4}(1 - f_2)$ where f_2 is the fraction of neutrons remaining in these points. However, in the forward direction, i.e. at point D, the fraction of neutrons remaining will be $(\frac{f_1}{4} + f_1)$, and the fraction of the neutrons interacting at this point is $(\frac{f_1}{4} + f_1)(1 - f_2')$, where again f_2' is the fraction of the neutrons remaining at point D. Identical arguments allow the number of neutrons at each point to be calculated and the overall fractions of the neutrons interacting at each point can be found. Energy of the neutron changes after each interaction, therefore the value of Σ_{in} changes at each point. In addition, the value of Σ_{in} is not the same in all directions because the angular distribution of inelastic scattered neutrons are mostly forward peaked and markedly anistropic. Statistical theory preicts that the angular distribution is symmetric about

the 90^{o} angle, provided that the levels of the compound nucleus are closely spaced.

In order to use the values of Σ_{in} in the above calculations it is possible to find the σ_{in} values for a defined range of angles from a differential cross-section's curve and then weighted the inelastic cross-section values to obtain the average value for calculation.

The gamma-ray yield from the inelastic scattering of neutrons with an element can be found from the relation shown below:

$$Y_A = N_o f\left(1 - e^{-\mu(x - 1)/\cos\theta}\right)\left(\frac{\sigma_{in}}{\sigma_t}\right) \quad \ldots\ldots\ldots \quad (6.2)$$

where N_o is the number of incident neutrons at a point on the scatterer, f is the fraction of the neutrons interacting at point A, x is the sample thickness, μ is the absorption coefficient of γ-rays in an element, which is a factor of atomic number of the element and the γ-ray energy. θ is the angle of outgoing γ-ray with respect to the incident neutron direction, and finally σ_{in} is the microscopic inelastic scattering, σ_t is the total microscopic cross-section and Y_A is the γ-ray yield at point A.

Now as it can be seen from figure 6.2, the total number of γ-rays resulting from the inelastic scattering of the neutrons in many points in the sample and leaving the sample towards the γ-ray detector can be found by summing the number of γ-rays from different points.

In order to find the total number of γ-rays reaching the detector at different detector positions, many factors must be known, such as the distance between the scatterer and detector, the length of the scatterer illuminated by neutron beam, the diameter of the NaI(Tℓ) crystal, the angles between the detector

and the direction of the incident neutron beam, and other necessary factors. These factors are all included in the Monte Carlo type Computer programme which is prepared in Algol language and shown in appendix C.

6.4 Comparison of theory and experiment for large iron sample

For comparison of the energy spectra, as predicted by the multiple scattering theory described in this chapter with the experimental results, all of the energy spectra have been normalised.

Figures 6.3 to 6.5 show the normalised energy spectra from large iron sample at three different angles, i.e. 30°, 45° and 60°, resulting both from the theory and from the experimental measurements.

The solid curves are the theoretical predictions and the crosses are the experimental results. The uncertainties given in the experimental results are absolute, and include both statistical and systematics errors.

6.5 Comparison of theory and experiment for large LiF sample

In order to compare the energy spectra obtained from the large size LiF sample as predicted by the multiple scattering theory described in this chapter, with the experimental results, the energy spectra have been normalised.

Figures 6.6 to 6.8 show the normalised energy spectra from large LiF sample for the 0.48 MeV gamma-ray from ^{7}Li at three different angles of 30°, 45° and 60°, resulting both from the theory and from the experimental measurements.

Again, as in the case of large iron sample, the solid curves represent the theoretical predictions, and the crosses are the experimental measurements.

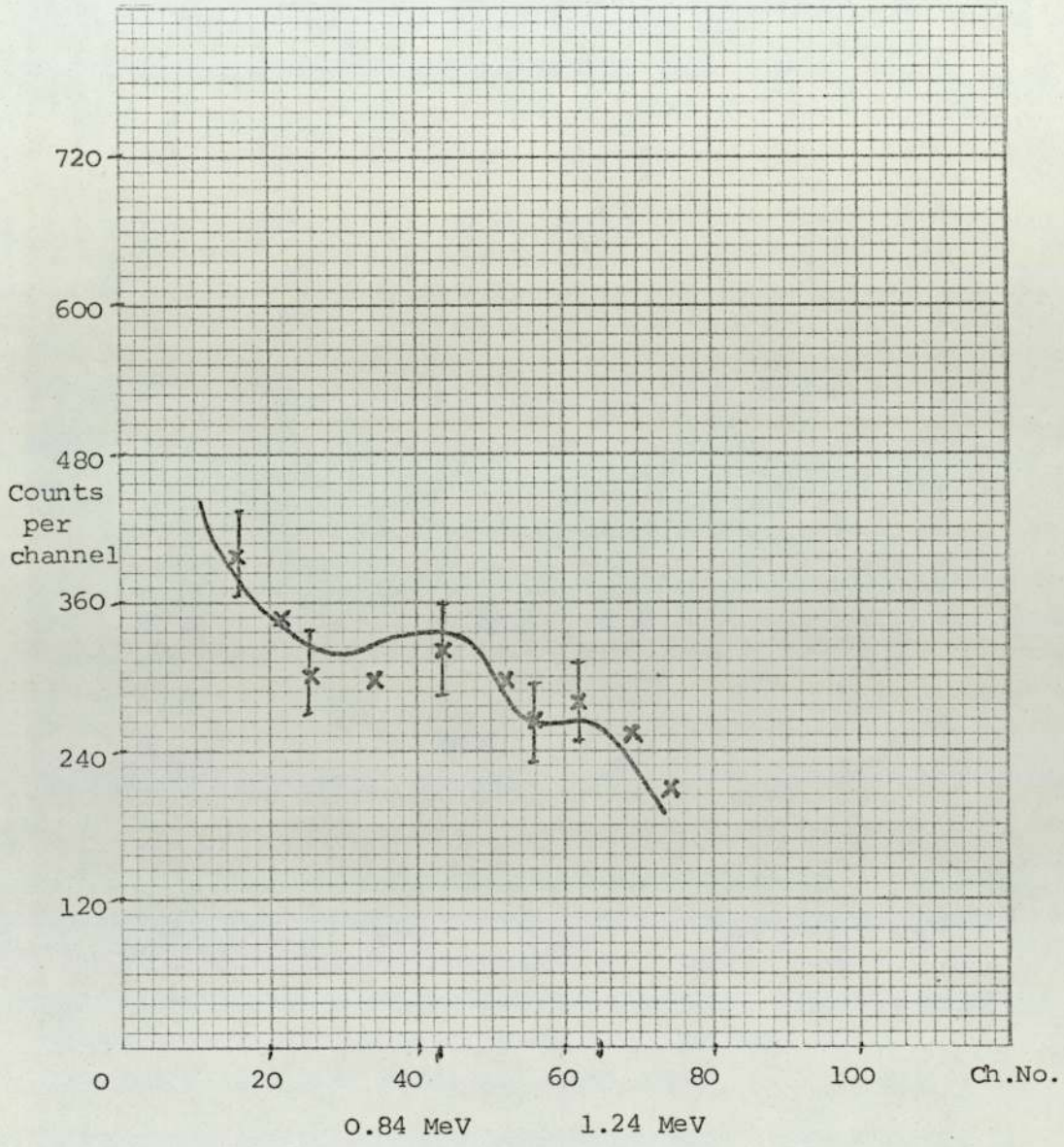

Figure 6.3 Normalised spectrum of gamma-ray energies from ^{56}Fe (scattering angle 30^{o}).

_____ Theoretical result.

xxxxxxxxxx Experimental result.

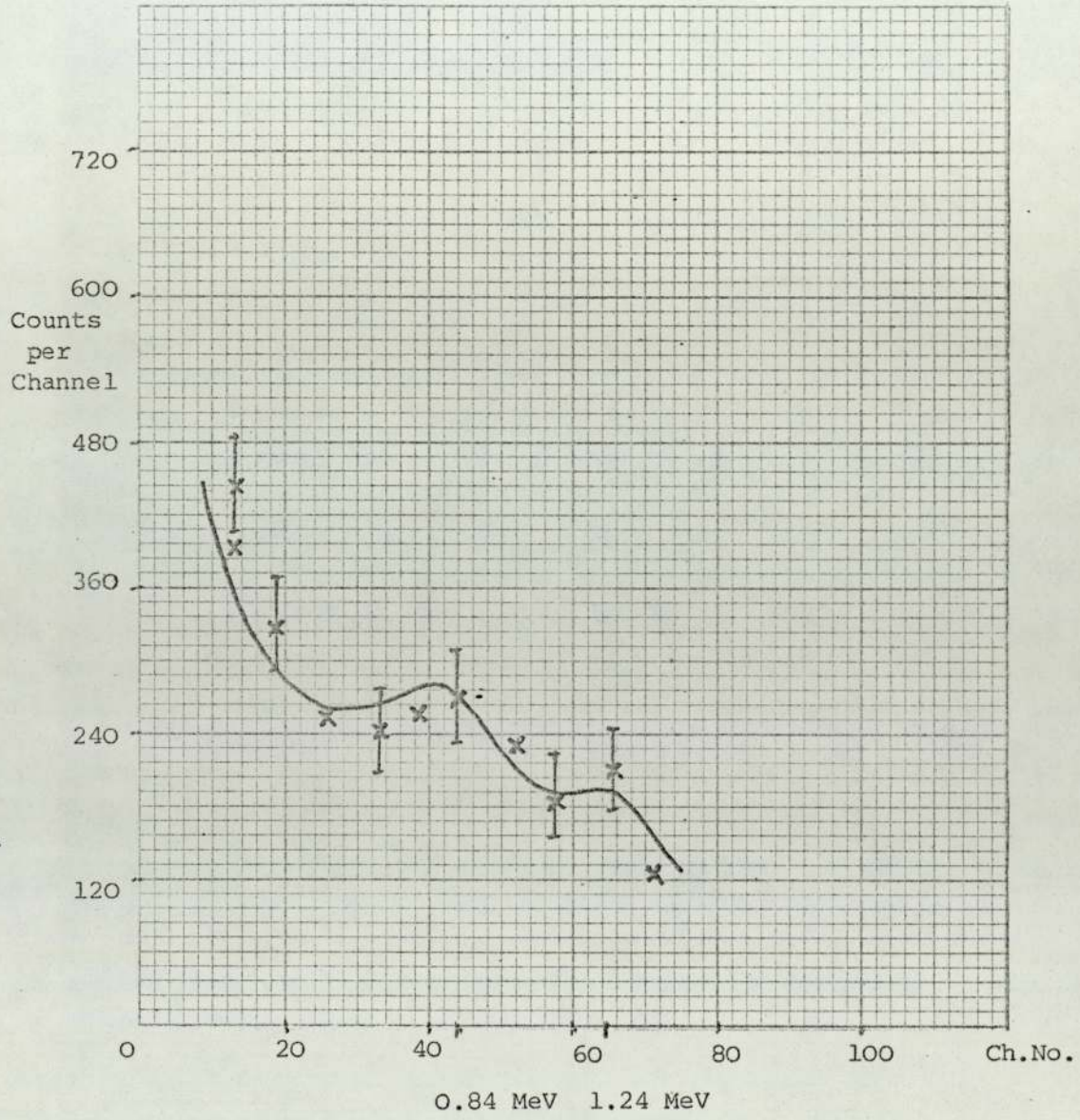

Figure 6.4 Normalised spectrum of gamma-ray energies from ^{56}Fe (scattering angle 45^{o}).

_____ Theoretical Result.

xxxxxxxxxxx Experimental Result.

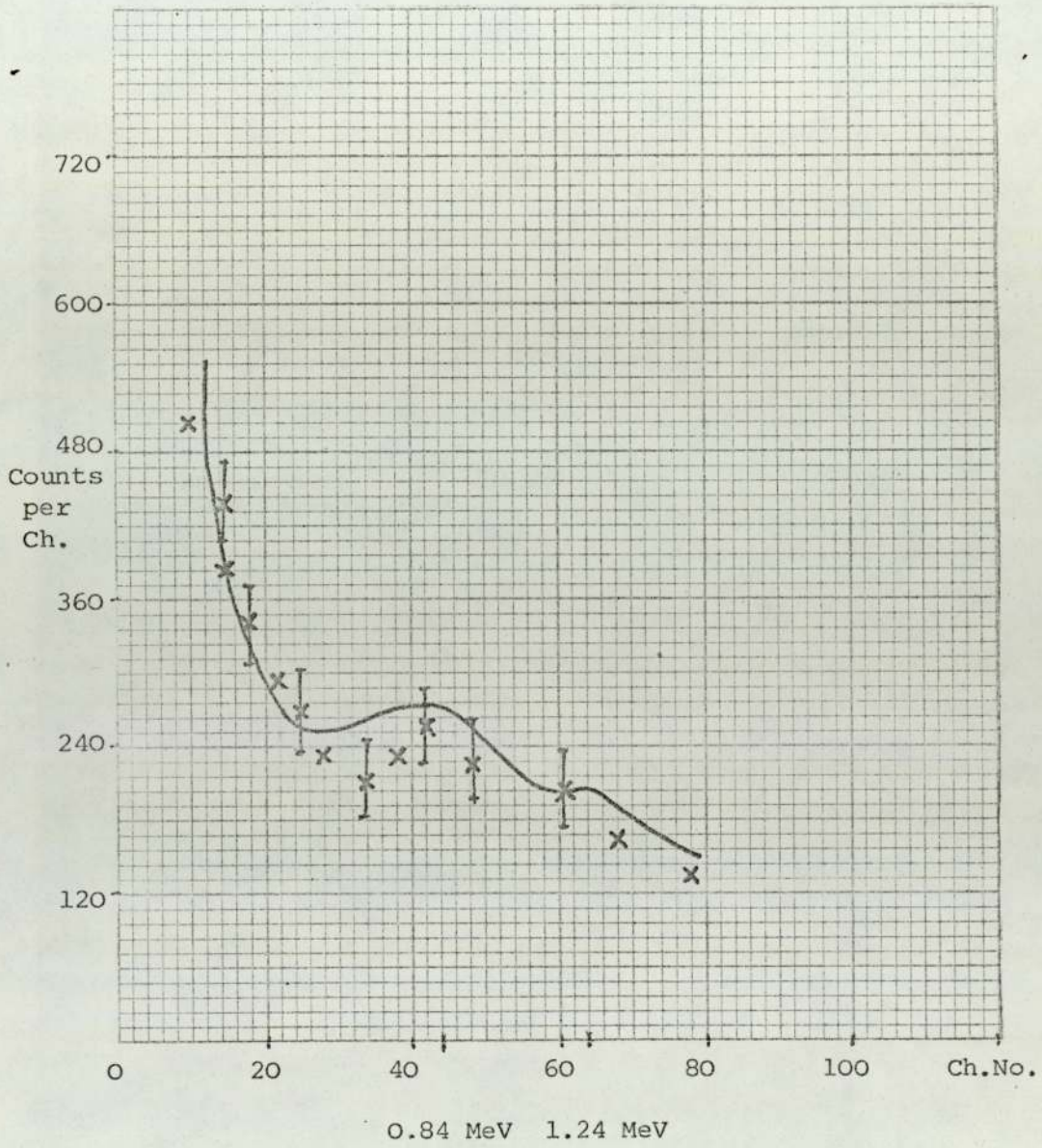

Figure 6.5 Normalised spectrum of gamma-ray energies from ^{56}Fe (scattering angle 60^{o}).

_____ Theoretical Result

xxxxxxxxxxx Experimental Result.

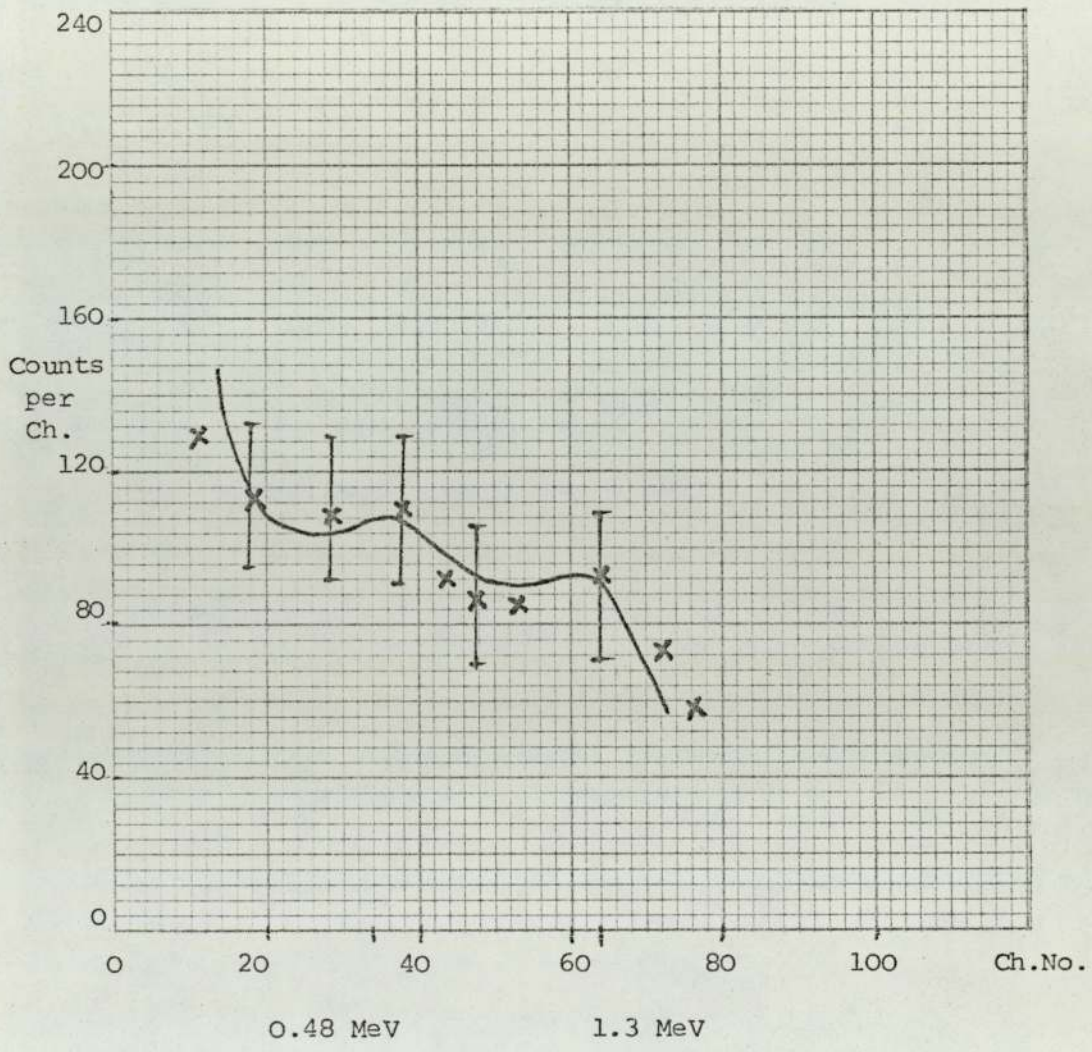

Figure 6.6 Normalised spectrum of gamma-ray energies from LiF (scattering angle 30^{o}).

_____ Theoretical result.

xxxxxxxxxx Experimental result.

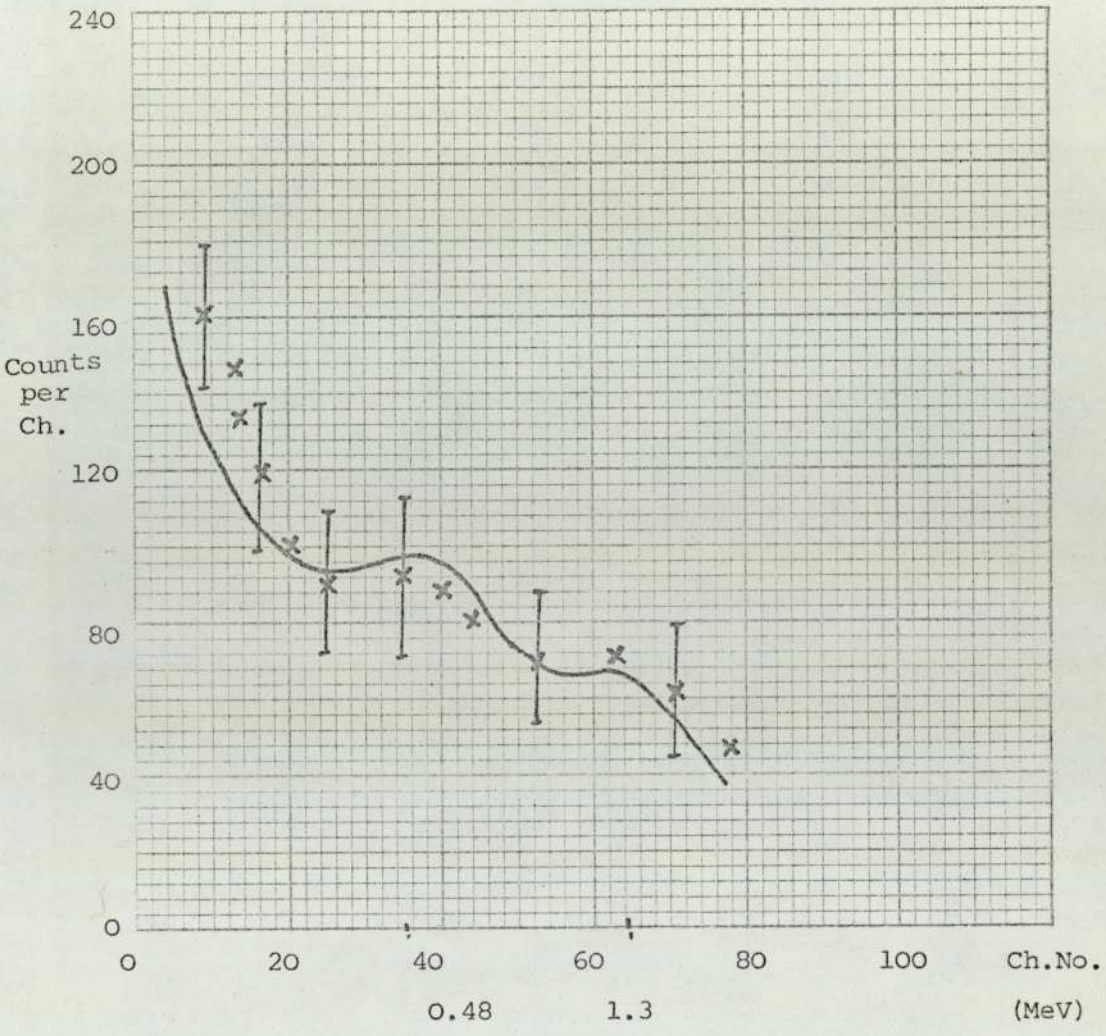

Figure 6.7 Normalised spectrum of gamma-ray energies from LiF (scattering angle 45^{o}).

_____ Theoretical Result

xxxxxxxxxx Experimental Result

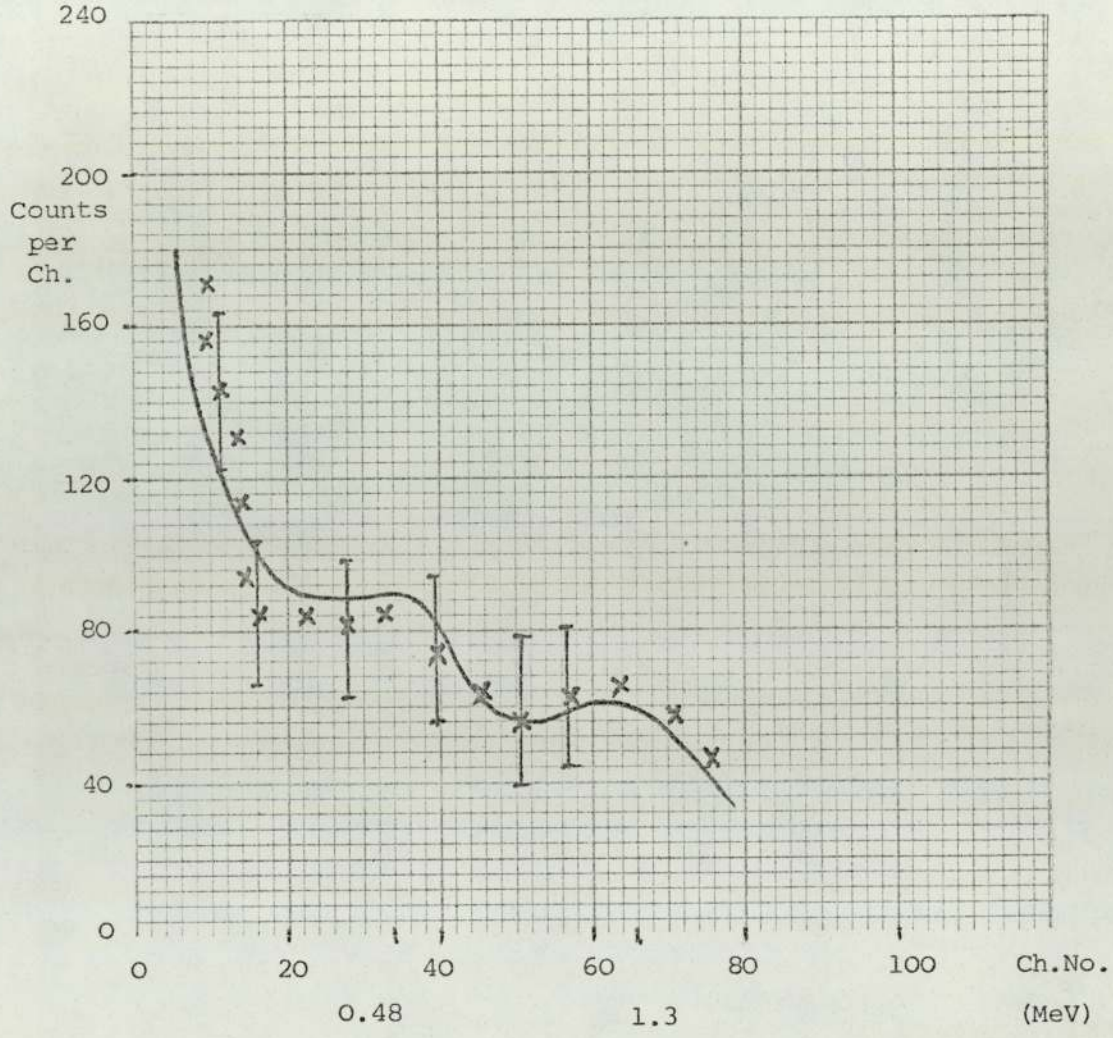

Figure 6.8 Normalised spectrum of gamma-ray energies from LiF (scattering angle 60^{o}).

———— Theoretical Result

xxxxxxxxxx Experimental Result

6.6 Conclusion

From the comparison of the theory and the experimental measurements obtained in Chapter 5, it can be seen that the overall shapes of the experimental γ-ray energy spectra are reasonably well represented by the theoretical prediction. So it can be concluded that the multiple scattering theory produces a good prediction of the experimental measurements notwithstanding the very simplified approach used.

Chapter 7

7. Introduction to Part II

One main reason for shielding a reactor is that the radiations emitted are biologically harmful. A reactor can produce practically all types of nuclear radiation which may be classified into two groups, charged and neutral particles. The charged particles, because of their strong interactions with the material through which they pass, do not travel great distances, and present no particular shielding problem for reactors. This includes the fission fragments, α and β-particles, and protons, deuterons, etc. On the other hand, the radiations that do not interact as strongly, the neutrons and γ-rays, penetrate further and present problems where personnel protection is concerned. In fission two fission fragments are formed, two to three fast neutrons are released and, in general, two prompt-fission gammas having a total energy of about 7.0 MeV are produced. Fission fragments are radioactive, and in decaying, they produce β-particles and decay gammas. The fast neutrons suffer scattering of two types, inelastic, which produces gammas, and elastic. These two processes eventually result in the slowing down of the neutrons, and their capture.

When the neutrons are captured they produce excited compound nuclei which, in turn, give off capture gammas and, if in addition they are radioactive, they in turn emit decay gammas. All of the preceding processes result in a great deal of gamma radiation, which is produced in some cases directly in the fuel and in other cases throughout the reactor and reactor shielding. This gamma-radiation must be absorbed. The secondary γ-rays, which are formed as a result of the inelastic scattering of the neutrons or their captures, arise at various places throughout the reactor and their locations, as well as their intensity, must be taken

into consideration. A neutron or gamma-ray may be completely absorbed in the first collision it makes, or may frequently suffer large changes in energy and direction in a single collision. As the average distance between collisions is characterised by the "mean-free-path" and the probability of collision is exponential, there is no sharply defined distance for neutrons and γ-rays beyond which they are completely eliminated. Therefore, the attenuation of the intense beams of neutrons and γ-rays requires thickness of material that may be many times greater than the "mean-free-path" length.

Thermal neutrons produce less biological damage for the same flux than fast neutrons, and moreover can be stopped quite easily, therefore emphasis in shielding should be on fast neutrons.

Gamma-rays with energies less than about 20KeV do not readily penetrate air or tissue. Gamma radiation of several hundred KeV is easily absorbed in heavy materials, and shielding against sources of such radiation is not difficult. However, gamma-rays of lower energy may appear as secondaries from harder γ-rays, and must be included in determining biological doses.

Neutron shielding is usually produced by slowing down the fast neutrons to thermal energies, and then capturing them in a suitable material. The slowing down is accomplished by elastic or inelastic collision with very light nuclei such as hydrogen, but light elements are not normally the best material for gamma-ray shielding.

Shielding for fast reactors

As mentioned already, shielding a reactor involves problems dealing with the intrinsic behaviour of neutrons and γ-rays in their passage through the materials. The best neutron shields are those of light materials, and the best gamma-ray

shields are made of heavy materials. The selection of the right material depends upon the type of the reactor, reactor power, location of the shield, and the cost and availability of the material. The shield moderates and absorbs neutrons and γ-rays which are the two most important types of radiation from a shielding point of view.

Shielding against gamma-radiation

The most penetrating component of the radiation passing through the bulk shield of a reactor is due to gamma-radiation. Gamma-rays are absorbed within materials mainly by interacting with the electrons surrounding the nucleus of atoms. Heavy elements make the best γ-ray shields, because the electron density within a material is proportional to the atomic number Z. The gamma-radiation penetrating the main shield in a fast reactor is predominantly due to neutron capture in the pressure vessel, the remaining source of γ-radiation which is of importance during the operation of the reactor is due to inelastically scattered neutrons.

The source density of inelastic gamma-radiation is given by:

$$S = \eta \phi \Sigma_{in} \quad \text{MeV Cm}^{-3} \text{ sec}^{-1} \quad \ldots\ldots\ldots\ldots \quad (7.1)$$

where η is the energy released in gamma-radiation per inelastic event, ϕ is the total integrated fast neutron flux above the inelastic scattering threshold, and Σ_{in} is the macroscopic inelastic cross-section.

As a consequence the shielding problem may involve the following aspects:

(i) slowing down of fast neutrons (ii) capturing the slowed down neutrons (iii) absorption of all the forms of gamma-ray activity. The problem of shielding the nuclear reactor has

received intense study in recent years, and many useful presentations have been given by various authors.[40 &48]

In what follows a feasibility study is undertaken to investigate the possibility of measuring the gamma-ray flux produced in (n, n' γ) reactions in extended samples of reactor materials for neutrons of 2-5 MeV produced by the D(d,n)^{3}He reaction. The results of such an experiment will be of importance to the shielding of reactors for the reasons given above.

Chapter 8

8. Design study for use on Dynamitron

8.1 Introduction

It is intended to use the associated particle method for the studying of the γ-rays associated with the scattering of 2-5 MeV neutrons produced by the $D(d,n)^3He$ reaction using the 3 MV Dynamitron to accelerate the deuterons. In order to use this several factors have to be considered, these are:-

(i) D-d kinematics

(ii) Deuterium target design

(iii) Separation of ^3He-particles from elastically scattered deuterons and other charged particles,

(iv) Electronic system.

These are discussed respectively in this chapter and in Chapters 9 and 10.

8.2 Associated particle method for the $D(d,n)^3He$ reaction.

The associated particle method using the D-d reaction is based on the principle that the ^3He-particles are associated with the neutrons incident onto the scattering sample. It is thus necessary to calculate the relation between the ^3He production angles and those of the neutrons. The associated particle method has been used [82-90] extensively to produce accurately collimated neutron beams of small angular width and known absolute intensity and energy. It provides a mono-energetic neutron beam in the range of 2 to 5 MeV, and the associated ^3He-recoil particles could be counted with a good resolution in a solid state detector. The timing resolution between the ^3He-recoil particles and the neutrons associated with them are reported [56,57] a few nanoseconds.

In applying the associated particle method by detecting the associated recoil nuclei not only can the starting time be

determined, but also the cone of the coincident neutrons can be defined. This is seen by considering the kinematics of the reaction. For most experiments requiring a neutron beam the principal disadvantage of this method is the limit imposed on the source strength by the maximum counting rate that can be tolerated in the recoil-particle detector. In fact it is much more difficult to use the associated particle method with the D-d reaction than the d-T reaction, because the ^{3}He-particles produced in the D-d reaction have lower energy than the α-particles from the d-T reaction.

8.3 Kinematics of the D(d,n)^{3}He reaction

One of the well-known neutron sources from the interactions of the hydrogen isotopes is the D(d,n)^{3}He reaction. This reaction has a Q-value of 3.26 MeV. The determination of the energies of neutrons emitted from a nuclear reaction as a function of the angles of observations and the incident particle energy can be calculated from the equations of conservation of energy and momentum in the Lab. system. Consider an incident particle of mass M_1 with kinetic energy of E_1 which collides with a stationary nucleus of mass M_2, producing two particles of masses M_3 and M_4 and energies of E_3 and E_4 respectively. If the momenta of these particles are $\vec{P}_1$, $\vec{P}_2$, $\vec{P}_3$, and $\vec{P}_4$ respectively, where $\vec{P}_2 = o$ because it is assumed a stationary nucleus, therefore, the conservation of momentum gives the following two equations:

$$\vec{P}_1 = \vec{P}_3 + \vec{P}_4 \quad \ldots\ldots\ldots\ldots\ldots\ldots\ldots\ldots \quad (8.1)$$

$$P_4^2 = P_1^2 + P_3^2 - 2P_1P_3 \cos\theta_3 \quad \ldots\ldots\ldots\ldots \quad (8.2)$$

where θ_3 is the angle of emission of particle M_3 with respect to the incident particle direction. Fig.8.1 shows the schematic

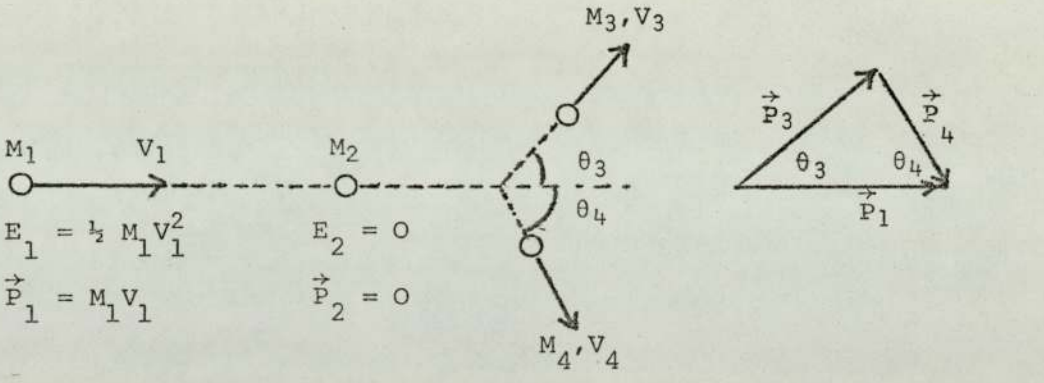

Figure 8.1. Schematic of a nuclear reaction in the Laboratory system of frame.

representation of the reaction in the Laboratory system. The equation expressing the conservation of energy including the energy released during the nuclear reaction, i.e. Q-value is shown as:

$$E_3 + E_4 = E_1 + Q \quad \ldots\ldots\ldots\ldots\ldots\ldots \quad (8.3)$$

Since $P^2 = 2ME$ the equation (8.3) in terms of the momenta can be shown as below:

$$\frac{P_3^2}{2M_3} + \frac{P_4^2}{2M_4} = \frac{P_1^2}{2M_1} + Q \quad \ldots\ldots\ldots\ldots\ldots\ldots \quad (8.4)$$

If the energy of interest is that of particle M_3 where in the case of $D(d,n)^3He$ reaction it can be considered to be neutron, then the relation for E_3 from combining the equations 8.2 and 8.4 can be given as follows:

$$E_3 = E_1 \frac{M_1 M_3}{(M_3+M_4)^2}\left\{ 2\,\mathrm{Cos}^2\theta_3 + \frac{M_4(M_3+M_4)}{M_1 M_3}\left[\frac{Q}{E_1} + \left(1 - \frac{M_1}{M_4}\right)\right]\right.$$

$$\left. \pm\, 2\,\mathrm{Cos}\theta_3 \left[\mathrm{Cos}^2\theta_3 + \frac{M_4(M_3+M_4)}{M_1 M_3}\left(\frac{Q}{E_1} + \left(1 - \frac{M_1}{M_4}\right)\right)\right]^{\frac{1}{2}}\right\} \ldots\ldots \quad (8.5)$$

The value of E_4 which in this case is the energy of ^3He-particle can be obtained from the equation 8.3 knowing the values of E_1 and Q.

The angle of emission of particle M_4 (i.e. ^3He) can be obtained from the momentum diagram, figure 8.1, and is given by:

$$\mathrm{Sin}\ \theta_4 = \left(\frac{M_3 E_3}{M_4 E_4}\right)^{\frac{1}{2}} \mathrm{Sin}\ \theta_3 \quad \ldots\ldots\ldots\ldots\ldots\ldots \quad (8.6)$$

As an example, assuming $E_1 = 3MeV$, $\theta_3 = 40^\circ$, the following results were obtained by using the above formulae:

E_3 (neutron energy) = 5.368 MeV

E_4 (^{3}He-particle energy) = 0.891 MeV

θ_4 (^{3}He-particle emission angle) =65.636^o

Figure 8.2 shows the relation between ^{3}He-particle angle and the neutron angle with respect to the deuteron beam direction for various deuteron energies.

The neutron energies from the D-d reaction are seen to be in the range of 2 to 6.5MeV for the incident deuteron energies of about 3 MeV.

Figure 8.3 shows the neutron energy available in the Laboratory frame of reference for different values of incident deuteron energies. Figure 8.4 shows the curve for the total cross-section for neutron production from D(d,n)^{3}He reaction given by Hanter and Richards[50] who made an extensive study of the yield of neutrons from the D-d reaction. The competing reaction D(d,p)^{3}H always occur along with the (d,n) reaction when deuterium targets are bombarded by deuterons. In fact the cross-section for the two competing reactions are slightly different. Figure 8.5 given by Blair et al.[51] shows the differences in the cross sections for the two reactions. At an incident deuteron energy of 3 MeV the total cross-section for the D(d,n)^{3}He and D(d,P)T are about 104mb and 90mb respectively.

A computer programme in Algol language is used to calculate the angular correlation and energy relationship between the neutrons and the ^{3}He-particles from the D-d reaction which also can be used for the d-T reaction as well. The layout of this computer programme and the outputs for various incident deuteron energies for the D-d reaction is shown in Appendix A.

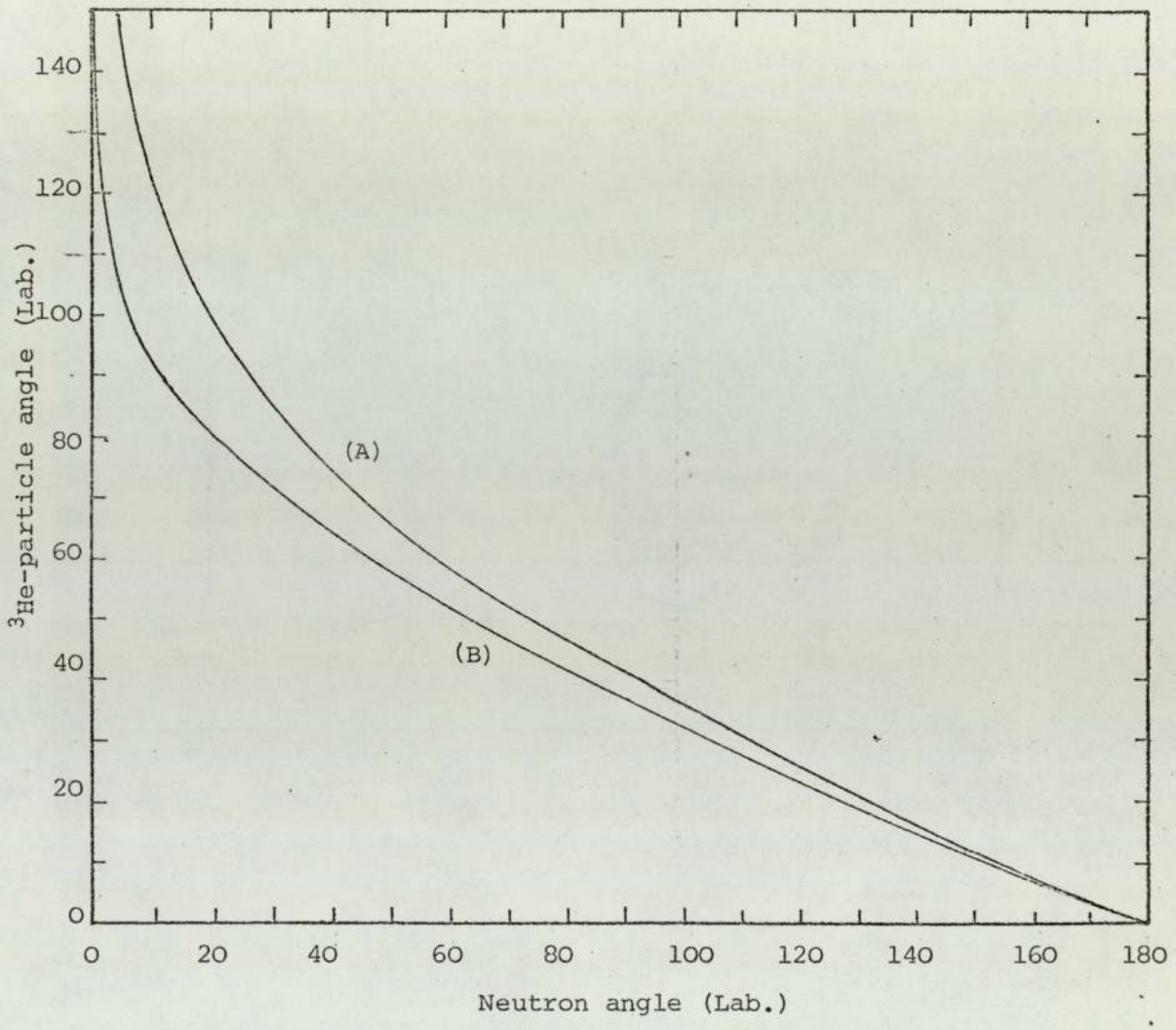

Figure 8.2. The relation between ^{3}He-particle angle and neutron angle for different incident deuteron energies.

(A) - E_d = 2 MeV

(B) - E_d = 3 MeV

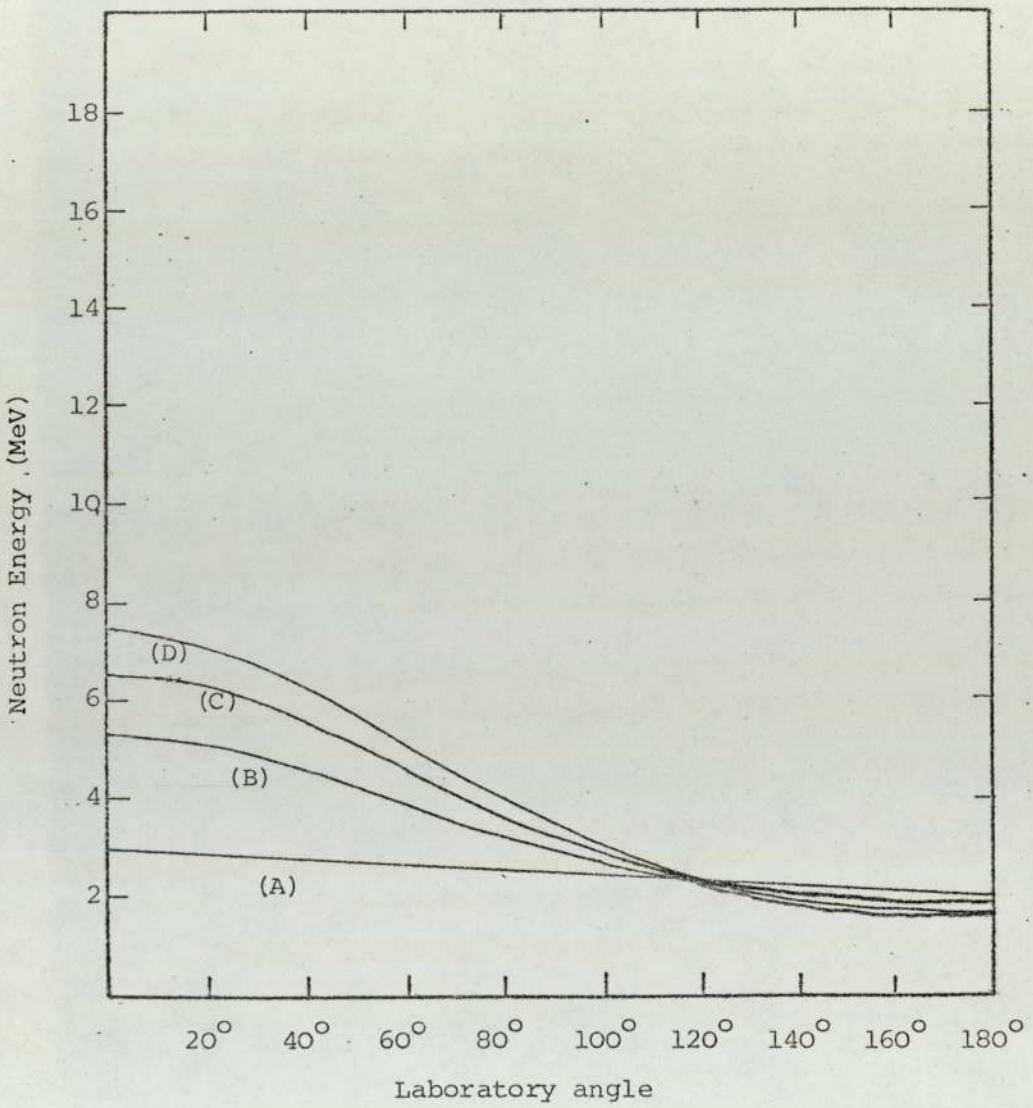

Figure 8.3. Neutron energy versus neutron angle for various deuteron energies in the Laboratory system.

(A) : E_d = 0.1 MeV

(B) : E_d = 2.0 MeV

(C) : E_d = 3.0 MeV

(D) : E_d = 4.0 MeV

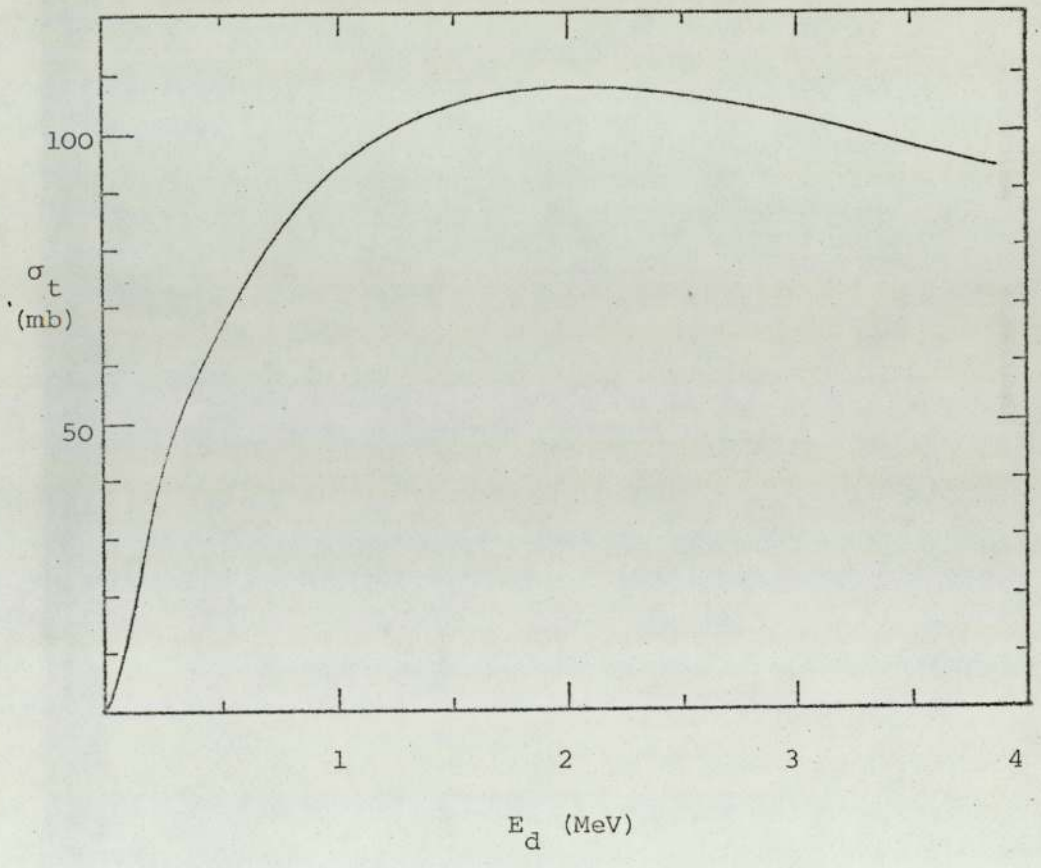

Figure 8.4. Total cross-section of the reaction $D(d,n)^3He$ as a function of the incident deuteron energy.[50]

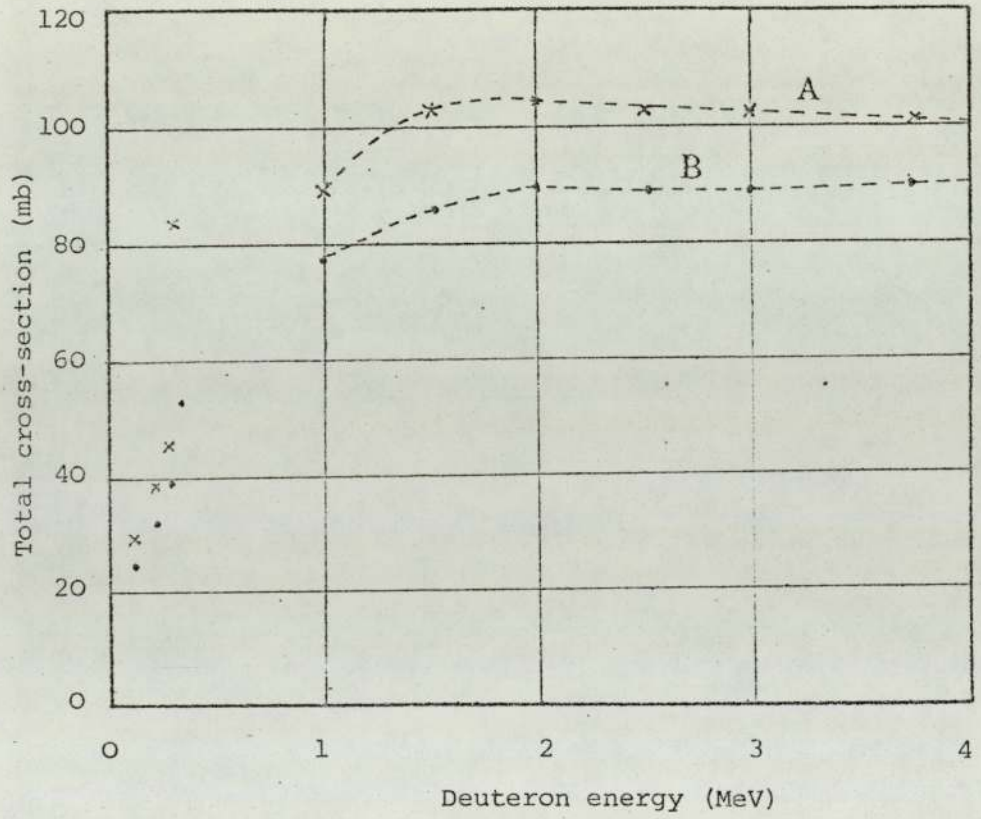

Figure 8.5. Total gross sections for the reactions $D(d,n)^3He$ (Curve A) and $D(d,P)^3He$ (Curve B) for various deuteron energies. (51)

8.4 The Dynamitron accelerator

The Dynamitron is a high-current machine manufactured by the Radiation Dynamic Inc. it can operate at voltages up to three million volts and accelerate either electrons or positive ions such as deuterons and protons; the maximum power in the electron beam is practically high at 30kw. Both the electron and ion beams can be provided continuously or pulsed with the pulse duration and repetition rate capable of being selected over wide ranges. The deuterons can be accelerated to produce secondary radiations and in this case, the secondaries are neutrons from appropriate nuclear reactions. Because the energies of the positive ions can be selected precisely, it is possible to produce neutrons of precise energies. The energy range for electrons and positive ions is from 0.2 to 3 MeV. The current range at 3 MeV for positive ions is from 100μA to 2mA and for electrons from 10μA to 10mA.

Chapter 9

9. Possible deuterium targets for the $D(d,n)^3He$ reaction

It is possible to use four types of deuterium targets, these being: a heavy ice target, a deuterium gas target, a deuterated titanium target, and a deuterated polyethylene target.

The following sections discuss each and their respective advantages and disadvantages:

9.1 Heavy ice target

This target is heavy water, D_2O, frozen onto the surface of a copper drum maintained at liquid nitrogen temperature. Because of the good thermal conductivity of copper the heavy ice is in good thermal contact with the liquid nitrogen, and can withstand the intense deuteron bombarding current. Heavy ice targets have been used in [91,92] $D(d,n)^3He$ reactions for neutron production. The detailed preparation of the present heavy ice target is described below, together with its manufacture and assessment.

Figure 9.1 shows the target. As can be seen the main chamber is evacuated and a small amount of D_2O is released into the chamber where it condenses onto the liquid nitrogen cooled copper drum. The experimental arrangement in figure 9.1 was used for the calibration of the heavy ice thickness deposited on the surface of the copper drum maintained at liquid nitrogen temperature, which is described in section 9.1.2.

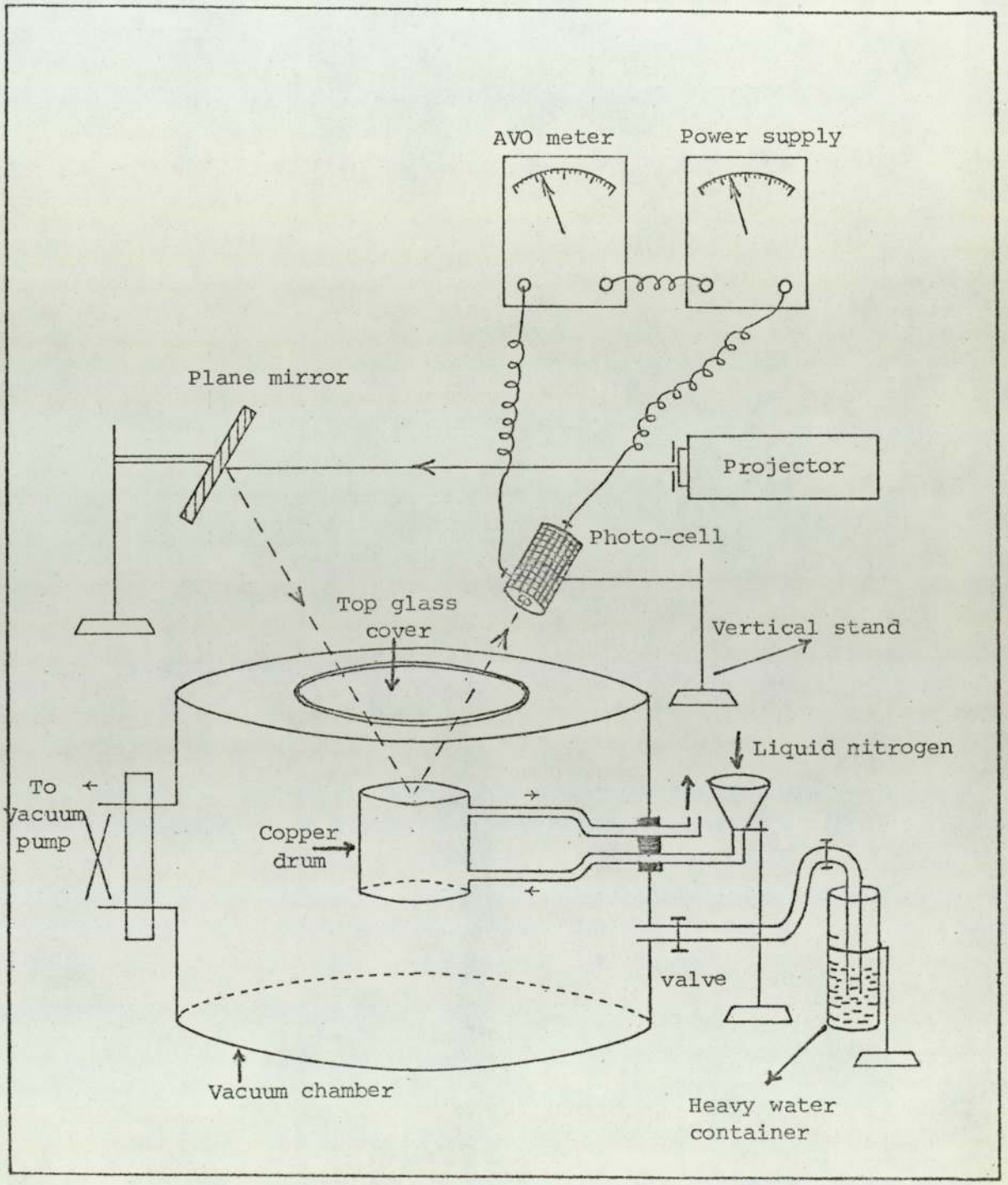

Figure 9.1. Experimental arrangement for calibrating the thickness of heavy ice by light reflection.

9.1.1 Vacuum chamber design for heavy ice target.

In the $D(d,n)^3He$ associated particle time of flight experiment a beam of 3 MeV deuteron from the Dynamitron accelerator will be collimated and focussed onto a copper drum heavy ice target. The vacuum chamber is made of stainless steel by the Edward Co. Ltd., with an inner diameter of 9 inches and depth of 5 inches. The thickness of the vacuum chamber for the top and bottom parts is $\frac{1}{2}$ inch, but the sides are $\frac{1}{4}$ inch. The large size of the vacuum chamber is necessary to accommodate the heavy ice target consisting of the copper drum of 3 inches inner diameter and 4 inches in height with a wall thickness of 4×10^{-3} inches placed off centre in the vacuum chamber.

Figure 9.2 shows the vacuum chamber which was designed for the use of heavy ice target and Dynamitron accelerator. In figure 9.3 the copper drums which were used in the experiment can be seen. The flat plane top is the one used for the measuring of heavy ice thickness and the inclined plane top was used in the experiment with the incident deuteron beam from the S.A.M.E.S. accelerator for testing the target.

From the experiment for testing the heavy ice target with S.A.M.E.S. accelerator it was noticed that by increasing the beam current and incident deuteron energy, the neutron yield was increased. The total neutron yield, for incident deuteron energies up to 1.0 MeV from a thick heavy ice target [37] is shown in figure 9.4.

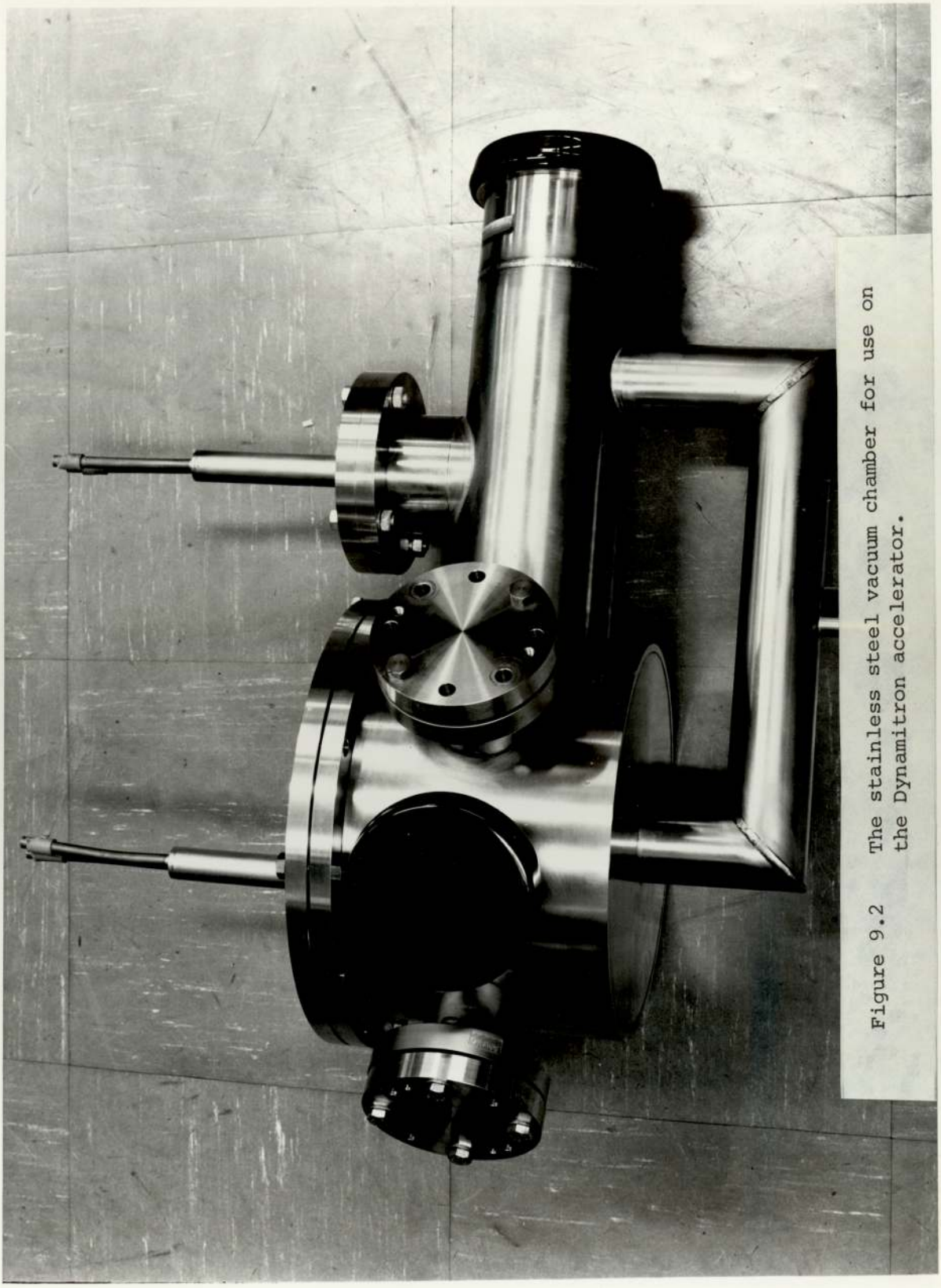

Figure 9.2 The stainless steel vacuum chamber for use on the Dynamitron accelerator.

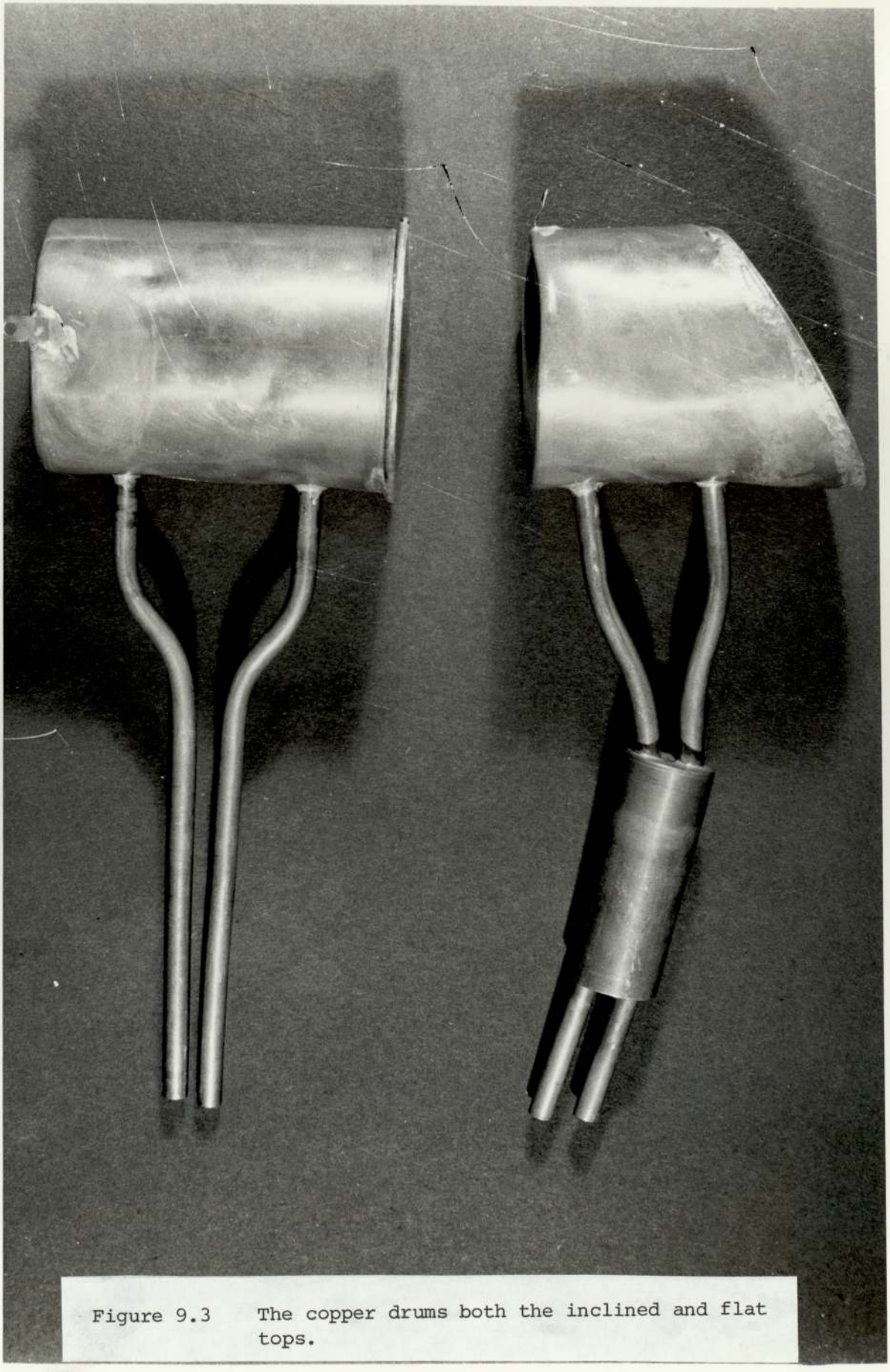

Figure 9.3 The copper drums both the inclined and flat tops.

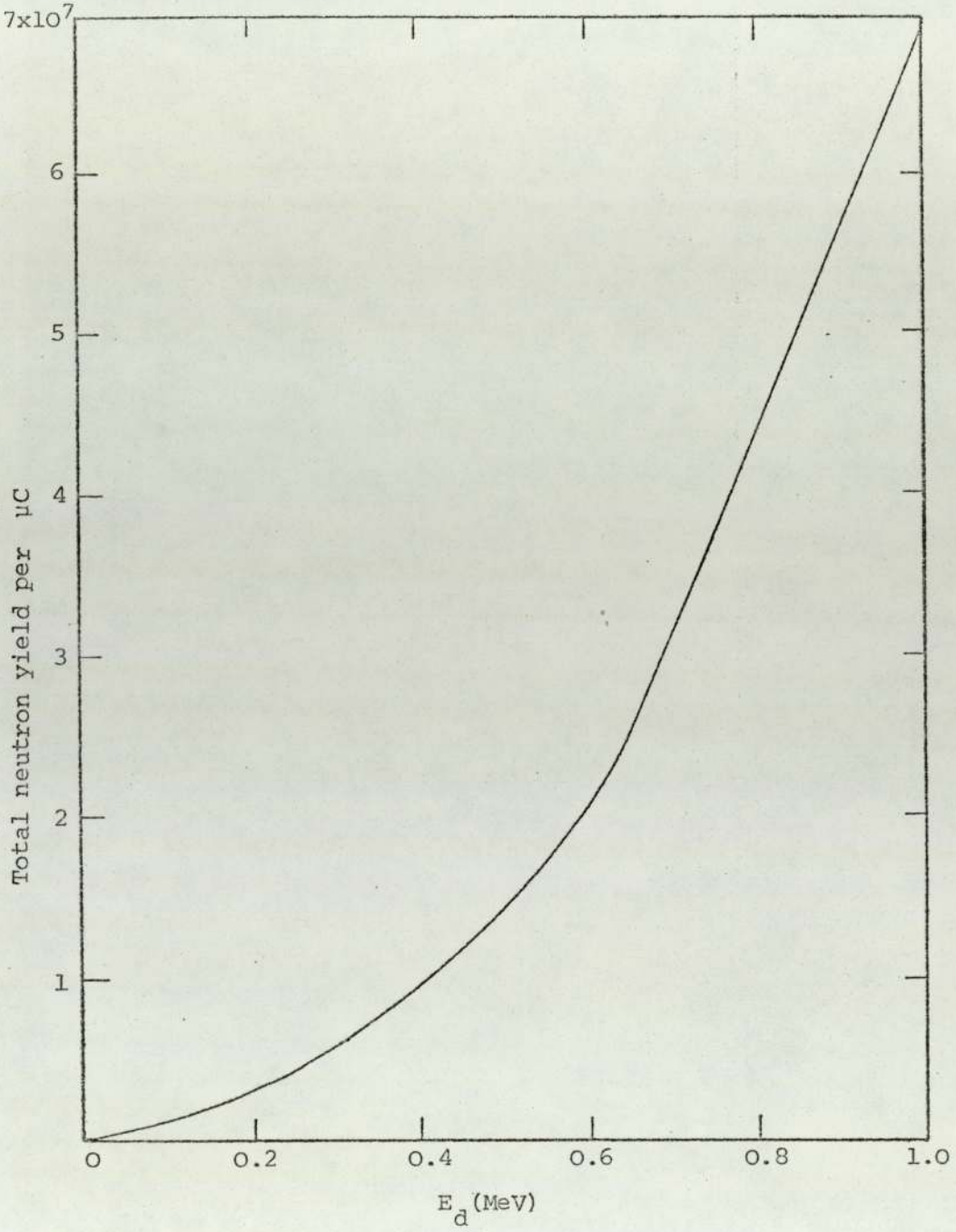

Figure 9.4 Variation of the total neutron yield for heavy ice target as a function of deuteron energy.

9.1.2 Measurement of the heavy ice thickness

In order to find the thickness of heavy ice deposited on the surface of the copper drum target, a method dependent on measuring the intensity of reflected light from the surface area of the target was used as the reflected intensity depended on the thickness of heavy ice.

As an incident beam of light passes through a layer of heavy ice of thickness Δx, a certain amount of intensity of light (ΔI) will be absorbed, while the remainder will be reflected. The amount absorbed per element of thickness is proportional to the incident beam intensity, i.e. $\frac{dI}{dx} \alpha I$ or $\frac{dI}{I} \alpha dx$. Therefore it can be written as:

$$\frac{dI}{I} = - k dx \quad \ldots\ldots\ldots\ldots\ldots\ldots \quad (9.1)$$

where the proportionality constant k is the absorption coefficient. If I_o is the incident beam intensity, and I_x is the reflected beam intensity passes through a thickness of x, then by integrating both sides of the equation 9.1 between zero and x, it gives the following relation:

$$I_x = I_o \exp(- k x) \quad \ldots\ldots\ldots\ldots\ldots\ldots \quad (9.2)$$

Figure 9.1 shows the experimental arrangement. With no layer of heavy ice on the surface of copper drum, the current through the circuit which is proportional to the reflected light intensity from the polished smooth flat top of the drum was measured, then by opening the valve for a short period a certain amount of heavy water was deposited on the surface area of the drum, while it was filled with liquid nitrogen, and as a consequence a layer of heavy ice was formed on the surface. Again the current through the circuit which was related to the intensity of reflected light

passing through the heavy ice layer was measured.

Since the surface area, and the heavy water deposited on the surface, and the density of heavy ice were known, the thickness of heavy ice was measured. Knowing the relation $I_x = I_o \exp(-kx)$ a graph for the $\log \frac{I_x}{I_o}$ against x can be drawn in a semi-log paper from the experimental data, and as it can be seen in figure 9.5 it gives a straight line. Therefore by this calibration, and knowing the intensity ratio, the thickness of heavy ice in the future experiments could be measured.

9.1.3 The possible competing reactions in using heavy ice target.

In using a heavy ice target for the D-d reaction, the possible competing reactions with the $D(d,n)^3He$ of the forms $^{16}O(d,x)y$ and $D(d,x)y$ should be taken into consideration.

For these reactions several factors, such as Q-values, threshold energies, kinetic energies of the recoil particles have been calculated.

(i) Q-values

A general nuclear reaction can be written as A(a,b)B, where the bombarding particle a, strikes the target nucleus, A, and produces the nucleus B and the outgoing particle b. The energy released in the reaction is Q, so that Q is positive for an exothermic reaction and negative for an endothermic reaction.

In the present case the bombarding particle is deuteron, and the target nuclei are deuterium and oxygen. The Q-value can be calculated from the following relation:

$$Q = [(m_a + m_A) - (m_b + m_B)] \text{ a.m.u.x } 931 \text{ Mev}/_{\text{a.m.u}} \quad \ldots\ldots\ldots (9.3)$$

where the particle masses are in atomic mass unit (a.m.u.)

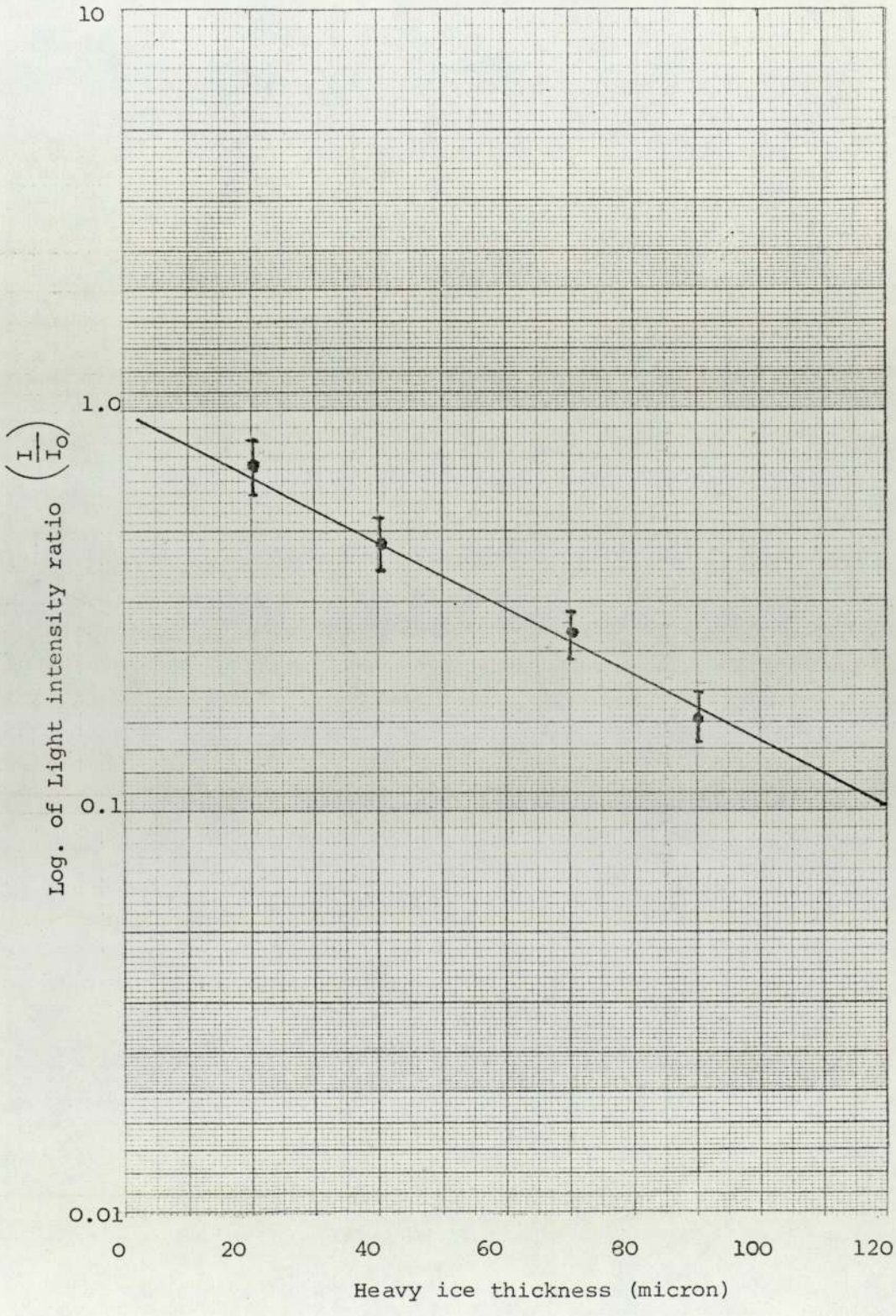

Figure 9.5. The result of the calibration for measuring the heavy ice thickness.

Two examples are given below:

1 - D(d,Pn)D

$$ {}^{2}_{1}H + {}^{2}_{1}H \rightarrow {}^{1}_{1}H + {}^{1}_{0}n + {}^{2}_{1}H + Q $$

$$ Q = \left[(2x2.01471)-(1.00813+1.00896+2.01471)\right] \times 931 $$

$$ = - 2.2 \text{ MeV}. $$

2 - D(d,P)t

$$ {}^{2}_{1}H + {}^{2}_{1}H \rightarrow {}^{1}_{1}H + {}^{3}_{1}H + Q $$

$$ Q = \left[(2x2.01471)-(1.00813+3.01695)\right] \times 931 = 4.04 \text{ MeV}. $$

The values for the atomic mass units of the particles are taken from the Handbook of Chemistry and Physics.[64] All the other Q-values calculations for the possible reactions have been done in this manner.

(ii) Threshold energy

The minimum value of the kinetic energy of the bombarding particle which the reaction just becomes possible is called the threshold energy. The threshold energy must be found for the endothermic reaction, i.e. the value of Q is negative.

The threshold energy is zero when Q is positive, and it is greater than zero when Q is negative. The relation between threshold energy (E_{th}) and the Q-value of a reaction is given by:

$$ E_{th} = - Q \left(\frac{m_i + m_t}{m_t} \right) \quad \ldots\ldots\ldots\ldots\ldots\ldots\ldots\ldots \quad (9.4) $$

where m_i and m_t are the masses of the bombarding and target nuclei.

In order to find the threshold energy for the D(d,Pn)D reaction which has Q = -2.2 MeV, and $m_i = m_t \simeq 2$ a.m.u., therefore

$$ E_{th} = - Q \left(\frac{m_i + m_t}{m_t} \right) = - (-2.2) \left(\frac{2 + 2}{2} \right) = 4.4 \text{ MeV}. $$

The other threshold energies have been found in the same way.

(iii) Kinetic energy of the recoil particle

The kinetic energy of the recoil particle can be calculated from the equation 8.5. and was discussed in the kinematic of the D-d reaction.

In table 9.1 the possible reactions, including Q-values, and threshold energies discussed above have been shown.

In table 9.2 those reactions in this investigation due to their importance are listed. The charged particle energies of interest calculated from equation 8.5 and the radius of curvature of these charged particles in the magnetic analyser (see section 10.6) have been shown in this table.

9.2 Deuterium gas target

The aim of using deuterium gas target for the $D(d,n)^3He$ reaction is to reduce the number of elastically scattered deuterons reaching the ^3He-detector, especially if the ^3He-detector angle is $> 90^o$ with respect to the incident deuteron beam.

This is also the aim of the heavy ice target. However, because of the copper backing this must always be a thick target. A gas target offers the possibility of thin targets.

When producing neutrons from the accelerator induced reaction $D(d,n)^3He$, a gas target has the following advantages compared to heavy backing targets:

(i) The number of target nuclei is a known function of the pressure and temperature of the gas target, and in addition the effective target thickness can be easily varied.

(ii) Contamination problems can be avoided and targets of very high purity are attainable.

One of the problems with gas targets is inherent in the use of a window and a large amount of the gas necessary between reaction point and the detector which introduces the disadvantages of having

Reactions	Q-values (MeV)	Threshold energies (MeV)
$D(d,\gamma)He^4$	23.8	-
D(d,pn)D	-2.2	4.4
$D(d,n)He^3$	3.26	-
$D(d,p)H^3$	4.04	-
D(d,2n2p)	-4.43	8.86
D(d,d)D	0.0	-
$O^{16}(d,\gamma)F^{18}$	7.53	-
$O^{16}(d,n)F^{17}$	-1.66	1.86
$O^{16}(d,p)O^{17}$	1.89	-
$O^{16}(d,\alpha)N^{14}$	3.1	-
$O^{16}(d,t)O^{15}$	-9.3	10.46
$O^{16}(d,\alpha p)C^{13}$	-4.41	4.95
$O^{16}(d,n\alpha)N^{13}$	-6.62	7.44
$O^{16}(d,d)O^{16}$	0.0	-

Table 9.1 The possible reactions of the forms D(d, x)y and ^{16}O(d, x)y

Reactions	Particles' energies	Radius of Curvatures
	($\theta = 40°$)	
$D(d,n)He^3$	$E_{He^3} = 2.2$ MeV	$r_{He^3} = 18$cm
$D(d,p)H^3$	$E_p = 5.62$ MeV	$r_p = 33$cm
	$E_{H^3} = 1.43$ MeV	$r_{H^3} = 32$cm
$D(d,d)D$	$E_d = 1.35$ MeV	$r_d = 23.5$cm
$O^{16}(d,p)O^{17}$	$E_p = 2.68$ MeV	$r_p = 23.2$cm
$O^{16}(d,\alpha)N^{14}$	$E_{He^4} = 4.18$ MeV	$r_{He^4} = 29$cm

Table 9.2 The five important reactions concerned in the experiment for 3 MeV incident deuteron energy and a magnetic field of 1.0 tesla.

very low power-handling capacity, because the window must be thin and supported firmly and, also, it must withstand about one atmosphere differential pressure. In order to make use of high gas density targets without using the window the technique of differential pumping[93,94] is employed. However, the design and construction of this kind of gas target is difficult. A number of investigators have used gas targets[95,96,59] with thin foil windows for the neutron production from D-d reaction.

9.3 Deuterated titanium target

Deuterium absorbed in a thin layer of titanium and deposited on suitable backing metals provides convenient sources of monoenergetic neutrons when bombarded with deuterons.

Such targets can withstand temperatures of up to about 200°C according to the manufacturers in the vacuo without losing significant quantities of gas. 200°C is the temperature at which deuterium boils out. Thus Copper-backed targets can be soft-soldered to target assemblies. This type of deuterium target has been used by many experimenters.[24,58]

The heavy backing of this type of target and also thin heavy ice target scatters deuterons at most angles, therefore it is necessary to discriminate between the ^{3}He-particles and deuterons elastically scattered from the target, otherise the ^{3}He-detector will be swamped by these latter particles. The detailed discussion of discriminating between ^{3}He-particles and elastically scattered deuterons is given in Chapter 10.

9.4 Deuterated polyethylene target

The deuterated polyethylene targets are thin films of $(C_2D_4)_n$. These are the two constituents only, carbon and deuterium, with twice as many deuterium atoms as carbon atoms.

Targets with excellent uniformity and strength have been

prepared by Bartle and Meyer.[108] The fact that the target is very thin (in the range of about 0.5 to 7.0μ) reduces the number of elastically scattered deuterons into the ^{3}He-detector. The polyethylene films are prepared by dissolving a little deuterated polyethylene in boiling xylene. The solution is kept near to the boiling point until the deuterated polyethylene is completely dissolved, and while still hot, the solution is poured on the process clean micro slides. The slides are then dried in a dust free place for a period of several hours.

Chapter 10

10. Separation of recoil-^{3}He and ^{2}H in D-d reaction

The principal problem in applying the associated particle time of flight technique for the $D(d,n)^{3}He$ reaction is to separate the numerous elastically scattered deuterons from the recoil ^{3}He-particles, and also to separate P and T resulting from the competing D(d,P)T reaction. This is advisable even in the case of targets not expected to scatter deuterons beyond 90^{o}. The technique which is used to overcome this problem depends upon the incident deuteron energy.

10.1 Low deuteron energy <100 KeV

For low deuteron energies it is possible to put a thin metal foil in front of the ^{3}He-particle detector. Here for the correct foil thickness the elastically scattered deuterons will be stopped by the foil, while the ^{3}He-particles pass through to be detected. Many researchers[97,98,99,100] have applied this method at low incident deuteron energies. The low energy does, however, mean that the neutron yield tends to be low because of the dependence of neutron production cross-section on deuteron energy.

10.2 Deuteron energies >100 KeV

At higher deuteron bombarding energies the foils cannot be used for stopping the elastically scattered deuteron from entering the ^{3}He-detector as the ^{3}He-particles are also stopped because the ^{3}He range is shorter than the deuteron range. Instead electrostatic or magnetic separation systems must be used. These are described below:

10.2.1 Electrostatic deflection

In a given electrostatic field deuterons with an Energy of E_{d} and ^{3}He-particles with an energy of $E_{^{3}He} = 2E_{d}$ will have the same deflection as shown in the following:

In an electrostatic field, E :

$$Ee = m x'' \quad \ldots\ldots\ldots\ldots\ldots\ldots\ldots\ldots\ldots\ldots \quad (10.1)$$

where x" is the second differential coefficient of x, and m and e are the mass and electric charge of the particle respectively.

$$\text{then } x'' = \frac{Ee}{m} \text{ and } x' = \frac{Eet}{m}, \left(x' \cong \frac{dx}{dt}, x'' \cong \frac{d^2x}{dt^2} \right)$$

Finally the deflection is given by:

$$x = \frac{Eet^2}{2m} \quad \ldots\ldots\ldots\ldots\ldots\ldots\ldots\ldots\ldots\ldots \quad (10.2)$$

where $t = \frac{\ell}{v}$ (ℓ is the length of the plate, and v is the velocity of the charged particle).

Therefore for the same deflection of ^3He and ^2H

$$\frac{2e}{E_{^3He}} = \frac{e}{E_d} \quad \text{or} \quad E_{^3He} = 2E_d$$

and for discrimination between them $E_{^3He}$ should be greater than $2E_d \left(E_{^3He} > 2E_d \right)$ The electrostatic deflectors have been used by several authors.[58,85]

10.2.2 Magnetic deflection

In a magnetic field deuterons with an energy of E_d and ^3He-particles with an energy of $E_{^3He} = \frac{8}{3} E_d$ will be deflected in the same path as comes below:

In a magnetic field,

$$Bev = mx'' \quad \ldots\ldots\ldots\ldots\ldots\ldots\ldots\ldots\ldots\ldots \quad (10.3)$$

where B is the magnetic field, and other factors have been indicated before

$$\text{then } x'' = \frac{Bev}{m} \text{ and } x' = \frac{Bevt}{m}$$

and as a result the deflection path is:

$$x = \frac{Bevt^2}{2m} = \frac{Bev\ell^2}{2mv^2} = \frac{Be\ell^2}{2mv} = \frac{Be\ell^2}{2\sqrt{2mE}} \quad \ldots\ldots\ldots\ldots\ldots \quad (10.4)$$

Therefore, for the same deflection of ^3He and ^2H it is easily found that $E_{^3He} = \frac{8}{3} E_d$, and in order to discriminate between deuterons and ^3He-particles $E_{^3He}$ should be greater than $\frac{8}{3} E_d$ $(E_{^3He} > \frac{8}{3} E_d)$.

The magnetic deflection system has been used by several experimenters. (101,102)

10.3 Comparison between the two systems of deflection

One of the disadvantages of using electrostatic deflection is the long flight path of the ^3He-particles necessary in electrostatic deflection, and this will have an effect on the time resolution in associated particle time-of-flight technique. In addition, for high incident deuteron beam energies such as produced in the Dynamitron accelerator in the range of up to 3 MeV, the deflection in an electrostatic field requires a very high voltage. Thus electrical breakdown is a major problem.

Especially at high deuteron energy the magnetic analyser is to be preferred over electrostatic deflector, because the deflection path length compared with the electrostatic deflector is shorter.

The energy of the ^3He-particles must be large enough to give a signal well discriminated from the noise, and it is therefore preferable to use a high deuteron energy.

In the present investigation, a magnetic analyser has been designed for the 3 MeV deuterons produced on the Dynamitron. This is discussed in detail in the following section.

10.4 Design of a magnetic analyser

The use of a magnetic analyser provides a reliable method of efficient detection of ^{3}He-particles produced in the D(d,n)^{3}He reaction in the presence of other reaction products and scattered deuterons.

A double focussing magnetic analyser can be designed to have a low energy dispersion so that ^{3}He ions of as wide a range as possible could be deflected in the focal plane. The advantage of having the source and image outside the field, however, is that a reasonably good resolving power and solid angle could be obtained with a relatively small magnet. Symmetrical location of the source and the image and normal entry of the median ions into a curved pole boundary is more satisfactory for most analytical purposes.(105)

The observation of the recoil events for reaction energies up to 3 MeV fixes a limit on the minimum value of R and the maximum value of ϕ(103) in an estigmatic magnetic field, where R is the radius of curvature, and ϕ is the deflection angle. The process of designing a magnet system for a particular function consists of the following steps:

(i) First a system is laid out which has the desired qualitative features.

(ii) Determining the parameters of the system.

(iii) Tracing a number of rays through the system to verify its behaviour.

From the basic mass spectrometer formula:

$$\frac{mv^2}{r} = Bev \quad \ldots\ldots\ldots\ldots\ldots\ldots\ldots\ldots \quad (10.5)$$

where m is the mass of the ion, v is its velocity, r is the radius of curvature of the ion path in the magnetic field B, and finally

e is the ion's charge. Since $E = \frac{1}{2}mv^2$, therefore the relation for obtaining the magnetic field with respect to the kinetic energy of the ion (E), by a simple modification to the relation 10.5, it gives:

$$B = \frac{(2mE)^{\frac{1}{2}}}{re} \quad \ldots\ldots\ldots\ldots\ldots\ldots\ldots\ldots\ldots\ldots \quad (10.6)$$

As an example for deflecting the ^{3}He-particle of an energy of 1.0 MeV, and the radius of curvature of 30cm, the required magnetic field will be as below:

$$B = \frac{(2mE)^{\frac{1}{2}}}{re} = \frac{(2 \times 3 \times 1.67 \times 10^{-27} \times 1 \times 1.6 \times 10^{-13})^{\frac{1}{2}}}{0.3 \times 2 \times 1.6 \times 10^{-19}} = 0.48 \text{ tesla}$$

where recalling that 1 MeV = 1.6×10^{-13} Joules, $m_{^3He} = 3 \times 1.67 \times 10^{-27}$ Kg. and the charge of the ^{3}He-particle is $2 \times 1.6 \times 10^{-19}$ coulombs. (All units are given in M.K.S. system).

Therefore a magnetic field of 0.48 tesla (4.8×10^3 gauss) is needed. The pole-face gap is assumed to be 8.0cm., then the ampere turns (Ni) given by the following equation can be calculated:

$$Ni = \frac{Bg}{\mu} \quad \ldots\ldots\ldots\ldots\ldots\ldots\ldots\ldots\ldots\ldots \quad (10.7)$$

where g is the pole-face gap, and μ is a constant ($\mu = 4\pi \times 10^{-7}$). To achieve a magnetic field of 0.48 tesla with a gap of 8.0 cm. the ampere turn required is:

$$Ni = \frac{0.48 \times 8 \times 10^{-2}}{4\pi \times 10^{-7}} = 3 \times 10^4 \text{ amp-turns.}$$

The power dissipated in the magnet coils is given by:

$$P = Ni\ \rho\ \ell\ J \quad \ldots\ldots\ldots\ldots\ldots\ldots\ldots\ldots\ldots\ldots \quad (10.8)$$

where Ni is the ampere turns, ρ is the resistivity of the winding copper wire, ℓ is the length of the average turn, and finally J is the

current density. Considering a surface area of the pole tip of 60 square inches, and a winding depth of 6.0 inches, therefore the perimeter of inner turn will be $\left(\frac{60}{\pi}\right)^{\frac{1}{2}} \times 2\pi \simeq 27$ inches, and since the thickness of winding is 6.0 inches, then the perimeter of average turn (Pm) or ℓ will be :

$$Pm = \ell = \left(6 + \frac{\left(\frac{60}{\pi}\right)^{\frac{1}{2}}}{2}\right) \times 2\pi \simeq 50" = 127 \text{ cm.}$$

The value of current density (J) is 50 amps/$_{cm^2}$ (104), and resistivity of copper (64), $\rho_{cu} = 1.7 \times 10^{-6}$ Ω cm. So that the power dissipation is:

$$P = Ni\ \rho\ \ell\ J = 3 \times 10^{4} \times 1.7 \times 10^{-6} \times 127 \times 50 \simeq 324 \text{ watts.}$$

In the case of using 100 volts power supply, the current will be:

$$I = \frac{P}{V} = \frac{324}{100} = 3.24 \text{ amperes}$$

Now to find out the wire size, from the definition of current density:

$$J = \frac{I}{\pi r^2} \quad \ldots\ldots\ldots\ldots\ldots\ldots\ldots\ldots\ldots\ldots \quad (10.9)$$

Therefore, $r = \left(\frac{I}{J\pi}\right)^{\frac{1}{2}} = \left(\frac{3.24}{50\pi}\right)^{\frac{1}{2}} = 0.14\text{cm.} = 1.4\text{mm.}$

The temperature rise of the winding wires can be calculated from the following relation. (107)

$$\theta_f = \frac{RI^2}{2khPm} \quad \ldots\ldots\ldots\ldots\ldots\ldots\ldots\ldots\ldots\ldots \quad (10.10)$$

where RI^2 is the power dissipation, k is the heat dissipation coefficient ($k_{cu} \simeq 7 \times 10^{-3}$ watts/^{o}C x sq.inch). P_m is measured before, and finally h is the length of each coil. In this measurement two coils each of 15 inches long were assumed.

As a result, the temperature rise (θ_f) will be

$$\theta_f = \frac{324}{2 \times 7 \times 10^{-3} \times 30" \times 50"} = 15.4^{o}C.$$

In designing the pole pieces to satisfy the focus parameters, it should be assumed that the fringing field at the field boundary of a pole section extended a perpendicular distance equal to the pole separation; this has been shown to be a typical estimate for geometrically simple pole boundary.(105)

The electromagnet design can be simplified by seeking for an existing 7" diameter type E electromagnet manufactured by the Newport Instruments Ltd.

The 7" diameter type E electromagnet is shown in figure 10.1.

Since the path of the ions in the magnetic field must be evacuated, therefore a part of the vacuum box connected to the vacuum chamber could be a part of the flux path.

10.5 Radius of Curvature of the charged particles in the magnetic field.

Since the aim of the present work is to discriminate between ^{3}He-particles from other charged particles such as elastically scattered deuterons and tritons, etc., the radius of curvature of the charged particles concerned should be calculated in the magnetic analyser. The formula which can be used is already given in equation 10.6 which is $r = \frac{(2mE)^{\frac{1}{2}}}{Be}$ where m and E are the mass and the energy of the charged particle respectively, and B is the magnetic field, and finally e is the particle's electric charge. As an example, the calculation of r for the ^{3}He-particle of energy 2.2 MeV in a magnetic field of B = 1.0 tesla is given below:

$$r = \frac{(2mE)^{\frac{1}{2}}}{Be} = \frac{(2 \times 3 \times 1.67 \times 10^{-27} \times 2.2 \times 1.6 \times 10^{-13})^{\frac{1}{2}}}{1 \times 2 \times 1.6 \times 10^{-19}} \simeq 0.18m$$

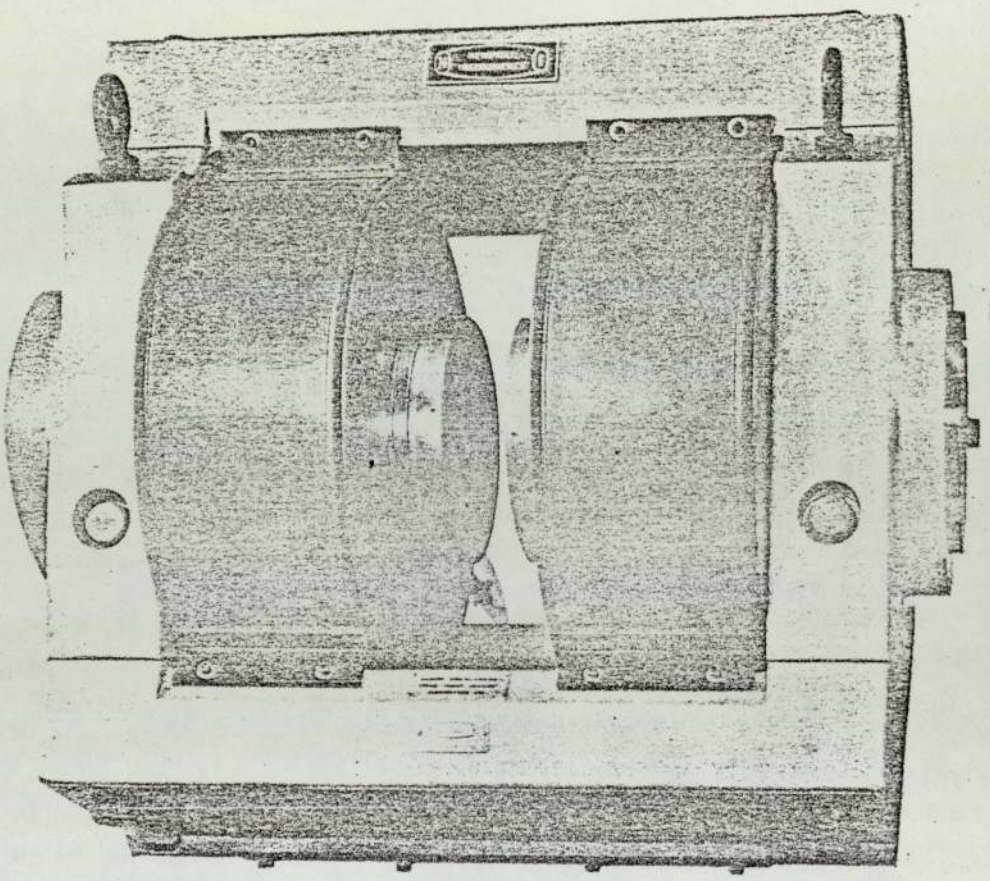

Figure 10.1. The 7" diameter type E electromagnet.

where $m_{^3He} = 3 \times 1.67 \times 10^{-27}$kg, $E_{^3He} = 2.2 \times 1.6 \times 10^{-13}$J, and $e = 2 \times 1.6 \times 10^{-19}$ Coulomb.

The r-values in table (9.2) have been calculated from the above formula.

10.6 The ^{3}He-particle detector.

In using the associated particle method with the D-d reaction, the pulse spectrum of the ^{3}He-detector must give a peak for the ^{3}He-particles, well resolved from the noise and scattered deuteron signal and also that from the protons and tritons resulting from the competing D(d,p)t reaction. The two types of detectors mostly used are the thin plastic scintillator (NE102A), and the surface barrier detector.

In the case of plastic scintillator, care must be taken with the mounting of the thin sheet of plastic on the front surface of the photomultiplier tube in order to obtain a good optical contact. In addition, the energy resolution is not adequate to detect the low energy ^{3}He-particles.

A surface barrier detector is to be preferred, because it gives pulses whose heights are proportional to the energy lost by the particles in the detector, independently of the kind of particles. Furthermore, it has a good and constant energy resolution, therefore the ^{3}He-peak can be resolved from the scattered deuteron peak, provided the numbers of deuterons are not so high that pile up in the electronic circuit occurs.

The ^{3}He-particles spectra for various incident deuteron engergies by using a 150mm surface barrier detector with energy resolution of 60 KeV and a magnetic analyser for the separation of scattered deuterons and other charged particles from the ^{3}He-recoil particles reported by Bartle et al.[90] are shown in fig.10.2.

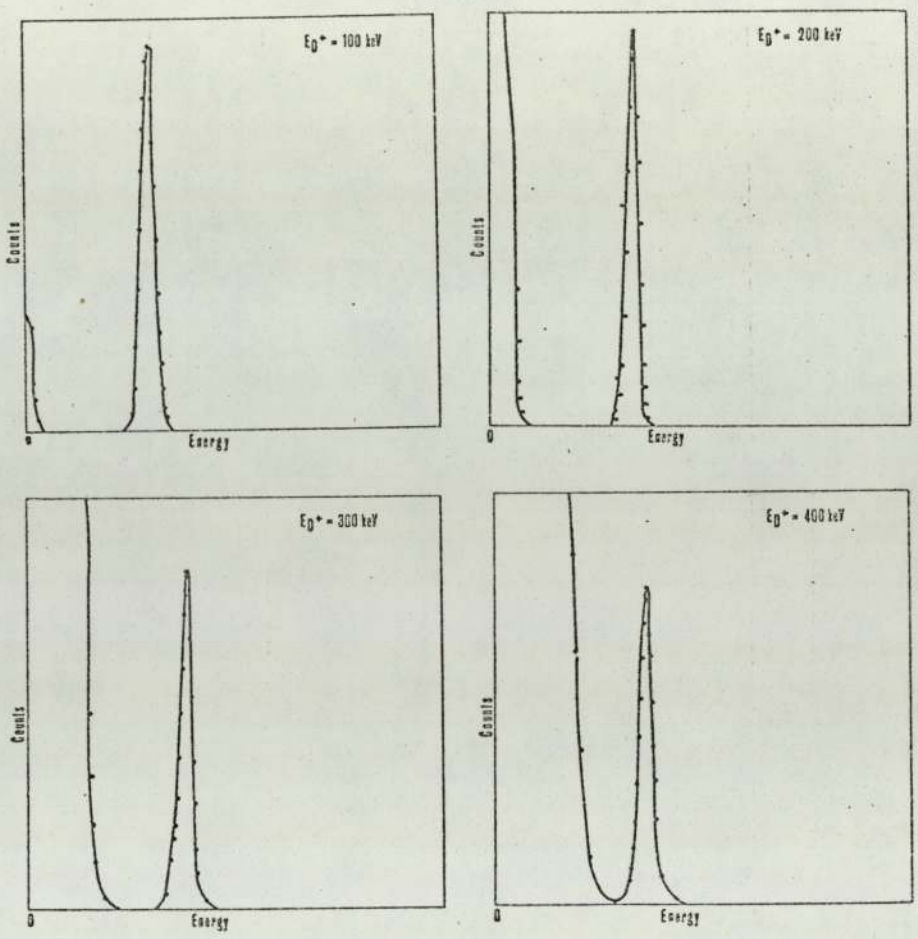

Figure 10.2. The ^{3}He-particle spectra for various incident deuteron energy.(90)

The protons and tritons from the competing reaction are not a serious problem. Because of the higher Q-value in the $D(d,p)^3H$ reaction relative to the $D(d,n)^3He$ reaction the proton and triton energies are larger than the ^3He-particle's energy.

A typical spectrum of the charged particle reaction products from the D-d reaction reported by Bartle et al[90] is shown in figure 10.3 .

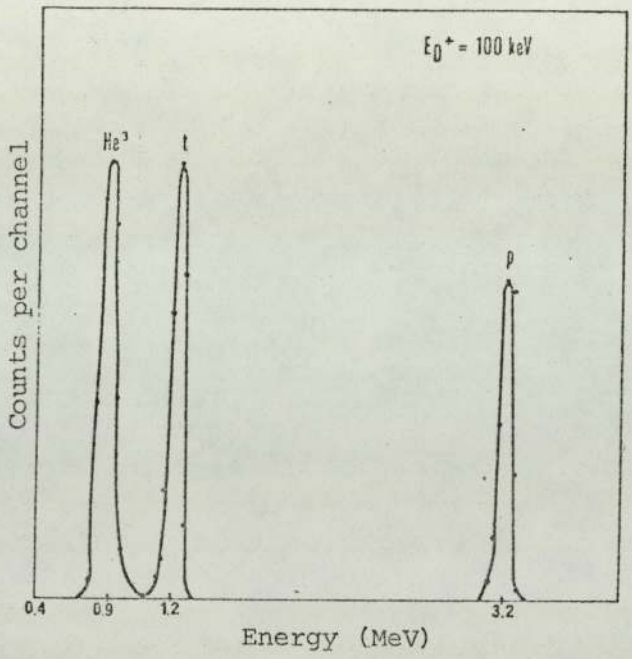

Figure 10.3. A typical pulse-height spectrum for charged particles from the D-d reaction. (90)

10.7 The experimental arrangement

In figure 10.4 a typical experimental arrangement designed for use with Dynamitron is shown. The heavy ice copper drum target and the magnetic analyser can be seen in this figure. As mentioned in the previous section, in order to prevent the elastically scattered deuterons originating at the target from reaching the ^{3}He-detector, and swamping the electronics with high deuteron counts, it is necessary to use a magnetic analyser to transmit the desired ^{3}He-particles and reject most of the scattered deuterons, and other charged particles, i.e. the protons and tritons.

10.8 The electronics circuitry

A block diagram of the electronics circuitry for use with the dynamitron accelerator is shown in figure 10.5, and is very similar to that used for the 14 MeV neutron scattering work described in Chapter 4, except for the change in recoil charged-particle detector.

The ^{3}He-detector described in section 10.6 is a silicon surface barrier detector. The detail of the properties of the surface barrier detector is reported by Goulding and Hansen.[106] The signals from the ^{3}He-detector should be amplified in a charge-sensitive amplifier, because the output pulses of the detector are charged-pulses.

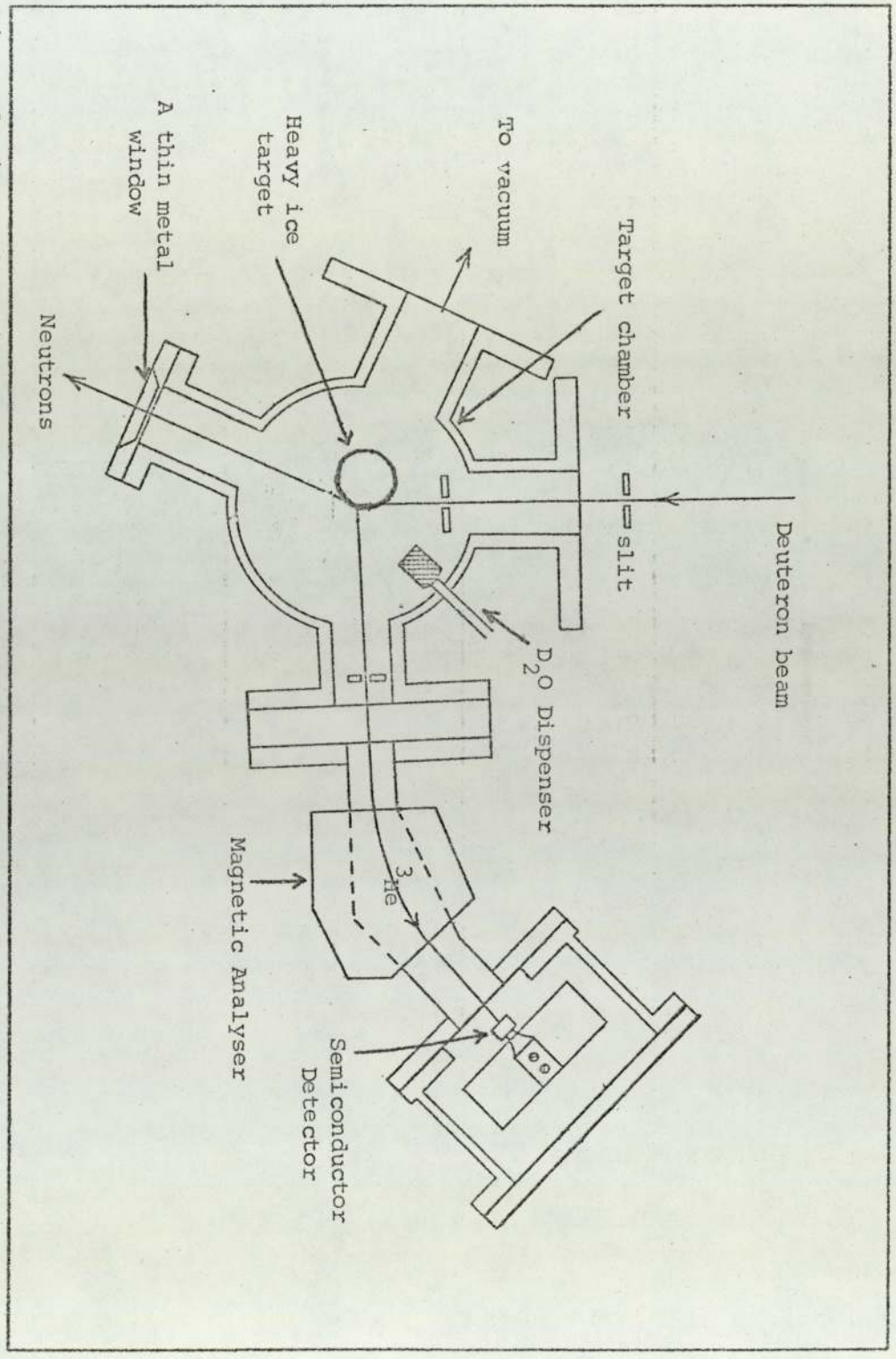

Figure 10.4 A schematic arrangement of a target chamber, heavy ice target, magnetic analyser and ^3He-detector.

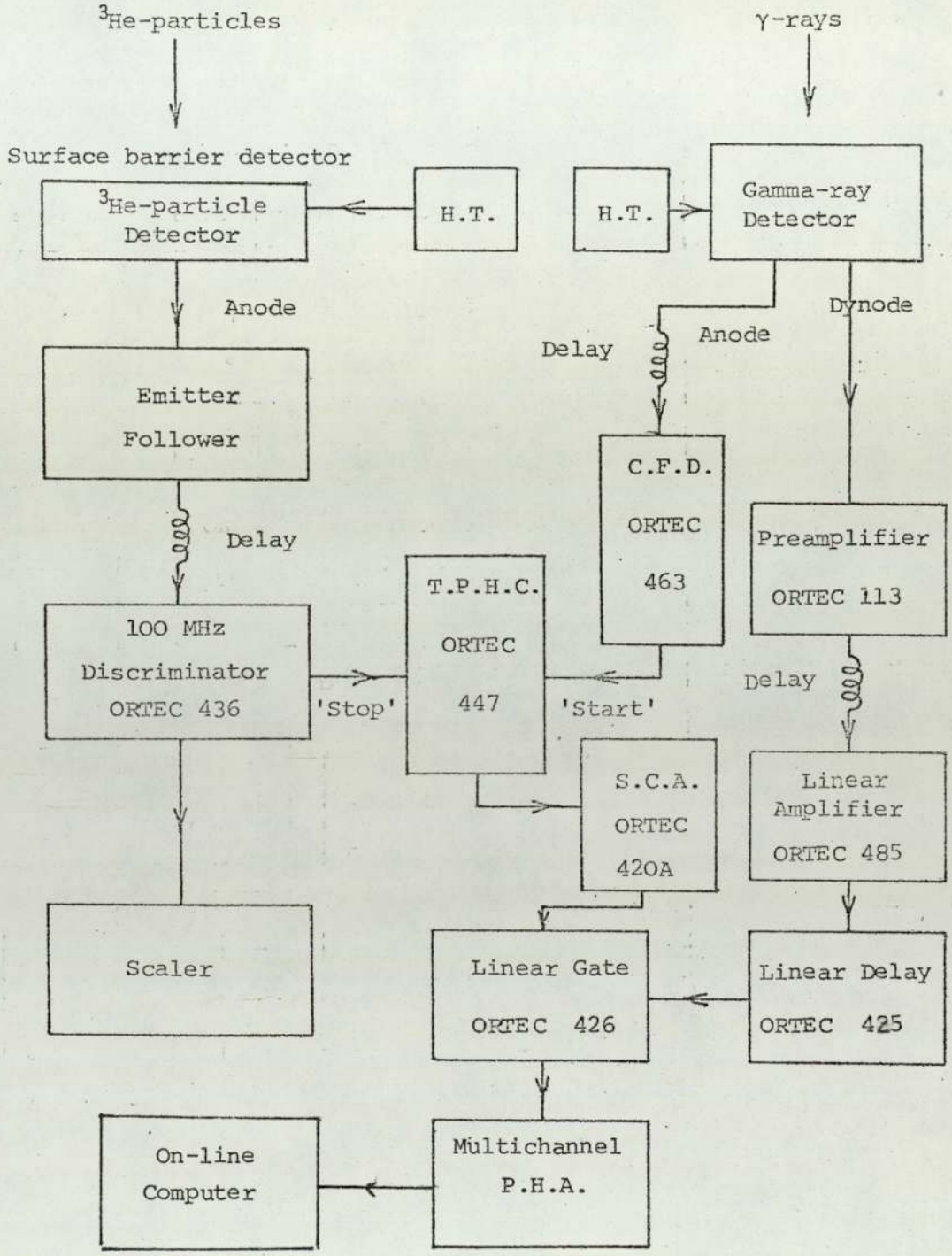

Figure 10.5 A block diagram of the Associated Particle time of flight system for γ-ray energy accumulation using the source neutron from the D(d,n)^{3}He reaction.

Chapter 11

11. Conclusions to Part II

The study of the scattering of nuclear particles by nuclei can give much information about interaction between nuclei and incident particles and about the properties of nuclei and their excited states, etc. The experiments require to measure the energy distribution and angular distribution of the scattered particles and the radiations following the scattering process. Nearly all neutron scattering experiments are hampered by the large spurious background caused by scattered neutrons and γ-rays not originating from the scatterer. Hence, much shielding material has to be used, but such a large amount of the material in the neighbourhood of scatterer or detector causes more background due to processes within this shield. Part II of this thesis has investigated the possibility of inelastic neutron scattering experiments using the $D(d,n)^3He$ reaction on the Dynamitron facility at Radiation Centre, University of Birmingham. It has been shown that background reduction can be achieved by using an associated particle method.

Curtis[109], et al. first used this method at a deuteron energy of 10 MeV.

In most other experiments the neutron intensity was low due to the small cross-section for the D-d reaction at low deuteron energy. The use of Ni-foils for the separation of the gas target from the vacuum system in the experiment by Franzen, et al.[110] involves rather low values for the deuteron current and consequently a low intensity of the neutron beam.

As to the discrimination between ^3He-particles and scattered deuterons several methods can be used. Franzen, et al. chose an

angle of 90° between the direction of the ^{3}He-particles and the deuteron beam since with a gas target no deuterons can be scattered over an angle larger than 90°. In some experiments at low deuteron energies metal-foils in front of the ^{3}He-detector were used, but for higher values of deuteron energies discrimination is hardly possible.

In the investigation studies of neutron beam production with the D(d,n)^{3}He reaction and a 3 MeV deuteron bombarding energy, the major limitation for a sufficient flux of neutrons is an inadequate deuterium target. The main problem is the need for a target backing, either to maintain a liquid nitrogen heavy ice target or to support some heavy metal that contained interstitial deuterium. The second possibility was ruled out because the available thickness of the deuterium target is severely limited by the large energy loss of ^{3}He-recoil particles in heavy elements.

A gas target was not considered because it would necessarily have either a thin foil window which would degrade the ^{3}He-particle's energy or a large volume of deuterium gas between the reaction point and the detector for the particles to traverse. Liquid nitrogen cooled copper drum was satisfactory as a target backing for heavy ice at low beam current.

For the discimination of ^{3}He-particles and scattered deuterons at high incident deuteron energies a magnetic analyser must be used, and in order to obtain intense neutron beams and a tolerable level of scattered deuterons it is possible to use a thin heavy ice target. A rotating copper drum heavy ice target would have to be utilized to permit an increase in target current without deteriorating the target.

Chapter 12

12. General Conclusions

The first part of the research project was devoted to the use of Associated Particle time-of-flight technique and using the 14.0 MeV neutrons from the $T(d,n)^4He$ reaction with the 120 Kev deuteron beam from the S.A.M.E.S. type J accelerator.

The aim of the study was the measurements of the γ-ray energy spectra and γ-ray angular distribution with small and large samples of iron and lithium fluoride to investigate the effect of multiple scattering on large samples. To predict the energy spectra measurements in large samples, a Monte Carlo approach computer programme was used, and the predictions of this were compared with the experimental data and a good agreement between theory and experiment was achieved. Also, in the study of the γ-rays following the inelastic scattering of 14.0 MeV neutrons with the large samples, the measurements were concerned with the energy and angular distribution and this is of obvious importance to the fusion reactor programme. The differential γ-ray production cross-sections and angular distributions obtained from small samples were in a good agreement with those measured by other workers but in the case of large samples no other references could be found in literature concerning this type of measurement.

The second part of the research project was to design and investigate the possibility of using Dynamitron accelerator with application of $D(d,n)^3He$ reaction and the associated particle technique for the measurement of γ-ray angular distributions. The electronic system for this work was investigated.

The magnetic analyser design and the performance of a heavy ice target were completed. There was found to be no reason why this type of experiment should not be successfully carried out

using the 3 MeV deuteron beam from the Dynamitron accelerator at the Radiation Centre, University of Birmingham. The study of the γ-ray angular distribution from the d-D reaction for incident neutron energies in the range of 2 to 5 MeV is important for reactor shielding from a practical point of view.

APPENDIX A

```
STATEMENT NO.
        0           'BEGIN'
        1       'COMMENT'ENERGY'AND'ANGLE'OF'EMISSION'OF'NEUTRON'AND'MEAN'IN
        1       D(D,N)HE3'REACTION'AND'ANISOTROPY'FACTORS;
        1       'REAL' M1,M2,M3,M4,Q,B3,B4,E1,C,ANG,W,F,D3,E3,A3,E33,ANG4,D4,E4,A4,Z;
        2           NEXT:
        2           M1:=READ;
        3           'IF'M1<0'THEN''GOTO'FINISH;
        4           M2:=READ;
        5           M3:=READ;
        6           M4:=READ;
        7           Q:=READ;
        8           NEWLINE(3);
        9           PRINT(M1,2,4);
       10       WRITETEXT('('+1')');
       11           PRINT(M2,2,4);
       12       WRITETEXT('('+1')');
       13       WRITETEXT('('=')');
       14           PRINT(M3,2,4);
       15       WRITETEXT('('+1')');
       16           PRINT(M4,2,4);
       17           PRINT(Q,2,3); WRITETEXT('('MEV')');
       19           B3:=M1*M3/((M1+M2)*(M1+M2));
       20           B4:=M1*M4/((M1+M2)*(M1+M2));
       21           AGAIN:
       21           E1:=READ; 'IF'E1<0'THEN''GOTO'NEXT;
       23           C:=(E1*M2/(M1+M2)+Q)/(M3+M4);
       24           NEWLINE(2);
       25           WRITETEXT('('INCIDENT'ENERGY='')');
       26           PRINT(E1,2,4); WRITETEXT('('MEV')');
       28           NEWLINE(1);
       29           WRITETEXT('('ANISTROPY'ENERGY'ANGLE'ENERGY'ANISTROPY'
       29           ENERGY'ANGLE')');
       30       'FOR'ANG:=0'STEP'10'UNTIL'180'DO'
       30           'BEGIN'
       31           W:=ANG/57.296;
       32           F:=E1*SIN(W);
       33           F:=F*F;
       34           D3:=E1*C*M4/B3-F;
       35           'IF'D3'LE'0'THEN'
       35           'BEGIN'
       36           E3:=0;
       37           A3:=0;
       38       E33:=0;
       39           ANG4:=0;
       40           'GOTO'PASS1;
       41           'END';
       42           E3:=C*M4+E1*B3*COS(2*W)+2*B3*SQRT(D3)*COS(W);
       43           A3:=SQRT(E3/(C*M4))/(1-M1/(M1+M2)*SQRT(E1*M3/(E3*M1)))*COS(W));
       44       E33:=M4*E3-E3;
       45       Z1=SQRT(M1*E1/(M4*E33))-SQRT(M3*E3/(M4*E33))*COS(W);
       46           'IF'Z>0.999999'THEN'
       46           'BEGIN'ANG4:=0; 'GOTO'PASS1; 'END';
       50           'IF'ABS(Z)<0.0001'THEN'
       50           'BEGIN'ANG4:=90; 'GOTO'PASS1;'END';
       54           'IF'Z<-0.999999'THEN'
       54       'BEGIN'ANG4:=180;  'GOTO'PASS1; 'END';
       58           Z1:=ARCTAN(SQRT(1-Z*Z)/Z);
       59           ANG4:=90-(1-SIGN(Z))*57.296*Z;
       60           PASS1:
       60           D4:=E1*C*M3/M4-F;
       61           'IF'D4'LE'0'THEN'
       61           'BEGIN'
       62           E4:=0;
       63           A4:=0;
       64           'GOTO'PASS2;
       65           'END';
       66           E4:=C*M3+E1*F+2*COS(Z*W)+2*M4*SQRT(D4)*COS(W);
       67           A4:=SQRT(E4/(C*M3))/(1-M1/(M3+M2)*SQRT(E1*M4/(E4*M1)))*COS(W));
       68           E33:
       68           NEWLINE(1);
       69           PRINT(E4,2,4);
       70           PRINT(E4,2,4);
       71           PRINT(A4,2,4);
       72           PRINT(E3,2,4);
       73           PRINT(A3,2,4);
       74       PRINT(E33,2,4);
       75           PRINT(ANG4,3,3);
       76           'END';
       77           'GOTO'AGAIN;
       78           FINISH: 'END';
```

INCIDENT ENERGY= 2.0000 MEV

ANSTROPY4	ENERGY4	ANGLE3	ENERGY3	ANSTROPY3	ENERGY4	ANGLE4
3.3759	3.6046	0.000	3.2308	1.6386	0.0292	161.936
3.3260	3.5133	10.000	3.1865	1.6266	0.0735	121.424
3.1781	3.2516	20.000	3.0567	1.5914	0.2033	98.462
2.9376	2.8484	30.000	4.8508	1.5347	0.4092	85.282
2.6139	2.3526	40.000	4.5832	1.4596	0.6768	75.408
2.2213	1.8193	50.000	4.2714	1.3700	0.9886	67.068
1.7805	1.3090	60.000	3.9345	1.2704	1.3255	59.627
1.3228	0.8716	70.000	3.5905	1.1658	1.6695	52.816
0.8939	0.5399	80.000	3.2554	1.0609	2.0046	46.504
0.5467	0.3191	90.000	2.9419	0.9600	2.3181	40.618
0.3122	0.1886	100.000	2.6585	0.8664	2.6015	35.109
0.1772	0.1168	110.000	2.4104	0.7827	2.8496	29.938
0.1058	0.0778	120.000	2.1997	0.7103	3.0603	25.068
0.0683	0.0559	130.000	2.0262	0.6498	3.2338	20.457
0.0481	0.0435	140.000	1.8883	0.6014	3.3717	16.063
0.0369	0.0357	150.000	1.7842	0.5645	3.4758	11.836
0.0306	0.0313	160.000	1.7115	0.5386	3.5485	7.714
0.0274	0.0290	170.000	1.6687	0.5233	3.5913	3.646
0.0264	0.0284	180.000	1.6545	0.5183	3.6055	0.000

TABLE A.1

INCIDENT ENERGY= 2.5000 MEV

ANSTROPY4	ENERGY4	ANGLE3	ENERGY3	ANSTROPY3	ENERGY4	ANGLE4
3.6477	4.1233	0.000	5.7497	1.7013	0.0103	158.609
3.5927	4.0101	10.000	5.6967	1.6880	0.0633	105.505
3.4296	3.6843	20.000	5.5419	1.6488	0.2181	88.433
3.1638	3.1847	30.000	5.2968	1.5858	0.4632	78.178
2.8041	2.5711	40.000	4.9793	1.5024	0.7807	69.907
2.3638	1.9160	50.000	4.6111	1.4030	1.1489	62.565
1.8618	1.2957	60.000	4.2153	1.2930	1.5447	55.809
1.3278	0.7784	70.000	3.8140	1.1777	1.9460	49.507
0.8162	0.4096	80.000	3.4263	1.0627	2.3337	43.602
0.4149	0.1945	90.000	3.0666	0.9526	2.6934	38.063
0.1842	0.0924	100.000	2.7447	0.8513	3.0153	32.867
0.0829	0.0486	110.000	2.4657	0.7614	3.2943	27.990
0.0420	0.0296	120.000	2.2310	0.6843	3.5290	23.402
0.0244	0.0198	130.000	2.0395	0.6206	3.7205	19.069
0.0161	0.0147	140.000	1.8886	0.5698	3.8714	14.950
0.0118	0.0119	150.000	1.7754	0.5315	3.9846	10.996
0.0096	0.0103	160.000	1.6960	0.5048	4.0651	7.142
0.0085	0.0094	170.000	1.6508	0.4891	4.1092	3.224
0.0081	0.0092	180.000	1.6356	0.4840	4.1244	0.000

TABLE A.2

INCIDENT ENERGY= 3.0000 MEV

ANSTROPY4	ENERGY4	ANGLE3	ENERGY3	ANSTROPY3	ENERGY4	ANGLE4
3.8817	4.6510	0.000	6.2576	1.7543	0.0024	129.271
3.8228	4.4956	10.000	6.1961	1.7399	0.0659	90.511
3.6478	4.1054	20.000	6.0166	1.6973	0.2434	80.382
3.3622	3.5077	30.000	5.7350	1.6288	0.5270	72.670
2.9748	2.7743	40.000	5.3666	1.5384	0.8934	65.688
2.4976	1.9936	50.000	4.9431	1.4307	1.3169	59.122
1.9464	1.2592	60.000	4.4900	1.3116	1.7700	52.889
1.3425	0.6581	70.000	4.0353	1.1873	2.2267	46.973
0.7283	0.2564	80.000	3.5949	1.0636	2.6651	41.374
0.2423	0.0700	90.000	3.1914	0.9459	3.0686	36.097
0.0543	0.0191	100.000	2.8351	0.8382	3.4269	31.137
0.0152	0.0075	110.000	2.5252	0.7433	3.7348	26.483
0.0060	0.0039	120.000	2.2683	0.6626	3.9917	22.112
0.0031	0.0025	130.000	2.0604	0.5964	4.1996	17.995
0.0019	0.0018	140.000	1.8978	0.5440	4.3622	14.086
0.0013	0.0014	150.000	1.7765	0.5047	4.4835	10.343
0.0011	0.0012	160.000	1.6928	0.4775	4.5672	6.696
0.0009	0.0011	170.000	1.6457	0.4616	4.6163	2.969
0.0009	0.0011	180.000	1.6276	0.4563	4.6324	0.000

TABLE A.3

APPENDIX B

```
STATEMENT NO.
 0          'BEGIN'
 1          'COMMENT'COMPTON%SCATTERING,%AND%RECOIL%ELECTRON%ENERGIES;
 1          'REAL'EC,ES,EG,ANG,W;
 2          AGAIN:
 2          EG:=READ;
 3          NEWLINE(2);
 4          WRITETEXT('('INCIDENT%GAMMA-RAY%ENERGY='')');
 5          PRINT(EG,2,3);
 6          WRITETEXT('('MEV')');
 7          NEWLINE(2);
 8          WRITETEXT('('ES')');
 9          SPACE(8);
10          WRITETEXT('('EC')');
11          SPACE(8);
12          WRITETEXT('('ANG')');
13          NEWLINE(2);
14          'FOR'ANG:=0.0'STEP'10'UNTIL'180'DO'
14          'BEGIN'
15          W:=ANG/57.3;
16          ES:=EG/(1+((EG/0.5)*(1-COS(W))));
17          EC:=(EG*(EG/0.5)*(1-COS(W)))/(1+((EG/0.51)*(1-COS(W))));
18          NEWLINE(2);
19          PRINT(ES,2,5);
20          PRINT(EC,2,5);
21          PRINT(ANG,2,3);
22          'END';
23          'GOTO'AGAIN;
24          'END';
```

INCIDENT GAMMA-RAY ENERGY= 0.480 MEV		
ES	EC	ANG
0.480	0.000	0.000
0.473	0.007	10.000
0.454	0.026	20.000
0.425	0.055	30.000
0.392	0.088	40.000
0.357	0.123	50.000
0.324	0.157	60.000
0.294	0.187	70.000
0.268	0.214	80.000
0.245	0.237	90.000
0.226	0.257	100.000
0.210	0.273	110.000
0.197	0.287	120.000
0.186	0.297	130.000
0.178	0.306	140.000
0.172	0.312	150.000
0.168	0.316	160.000
0.165	0.319	170.000
0.164	0.320	180.000

Table B.1

INCIDENT GAMMA-RAY ENERGY= 0.840 MEV		
ES	EC	ANG
0.840	0.000	0.000
0.819	0.021	10.000
0.763	0.077	20.000
0.686	0.155	30.000
0.603	0.238	40.000
0.525	0.317	50.000
0.457	0.387	60.000
0.399	0.446	70.000
0.352	0.494	80.000
0.313	0.533	90.000
0.283	0.565	100.000
0.258	0.590	110.000
0.239	0.610	120.000
0.223	0.626	130.000
0.212	0.638	140.000
0.203	0.646	150.000
0.197	0.653	160.000
0.194	0.656	170.000
0.193	0.657	180.000

Table B.2

APPENDIX C

```
STATEMENT NO.
        0       'BEGIN'
        1       'COMMENT'MULTIPLE%SCATTERING%OF%NEUTRONS%IN%EXTENDED%SAMPLES
        1       AND%GAMMA-RAY%YIELD%FOLLOWING%THE%INELASTIC%SCATTERING
        1       OF%NEUTRONS%AS%A%FUNCTION%OF%SCATTERING%ANGLES;
        1       'REAL'MI,MT,ME,MR,Q,A,B,C,D,F,ANG,W,ER,EE,EI,P,X,M,EL;
        2       'REAL'W3,EG3;
        3       'REAL'NA1,NA2,NA3,YTA1,NB0,NB1,NB2,YB0,YB1,YB2,YTB1;
        4       'REAL'NC0,NC1,YC0,YC1,YTC1,ND0,YD0,YTD1;
        5       'REAL'ND1,YA1;
        6       'REAL'NA4,NA5,NA6,YD1,YA5,YA6,YTA2,NB3;
        7       'REAL'NB4,NB5,YB3,YTB2,NC2,NC3,YTC2,YTD2;
        8       'REAL'NBA,NBB,NBD,DGIT,SIGMA1,SIGMA2,SIGMA3;
        9       'REAL'SIGMAT,NBL,YA,YB,YC;
       10       'REAL'W1,W2,X1,EG1,EG2;
       11       'REAL'ANG1,ANG2;
       12       'REAL'Z1,Z2,Z3;
       13       'REAL'SIGINE;
       14       'REAL'Y0,Y0;
       15       'REAL'YA3,YC4;
       16       'REAL'YB3,YC3,YA4,YB4;
       17       'REAL'YA2,YC2;
       18       'REAL'EG;
       19       'REAL'E0;
       20       'INTEGER'N,I;
       21       MI:=READ;
       22       MT:=READ;
       23       ME:=READ;
       24       MR:=READ;
       25       Q:=READ;
       26       M:=READ;
       27       SIGMAT:=READ;
       28       EU:=READ;
       29       NI:=READ;
       30       NU:=READ;
       31       Z1:=READ;
       32       Z2:=READ;
       33       Z3:=READ;
       34       NEWLINE(2);
       35       PRINT(MI,2,2);
       36       WRITETEXT('('+')');
       37       PRINT(MT,2,2);
       38       WRITETEXT('('=')');
       39       PRINT(ME,2,2);
       40       WRITETEXT('('+')');
       41       PRINT(MR,2,2);
       42       WRITETEXT('('+')');
       43       PRINT(Q,2,3);
       44       WRITETEXT('('MEV')');
       45       NEWLINE(2);
       46       WRITETEXT('('EG1')');
       47       SPACE(2);
       48       WRITETEXT('('EG2')');
       49       SPACE(2);
       50       WRITETEXT('('EG3')');
       51       SPACE(2);
       52       WRITETEXT('('EG')');
```

```
53          SPACE(8);
54          WRITETEXT('('YN')');
55          SPACE(8);
56          WRITETEXT('('ANG')');
57          NEWLINE(2);
58          A1:=(2.0*MI+ME)/((MB+MF)*(MR+ME));
59          AGAIN:
59          'FOR'I:=1'STEP'1'UNTIL'N'DO'
59          'BEGIN'
60          EI:=READ;
61          SIGMA1:=READ;
62          SIGMA2:=READ;
63          SIGMA3:=READ;
64          SIGINE:=READ;
65          XI:=READ;
66          CI:=((NB+MI)*EI+Q*MR)/(MR+ME);
67          NEWLINE(2);
68          'FOR'ANG:=0'STEP'10'UNTIL'80'DO'
68          'BEGIN'
69          W1:=ANG/57.296;
70          B1:=COS(W);
71          P1:=B*B;
72          'FOR'X1:=0'STEP'1'UNTIL'3'DO'
72          'BEGIN'
73          W1:=ARCTAN(80/Z1*X1);
74          W2:=ARCTAN(80/Z2*X1);
75          W3:=ARCTAN(80/Z3*X1);
76          EB1:=E0/(1+((E0/0.51)*(1-COS(W))));
77          EW1:=E0/(1+((E0/0.51)*(1-COS(W1))));
78          EW2:=E0/(1+((E0/0.51)*(1-COS(W2))));
79          EW3:=E0/(1+((E0/0.51)*(1-COS(W3))));
80          D1:=(2.0*SQRT(MI*ME*EI))/(MR+ME);
81          F1:=A*EI*P+C;
82          EE:=A*EI*P+C+D*B*SQRT(E);
83          NRA:=1-EXP(-SIGMA1);
84          NRB:=(NRA/4)*(1-(1-EXP(-SIGMA2)));
85          NRC:=(NRA/4)*(1-(1-EXP(-SIGMA2)));
86          NRD:=(NRA/4+EXP(-SIGMA1))*(1-(1-EXP(-SIGMA2)));
87          NB0:=NRA;
88          NB1:=NRF;
89          NB2:=(NRA/4)*(1/4)*(1-EXP(-SIGMA2))*(1-(1-EXP(-SIGMA3)));
90          NC2:=(NRA/4)*(1-(1-EXP(-SIGMA2)));
91          NC3:=(NRA/4)*(1/4)*(1-EXP(-SIGMA2))*(1-(1-EXP(-SIGMA3)));
92          ND1:=(NRA/4+EXP(-SIGMA1))*(1/4)*(1-EXP(-SIGMA2))*(1-(1-EXP(-SIGMA3)));
93          NA4:=1-EXP(-SIGMA1);
94          NA5:=(NRA/4)*(1-(1-EXP(-SIGMA2)));
95          NA6:=(NRA/4)*(1/4)*(1-EXP(-SIGMA2))*(1-(1-EXP(-SIGMA3)));
96          NB3:=1-EXP(-SIGMA1);
97          NB4:=(NRA/4)*(1-(1-EXP(-SIGMA2)));
98          NB5:=(NRA/4)*(1/4)*(1-EXP(-SIGMA2))*(1-(1-EXP(-SIGMA3)));
99          NC0:=(NRA/4)*(1-(1-EXP(-SIGMA2)));
100         NC1:=(NRA/4)*(1/4)*(1-EXP(-SIGMA2))*(1-(1-EXP(-SIGMA3)));
101         ND0:=(NRA/4)*EXP(-SIGMA1)*(1/4)*(1-EXP(-SIGMA2))*(1-EXP(-SIGMA3));
102         YA:=NRA*(1-EXP(-M*(X-1)/COS(W3)))*(SIGINE/SIGMAT)*N0;
103         YB:=NRB*(1-EXP(-M*(X-1)/COS(W3)))*(SIGINE/SIGMAT)*N0;
104         YC:=NRC*(1-EXP(-M*(X-1)/COS(W3)))*(SIGINE/SIGMAT)*N0;
105         YA3:=NDA*(1-EXP(-M*(X-1)/COS(W1)))*(SIGINE/SIGMAT)*N0;
106         YB3:=NDF*(1-EXP(-M*(X-1)/COS(W1)))*(SIGINE/SIGMAT)*N0;
107         YC3:=NDC*(1-EXP(-M*(X-1)/COS(W1)))*(SIGINE/SIGMAT)*N0;
108         YA2:=N0*(1-EXP(-SIGMA1))*((1-EXP(-SIGMA2))/4)*(1-EXP(-M*(X-2)/COS(W1)))*
```

```
108         (SIGINE/SIGMAT);
109         YA4:=NO*(1-EXP(-SIGMA1))*((1-EXP(-SIGMA2))/4)*(1-EXP(-M*(X-2)/COS(W2)))*
109         (SIGINE/SIGMAT);
110         YB2:=NO*(1-EXP(-SIGMA1))*((1-EXP(-SIGMA2))/4)*((EXP(-SIGMA2))/4)*
110         (1-EXP(-M*(X-2)/COS(W1)))*(SIGINE/SIGMAT);
111         YB4:=NO*(1-EXP(-SIGMA1))*((1-EXP(-SIGMA2))/4)*((EXP(-SIGMA2))/4)*
111         (1-EXP(-M*(X-2)/COS(W2)))*(SIGINE/SIGMAT);
112         YC2:=NO*(1-EXP(-SIGMA1))*((1-EXP(-SIGMA3))/4)*((EXP(-SIGMA2))/4)*
112         (1-EXP(-M*(X-2)/COS(W1)))*(SIGINE/SIGMAT);
113         YA1:=NA1*(1-EXP(-M*(X-1)/COS(W1)))*(SIGINE/SIGMAT)*NO;
114         YA3:=NO*(1-EXP(-SIGMA1))*((1-EXP(-SIGMA3))/4)*((EXP(-SIGMA2))/4)*
114         (1-EXP(-M*(X-2)/COS(W1)))*(SIGINE/SIGMAT);
115         YB0:=NB0*(1-EXP(-SIGMA1))*((1-EXP(-SIGMA2))/4)*
115         (1-EXP(-M*(X-2)/COS(W2)))*(SIGINE/SIGMAT);
116         YB1:=NB1*(1-EXP(-M*(X-1)/COS(W1)))*(SIGINE/SIGMAT)*NO;
117         YTA1:=2*(YA1+YA2+YA3);
118         YTB1:=YB0+2*(YB1+YB2);
119         YTC1:=YC0+2*YC1;
120         YTC2:=YC2+2*YC3;
121         YTB2:=YB3+2*(YB4+YB5);
122         YTD2:=YD1;
123         YTA2:=2*(YA4+YA5+YA6);
124         YC4:=NO*(1-EXP(-SIGMA1))*((1-EXP(-SIGMA3))/4)*((EXP(-SIGMA2))/4)*
124         (1-EXP(-M*(X-2)/COS(W2)))*(SIGINE/SIGMAT);
125         YN:=YA+YB+YC+YA2+YB2+YC2+YA3+YB3+YC3+YA4+YB4+YC4
125         +YTA1+YTB1+YTC1+YTD1+YTA2+YTB2+YTC2+YTD2;
126         NEWLINE(2);
127         PRINT(EQ1,2,3);
128         PRINT(EQ2,2,3);
129         PRINT(EQ3,2,3);
130         PRINT(EQ,2,3);
131         PRINT(YN,5,3);
132         PRINT(ANG,2,3);
133         NEWLINE(2);
134         'END';
135         FINISH;
135         'END';
136         'END';
137         'END';
```

Appendix D

Least Squares fit

The differential cross-section of the γ-ray is described by an equation of the form:

$$\frac{d\sigma(\theta)}{d\Omega} = A_o + A_2 P_2(\text{Cos }\theta) + A_4 P_4(\text{Cos }\theta) \quad \ldots\ldots\ldots \text{(D-1)}$$

where $P_n(\text{Cos }\theta)$ is the Legendre Polynomial of degree n. Since the even order Legendre polynomials are functions of $\text{Cos}^2\theta$, it is possible to express equation (D-1) as a power series in $\text{Cos}^2\theta$, that is:

$$\frac{d\sigma(\theta)}{d\Omega} = a_o + a_2 \text{Cos}^2\theta + a_4 \text{Cos}^4\theta \quad \ldots\ldots\ldots\ldots \text{(D-2)}$$

where a_o, a_2 and a_4 are new constants.

In order to fit a curve to differential cross-section measurements it is assumed that an experimental error exists only in the values of differential cross-sections, and there is not any error in the values of scattering angle θ.

Now let $y_i = \frac{d\sigma(\theta)}{d\Omega}$ and $x_i = \text{Cos }\theta$, and in this case the coefficients of the polynomial by using the least squares principles, i.e. minimizing the relation $\sum_{i=1}^{n} \left[y_i - (a_o + a_2 x_i^2 + a_4 x_i^4) \right]^2$ for the n data point could be found.

Differentiating the above relation partially with respect to a_o, a_2 and a_4, and letting the partial derivatives be zero, and considering b_i to be the best estimate of a_i, gives the following equations:

$$\begin{aligned} \Sigma y_i &= n b_o + b_2 \Sigma x_i^2 + b_4 \Sigma x_i^4 \\ \Sigma y_i x_i^2 &= b_o \Sigma x_i^2 + b_2 \Sigma x_i^4 + b_4 \Sigma x_i^6 \\ \Sigma y_i x_i^4 &= b_o \Sigma x_i^4 + b_2 \Sigma x_i^6 + b_4 \Sigma x_i^8 \end{aligned} \quad \ldots\ldots\ldots \text{(D-3)}$$

where in the above relations the summation, Σ extends from one to n, which n is the number of data points in each case.

The coefficients b_o, b_2 and b_4 of the polynomials of the form:

$$\frac{d\sigma(\theta)}{d\Omega} = b_o + b_2 \cos^2\theta + b_4 \cos^4\theta \quad \text{..... (D-4)}$$

fitted to the measured γ-ray angular distributions were calculated by using the equations (D-3) and these equations were solved by Cramer's rule with the aid of a desk calculator.

Error estimation in fitted curve

As mentioned already b_o, b_2 and b_4 are the even order coefficient of the fitted Legendre polynomial to the γ-ray angular distribution measurements. Hence the residuals, r_i, for different values of i can be shown by:

$$r_i = y_i - (b_o + b_2 x_i^2 + b_4 x_i^4) \quad \text{..... (D-5)}$$

The standard error, α, in the above expression can be shown by the following relation:

$$\alpha^2 = \frac{\sum_{i=1}^{n} r_i^2}{n - k} \quad \text{..... (D-6)}$$

where in this formula k is the number of calculated coefficients, b_i, and therefore k = 3. If α_i is the standard error for b_i, then the errors α_o, α_2 and α_4 is given[111] by the following relation:

$$\frac{\alpha_o^2}{\Delta_1} = \frac{\alpha_2^2}{\Delta_2} = \frac{\alpha_4^2}{\Delta_3} = \frac{\alpha^2}{\Delta} \quad \text{..... (D-7)}$$

where $\Delta_1 = \begin{vmatrix} n & \sum_1 x_i^4 & \sum_1 x_i^6 \\ \sum_1 x_i^4 & \sum_1 x_i^8 & \\ \sum_1 x_i^8 & & \end{vmatrix}$, $\Delta_2 = \begin{vmatrix} n & \sum_1 x_i^4 & \\ \sum_1 x_i^4 & \sum_1 x_i^8 & \\ & & \end{vmatrix}$,

$\Delta_3 = \begin{vmatrix} n & \sum_1 x_i^2 & \\ \sum_1 x_i^2 & \sum_1 x_i^4 & \\ & & \end{vmatrix}$ and $\Delta = \begin{vmatrix} n & \sum_1 x_i^2 & \sum_1 x_i^4 \\ \sum_1 x_i^2 & \sum_1 x_i^4 & \sum_1 x_i^6 \\ \sum_1 x_i^4 & \sum_1 x_i^6 & \sum_1 x_i^8 \end{vmatrix}$

REFERENCES

1. N. Bohr, Nature, 137 (1936) 344

2. E. Sheldon and D. M. Van Patter, Reviews of Modern Physics, 38 (1966) 143

3. R. B. Day, "Progress in Fast Neutron Physics", edited by G. Philips, J. Marion, and J. Risser, University of Chicago Press (1963)

4. R. L. Clarke and W. G. Cross, Nuclear Physics 53 (1964) 177

5. R. W. Benjamin, P. S. Buchanan and I. L. Morgan, Nuclear Physics 79 (1966) 241

6. A. Gallmann et al. Nuclear Physics 88 (1966) 654

7. P. Marmier and E. Sheldon, "Physics of nuclei and particles" Vol.II Page 1128

8. F. C. Engesser and W. E. Thomson, Journal of Nuclear Energy 21 (1967) 487

9. W. M. Deuchers and D. Dandy, Proc. Phys. Soc. 75 (1960) 855

10. P. W. Martin and D. T. Stewart, Journal of Nuclear Energy A/B 19 (1965) 447

11. B. I. Sukhanow and N. P. Tkach, Sov. Jour. Nucl. Phys. 11 (1970) 17

12. D. T. Stewart and P. W. Martin, Nuclear Physics 60 (1964) 349

13. A. J. Pointon, "Introduction to Statistical Physics" Longmans (1967)

14. Hosoe and S. Suzuki, Jour. Phys. Soc. Japan 14 (1959) 699

15. R. L. Caldwell, W. R. Mills, Jr. and J. B. Hickman, Jr., Nucl. Sci. and Eng. 8 (1960) 173

16. D. M. van Patter, N. Nath, S. M. Shafroth, S. S. Malik and M. A. Rothman, Phys. Rev. 128 (1962) 1246

17. D. O. Nellis, R. W. Benjamin, J. H. Henderson, R. L. Pewett, J. B. Ashe, I. L. Morgan and J. T. Prud'homme, Texas Nucl. Corp. Report. TID-20657 (1962)

18. I. L. Morgan, J. B. Ashe, D. O. Nellis, Texas Nucl. Corp. Report. TID-22012 (1964)

19. P. H. Stelson, R. L. Robinson, H. J. Kim, J. Rapaport and G. R. Satchler, Nuclear Physics 68 (1965) 97

20. L. Cranberg et al. Nucl. Inst. and Methods 12 (1961) 335

21. W. R. Dixon and J. H. Aitken, Nuclear Physics 24 (1961) 456

22. H. R. Wilcox, Phys.Rev. 74 (1948) 1743.

23. P. Shapiro and R. W. Higgs, Phys. Rev. 108 (1957) 760

24. D. G. Schuster, Nucl. Inst. and Methods 76 (1969) 35

25. G. R. White, U.S. Nat. Bur. Stand. Report NBS-1003 (1952)

26. G. D. Latysheve, Reviews of Modern Physics 19 (1947) 132

27. T. A. Victoreen, Jour. Appl. Phys. 20 (1949) 1141

28. G. K. O'Neill, Phys. Rev. 95 (1954) 1235

29. J. B. Marion and F. C. Young, "Nuclear Reaction Analysis", Published North-Holland, (1968)

30. W. Whaling, Handbuck der Physik, Vol.32, 193

31. K. Allenby, University of Aston in Birmingham, Ph.D. Thesis (1974)

32. W. McDonald and D. Gedcke, Nucl. Inst. and Methods 55 (1967)1

33. Present et al. Nucl. Inst. and Methods 31 (1964) 71

34. J. Benveniste and J. Zenger, UCRL - 4266 (1954)

35. S. J. Bame and J. E. Perry, Phys. Rev. 107 (1957) 1616

36. H. Argo et al. Phys. Rev. 87 (1952) 612

37. L. F. Curtiss "Introduction to Neutron Physics" (1958) D. Van Nostrand Company, INC.

38. H. M. Mann and J. L. Yntema, I.E.E.E. Trans. Nucl. Sci. NS.11 No.3 (1964) 201

39. Neutron Cross-sections, BNL-325 (1964) Supplement No.2.

40. E. P. Blizard and Lorraine S. Abbott, "Reactor Handbook" Vol.III Part B (1962) Interscience Publishers

41. S. M. Shafroth, E. N. Strait and Carpenter, Nucl. Inst. and Methods 3 (1958) 298

42 J. J. Van Loef and D. A. Lind, Phys. Rev. 101 (1956) 103

43. A. K. Gupta and N. Nath, Nucl. Inst. and Methods, 53 (1967) 352

44. R. L. Heath, Scintillation Spectrometry IDO-16880-1 (1964)

45. D. F. Covell, Anal. Chem. 31 (1959) 1785

46. R. Post and L. Schiff, Phys. Rev. 80 (1950) 1113

47 R. C. A. Photomultiplier Manual PT-61

48 B. T. Price, C. C. Horton and K. T. Spinny "Radiation Shielding" (1957) Pergamon Press.

49. O. Klein and R. C. Nishina, Z. Physik, 52 (1929) 853

50. G. T. Hunter and H. T. Richards, Phys. Rev. 76 (1949) 1445

51. J. M. Blair, et al. Phys. Rev. 74 (1948) 1599

52. H. A. Bethe and J. Ashkin "Experimental Nuclear Physics" Vol.I, Part II, edited by Segrè (1952) Wiley

53. D. E. Baynham, University of Aston in Birmingham, Ph.D. Thesis (1971)

54. L. Rosen and L. Stewart, LA-2643 (1956)

55. A. J. Duivenstijn and L. A. J. Ven verloo, "Practical Gamma Spectrometry" (1963) Cleaver-Hume Press Ltd.

56. G. E. Tripard, et al. Nucl.Inst. and Methods, 66 (1968) 261

57. R. McFadden, et al. Nucl. Inst. and Methods, 92 (1971) 563

58. D. Holland, University of Aston in Birmingham, Ph.D. Thesis (1974)

59. H. P. Morsch, T. Becker and W. Fitz, Nucl. Inst. and Methods 68 (1969) 39

60. R. Batchelor and J. H. Towle, Nuclear Physics 47 (1963) 385

61. J. K. Dickens, et al. ORNL-TM-4538 (1974)

62. K. Nyberg-Ponnet, et al. Physica Scripta 4 (1971) 165

63. K. A. Connell, University of Aston in Birmingham, Ph.D. Thesis (1972)

64. Handbook of Chemistry and Physics, 44th ed. (1963) Chemical Rubber Company.

65. M. N. Rao, Nuclear data sheets B3-3, (1970) 4-43

66. J. R. Stehn et al., BNL-325 TID-4500 Second ed.(1964)

67. C. M. Lederer, J. M. Hollander and I.Perlman, "Table of Isotopes", (1967) Wiley

68. Goldberg AFWG-TR-60-30 BNL-400 Second ed.(1962)

69. A. Stamp and J. Rook, Nuclear Physics 53 (1964) 657

70. G. C. Bonazzola, E. Chiavassa and T. Bressani, Nuclear Physics 86 (1966) 375

71. Argon National Laboratory, ANL-4515, Oct. 1950

72. H. Catron, et al. UCRL-5880, March 1960

73. M. E. Battat and F. L. Ribe, Phys.Rev. 89 (1953) 80

74. J. Benveniste et al., Nuclear Physics 38 (1962) 300

75. J. Lachkar, J. Sigaud, Y. Patin, and G. Haouat, Nucl. Sci. and Eng. 55 (1974) 168

76. U. Abbondano et al., Jour. Nucl. Energy 27 (1973) 227

77. R. B. Day, Phys. Rev. 102 (1956) 767

78. M. Walt, "Fast Neutron Physics", Vol.IV, Part II edited by J. B. Marion and J. L. Fowler, Interscience (1963)

79. J. B. Parker, J. H. Towle, D. Sams and P. G. Jones, Nucl. Inst. and Methods 14 (1961) 1

80. H. O. Lane and W. F. Miller, Nucl. Inst. and Methods 16 (1962) 1

81. J. B. Parker, J. H. Towle, D. Sams, W. B. Gilboy, A. D. Purnell and H. J. Stevens, Nucl. Inst. and Methods 30 (1964) 77

82. G. Lindström and H, Neuert, Zeit, F. Naturforsch 13a (1958) 826

83. P. B. Johnson, N. G. Chapman and J. E. Callaghan, Nuclear Physics A94 (1967) 617

84. R. A. I. Bell, N. G. Chapman and P. B. Johnson, Nucl. Inst. and Methods 33 (1965) 13

85. L. W. Put, C. Bot, W. J. Coenders, J. W. Koene and J. Blok, Physica 32 (1966) 1397

86. G. C. Neilson and D. B. James, Rev. Sci. Inst. 26 (1955) 1018.

87. V. Naggiar, L. Lafaye and P. Breance, Nucl. Inst. and Methods 41 (1966) 77

88. H. Prade and J. Csikai, Nuclear Physics A123 (1969) 365

89. R. W. Finley, "Nuclear research with low energy accelerators" (Academic Press, New York, 1967) Page 311

90. C. M. Bartle, et al. Nucl. Inst. and Methods 63 (1968) 39

91. Manley, et al. Phys. Rev. 70 (1946) 101

92. L. F. C. Monier, G. E. Tripard and B. L. White. Nucl. Inst. and Methods 45 (1966) 282

93. G. Gobert, G. S. Mani and A. Sadeghi, Nucl. Inst. and Methods 42 (1966) 250

94. C. M. Jones, J. W. Johnson and R. M. Beckers, Nucl. Inst. and Methods 68 (1969) 77

95. R. P. Singhal, H. Purdie, A. Cave, E. Pearce and R. Caplan, Nucl. Inst. and Methods 73 (1969) 237

96. W. J. Wallac, A. E. Bisson and R. H. Davis, Nucl. Inst. and Methods 68 (1969) 337

97. T. H. Hsu and J. M. Robson, Nucl. Inst. and Methods 39 (1966) 8

98. P. L. Okhuysen, E. W. Bennett, J. B. Ashe and W. E. Millet, Rev. Sci. Inst. 29 (1958) 982

99. C. F. Cook, Nucl. Inst. and Methods 15 (1962) 137

100. A. J. Frasca, R. W. Finlay, R. D. Koshel and R. L. Cassola, Phys. Rev. 144 (1966) 854

101. C. M. Bartle, et al. Nucl. Inst. and Methods 95 (1971) 221

102. M. C. Gupta and G. E. Tripard, Can. J. Phys. 51 (1973) 121

103. W. G. Cross, Rev. Sci. Inst. 22 (1951) 717

104. S. E. Hunt and E. C. Fellows, Nucl. Inst. and Methods 16 (1962) 326

105. E. Segrè, "Experimental Nuclear Physics" Vol.1 Part V (1953) John Wiley and Sons, Inc.

106. F. S. Goulding and W. L. Hansen, Nucl. Inst. and Methods 12 (1961) 249

107. H. C. Roters, "Electromagnetic Devices", Chapt. VII (1941) John Wiley and Sons, Inc.

108. C. M. Bartle and H. O. Meyer, Nucl. Inst. and Methods 112 (1973) 615

109. R. C. Curtis, J. L. Fowler and L. Rosen, Rev. Sci. Inst. 20 (1949) 388

110. W. Franzen, P. Huber and L. Schellenberg, Z. Naturf. 10a (1955) 820

111. J. Topping, "Errors of Observation and their Treatment", The Institute of Physics and the Physical Society Monograph.